The Simulation of Contact Acoustic Non-linearity from a Semi-analytical Perspective

Von der Fakultät für Ingenieurwissenschaften,
Abteilung Bauwissenschaften,
der Universität Duisburg-Essen
zur Erlangung des akademischen Grades

Doktor der Naturwissenschaften (Dr. rer. nat.)

genehmigte Dissertation
von

Georg Jannis Bulling, M. Sc.

Tag der Einreichung: 01. Februar 2022
Tag der mündlichen Prüfung: 20. Juni 2022

Berichterinnen: Univ.-Prof. Dr.-Ing. habil. Carolin Birk
Univ.-Prof. Dr. rer. nat. Andrea Walther

DOI: 10.17185/duepublico/78403
URN: urn:nbn:de:hbz:465-20230606-084101-4

Abstract: One of the most common methods for non-destructive testing is ultrasonic inspection. The basic idea of this technique is to excite ultrasonic wave pulses inside the inspected structure. While propagating, the traveling wave packages interact with the flaws inside the material, and the analysis of reflected or transmitted signals reveals information about possible damage. The state-of-the-art evaluation methods to detect cracks and other types of damage are based on linear models for the wave-flaw-interaction. Detecting small and closed cracks is challenging because the ultrasonic waves lead to low reflected amplitudes. This thesis incorporates non-linear crack behavior due to contacting crack sides into the modeling of ultrasonic wave propagation to improve the detectability of small and closed cracks. A non-linearity index is obtained and utilized to evaluate the damage. Shell-like structures which act as a waveguide and can be simplified to a cross-sectional model are the focus of methods and applications described in this work.

Knowing the relationship between damage size and non-linearity index is required to assess the size of the so-called breathing cracks with contacting crack sides. A numerical model is needed to compute this relationship. The numerical model must take care of the crack tip singularity. In this thesis, the dependency of the crack tip singularity and the crack's contacting side is analyzed with the Scaled Boundary Finite Element Method (SBFEM). The crack tips are the only points with singular stress in the considered cases. This analysis is presented in a general manner such that many different material configurations can be investigated using the same method.

As the main contribution, two approaches for the simulation of breathing cracks are proposed. The first approach enriches the Finite Element Method on a triangulation with singular modes from the SBFEM. It is shown that this enrichment significantly reduces the approximation error in singular problems. The approach is straightforwardly automatable because only information contained in a standard triangulation is utilized. The enrichment with the singular modes is further extended through two contact models based on the Penalty Method and Lagrange Multiplier Method. In the presented implementation, the numerical experiments show that the Penalty Method leads to more precise results than the Lagrange Multiplier Method. The reference solution for the comparison is based on locally refined finite element meshes.

The second approach is based on the SBFEM-formulation for shape functions on polygonal meshes. A new formulation for a crack tip element is proposed. This element incorporates polynomial tractions and polynomial body loads and is shown to pass a patch-test. Also, it reaches higher-order convergence in non-singular problems. Additionally, the crack tip element significantly reduces the approximation error in dynamic simulations with singularities. Furthermore, this thesis shows that different polygonal meshes can be tied together with Lagrange multipliers. The mesh-tying serves as a preliminary study for the contact conditions with breathing cracks. Finally, the polygonal meshes with the presented shape functions are shown to be appropriate for parametric studies in the context of waveguides, including breathing cracks.

The parametric studies extend the evaluation of breathing cracks in waveguides: The non-linearity index mentioned above is examined depending on different damage parameters like crack length and crack angle, resulting in contour plots for different testing constellations varying excitation-mode, evaluation in reflection and transmission, as well as frequency dependency and defect parameter.

Zusammenfassung: Ultraschalluntersuchungen gehören zu den gängigsten Methoden in der Zerstörungsfreien Prüfung. Das Grundprinzip ist die Anregung von Ultraschallwellen in einem Bauteil. Während sich der Wellenpuls durch das Bauteil bewegt, interagiert er mit Fehlern innerhalb des Materials. Die Analyse der reflektierten und transmittierten Signale erlaubt Rückschlüsse auf mögliche Schäden im Bauteil. Die etablierten Auswertungsmethoden für die Detektion von Rissen und anderen Schäden basieren auf linearen Modellen, die die Interaktion von Riss und Ultraschallwelle beschreiben. Dabei stellen kurze, geschlossene Risse eine besondere Herausforderung dar, da die Ultraschallwellen an diesen zu sehr kleinen Amplituden der Reflektion führen. Diese Arbeit bezieht für eine bessere Detektion von kurzen, geschlossenen Rissen nichtlineare Risseffekte, die durch kontaktierende Rissflanken entstehen, mit ein. Ein Nichtlinearitätsindex ermöglicht die Bewertung der Schäden. Ein besonderes Interesse dieser Arbeit liegt dabei auf plattenartigen Bauteilen, die als Wellenleiter fungieren und sich zu zweidimensionalen Querschnittsmodellen vereinfachen lassen.

Um die Größe von klappernden Rissen bewerten zu können, muss der Zusammenhang zwischen der Rissgröße und dem Nichtlinearitätsindex bekannt sein. Um diesen Zusammenhang zu erhalten, sind numerische Simulationen notwendig. Risse sollten bei vielen numerischen Simulationen durch ein gesondertes Verfahren für die Rissspitze behandelt werden, da diese eine Spannungssingularität aufweist. Mithilfe der "Scaled Boundary Finite Element Methode" (SBFEM) klärt diese Arbeit, wie die Spannungssingularität von den sich kontaktierenden Rissflanken abhängt. Es wird eine Argumentationskette vorgestellt, wonach die Rissspitzen die einzigen Punkte mit singulären Spannungen sind und wie diese Aussage für verschiedenste Materialkonstellationen bestätigt werden kann.

Als Hauptbeitrag, werden zwei verschiedene Verfahren für die Simulation von Rissen unter dynamischen Kontaktbedingungen präsentiert. Das erste Verfahren erweitert die Finite Elemente Methode auf dreieckigen Elementen um eine Anreicherung mit singulären Moden aus der SBFEM. Es wird gezeigt, dass die Anreicherung den Fehler in singulären Problemen signifikant senkt. Das Verfahren zeichnet sich durch seine hohe Automatisierbarkeit aus, da es nur Informationen verwendet, die in einer Standardtriangulation vorhanden sind. Die Anreicherung mit singulären Moden wird um zwei Kontaktalgorithmen basierend auf der "Penalty Method" und der "Lagrange Multiplier Method" erweitert. Numerische Versuche zu dem Verfahren zeigen, dass die "Penalty Method" genauere Ergebnisse liefert. Dabei dienen Approximationen auf lokal verfeinerten Gittern als Referenzlösungen.

Das zweite Verfahren basiert auf der SBFEM-Formulierung für Formfunktionen auf polygonalen Gittern. Hier wird eine neue Formulierung für ein Rissspitzenelement vorgestellt, das sowohl polynomiale Randkräfte als auch polynomiale Körperkräfte abbilden kann. Dieses Element wird untersucht und gezeigt, dass es sowohl Patch-Tests besteht als auch in analytischen, nicht-singulären Beispielen höhergradige Konvergenz erreicht. Es werden numerische Versuche zu dynamischen Simulationen mit Spannungssingularitäten vorgestellt und gezeigt, dass auch dieses Verfahren den Fehler signifikant reduziert. Weitere Untersuchungen präsentieren, dass man mehrere verschiedene polygonale Gitter mit Lagrange Multiplikatoren zusammenfügen kann. Dies wird als Vorstudie für die Kontaktbedingungen an klappernden Rissen durchgeführt. Es wird gezeigt, dass sich polygonale Gitter mit den präsentierten Formfunktionen zum Durchführen von parametrischen Studien an Wellenleitern mit klappernden Rissen eignen.

Die parametrischen Studien erweitern die Erkenntnisse zu klappernden Rissen in Wellenleitern. Der oben angesprochene Nichtlinearitätsindex wird in Abhängigkeit von verschiedenen Defektparametern wie Risslänge und Winkel untersucht. Das Ergebnis sind Höhenkarten für mehrere Testkonstellationen. Variiert werden die Anregungsmode, Auswertung in Reflektion und Transmission, sowie Frequenzabhängigkeit und Defektparameter.

Contents

Nomenclature **ix**

1 Introduction for the Simulation of Contact Acoustic Non-linearity **1**
1.1 Modelling Aspects of CAN . . . 2
1.2 Scope of the Thesis . . . 3

2 Mathematical Background **5**
2.1 The Galerkin Method for Linear Elasticity . . . 5
2.2 General Structure of Mesh-Based Approximations . . . 7
2.2.1 Nodal Shape Functions . . . 8
2.2.2 General Structure of Contact Algorithms . . . 13

3 Singularities in Static Problems **17**
3.1 Contact and Points of Singularity . . . 18
3.1.1 Different Contact Zones . . . 19
3.1.2 Modelling Cracks and Delaminations with a Contact Model . . . 19
3.1.3 The Interface Crack between two Isotropic Materials . . . 21
3.1.4 The Interface Crack for two Anisotropic Materials . . . 23
3.1.5 Dynamic Cases . . . 23
3.2 Semi-analytical Methods for the Computation of Stress Singularities . . . 23
3.3 The Scaled Boundary Shape Functions for a Single Super-element . . . 24
3.3.1 SBFEM Solution by Case-by-Case Analysis for Frictionless Contact . . . 27
3.3.1.1 SB Shape Functions of the Separation Case for a Polygonal Element 27
3.3.1.2 SB Shape Functions of the Slip Case for a Polygonal Element . . . 28
3.4 Numerical Experiments for the Eigenvalues . . . 29
3.4.1 Transition between a Frictionless Contact Zone and a Separation Zone by Direct Elimination . . . 29
3.4.2 Isotropic Case . . . 31
3.4.3 Transverse Isotropic Case . . . 32
3.4.4 Conclusion on the Transition Problem . . . 32
3.5 The Galerkin Approach for SB Shape Functions . . . 32
3.5.1 Static Stiffness Matrix . . . 33
3.5.2 Mean Gap Matrix . . . 34
3.5.3 SB Shape Function with Traction Bubble Functions . . . 35
3.5.4 Lagrange Multiplier Matrix for Domains with Common Scaling Center . . . 37
3.5.5 Lagrange Multiplier Method for a Single Super-element . . . 38
3.6 Numerical Experiments for Loaded Structures . . . 38
3.6.1 Patch Test of a Domain with a Crack . . . 39
3.6.2 Test with a Non-polynomial Traction of a Domain with a Crack . . . 39
3.6.3 Test of a Domain with an Interface Crack between two Materials . . . 39
3.6.4 Conclusion for Loaded Structures . . . 41
3.7 Introduction to the Construction of the Enrichment Functions . . . 42
3.8 Construction of the Enrichment Functions . . . 43
3.9 Numerical Treatment of the Singular Behavior . . . 47
3.9.1 Graded hp-refined Gauss Quadrature . . . 47

3.9.2 Computation of Stress Intensity Factors (SIFs) . . . 47
3.9.2.1 Stress-based Evaluation of the Stress Intensity Factors . . . 48
3.9.2.2 Displacement-based Evaluation of the Stress Intensity Factors . . . 48
3.10 Numerical Examples for the Enrichment Approach . . . 49
3.10.1 Polygonal Domain with DIRICHLET Boundary Conditions . . . 49
3.10.2 Crack under Shear . . . 51
3.10.3 Bi-material Crack under Tension . . . 52
3.10.4 Crack under Tension at an Anisotropic-Isotropic Interface . . . 53
3.10.5 Multiple Singularities . . . 55
3.11 Conclusion for the Enrichment Approach . . . 55

4 Linear Dynamic Problems 59
4.1 SB Shape Functions with Body Loads . . . 60
4.2 SB Shape Functions with Body Loads and Traction Functions . . . 62
4.3 Derivation of the Mass Matrix . . . 62
4.4 Summary of the Matrices Analysis for the SB Shape Functions . . . 63
4.5 Polygonal Meshes and their h-refinement . . . 64
4.6 Numerical Experiments for the SB Shape Functions . . . 66
4.6.1 Error Analysis for an Analytical Case in the Trapezoidal Domain . . . 66
4.6.2 Convergence Analysis for the Eigenfrequencies . . . 69
4.6.3 Comparison with the Finite Element Method . . . 70
4.7 Theory for Dynamic Problems with Singularity . . . 71
4.8 Numerical Experiments for Dynamic Problems with Singularity . . . 72
4.8.1 L-shaped Domain under Dynamic Load . . . 72
4.8.2 Waveguide with a Crack . . . 72
4.9 Conclusion to Dynamic Problems with Singularities . . . 76
4.10 Dynamic Problems with Continuity Conditions . . . 77
4.11 Methods for Continuity Conditions . . . 77
4.11.1 LAGRANGE Multiplier Method (LMM) . . . 78
4.11.2 Direct Elimination Method (DEM) . . . 79
4.11.3 Penalty Method (PM) . . . 80
4.11.4 NITSCHE Method . . . 81
4.11.5 Other Methods . . . 82
4.12 Aspects of Discrete Boundaries . . . 82
4.13 Numerical Experiments with Continuity Conditions . . . 83
4.13.1 Patch Test for LMM, DEM, and PM . . . 83
4.13.2 Domains with Internal Interfaces . . . 84
4.13.3 Tests with Vanishing Normal Gap . . . 85
4.14 Conclusion for Continuity Conditions . . . 87

5 Dynamic Contact Problems 89
5.1 Model problem for CAN . . . 90
5.1.1 Time Stepping Scheme for Contact Problems . . . 90
5.2 Generalized α-Method . . . 91
5.3 Numerical Experiments for CAN . . . 95
5.3.1 Comparison with ANSYS . . . 95
5.3.2 Waveguide with a Breathing Crack . . . 96
5.3.3 Waveguide with a Breathing Delamination . . . 101
5.3.4 Waveguide with Multiple Cracks . . . 102
5.4 Conclusion for CAN . . . 104

6 Conclusion and Outlook 107
6.1 Conclusion . . . 107
6.2 Outlook . . . 109

A Appendix **111**
A.1 Additional Information about Material Models 111
A.1.1 Isotropic Material 111
A.1.2 Transversely Isotropic Material 112
A.1.3 Rotation Matrix 112
A.1.4 Plane Strain and Plane Stress 113
A.1.5 Tables 113
A.2 Appendix Matrix Decompositions 114
A.3 hp-refined Quadrature 115

References **127**

List of Figures **129**

List of Tables **133**

Acknowledgement **135**

Nomenclature

Abbreviations

eFEM	enriched Finite Element Method (Section 3.8)
FEM	Finite Element Method (Section 2.2.1)
GLL-points	Gauss-Lobatto-Legendre-points
GW	Guided Wave
HHT	Hilber-Hughes-Taylor
IGA	IsoGeometric Analysis
LBB	Ladyzhenskaya–Babuška–Brezzi
NDT	Non-Destructive Testing
NTN	node-to-node (contact detection)
NTS	node-to-segment (contact detection)
ODE	ordinary differential equation
SB	Scaled Boundary
SBFEM	Scaled Boundary Finite Element Method (Section 3.3)
SBpoly	Scaled Boundary POLYgonal shape functions (Section 4.4)
SHM	Structural Health Monitoring
STS	segment-to-segment (contact detection)
VEM	Virtual Element Method
XFEM	eXtended Finite Element Method
XIGA	eXtended IsoGeometric Analysis

Lowercase Greek Letters

α	first mismatch parameter
$\hat{\alpha}$	first local coordinate for a triangle
β	second mismatch parameter
$\hat{\beta}$	second local coordinate for a triangle
δ_{ij}	Kronecker-delta
$\boldsymbol{\gamma}$	element boundary curve for the SBFEM
ϵ	penalty function

ϵ_0	penalty parameter
ϵ	oscillation index
$\underline{\underline{\boldsymbol{\varepsilon}}}$	linear strain tensor
$\boldsymbol{\varepsilon}$	strain in VOIGT-notation
$\hat{\eta}$	local coordinate for the SBFEM
κ	KOLOSOV constant
λ, λ_k	eigenvalue of $\mathbf{Z}$
$\lambda_{\min}$	minimal non-zero eigenvalue
$\boldsymbol{\delta\lambda}, \delta\lambda$	virtual LAGRANGE multiplier
$\boldsymbol{\lambda}, \lambda$	LAGRANGE multiplier
ν	POISSON's ratio
$\xi, \boldsymbol{\xi}$	local coordinates
$\xi_j, \boldsymbol{\xi}_j$	local node
$\hat{\xi}$	local coordinate for the SBFEM
ρ	density
$\underline{\underline{\boldsymbol{\sigma}}}$	linear stress tensor
$\boldsymbol{\sigma}$	stress in VOIGT-notation
$\bar{\boldsymbol{\tau}}$	formally extended traction
τ_0	characteristic pressure
$\bar{\boldsymbol{\tau}}$	mean traction flux
$\tau_{\mathbf{n}}$	normal contact pressure
$\tau_{\mathbf{t}}$	tangential contact pressure
$\boldsymbol{\tau}$	surface traction
φ	crack angle
$\boldsymbol{\phi}$	particular solution in the SBFEM
$\boldsymbol{\varphi}_e$	element mapping
$\boldsymbol{\psi}$	analytical mode
$\boldsymbol{\psi}^\theta$	θ dependent part of an analytical mode
$\boldsymbol{\psi}^r$	r dependent part of an analytical mode
$\boldsymbol{\psi}_k$	analytical mode
$\boldsymbol{\psi}_k^\theta$	analytical circumferential mode
$\boldsymbol{\psi}_u$	SBFEM mode
ω_j	quadrature weight
$\boldsymbol{\omega}$	vector of eigenfrequencies

Uppercase Greek Letters

Γ	general boundary
Γ_{ad}	boundary with adhesion conditions
Γ_c	boundary with contact conditions
$\Gamma_{\boldsymbol{\gamma}}$	boundary along the curve $\boldsymbol{\gamma}$
Γ_n	boundary with NEUMANN conditions
Γ_{sl}	boundary with sliding conditions
Γ_{sp}	boundary with separation conditions
Γ_{st}	boundary with stick conditions
Γ_u	boundary with DIRICHLET conditions
Γ_ξ	boundary in scaling direction
$\boldsymbol{\Theta}_\tau$	power matrix due to polynomial tractions
$\boldsymbol{\Theta}_n$	power matrix due to polynomial body loads
$\boldsymbol{\Lambda}$	eigenvalue matrix
$\boldsymbol{\Phi}_\tau$	mode matrix due to polynomial tractions
$\boldsymbol{\Phi}_b$	mode matrix due to polynomial body loads
$\boldsymbol{\Psi}_q$	SCHUR block associated with the inner forces
$\boldsymbol{\Psi}_u$	SCHUR block associated with the displacement

Lowercase Latin Letters

a	characteristic crack length
$\mathbf{a}$	acceleration vector
$\mathbf{a}^p$	predictor of the nodal acceleration vector
$\hat{\boldsymbol{b}}_1, \hat{\boldsymbol{b}}_2$	component matrix
c^{friction}	general friction coefficient
$c_{\text{sl}}^{\text{friction}}$	friction coefficient in the case of sliding
$c_{\text{st}}^{\text{friction}}$	friction coefficient in the case of stick
$\mathbf{c}, \mathbf{c}_1, \mathbf{c}_2$	coefficent vector
d	dimension
$\mathfrak{d}$	DUFFY's transformation
$\hat{e}$	reference element
$\mathbf{e}_i$	i-th unit vector
e	element index
$\boldsymbol{f}$	body load total force for the SBFEM
$\mathbf{f}$	total force vector

$\mathbf{f}^p$	predictor of the nodal force vector
f_0	center frequency
g	gap function
$\overline{g}$	mean gap function
$\mathbf{g}$	nodal gap vector
h	element size
h	shift function
i	imaginary unit
$\mathbf{j}_i^{-1}$	i-th row of the inverse JACOBIAN matrix
j	JACOBIAN determinante
$\mathrm{n}_{\mathrm{node}}$	number of nodes
$\mathbf{n}$	normal vector
p	polynomial degree
$\boldsymbol{q}$	inner nodal forces
q	polynomial degree
r	convergence rate
$\mathbf{r}$	nodal residual vector
$\mathfrak{s}$	scaled boundary transformation
$\mathbf{t}$	triangle transformation
tol	numerical tolerance
$\mathbf{t}$	tangential vector
$\boldsymbol{u}$	displacement
$\boldsymbol{\delta u}$	virtual displacement
$\mathbf{u}$	nodal displacement
$\mathbf{u}^p$	predictor of the nodal displacement vector
$\boldsymbol{v}$	nodal displacement and inner nodal forces
$\mathbf{v}$	velocity vector
$\mathbf{v}^p$	predictor of the nodal velocity vector
$\boldsymbol{w}$	TAYLOR term
$\mathbf{w}$	nodal displacement and LAGRANGE multiplier vector
$\mathbf{w}_\ell$	nodal TAYLOR-term
$\mathbf{x}^c$	scaling center
$\mathbf{x}$	spatial coordinate

Uppercase Latin Letters

$A^{\max}$	maximal amplitude for normalization
$\mathcal{A}$	active set
$\mathbb{A}$	assembly operator
$\mathbf{A}$	amplitude vector
$\hat{\boldsymbol{B}}_1, \hat{\boldsymbol{B}}_2$	component matrix of the shape functions
$\mathbb{C}$	complex numbers
C_K	coefficient for SIF evaluation
$\mathcal{C}$	genral constant
$\mathbf{C}$	SCHUR complement of a saddle point problem
$\mathbf{D}$	elastic matrix in VOIGT notation
$\underline{\underline{\mathbf{D}}}$	elastic tensor
$\mathbf{E}_0, \mathbf{E}_1, \mathbf{E}_2$	SBFEM-coefficient-matrix
$\mathrm{D}_{\mathbf{u}}$	total derivative with respect to $\mathbf{u}$
$\mathcal{E}$	energy
E	YOUNG's modulus
$\mathbf{G}$	gap matrix
G	shear modulus
$\mathrm{H}^k(\Omega)$	k-th SOBOLEV-space for p=2
$\mathbf{H}$	transformation matrix for shape functions
$\mathbf{H}_c$	local transformation matrix for shape functions
$\mathbf{I}$	identity matrix
$\mathbf{I}_{\mathrm{d}}$	identity matrix of size d
$\mathbf{J}$	JACOBIAN matrix
K_c	complex SIF
K_I, K_{II}	first and second SIF
$\mathbf{K}$	static stiffness matrix
$\boldsymbol{\mathcal{K}}$	non-linear displacement operator
L_0	characteristic length
L^2	space of square-integrable functions
$\mathbf{L}$	LAGRANGE multiplier matrix
$\mathcal{L}$	elastic differential operator in VOIGT notation
$\boldsymbol{M}$	matrix of shape functions for the boundary in the SBFEM
M_i	single shape function for the boundary in the SBFEM

$\mathbf{M}$	mass matrix
$\mathbf{M}_0$	boundary mass matrix
$\boldsymbol{N}^{\boldsymbol{\gamma}}$	ordinarily matrix of shape functions associated with the curve $\boldsymbol{\gamma}$
$\boldsymbol{N}$	shape function
$\boldsymbol{N}^{\lambda}$	LAGRANGE multiplier matrix of shape functions
$\boldsymbol{N}^{\mathbf{u}}$	displacement matrix of shape functions
$\boldsymbol{N}^{*}$	enrichment shape function
$\boldsymbol{N}$	matrix of shape functions
$\hat{\boldsymbol{N}}$	local matrix of shape functions
$\mathbf{N}$	NITSCHE matrix
NI	non-linearity index
$\mathbb{N}$	natural numbers
$\mathbf{N}$	normal matrix in VOIGT notation
$\boldsymbol{P}$	polynomial basis
$\mathbf{P}$	pre-multiplier coefficient matrix for the SB shape functions
P	point
$\mathcal{P}$	polynomial space
$\mathcal{P}$	closest point projection
$\mathbf{Q}$	general unitary matrix
$\boldsymbol{\mathcal{R}}$	non-linear residual
$\mathbf{R}$	rotation matrix
$\mathbb{R}$	real numbers
$\mathbf{S}$	power matrix for the SB shape functions dynamic or static stiffness matrix
$\mathbf{S}_n$	block diagonal SCHUR matrix for the non-positive eigenvalues
$\mathbf{S}_p$	block diagonal SCHUR matrix for the non-negative eigenvalues
$\mathbf{T}$	post-multiplier coefficient matrix for the SB shape functions
$\mathbf{U}$	quasi-upper triangular matrix
$\mathbf{V}$	generalized VANDERMONDE-matrix eigenvector matrix
$\mathcal{V}$	VOIGT operator (Equation (2.5))
$\mathbf{W}$	TAYLOR matrix for tractions or body loads
$\mathbf{X}, \mathbf{X}^{\lambda}$	matrix for LYAPUNOV-equation
$\mathbf{Y}, \mathbf{Y}^{\lambda}$	matrix for LYAPUNOV-equation
$\mathbf{Z}$	First-order coefficient matrix for the SBFEM

Other Symbols

$(\cdot)_{(a)}, (\cdot)^{(a)}$	associated with side/domain (a)
$(\cdot)_{(b)}, (\cdot)^{(b)}$	associated with side/domain (b)
Δt	time step
$\boldsymbol{\Delta u}$	second variation of the displacement
$\mathbf{A}^{\mathsf{H}}$	conjugate transpose of $\mathbf{A}$
$\mathbf{A}^{\mathsf{T}}$	transposed matrix of $\mathbf{A}$
$\#\,\mathrm{DoF}$	number of degrees of freedom
$\otimes$	KRONECKER-product
∂_x	partial derivative with respect to x
$\boldsymbol{\Delta}\mathbf{u}$	second nodal variation of the displacement
$\boldsymbol{\Delta}\mathbf{w}$	second variation
$\boldsymbol{\nabla}$	nabla operator

Chapter 1

Introduction for the Simulation of Contact Acoustic Non-linearity

Damage to engineering structures poses a risk to structural integrity and durability. Without an early awareness of the damage, damage growth can potentially lead to tragic consequences for the people relying on the integrity of the structures. Thus, finding the damage and monitoring its growth is important for many areas of engineering.

Finding and characterizing damage in its early stages is one of the main parts of Non-Destructive Testing (NDT) and Structural Health Monitoring (SHM) [53]. Here, SHM is regarded as permanent monitoring, while NDT includes tests that are repeated at certain time intervals. Test engineers can utilize ultrasonic waves to detect and locate damage, among other methods. For this active method, the basic principle is as follows. A transmitter is put on the surface of a test object to excite ultrasonic waves which propagate inside it. Then, the waves are recorded with the same transmitter in a receiving mode or by sensors at other locations. If the test object is damaged, additional reflections or damping will occur. For passive methods, only natural sources of ultrasonic waves are utilized, for example, induced by crack growth events. In this thesis, we will concentrate on active methods. An active approach's reflected, or transmitted signals can be evaluated in different ways to gather information about the location, the size, and other damage features.

In most cases, ultrasonic wave packages or short pulses are used. The amplitude and travel time can be evaluated in the time domain for these pulses, while the spectrum can be analyzed in the frequency domain. If the surface of the structure is scanned, e.g., with a laser vibrometer, also the wavenumber [84] can be evaluated. The test engineer must further use the gathered data to assess the damage qualitatively and quantitatively. This assessment, however, currently relies mainly on a linear model of the ultrasonic propagation [18]. While these linear models have been successfully utilized for many years, there are some cases where the linear effects are not sensitive enough to detect the damage. One of these examples is nearly closed cracks [169]. For closed crack, a special evaluation can be applied with a non-linear model [18].

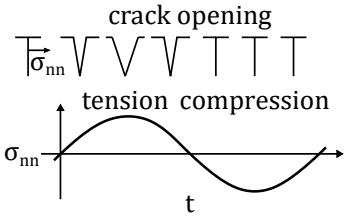

Figure 1.1: Schematic diagram of a breathing crack

The nearly closed cracks are called "breathing" or "clapping" cracks. Figure 1.1 illustrates the "breathing" motion. A breathing crack is very thin. For such a thin crack, the compressive part of the ultrasonic wave will close the gap, and the contact pressure will transfer the energy partly from one crack face to the other [75]. The tension part of the wave will open the crack, and

thus, the crack face will reflect the energy. Breathing cracks are one example of Contact Acoustic Non-linearity (CAN), where the non-linear effect is induced by contacting surfaces.

The effects of CAN and especially breathing cracks were analyzed experimentally [128]. The non-linear effect leads to the generation of higher harmonics, which is better observable if a narrow-band signal is excited. These higher harmonics are evaluated with a non-linear damage parameter, which is linked to the damage severeness [123–125]. A numerical model is helpful to predict the non-linear effects and evaluate these quantitatively. Because of the complexity of the problem, a numerical model is more promising than an analytical model. Most studies [73, 75, 76, 97, 110, 123–125, 155] approximate the ultrasonic wave with the Finite Element Method (FEM). The two main models will follow later. Only a few approaches [76] among those cited above try to incorporate previous knowledge about the mathematical model of cracks, namely the singular stress at the crack tip, in their approximation method. It is well known that the stress near the crack tip in an isotropic material can be approximated with $r^{-0.5}$, where r is the radius from the crack tip [40, 157]. The singular stress, however, reduces the quality of Finite Element models for uniform refinement [107, 147, 148].

The second aspect of this thesis is that mainly guided waves (GWs) are studied. Ultrasonic waves propagate as guided waves in many shell-like structures, such as plates, pipes, or laminate components. A shell-like structure acts as a waveguide if its thickness is in the same order of magnitude as the wavelengths of bulk waves. Here, the boundary reflections will lead to constructive and destructive interferences, such that the wave can only propagate in specific modes. On the one hand, GWs facilitate comparably long inspection ranges in NDT applications, making them applicable even for larger shell structures. On the other hand, the GWs are dispersive, meaning that their phase and group velocities are not equal and change as a function of the frequency and thickness of the waveguide. The dispersive and multi-modal nature of GWs requires special considerations in many applications. For example, some modes are more sensitive to a specific damage type than others, so it is of interest to evaluate the non-linear damage parameter separately for different modes [123–125].

1.1 Modelling Aspects of CAN

There are mainly two models for the simulation of CAN, which will be summarized in the following.

Modelling CAN as a Discrete Crack Many researchers assume that damage can be modeled as an internal boundary [73, 76, 110, 123–125, 155]. This assumption is prevalent when modeling cracks and delaminations. It is derived intuitively from the observation of cracks but also includes some simplifying assumptions. In contrast to natural cracks with rough surfaces [18, 146], the modeled damage is often assumed to be straight or with only a slight curvature. The actual crack geometry is nearly always much smaller than the geometric features that can be resolved by a numerical method [18]. Additionally, the thickness of the damage is often neglected and assumed to be zero. These are the well-known assumptions of Linear Fracture Mechanics [4, 31, 50]. However, these assumptions also lead to the prediction of singular stress concentrations on the edge of the damage. On the other hand, the singular stress explains why cracks are growing. The strength of the singularity is usually captured by the Stress Intensity Factors, which indicate whether the crack is growing or not.

For the “breathing” crack, a contact model is needed. In principle, there is a possibility of considering the various laws of friction and the surface structure [18, 146]. In practice, however, these quantities are mostly unknown. Therefore, an idealized crack structure and contact model must be assumed [76, 123]. This thesis concentrates on frictionless contact. According to the current literature and the author’s best knowledge, whether these idealizations significantly change the interaction of GWs and the “breathing” crack is unclear. The only investigations regarding ultrasonic waves consider bulk waves, longitudinal and transversal waves. They were done by Achenbach [2] and deal with the influence of the surface structure on the reflection behavior of “breathing” cracks.

In general, contact problems are not well-posed. As an example, a vibrating beam with a delaminated layer leads to chaotic behavior in the tested FE model [92]. The displacement field is

not globally differentiable, making many mathematical results - normally applicable to ultrasonic waves - invalid. These properties make a numerical model's performance challenging to predict a-priori.

Modelling CAN as a Non-linear Material A second option is to model the crack indirectly. Here, the crack's geometry is not included in the structure, but its influence in a certain area is modeled, which is then considered damaged. This area with a breathing crack will behave differently under compression than under tension (see Figure 1.1). This behavior can be considered by applying a non-linear material model, which results in different stresses depending on the sign of the strain. The material models range from simple piece-wise linear relationships between strain and stress [18] to more complex material models [75, 97]. The simulation of one-dimensional beams widely uses a non-linear material model for breathing cracks (see references in [18]), but it is also used for two-dimensional models [75, 97]. If "breathing" cracks are microscopic and below the resolution of the numerical model, this approach might be appropriate. Since these models do not directly incorporate the crack geometry, they offer qualitative rather than quantitative results [18]. On the other hand, the models explain the emergence of higher harmonics as the most important consequence of a "breathing" crack. Additionally, the material models described in [75, 97] are differentiable. A non-linear material model is likely to lead to numerically stable methods.

1.2 Scope of the Thesis

This thesis aims to develop numerical algorithms for the simulation of breathing cracks. Here, the direct modeling of cracks is used as it is more descriptive. Additionally, it is desired to know the size of a crack for SHM and NDT applications. Explicit modeling of cracks in the simulation can derive a relationship between the crack size and a damage index. The idea for developing the numerical method is to get additional insight into the problem of a "breathing" crack by applying a semi-analytical approach. The additional semi-analytical insight contributes to the formulation of different methods for two-dimensional simulations, and it is directly utilized. The simulation in two dimensions is a fundamental step before an extension to three dimensions can be achieved. Further reasons for a study of two-dimensional cases are the following. First, waveguides are usually studied in two-dimensional cross-sectional models due to the reduction to plane waves [65, 77, 125]. Second, crack problems in general, and especially "breathing" cracks, are often analyzed in two dimensions. As a result of this thesis, different models for the "breathing" crack are investigated for Galerkin approaches on triangular and polygonal meshes, which directly utilize the semi-analytical part in their shape functions. For this purpose, the fundamentals of the continuous Galerkin approach are presented in Section 2. Additionally, the general structure of acoustic contact algorithms is shown.

For the semi-analytical part, two things are required: 1) a contact-mechanical model and 2) a special method for calculating the singular stress behavior at the damage. Section 3 presents the analysis of cracks under contact conditions for static loads. Here, the dependency between contact and singular stress distributions is reviewed, verified, and enhanced with the semi-analytical Scaled Boundary Finite Element Method (SBFEM) [132, 137, 160, 161]. In this thesis, the SBFEM fulfills two functions. On the one hand, it allows the calculation of singular stress modes. On the other hand, it is used for the definition of shape functions on polygonal super-elements [31, 99]. The section clarifies, when the singular stress modes are dependent on the contact pressure and when these are independent of it. It is verified that the endpoints of cracks are the only points with singular stresses [49]. Analogously to [181], a new super-element for a crack tip is proposed Section 3, which incorporates polynomial tractions to represent the contact forces. In contrast to [181], it has fewer degrees of freedom. Additionally, an enrichment method of the FEM on triangular meshes is proposed. This method incorporates the singular SBFEM mode. It can be fully automatized and incorporated into existing FEM codes [23].

Section 4 extends the two SBFEM-based approaches, the polygonal super-elements, and the enrichment method, of the previous section to dynamic loading conditions. The polygonal super-elements of [98], which incorporate body load terms in the super-element, are investigated for all non-crack-tip elements. The new crack tip super-element is extended with degrees of freedom

associated with body loads to reach higher-order convergence for dynamic problems. Additionally, the polygonal super-elements and the enrichment approach from the Section 3 is evaluated with regard to their numerical performance in examples with singular stress distributions.

Because of the complexity of the non-linear contact conditions, benchmark problems are rare, making the verification of the method difficult. Therefore, a related problem is solved to test the approach for the contact forces. The related problem is the simulation of perfect bonds on non-matching interfaces. In the literature, the simulation of perfect bonds is commonly referred to as domain decomposition or the simulation of continuity conditions [20, 85, 158]. Different approaches for the realization of continuity and contact conditions are presented, namely the LAGRANGE Multiplier Method, the Direct Elimination Method, the Penalty Method, and the NITSCHE Method. All methods are framed as Mortar Methods. Mainly, the polygonal super-elements are tested in combination with the LAGRANGE Multiplier Method to show the stability of the approach.

The Section 5 finally considers the simulation of "breathing" cracks. The two techniques for the simulation of domains with singular stresses, namely the polygonal super-elements and the enrichment approach, are investigated with appropriate methods for the contact conditions. Here, a non-linearity index is defined. It is shown that the non-linearity index is an appropriate damage index for open "breathing" cracks in plates.

In Section 6, the conclusions are drawn. Additionally, an outlook points towards topics that could be further investigated. The Appendix A gives additional information about the material matrices, matrix decompositions, and a special numerical quadrature.

Chapter 2

Mathematical Background

This Chapter starts with the mathematical background of the simulation approach. It mainly contains the fundamentals, while the quintessence of the thesis is presented in the other sections.

2.1 The Galerkin Method for Linear Elasticity

The continuous Galerkin Method is a framework for many approximation approaches in numerical analysis. It is the underlying concept for the Finite Element Method (FEM) and its related methods: The Extended/Generalized Finite Element Method [56] (XFEM), the Isogeometric Analysis (IGA) [24, 34], the Virtual Element Method (VEM) [37], many meshless methods [95], and more. Additionally, the scaled boundary polygonal shape functions [72, 98, 181], which are studied in this thesis, can be utilized in the continuous Galerkin Method. It is worth mentioning that the discontinuous Galerkin Method [5] is another framework, which this thesis will not cover. Hence, all investigated approaches can be seen as a special form of the continuous Galerkin Method. In this section, we will derive the framework for a typical model problem for the simulation of ultrasonic waves.

Find the displacement $\boldsymbol{u}(\mathbf{x}, t)$ inside the domain $\Omega \subset \mathbb{R}^{\mathrm{d}}$, such that

$$\rho \partial_{tt} \boldsymbol{u} = \boldsymbol{\nabla} \cdot \underline{\underline{\boldsymbol{\sigma}}}(\boldsymbol{u}) + \boldsymbol{f} \qquad \mathbf{x} \in \Omega \tag{2.1}$$

with the density ρ, the second order stress tensor $\underline{\underline{\boldsymbol{\sigma}}}$ and the body loads $\boldsymbol{f}$. As a model problem, we consider the typical boundary condition for an ultrasonic test

$$\underline{\underline{\boldsymbol{\sigma}}}(\boldsymbol{u})\mathbf{n} = \boldsymbol{\tau} \qquad \mathbf{x} \in \Gamma, \tag{2.2}$$

where $\mathbf{n}$ is the outer normal vector and $\boldsymbol{\tau}$ a prescribed traction representing a Neumann boundary condition at the boundary Γ.

Due to the small displacements of an ultrasonic wave, the material and the strain can be linearized, i.e., the linear strain tensor $\underline{\underline{\boldsymbol{\varepsilon}}}$

$$\underline{\underline{\boldsymbol{\varepsilon}}} = \frac{1}{2}\big((\boldsymbol{\nabla}\boldsymbol{u})^{\mathsf{T}} + (\boldsymbol{\nabla}\boldsymbol{u})\big), \tag{2.3}$$

and Hooke's law

$$\underline{\underline{\boldsymbol{\sigma}}} = \underline{\underline{\mathbf{D}}} : \underline{\underline{\boldsymbol{\varepsilon}}}, \tag{2.4}$$

can be applied, where $\underline{\underline{\mathbf{D}}}$ is the fourth order elasticity tensor.

We switch to Voigt notation for a more convenient formulation, where the second-order stress tensor $\underline{\underline{\boldsymbol{\sigma}}}$ is expressed as a vector $\boldsymbol{\sigma}$. Define the Voigt operator $\mathcal{V}$ for linear elasticity for an

arbitrary vector field $\mathbf{a}$ of dimension d as follows:

$$\text{for d} = 1: \quad \mathcal{V}(\mathbf{a}) = a_1, \quad \text{for d} = 2: \quad \mathcal{V}(\mathbf{a}) = \begin{pmatrix} a_1 & 0 \\ 0 & a_2 \\ a_2 & a_1 \end{pmatrix}, \quad \text{for d} = 3: \quad \mathcal{V}(\mathbf{a}) = \begin{pmatrix} a_1 & 0 & 0 \\ 0 & a_2 & 0 \\ 0 & 0 & a_3 \\ 0 & a_3 & a_2 \\ a_3 & 0 & a_1 \\ a_2 & a_1 & 0 \end{pmatrix}. \tag{2.5}$$

With this notation, we introduce the differential operator

$$\mathcal{L} = \mathcal{V}(\nabla) \tag{2.6}$$

and the normal operator

$$\mathbf{N} = \mathcal{V}(\mathbf{n}). \tag{2.7}$$

Equation (2.1) in Voigt notation is

$$\rho \partial_{tt} \boldsymbol{u} = \mathcal{L}^\mathsf{T} \mathbf{D} \mathcal{L} \boldsymbol{u} + \boldsymbol{f} \qquad \mathbf{x} \in \Omega \tag{2.8}$$

with the elasticity material matrix $\mathbf{D}$ (see Appendix A.1) and the boundary condition

$$\mathbf{N}^\mathsf{T} \mathbf{D} \mathcal{L} \boldsymbol{u} = \boldsymbol{\tau} \qquad \mathbf{x} \in \Gamma. \tag{2.9}$$

All investigated approximation methods follow the so-called Galerkin approach. First, the weak form of Equation (2.8) is required for this approach. Pre-multiplying with a virtual displacement $\boldsymbol{\delta u}$, integrating over the domain Ω, using integration by parts and substituting the boundary conditions leads to

$$\int \rho \boldsymbol{\delta u}^\mathsf{T} \partial_{tt} \boldsymbol{u} \, \mathrm{d}\Omega = -\int (\mathcal{L} \boldsymbol{\delta u})^\mathsf{T} \mathbf{D} \mathcal{L} \boldsymbol{u} \, \mathrm{d}\Omega + \int \boldsymbol{\delta u}^\mathsf{T} \boldsymbol{f} \, \mathrm{d}\Omega + \int \boldsymbol{\delta u}^\mathsf{T} \boldsymbol{\tau} \, \mathrm{d}\Gamma, \tag{2.10}$$

which must be valid for all virtual displacements $\boldsymbol{\delta u}$.

The Galerkin approach follows by defining a matrix of shape functions $\boldsymbol{N} \colon \mathbb{R}^\mathrm{d} \to \mathbb{R}^{\mathrm{d} \times N}$, where N is the number of degrees of freedom, and approximating the virtual displacement $\boldsymbol{\delta u}$ as well as the displacement $\boldsymbol{u}$ as a linear combination of these shape functions with time-dependent vectors, i.e.,

$$\boldsymbol{\delta u}(\mathbf{x}, t) = \boldsymbol{N}(\mathbf{x}) \boldsymbol{\delta \mathbf{u}}(t) \qquad \boldsymbol{u}(\mathbf{x}, t) = \boldsymbol{N}(\mathbf{x}) \mathbf{u}(t) \tag{2.11}$$

with $\boldsymbol{\delta \mathbf{u}}(t), \mathbf{u}(t) \in \mathbb{R}^N$. Due to the arbitrariness of the virtual displacement, this leads to a system of ordinary differential equations in time for the unknown displacement vector $\mathbf{u}(t)$

$$\mathbf{M} \partial_{tt} \mathbf{u} = -\mathbf{K} \mathbf{u} + \mathbf{f} \tag{2.12}$$

with the mass matrix $\mathbf{M}$, the static stiffness matrix $\mathbf{K}$ and the load vector $\mathbf{f}$ given by

$$\mathbf{M} = \int \rho \boldsymbol{N}^\mathsf{T} \boldsymbol{N} \, \mathrm{d}\Omega, \tag{2.13}$$

$$\mathbf{K} = \int (\mathcal{L} \boldsymbol{N})^\mathsf{T} \mathbf{D} (\mathcal{L} \boldsymbol{N}) \, \mathrm{d}\Omega, \tag{2.14}$$

$$\mathbf{f} = \mathbf{f}_b + \mathbf{f}_\tau \tag{2.15}$$

$$= \int \boldsymbol{N}^\mathsf{T} \boldsymbol{f} \, \mathrm{d}\Omega + \int \boldsymbol{N}^\mathsf{T} \boldsymbol{\tau} \, \mathrm{d}\Gamma, \tag{2.16}$$

where $\mathbf{f}_b$ and $\mathbf{f}_\tau$ are associated with the body loads and tractions, respectively. Typically, the system of ordinary differential equations is then solved by numerical integration in time, for appropriate

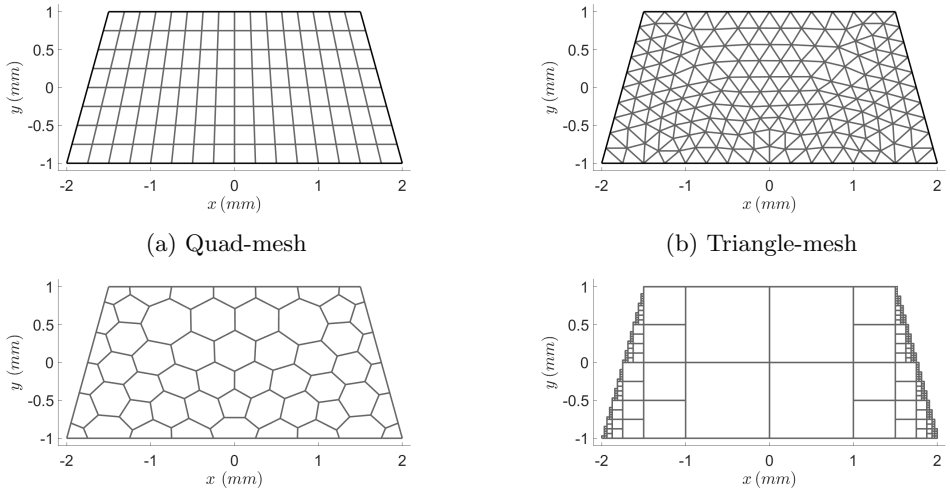

(a) Quad-mesh

(b) Triangle-mesh

(c) Polygon-mesh

(d) Quadtree-mesh

Figure 2.1: Different types of meshes for a trapezoidal domain

initial conditions. In this thesis, the implicit time schemes from the generalized α-Method are utilized (see Section 5.2).

This thesis constructs very different kinds of shape functions and compares them in their performance in theoretical examples as well as applications from the fields NDT and SHM. The goal is to construct high-performing shape functions for the simulation of CAN. For this, analytical insight into the problem should make the GALERKIN approach more effective. The target is to find shape functions that perform sufficiently well so that a complicated adaptive method [108, 173] is unnecessary. The following section summarizes approaches for the calculation of mesh-based shape functions. The most common type consists of the nodal shape functions, which build the FEM.

2.2 General Structure of Mesh-Based Approximations

One of the key aspects of the GALERKIN approach presented in the previous section is the choice of shape functions. While the approach is formulated very generally, most approximation algorithms use a mesh to define these shape functions. A mesh fulfills several tasks:

- The mesh approximates the domain Ω.
- The mesh defines the matrix of shape functions $\boldsymbol{N}$.
- The mesh can be refined to increase the number of shape functions and the accuracy of the approximation.
- The mesh often helps with the calculation of the spatial derivatives and spatial integrals in Equation (2.10).

The elements of a mesh can have different geometrical shapes, e.g., for 2D-meshes, the elements can be quads (Figure 2.1a), triangles (Figure 2.1b) or polygons (Figure 2.1c).

Many mesh-based methods do not allow a corner with a 180° inner angle. These corners are called *hanging nodes* and are present in a quadtree-mesh (Figure 2.1d). A quadtree-mesh is defined by iteratively choosing smaller quads that fit into the domain. The elements can be seen either as special quads [47] with hanging nodes or as polygons having corners with a 180° inner angle [100]. Even if quadtree meshes are not studied in detail in this thesis, they are an important type of meshes in the SBFEM literature and are presented here as an alternative scope of application for polygons. This thesis focuses on triangular and polygonal meshes (without degenerated polygons). Polygonal meshes are examined in more detail in Section 4.5.

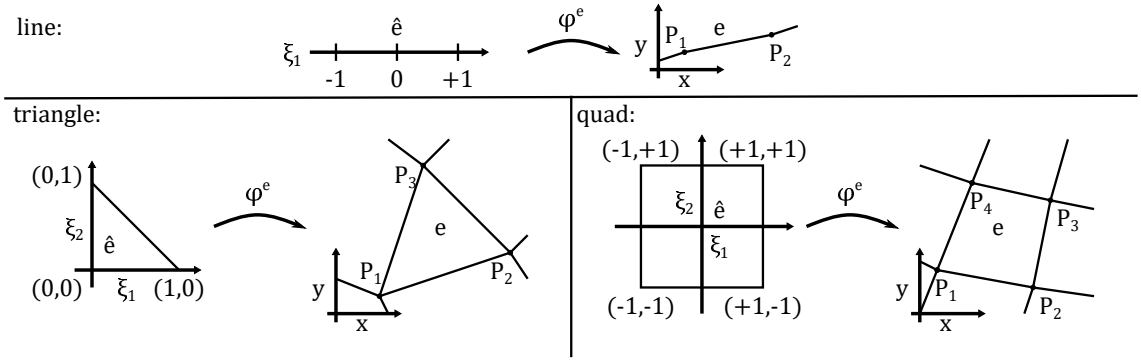

Figure 2.2: Element mappings

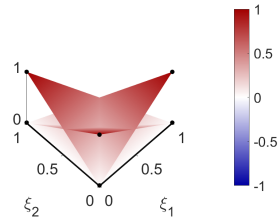

(a) All shape functions of a simplex with p=1

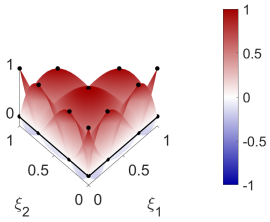

(b) All shape functions of a simplex with p=3

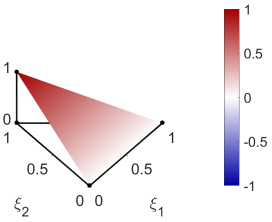

(c) A single shape function of a simplex with p=1

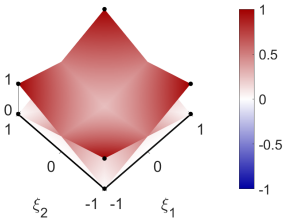

(d) All shape functions of a quad with p=1

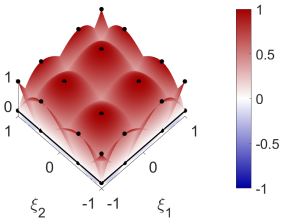

(e) All shape functions of a quad with p=3

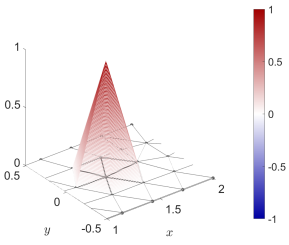

(f) A single shape function in global coordinates with p=1

Figure 2.3: Example of shape functions in 2D

2.2.1 Nodal Shape Functions

The most common shape functions are nodal shape functions. Other types of shape functions are summarized in Remark 2.2.4. For nodal shape functions on a triangle-mesh or a quad-mesh, the Galerkin Method leads to the classic FEM. These shape functions are one of the main building blocks of all approximations in this thesis. Their usage, however, is often in combination with other functions. Subsequently, only the fundamentals are summarized, while the combination with other functions will follow in other sections.

Nodal shape functions are assembled from one or more elements in the physical space. A physical element e is defined by a mapping $\boldsymbol{\varphi}^e$ and a reference element $\hat{e}$ - see Figure 2.2. We will start with the definition of nodal shape functions for the reference line element. Afterward, the shape functions for quads and triangles are defined. Finally, the global shape functions in the Galerkin approach are given.

Line element The i-th nodal shape function $\hat{N}_i^{\mathrm{p}}$ of degree p is the i-th Lagrange polynomial on the nodes $\xi_j \in [-1,+1]$ with $j = 1,\ldots,\mathrm{p}+1$. The Lagrange polynomial is the unique polynomial that fulfills the Kronecker-delta-property at the nodes, i.e.,

$$\hat{N}_i^{\mathrm{p}}(\xi_j) = \delta_{ij}. \tag{2.17}$$

For a line element, the shape functions are explicitly given by

$$\hat{N}_i^{\mathrm{p}}(\xi) = \prod_{1\leq j\leq \mathrm{p}+1, i\neq j} \frac{(\xi - \xi_j)}{(\xi_i - \xi_j)}. \tag{2.18}$$

We follow the spectral element concept for the choice of nodes and use the Gauss-Lobatto-Legendre-points (GLL-points) as nodes. Here, $\xi_1 = -1, \xi_{\mathrm{p}+1} = +1$, and $\xi_2, \dots \xi_{\mathrm{p}}$ are the roots of the first derivative of the p-th Legendre-polynomial P_{p}. These points are quadrature points with the weights ω_j,

$$\omega_j = \frac{1}{\mathrm{p}(\mathrm{p}+1)\big(P_{\mathrm{p}}(\xi_j)\big)^2}, \tag{2.19}$$

which lead to an exact integration of polynomials of degree $2\mathrm{p}-1$. Besides their quadrature property, GLL-points also have the best interpolation properties, which are summarized in the following two remarks.

Remark 2.2.1 (Fekete-points)**.** *The* Fekete*-points are the choice of points, where the nodal shape functions lead to the smallest* Lebesgue*-constant, i.e., these points have the best interpolation properties (in a worst-case scenario) [15, 150].*

Remark 2.2.2 (GLL-points are Fekete-points)**.** *The GLL-points for a line and a quad are the* Fekete*-points [15, 150].*

For a more convenient notation, the shape functions are often merged into a single matrix function $\hat{\boldsymbol{N}}\colon \mathbb{R} \to \mathbb{R}^{1\times \mathrm{p}+1}$

$$\hat{\boldsymbol{N}}(\xi) = \begin{pmatrix} \hat{N}_1^{\mathrm{p}}(\xi) & \dots & \hat{N}_{\mathrm{p}+1}^{\mathrm{p}}(\xi) \end{pmatrix}. \tag{2.20}$$

In this thesis, the spectral element refers to the GLL-points, but it should be remarked:

Remark 2.2.3 (Spectral Element Method)**.** *The Spectral Element Method refers to the choice of GLL-points as well as* Gauss-Lobatto-Chebyshev*-points [51] in the literature. The* Gauss-Lobatto-Chebyshev*-points are defined by the roots of the* Chebyshev*-polynomials of the second kind and are explicitly given by*

$$\xi_j = -\cos\left(\frac{j-1}{\mathrm{p}}\pi\right). \tag{2.21}$$

The points are simpler to compute compared to GLL-points, but these points are not Fekete*-points.*

Quad element The nodes $\boldsymbol{\xi}_i$ for a quad element are defined by a tensor product of two sets of GLL-points with degree p_1 and p_2, respectively, i.e., $\boldsymbol{\xi}_j = (\xi_a, \xi_b)^{\mathsf{T}}$ with $a = 1, \dots, \mathrm{p}_1 + 1$, $b = 1, \dots, \mathrm{p}_2 + 1$ and an arbitrary linear index j, e.g., $j = a + (b-1)(\mathrm{p}+1)$. The GLL-points for a quad are also quadrature points with the weight $\omega_i = \omega_a \cdot \omega_b$. The nodal shape functions, which fulfil the Kronecker-delta-property $\hat{N}_i^{(\mathrm{p}_1,\mathrm{p}_2)}(\boldsymbol{\xi}_j) = \delta_{ij}$ are given by

$$\hat{N}_i^{(\mathrm{p}_1,\mathrm{p}_2)}(\boldsymbol{\xi}) = \hat{N}_a^{\mathrm{p}_1}(\xi_1)\hat{N}_b^{\mathrm{p}_2}(\xi_2), \tag{2.22}$$

where i is the linear index of $a = 1, \dots, \mathrm{p}_1 + 1$ and $b = 1, \dots, \mathrm{p}_2 + 1$.

In this thesis, the polynomial degrees are equal, i.e., $\mathrm{p} = \mathrm{p}_1 = \mathrm{p}_2$, if not stated otherwise. Figure 2.3d and 2.3e show all shape functions of a quad element for degree 1 and 3, respectively.

Triangle element To the best of the author's knowledge, the Fekete-points for a triangle are unknown. To be more precise, there are candidates - see [14, 16, 150] - but no proof of their optimality. We follow the approach in [14], where a simple grid of points is constructed from the GLL-points of a line. Their main feature is a symmetry under rotation if the points are mapped to an equilateral triangle.

We start with the mapping of the GLL-points of a line from $[-1,+1]$ to $[0,1]$: $\bar{\xi}_i = 0.5(\xi_i + 1)$. The nodes $\boldsymbol{\xi}_{i(a,b)}$ of degree p are defined as

$$\boldsymbol{\xi}_{i(a,b)} = \begin{pmatrix} \frac{1}{3}(1 + 2\bar{\xi}_a - \bar{\xi}_b - \bar{\xi}_c) \\ \frac{1}{3}(1 - \bar{\xi}_a + 2\bar{\xi}_b - \bar{\xi}_c) \end{pmatrix} \tag{2.23}$$

with $a = 1, \ldots, \mathrm{p}+1$, $b = 1, \ldots, \mathrm{p}+2-a$, $c = 1, \ldots, \mathrm{p}+3-a-b$ and a $i(a,b)$.

For the construction of the shape function, we will use the generalized VANDERMONDE-matrix. Let $\hat{\boldsymbol{P}}\colon \mathbb{R}^2 \to \mathbb{R}^{1\times n}$ with $n = \binom{\mathrm{p}+1}{2}$ be a matrix with a complete polynomial basis. Then, the generalized VANDERMONDE-matrix $\mathbf{V} \in \mathbb{R}^{n\times n}$ is

$$\mathbf{V} = \begin{pmatrix} \hat{\boldsymbol{P}}(\boldsymbol{\xi}_1) \\ \cdots \\ \hat{\boldsymbol{P}}(\boldsymbol{\xi}_n) \end{pmatrix}, \tag{2.24}$$

and the nodal matrix of shape functions $\hat{\boldsymbol{N}}$ is given by

$$\hat{\boldsymbol{N}}(\boldsymbol{\xi}) = \hat{\boldsymbol{P}}(\boldsymbol{\xi})\mathbf{V}^{-1}. \tag{2.25}$$

By construction, the single shape function fulfils the KRONECKER-delta-property $\hat{N}_i(\boldsymbol{\xi}_j) = \delta_{ij}$, where $\hat{N}_i$ is an entry of $\hat{\boldsymbol{N}}$. Theoretically, an arbitrary complete basis of polynomials can be used for the construction. For numerical reasons, the orthogonal polynomials by PRORIOL [14] are implemented because the condition number of $\mathbf{V}$ is much better compared to monomials. Figure 2.3a and 2.3b show all shape functions of a simplex element for degree 1 and 3, respectively.

Partition of unity The shape functions for lines, quads and triangles build a partition of unity, i.e.,

$$\sum_i \hat{N}_i(\boldsymbol{\xi}) = 1. \tag{2.26}$$

Vector valued shape functions Vector valued shape functions $\hat{\boldsymbol{N}}_\mathrm{d}$, which are needed for the displacement in 2D and 3D, can be constructed from the one dimensional matrix of shape functions $\hat{\boldsymbol{N}}_1$ by

$$\hat{\boldsymbol{N}}_\mathrm{d}(\boldsymbol{\xi}) = \hat{\boldsymbol{N}}_1(\boldsymbol{\xi}) \otimes \mathbf{I}_\mathrm{d}, \tag{2.27}$$

where $\otimes$ is the KRONECKER tensor product and $\mathbf{I}_\mathrm{d}$ is the d-dimensional identity matrix. This leads to separate shape functions for each dimension d. Moreover, for two dimensions, one obtains alternating shape functions for the two directions. The shape function of the first degree defines only a displacement in x-direction, while the shape function of the second degree represents only a displacement in y-direction, and so on.

The global shape functions The global vector valued shape functions $\boldsymbol{N}_i(\mathbf{x})$ are assembled over the adjacent elements, where $\boldsymbol{N}_i(\mathbf{x})$ is a column of the global matrix of shape functions $\boldsymbol{N}(\mathbf{x})$. Let $\boldsymbol{\varphi}^e\colon \hat{e} \to e$ be the map between the reference element $\hat{e}$ and the physical element e (see Figure 2.2), $\mathrm{n_{node}}$ the number of all nodes, and $N_{\hat{e}}$ be the number of nodes in this element. Then, the set of all global nodes is $\{\mathbf{x}_j : j = 1, \ldots, \mathrm{n_{node}}\} = \bigcup_e \{\boldsymbol{\varphi}^e(\boldsymbol{\xi}_\ell) : \ell = 1, \ldots, N_{\hat{e}}\}$. The global shape functions fulfil the following properties:

- The shape functions fulfil the global KRONECKER-delta-property $\boldsymbol{N}_i(\mathbf{x}_j) = \delta_{ij}\mathbf{e}_{k(i)}$, where $\mathbf{x}_j$, $j = 1, \ldots, \mathrm{n_{node}}$, are the global nodes and $\mathbf{e}_{k(i)}$ is one of the unit vectors depending on the index i.
- For each element e, it holds $\boldsymbol{N}_i(\boldsymbol{\varphi}^e(\xi)) = \hat{\boldsymbol{N}}_{\ell(i)}(\xi)$ for a local index ℓ.
- The shape functions must be continuous over an element's boundary.

Figure 2.3c shows a local shape function, which is a part of the assembled global shape function in Figure 2.3f. Here, only a scalar shape function is depicted.

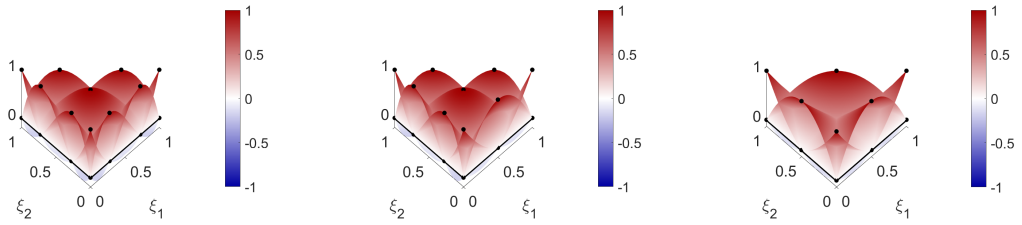

(a) All shape functions for a simplex with p = 3

(b) All shape functions for a simplex with p = 3 and a modified edge with a transition to q = 2

(c) A single shape function for a simplex with q = 2

Figure 2.4: Example of shape functions with a local degree; polynomial degree changes over an edge

Remark 2.2.4 (Other types of shape functions and connection methods)**.** *While this thesis considers only the nodal shape functions of the types which are presented above as well as the scaled boundary finite element shape functions, which are presented in Section 3 and 4, there is a large variability of possible alternatives. The following list should give an impression without raising a claim to completeness:*

- *serendipity shape functions for quads [47, 51], which have less nodes per element,*
- *hierarchical shape functions [47, 51],*
- *Non-Uniform Rational B-Splines (NURBS) [34], which are differentiable in larger sub-domains,*
- *the transfinite concept for quads with hanging nodes [47, 51],*
- *polygonal shape functions [55, 143].*

Additionally, there are concepts for differentiability across elements [67].

Local p-change over an edge In many applications, the polynomial degree is unchanged over the whole domain. If small and large elements are utilized in the same mesh, it can be advantageous to lower the polynomial degree for adjacent elements. The polynomial degree can be reduced by restricting the shape functions to the smaller degree q of the two elements. This technique is usually defined globally in the so-called hp-refined meshes, see e.g. [27, 39]. In the global formulation, hanging nodes can be considered. In this thesis, a local, nodal-based version is implemented, which only requires the polynomial degree q of the adjacent element - see Figure 2.4. This figure shows on the left-hand side the shape functions $\boldsymbol{N}$ of the high degree p = 3 (4 nodes), which will be the starting point. The central figure depicts the modified shape functions $\tilde{\boldsymbol{N}}$ with the first edge having three nodes. The right-hand side figure shows the degree q = 2 shape functions, which could connect to the modified shape functions. The modification process is based on the fact that shape functions of a higher degree can exactly represent shape functions of a lower degree and that LAGRANGE shape functions are used, which are interpolative at the nodes.

The modification process is explained for scalar shape functions. The vector-valued version can be constructed with Equation (2.27). Let $\boldsymbol{N}\colon \mathbb{R}^2 \to \mathbb{R}^{1\times n}$ be a matrix of shape functions with a degree p and p > q. Then, a matrix $\mathbf{H} \in \mathbb{R}^{n\times m}$ with $m = n - (\mathrm{p} - \mathrm{q})$ can be constructed, such that

$$\tilde{\boldsymbol{N}}(\boldsymbol{\xi}) = \boldsymbol{N}(\boldsymbol{\xi})\mathbf{H} \tag{2.28}$$

is a new set of shape functions $\tilde{\boldsymbol{N}}\colon \mathbb{R}^2 \to \mathbb{R}^{1\times m}$. For simplicity, assume that the first p + 1 shape functions are the ones to be modified and that only one edge needs modification. The transformation matrix takes the form

$$\mathbf{H} = \begin{pmatrix} \mathbf{H}^e & \mathbf{0} \\ \mathbf{0} & \mathbf{I}_{n-(\mathrm{p}+1)} \end{pmatrix} \tag{2.29}$$

with a smaller transformation matrix $\mathbf{H}^e \in \mathbb{R}^{\mathrm{p}+1\times\mathrm{q}+1}$ and the identity matrix $\mathbf{I}_{n-(\mathrm{p}+1)}$ of size $n-(\mathrm{p}+1)$. Let ξ_j, $j=1,\dots,\mathrm{p}+1$, be the one-dimensional nodes and $\hat{N}_i^q$ the i-th one-dimensional shape function of degree q, then

$$(\mathbf{H}^e)_{ji} = \hat{N}_i^q(\xi_j), \tag{2.30}$$

where $(\cdot)_{ji}$ is the j,i-th element and $i=1,\dots,\mathrm{q}+1$. Due to $\mathbf{H}^e$, the lower degree shape functions are interpolated at the nodes by the higher degree shape functions, and the basis gets smaller.

Element maps In general, the maps between the reference element and the physical element can be curved by applying the iso-parametric concept. The local shape functions are utilized for these mappings. In almost all examples, however, the linear and bi-linear mappings are used, i.e.,

$$\boldsymbol{\varphi}^e(\xi) = \mathrm{P}_1\, 0.5(1-\xi) + \mathrm{P}_2\, 0.5(\xi+1) \qquad \text{for lines,} \tag{2.31}$$

$$\boldsymbol{\varphi}^e(\boldsymbol{\xi}) = \begin{pmatrix}\mathrm{P}_2-\mathrm{P}_1 & \mathrm{P}_3-\mathrm{P}_1\end{pmatrix}\boldsymbol{\xi} + \mathrm{P}_1 \qquad \text{for triangles,} \tag{2.32}$$

$$\begin{aligned}\boldsymbol{\varphi}^e(\boldsymbol{\xi}) = {}& \mathrm{P}_1\, 0.25(1-\xi_1)(1-\xi_2)\\ &+ \mathrm{P}_2\, 0.25(\xi_1+1)(1-\xi_2)\\ &+ \mathrm{P}_3\, 0.25(\xi_1+1)(\xi_2+1)\\ &+ \mathrm{P}_4\, 0.25(1-\xi_1)(\xi_2+1) \qquad \text{for quads,}\end{aligned} \tag{2.33}$$

where the mesh control points P_i are ordered under the convention (see Figure 2.2). Most meshes in this thesis are generated with Gmsh [58]. The numbering of the control points can be found in the manual of Gmsh.

Computation of the global matrices As mentioned above, the mesh will also facilitate the computation of the integrals for the mass matrix $\mathbf{M}$, the static stiffness matrix $\mathbf{K}$ and the load vector $\mathbf{f}$ (Equations (2.13)-(2.16)). These matrices are assembled over the elements, i.e.,

$$\mathbf{M} = \mathop{\mathrm{A}}_{e\in\Omega} \mathbf{M}^e, \tag{2.34}$$

$$\mathbf{K} = \mathop{\mathrm{A}}_{e\in\Omega} \mathbf{K}^e, \tag{2.35}$$

$$\mathbf{f} = \mathop{\mathrm{A}}_{e\in\Omega} \mathbf{f}_b^e + \mathop{\mathrm{A}}_{e\in\Gamma} \mathbf{f}_\tau^e, \tag{2.36}$$

where $\mathbf{K}^e, \mathbf{M}^e, \mathbf{f}_b^e, \mathbf{f}_\tau^e$ are element based and A is the global assembly operator. The assembly operator is a notation that expresses the summation process of all local element matrices. Note that $\mathbf{f}_b^e$ is associated with the body load and assembled over the whole domain Ω, while $\mathbf{f}_\tau^e$ is associated with the traction and assembled over the boundary.

For the simple elements - lines, triangles and quadrilaterals - these local matrices for the element e are calculated as follows:

$$\mathbf{M}^e = \int_e \rho(\mathbf{x}) \boldsymbol{N}(\mathbf{x})^\mathsf{T} \boldsymbol{N}(\mathbf{x})\, \mathrm{d}\mathbf{x}, \tag{2.37}$$

$$\mathbf{K}^e = \int_e (\mathcal{L}\boldsymbol{N}(\mathbf{x}))^\mathsf{T} \mathbf{D}(\mathbf{x}) (\mathcal{L}\boldsymbol{N}(\mathbf{x}))\, \mathrm{d}\mathbf{x}, \tag{2.38}$$

$$\mathbf{f}_b^e = \int_e \boldsymbol{N}(\mathbf{x})^\mathsf{T} \boldsymbol{f}(\mathbf{x})\, \mathrm{d}\mathbf{x}, \tag{2.39}$$

$$\mathbf{f}_\tau^e = \int_e \boldsymbol{N}(\mathbf{x})^\mathsf{T} \boldsymbol{\tau}(\mathbf{x})\, \mathrm{d}\mathbf{x}. \tag{2.40}$$

We will carry on with the mass matrix $\mathbf{M}^e$ and the static stiffness matrix $\mathbf{K}^e$ - the load vectors are computed analogously. Let $\mathbf{J}_{\boldsymbol{\varphi}}(\boldsymbol{\xi})$ be the Jacobian matrix of the transformation, where the element index is dropped for convenience. Substituting $\mathbf{x} = \boldsymbol{\varphi}(\boldsymbol{\xi})$, $\boldsymbol{\varphi}(\hat{e}) = e$, $\boldsymbol{N}\big(\boldsymbol{\varphi}(\boldsymbol{\xi})\big) = \hat{\boldsymbol{N}}(\boldsymbol{\xi})$ and

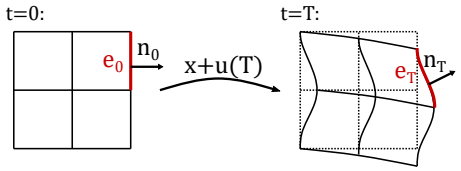

Figure 2.5: Finite deformation vs. small deformation

using the integral transformation leads to

$$\mathbf{M}^e = \int_{\hat{e}} \rho\big(\boldsymbol{\varphi}(\boldsymbol{\xi})\big)\hat{\boldsymbol{N}}(\boldsymbol{\xi})^\mathsf{T}\hat{\boldsymbol{N}}(\boldsymbol{\xi})j(\boldsymbol{\xi})\,\mathrm{d}\boldsymbol{\xi}, \tag{2.41}$$

$$\mathbf{K}^e = \int_{\hat{e}} (\mathcal{L}\hat{\boldsymbol{N}}(\boldsymbol{\xi}))^\mathsf{T}\mathbf{D}(\boldsymbol{\varphi}(\boldsymbol{\xi}))(\mathcal{L}\hat{\boldsymbol{N}}(\boldsymbol{\xi}))j(\boldsymbol{\xi})\,\mathrm{d}\boldsymbol{\xi}, \tag{2.42}$$

where $j(\boldsymbol{\xi}) = \sqrt{\det\left(\mathbf{J}_{\boldsymbol{\varphi}}(\boldsymbol{\xi})^\mathsf{T}\mathbf{J}_{\boldsymbol{\varphi}}(\boldsymbol{\xi})\right)}$ is Gram's determinant. For non-boundary elements, the Gram's determinant simplifies to the better known $j(\boldsymbol{\xi}) = |\det\left(\mathbf{J}_{\boldsymbol{\varphi}}(\boldsymbol{\xi})\right)|$ Jacobian determinant (with the square Jacobian matrix $\mathbf{J}_{\boldsymbol{\varphi}}$). While the mass matrix $\mathbf{M}^e$ is now only dependent on $\boldsymbol{\xi}$, the stiffness matrix $\mathbf{K}^e$ needs further consideration because the differential operator $\mathcal{L}$ is still formulated in global coordinates $\mathbf{x}$. Let $\mathbf{j}_i^{-1}$ be the i-th row of $\mathbf{J}_{\boldsymbol{\varphi}}(\boldsymbol{\xi})^{-1}$. Then it is

$$\hat{\boldsymbol{B}}(\boldsymbol{\xi}) = \mathcal{L}\hat{\boldsymbol{N}}(\boldsymbol{\xi}) \tag{2.43}$$

$$= \sum_{i=1}^{\mathrm{d}} \mathcal{V}(\mathbf{j}_i^{-1})\partial_{\xi_i}\hat{\boldsymbol{N}}(\boldsymbol{\xi}), \tag{2.44}$$

and the local static stiffness matrix can be computed as

$$\mathbf{K}^e = \int_{\hat{e}} \hat{\boldsymbol{B}}(\boldsymbol{\xi})^\mathsf{T}\mathbf{D}(\boldsymbol{\varphi}(\boldsymbol{\xi}))\hat{\boldsymbol{B}}(\boldsymbol{\xi})j(\boldsymbol{\xi})\,\mathrm{d}\boldsymbol{\xi}. \tag{2.45}$$

In general, there are cases where the differential operator is not transferred to the element's coordinates, e.g., [68], but this will not be presented in this thesis.

Numerical integration As the last step to compute Equations (2.13) to (2.16), it is necessary to evaluate the integrals for the local matrices from the previous paragraph. The integration is usually performed by numerical quadrature. Let $\boldsymbol{\xi}_i$ be quadrature points for the reference domain and ω_i their weights. As an example, consider the mass matrix $\mathbf{M}^e$, then Equation (2.41) is

$$\mathbf{M}^e = \int_{\hat{e}} \rho\big(\boldsymbol{\varphi}(\boldsymbol{\xi})\big)\hat{\boldsymbol{N}}(\boldsymbol{\xi})^\mathsf{T}\hat{\boldsymbol{N}}(\boldsymbol{\xi})j(\boldsymbol{\xi})\,\mathrm{d}\boldsymbol{\xi} \tag{2.46}$$

$$\approx \sum_i \rho\big(\boldsymbol{\varphi}(\boldsymbol{\xi}_i)\big)\hat{\boldsymbol{N}}(\boldsymbol{\xi}_i)^\mathsf{T}\hat{\boldsymbol{N}}(\boldsymbol{\xi}_i)j(\boldsymbol{\xi}_i)\omega_i. \tag{2.47}$$

If $j(\boldsymbol{\xi})$ is a low order polynomial, an exact quadrature can be chosen for terms like $\hat{\boldsymbol{N}}(\boldsymbol{\xi}_i)^\mathsf{T}\hat{\boldsymbol{N}}(\boldsymbol{\xi}_i)$ because the product of the shape functions have a maximal polynomial degree of 2p. In this thesis, we will almost always use straight elements with an appropriate number of quadrature points to achieve exact integration. In most cases, Gauss-quadrature with $p+1$ points in each parametric direction is utilized.

In general, it can be preferable to use an inexact quadrature if a diagonal matrix can be obtained and the numerical performance is similar. Furthermore, for strongly curved elements, it can be beneficial to increase the number of quadrature points.

2.2.2 General Structure of Contact Algorithms

Contact algorithms are widely studied in engineering and mathematics. In general, contact algorithms for finite deformation and small deformation can be distinguished [163]. Finite deformation

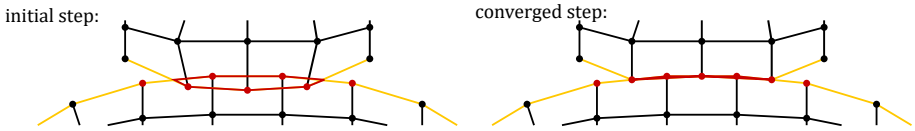

Figure 2.6: Schematic diagram of a discretized contact area

considers large movements of the structure. The theory of finite deformation of the structure considers geometrically non-linear effects at the boundary. Figure 2.5 shows a rectangle at rest at $t = 0$ and its deformed state at the current time $t = T$. It can be observed that the red boundary element changes its length. Therefore, the exact position and size of the contact area have to be measured at the current time $t = T$. Contact forces are usually separated into normal contact pressure and tangential forces associated with friction. Figure 2.5 illustrates that the normal vector is time-dependent and that the direction of the contact pressure changes.

The amplitude of ultrasonic waves is usually several magnitudes shorter than the smallest length of the structure. The ratio between the amplitude and the structure is very small, so geometric non-linear effects due to deformations can be neglected. The problem is classified in the "theory of small deformation". For the contact algorithm proposed in this thesis, the contact area and the direction of the contact pressure are computed at time $t = T$, but with no change in the area and the normal vector of the state at rest for $t = 0$.

These assumptions are common if the research is based on an in-house code (see [76, 121, 123–125]) and non-commercial software. Neglecting the stretching of the boundary and the change of the normal direction dramatically simplifies the computation in each time step because these quantities need no recalculation in each iterative step. A fast contact algorithm is essential in an inverse procedure, where the simulation model should reconstruct the defect.

The proposed contact algorithm leads to the following steps:
Before the time integration:

- Find all contact pairs, i.e., all elements which lie "opposite" to each other at the state of rest. A single element can be part of multiple contact pairs if it is "opposite" to more than one element. These elements form the possible contact area. In Figure 2.6, they are marked in yellow.
- Compute all normal and tangential vectors of the contact pairs.

During an implicit time integration, start with an initial guess without contact. Afterward, perform the following iteration:

- Contact detection: Find the current contact area (marked in red in Figure 2.6).
- Apply the contact forces on this area.
- Check if the solution has changed.

The complete algorithm is given in Section 5. In the following, only some general observations are made with Figure 2.6:

- The contact area is discretized differently for the two bodies.
- The contact area is not aligned with the elements.
- The red nodes mark the shape functions, which are directly involved in the computation of the contact forces. These shape functions have a support outside the contact area - so, the contact forces are smeared outside the contact area.

All these issues distinguish mesh-based, discretized contact from analytical contact conditions. There are different approaches to detecting the contact area. We distinguish between node-to-node (NTN), node-to-segment (NTS), segment-to-segment (STS), and weak contact detection. The NTN contact detection is the simplest, but it is restrictive to the mesh. The nodes of both contact sides must be opposite to each other. The contact condition is deduced from a point-wise view. Similarly, for NTS contact detection, the nodes of one contacting side are the contact area if they intersect with segments of the other side. It is worth mentioning that NTS contact detection does not fulfill the patch test. STS contact detection considers the contact area as pairs of sections

on both sides. It does not require any assumption on the mesh and fulfills the patch test. Week contact detection, on the other hand, uses an integral formulation including the shape functions to detect the contact area (see Section 5).

Chapter 3

Singularities in Static Problems

As mentioned in the introduction, singular behavior is one of the challenges when cracks are modeled. Cracks are the main focus in this thesis, but not the only configuration where singular stresses occur. It is reasonable to believe that dynamic problems in the low-frequency range behave similarly to static problems. For this reason, we will consider in this section only static problems, i.e., $\partial_{tt}\boldsymbol{u} = \mathbf{0}$ in Equation (2.8). It is well known that conventional finite element models, which are computed on a quasi-uniform mesh, do not accurately predict stresses in the vicinity of a singularity [107, 147, 148]. Additionally, the common refinement strategies, i.e., nearly uniform h-refinement as well as p-refinement, are not efficient because the solution is not in the HILBERT space $\mathrm{H}^2(\Omega)$ [7]. Singular stress fields can appear in the vicinity of corners, at angled material changes, and if abrupt changes in the boundary conditions occur [40, 157]. These situations involve a kind of discontinuity either in the geometry or boundary conditions. In general, boundary conditions influence the appearance and characteristics of a singular stress field. Most research to overcome the difficulties of representing the singularity by shape functions can be separated into two basic approaches:

1. The area in the vicinity of the singularity is locally refined [38].
2. A non-polynomial feature is introduced in the approximation.

Note that local refinement in general leads to more degrees of freedom and increases the meshing burden.

There are many approaches to include non-polynomial features. So, we will give an overview without raising a claim to completeness. One of the first approaches was the quarter-point element [69]. This element can represent the isotropic crack tip singularity $u_i \propto \sqrt{r}$, where r is the distance from the crack tip or another singular point (see Figure 3.1). For an arbitrary order λ with $u_i \propto r^\lambda$, HUGHES and AKIN [71] constructed elements. In 1974, Benzley [12] published a review of previous approaches. The mentioned techniques are all single-element-based and require the computation of the order in advance. Subsection 3.2 contains a review of semi-analytical methods for the calculation of the order of singularity.

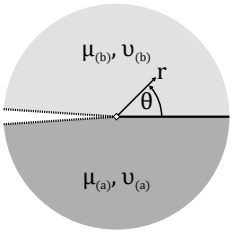

Figure 3.1: Crack coordinate system

Besides the element-based approaches, super-element approaches were investigated: the Hybrid Crack Element [164], the Super Singular Element Method [151], and the Symplectic Analytical Singular Element [174, 175]. These methods define a polygon or circle around the point singularity

which is connected to a finite element domain via the boundary. The research usually treats cases where the analytical expansion is known, and they are generally limited to cases of vanishing body loads. For the dynamic simulation in the time domain, the last time step is an artificial body load.

Another principle is an enrichment with a local feature of the problem, e.g., the stress singularity. Early versions, as in Benzley [12], were mesh dependent. Later, the local features were introduced based on the concept of partition of unity, and the method is called either eXtended or Generalized Finite Element Method [88, 140]. Excellent review articles on these developments can be found in the literature [56, 74, 140]. The feature of a mesh-independent definition of cracks was later introduced in the Hybrid Crack Element [165] and the SBFEM [93] by combining these methods with the XFEM.

Besides the already mentioned approaches, other GALERKIN methods incorporated singular behavior, e.g., meshless methods [95], the Isogeometric Analysis [34, 35], and the Extended Isogeometric Analysis [59]. Additionally, the Boundary Element Method [87, 115] has successfully solved singular problems.

The first aspect of this section is to present the dependency between singularity and contact for static problems in two dimensions. The dependencies also show the limits of the proposed models. The second aspect is the construction of special shape functions for the GALERKIN approach. Since shape functions are usually time-independent (see Equation (2.11)), for an efficient simulation, a basic condition is that the shape functions must be valid for both physical problems: an open crack and a closed crack. Additionally, one of the proposed approaches is investigated which concerns the evaluation of stress intensity factors used in Linear Fracture Mechanics.

3.1 Contact and Points of Singularity

For static linear elasticity, a possible difficulty in the simulation of contact problems is their connection to singular point problems. Configurations, where the boundary has some kind of discontinuity that leads to singular stress in a single point, are called singular point problems. The following section reviews the connection between singularity and contact for static problems in two dimensions. These results are later reproduced and extended by using the SBFEM. The main focus is on the singularities at the endpoints of cracks. A special treatment must consider the points of singularity for the numerical solution.

Consider the following example in two dimensions. If an unloaded, squared elastic body does not interact with a much bigger body modeled as a half-plane, both bodies do not contain any points of singularity. In Figure 3.2, the bodies are drawn with a gap. On the other hand, a squared body sliding over the half-plane has two possible singularities at each end of the slip zone [48, 57]. This situation is depicted in Figure 3.2, where the points of singularity P_1 and P_2 are marked with a diamond $\diamond$. This simple example illustrates that a contact condition can introduce "new" singularities. However, this thesis focuses on cracks.

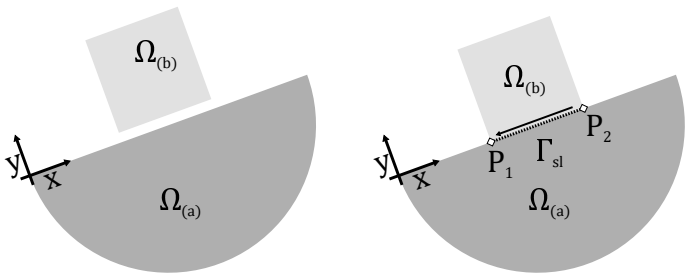

Figure 3.2: Sketch of a rectangular body sliding over a larger body

3.1.1 Different Contact Zones

To continue the discussion, some considerations are helpful. We want to solve Equation (2.1) in the static case with vanishing body loads, i.e.,

$$\boldsymbol{\nabla} \cdot \underline{\underline{\boldsymbol{\sigma}}}(\mathbf{u}) = 0, \tag{3.1}$$

where $\underline{\underline{\boldsymbol{\sigma}}}$ is the linear stress tensor and $\mathbf{u}$ is the displacement. In general, singular point problems are investigated by assuming the displacement to be a sum of different eigenfunctions [40, 157], i.e.,

$$\mathbf{u}(\mathbf{x}) = \sum_{k \in \mathbb{N}} c_k \boldsymbol{\psi}_k(\mathbf{x}) \text{ with } c_k \in \mathbb{C} \text{ and } \boldsymbol{\psi}_k \colon \mathbb{R}^2 \to \mathbb{C}^2. \tag{3.2}$$

This sum is often referred to as William's expansion. A frequently used alternative name to 'eigenfunction' is 'mode'. Each mode $\boldsymbol{\psi}_k$ is assumed to be a separable function in polar coordinates as displayed in Figure 3.1 given by

$$\boldsymbol{\psi}_k(r, \theta) = r^{\lambda_k + \mathrm{i}\,\epsilon_k} \cdot \boldsymbol{\psi}_k^{\theta}(\theta), \tag{3.3}$$

where $\boldsymbol{\psi}_k^{\theta}$ is the circumferential mode shape. The real number λ_k is called the order of the mode, while ϵ_k is the oscillating index. If λ_k is between zero and one, the mode is called singular because the associated stress is singular. A mode is called oscillating if ϵ_k is not zero. We write

$$\lambda_{\min} = \min_k \{\lambda_k : \lambda_k > 0\} \tag{3.4}$$

for the smallest non-zero order.

Remark 3.1.1 (Order of the Singularity)**.** *Many researchers refer to the order of the stress $\lambda_{\min}^{\sigma}$ instead of the order of the displacement $\lambda_{\min}$. Because of the simple relation $\lambda_{\min}^{\sigma} = \lambda_{\min} - 1$, both parameters can be used for the same reasoning, and it is only a matter of taste. In the following, we will use the order of the displacement.*

3.1.2 Modelling Cracks and Delaminations with a Contact Model

For a contact model, we need to introduce some notation. This section first uses the model of Comninou & Dundurs [49]. We assume the boundary to be straight and aligned with the x-axis. The normal gap

$$g(\mathbf{x}) = \mathbf{n}^{\mathsf{T}}(\boldsymbol{u}^{(b)}(\mathbf{x}) - \boldsymbol{u}^{(a)}(\mathbf{x})) \tag{3.5}$$

is in the coordinate system of Figure 3.3 only a function of x, where $\boldsymbol{u}^{(a)}$ and $\boldsymbol{u}^{(b)}$ are the displacement field restricted to the lower and upper half-plane, respectively. Thus, rewrite this equation into

$$g(x) = u_y^{(b)}(x, 0) - u_y^{(a)}(x, 0), \tag{3.6}$$

where $\mathbf{n} = (0, 1)$ is a normal vector of the interface and assumed independent of the displacement. This already includes a significant simplification compared to contact problems of finite deformation [163], where the normal vector itself depends on the displacement (see Section 2.2.2).

The tangential shift

$$h(\mathbf{x}) = \mathbf{t}^{\mathsf{T}}(\boldsymbol{u}^{(b)}(\mathbf{x}) - \boldsymbol{u}^{(a)}(\mathbf{x})) \tag{3.7}$$

is in the coordinate system of Figure 3.3 a function of x,

$$h(x) = u_x^{(b)}(x, 0) - u_x^{(a)}(x, 0), \tag{3.8}$$

where $\mathbf{t} = (1, 0)$ is a tangential vector of the interface. The normal traction $\tau_{\mathbf{n}}$ and the shear traction $\tau_{\mathbf{t}}$ are defined as functions of $\mathbf{x}$, i.e.,

$$\tau_{\mathbf{n}}(\mathbf{x}) = \sigma_{nn}(\mathbf{x}) = \mathbf{n}^{\mathsf{T}} \underline{\underline{\boldsymbol{\sigma}}}(\mathbf{x}) \mathbf{n}, \tag{3.9}$$

$$\tau_{\mathbf{t}}(\mathbf{x}) = \sigma_{nt}(\mathbf{x}) = \mathbf{n}^{\mathsf{T}} \underline{\underline{\boldsymbol{\sigma}}}(\mathbf{x}) \mathbf{t}, \tag{3.10}$$

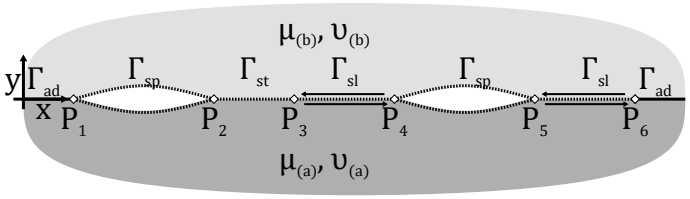

Figure 3.3: Crack with the different contact transitions

and in this special coordinate system

$$\tau_{\mathbf{n}}(x) = \sigma_{yy}^{(a)}(x,0) = \sigma_{yy}^{(b)}(x,0), \tag{3.11}$$

$$\tau_{\mathbf{t}}(x) = \sigma_{xy}^{(a)}(x,0) = \sigma_{xy}^{(b)}(x,0). \tag{3.12}$$

Note that this definition also incorporates the condition that the traction is continuous, and even if both sides are out of contact, the terms are all zero (traction-free).

Four different zones can be present along the x-axis:

1. a separation zone Γ_{sp}, where

$$g(x) > 0, \quad \tau_{\mathbf{n}}(x) = 0, \quad \tau_{\mathbf{t}}(x) = 0, \tag{3.13}$$

2. a slip zone Γ_{sl}, where

$$g(x) = 0, \quad \tau_{\mathbf{n}}(x) \leq 0, \quad |\tau_{\mathbf{t}}(x)| = c_{\mathrm{sl}}^{\mathrm{friction}} |\tau_{\mathbf{n}}(x)|, \quad \operatorname{sgn} \tau_{\mathbf{t}}(x) = \operatorname{sgn} \dot{h}(x), \tag{3.14}$$

3. a stick zone Γ_{st}, where

$$g(x) = 0, \quad \tau_{\mathbf{n}}(x) \leq 0, \quad |\tau_{\mathbf{t}}(x)| = c_{\mathrm{st}}^{\mathrm{friction}} |\tau_{\mathbf{n}}(x)|, \quad \dot{h}(x) = 0, \tag{3.15}$$

4. an adhesion zone Γ_{ad}, where

$$g(x) = 0, \quad h(x) = 0. \tag{3.16}$$

The coefficients $c_{\mathrm{sl}}^{\mathrm{friction}}$ and $c_{\mathrm{st}}^{\mathrm{friction}}$ are associated with the friction. Here, the nomenclature of Comninou & Dundurs [49] is used. The adhesion zone could also be called a perfect bonding zone.

In general, it is unknown which contact zone exists in a crack, so this information has to be determined by the numerical algorithm itself. As mentioned above, singularities can appear if the boundary conditions change abruptly. Between contact zones (slip and stick) and separation zones, the boundary conditions can vary depending on location and for dynamic problems additionally in time. There are three different transitions of boundary conditions. All three transitions are shown in Figure 3.3:

1. a transition from separation to stick - in point P_2,
2. a transition from stick to slip - in point P_3,
3. a transition from slip to separation - in point P_4.

Alternatively, the boundary values are simplified for static problems not to contain a time derivative. This enables a very compact notation, where all contact zones are unified into one boundary of possible contact $\Gamma_c = \Gamma_{\mathrm{sp}} \cup \Gamma_{\mathrm{sl}} \cup \Gamma_{\mathrm{st}}$ [181] with

$$g \geq 0, \quad \tau_{\mathbf{n}} \leq 0, \quad g \cdot \tau_{\mathbf{n}} = 0, \tag{3.17}$$

$$|h| > 0, \quad |\tau_{\mathbf{t}}(x)| + c^{\mathrm{friction}} \tau_{\mathbf{n}} = 0, \tag{3.18}$$

$$h = 0, \quad |\tau_{\mathbf{t}}(x)| + c^{\mathrm{friction}} \tau_{\mathbf{n}} < 0, \tag{3.19}$$

where the first equation gives the separation and closure of the possible contact area. The second and third equations distinguish between sticking and sliding contact, respectively. For simplicity, the friction coefficients are assumed to be equal, i.e., $c_{\mathrm{sl}}^{\mathrm{friction}} = c_{\mathrm{st}}^{\mathrm{friction}} = c^{\mathrm{friction}}$.

Frictionless Contact For frictionless contact ($c^{\text{friction}} = 0$), the constraints simplify for the boundary of possible contact Γ_c to the KUHN-TUCKER conditions

$$g \geq 0, \quad \tau_{\mathbf{n}} \leq 0 \quad g \cdot \tau_{\mathbf{n}} = 0 \quad \tau_{\mathbf{t}} = 0. \tag{3.20}$$

Alternatively, this can be written in terms of zones:

1. a separation zone Γ_{sp}, where

$$g(x) > 0, \quad \tau_{\mathbf{n}}(x) = 0, \quad \tau_{\mathbf{t}}(x) = 0, \tag{3.21}$$

2. a slip zone Γ_{sl}, where

$$g(x) = 0, \quad \tau_{\mathbf{n}}(x) \leq 0, \quad \tau_{\mathbf{t}}(x) = 0. \tag{3.22}$$

Stick-only Contact For a sufficiently large friction coefficient, sliding is not possible and the conditions (3.17)-(3.19) simplify to

$$g \geq 0, \quad \tau_{\mathbf{n}} \leq 0 \quad g \cdot \tau_{\mathbf{n}} = 0, \tag{3.23}$$

$$h = 0, \quad \tau_{\mathbf{n}} < 0. \tag{3.24}$$

For stick-only contact, there is a perfect bond ($g = h = 0$) between both contact sides if there is a negative contact pressure ($\tau_{\mathbf{n}} < 0$). This links contact methods to methods known for continuity conditions and domain decomposition, where perfect bonds are modeled.

3.1.3 The Interface Crack between two Isotropic Materials

COMNINOU & DUNDURS [49] investigated all three transitions between two isotropic materials with the analytical technique introduced by WILLIAMS [156, 157]. The inequalities of a contact problem restrict the possible solutions in such a way that the following result is obtained: 'Regardless of the level of friction, no singularities can appear at any of the possible transitions in contact problems' [49]. This can be summarized in the following remark:

Remark 3.1.2 (Points of Singularity are Endpoints)**.** *The two endpoints of a zone with contact and separation in an interface crack with two isotropic materials are the only points with singular stress behavior in two dimensions.*

This result simplifies the numerical analysis considerably because only the endpoints have to represent singularities.

The contact traction can influence the crack tip singularity when modeling cracks, delaminations, or debonding by a contact model. In the following, we will mention only crack tip singularities. Still, all statements also refer to singularities at the endpoints of delaminations and debonding because they are modeled in the same way as cracks. We first review the investigations of COMNINOU & DUNDURS [33] again and restrict ourselves to interface cracks with isotropic materials.

Consider an interface crack as in Figure 3.1 with shear modulus μ_ℓ, and POISSON's ratio ν_ℓ for each material. Define the first mismatch parameter

$$\alpha = \frac{\mu_{(b)}(\kappa_{(a)} + 1) - \mu_{(a)}(\kappa_{(b)} + 1)}{\mu_{(b)}(\kappa_{(a)} + 1) + \mu_{(a)}(\kappa_{(b)} + 1)} \tag{3.25}$$

and the second mismatch parameter

$$\beta = \frac{\mu_{(b)}(\kappa_{(a)} - 1) - \mu_{(a)}(\kappa_{(b)} - 1)}{\mu_{(b)}(\kappa_{(a)} + 1) + \mu_{(a)}(\kappa_{(b)} + 1)} \tag{3.26}$$

with the KOLOSOV constant for $\ell \in \{(a), (b)\}$

$$\kappa_\ell = \begin{cases} 3 - 4\nu_\ell & \text{for plane strain} \\ \frac{3-\nu_\ell}{1+\nu_\ell} & \text{for plane stress} \end{cases}. \tag{3.27}$$

For example, a combination of aluminum and steel has a mismatch parameter α of approx. ± 0.47. The sign depends on which materials are assigned to the upper and lower domain, respectively. There are two important cases:

(a) Crack mode I (b) Crack mode II

Figure 3.4: Singular modes of a crack

Matching material ($\beta = 0$) We begin with the simplest case where β is zero. This includes the important case, where both materials coincide or, in other words, where we have only a single material. As a first state, consider traction-free boundary conditions. This state can be physically reasonable if a gap exists between both crack sides. The eigenfunctions are called mode I (Figure 3.4a) and mode II (Figure 3.4b). The second state to consider is the contact state. For this state, mode II movement is still possible, and the mode is independent of a friction coefficient. This has implications for the numerical treatment of this case ($\beta = 0$). Various methods are either built on the order of the singularity or built on the modes. Examples are singular elements [12, 69, 71] or XFEM [56, 74, 140], respectively.

Mismatching material ($\beta \neq 0$) As a first state, consider traction-free boundary conditions. This state leads to an oscillating singularity [111] with

$$\epsilon = \frac{1}{2\pi} \ln \left(\frac{\kappa_{(a)}/\mu_{(a)} - 1/\mu_{(b)}}{\kappa_{(b)}/\mu_{(b)} - 1/\mu_{(a)}} \right). \tag{3.28}$$

An oscillating singularity predicts interpenetration of the material near the crack tip. England examined this situation [52]. For many authors, this physical contradiction is taken as a reason to disregard the solution of an open, traction-free bi-material crack [111].

The disregarded traction-free solution leads to the conclusion that a bi-material crack always has a contact zone near the crack tips. The contact state has two important sub-cases: (i) the contact is frictionless, or (ii) the contact is with friction.

1. If a friction-free state is considered, the order of the singularity is 0.5, and the boundary traction is singular.

2. If friction is considered, the order of the singularity depends on the coefficient of friction and the direction of slip. To quote Comninou: 'it is generally not possible to predict the direction of slip and thus the order of the singularity without solving a given problem' [33].

This again has implications for the numerical treatment of bi-material problems.

Remark 3.1.3 (Systematic Error)**.** *In general, the order of the singularity depends on the direction of the slip. As a result, in the case of friction, an approximation method based on a square root singularity has a systematic error.*

Rice [111] has drawn different conclusions from the oscillating singularity.

Remark 3.1.4 (Rice)**.** *For all practically occurring materials, the oscillating index is neglectable because of the logarithmic term in Equation* (3.28)*. In the case of a small contact area in relation to the crack length, the traction-free modes should be a suitable approximation for the mode at the crack tip.*

3.1.4 The Interface Crack for two Anisotropic Materials

To compute an analytical solution, the Stroh-formalism (1958) [138] is used for an anisotropic interface crack [145]. An equivalent calculation method was used by Lekhnitskii (1963), Green & Zerna (1954) and Eshelby *et al.* (1953) [145]. With the Stroh-formalism [139], it is possible to determine the stress singularity without calculating a complete asymptotic series. It is only necessary to determine general eigenvalues from three systems of 3×3 matrices. The derivation of these eigenvalue systems is based on complex analysis techniques. Suo discovered that there is an individual eigenvalue that corresponds to a root term [145] and a pair of complex conjugate eigenvalues. This is analogous to the interface crack with two isotropic materials.

Lee & Gao [79], Deng [41] and later Nazarov [94] investigated the case with the contact condition. A non-oscillatory condition was considered directly in the contact model [79]. The authors draw the conclusion that an interface crack under contact with two anisotropic materials has a square root singularity [79].

3.1.5 Dynamic Cases

Generally, the dynamic case can behave quite differently, but on small length scales (compared to the wavelength), it can be expected that the solution can be approximated locally by the static solution. In the vicinity of the crack tip, it is reasonable to assume that the singular mode dominates the solution and leads to very similar results to the static case. Sih *et al.* examined the dynamic case for an isotropic material where a finite crack is opened by normal and shear traction applied to its surface [127]. Their conclusion is: 'Through the analysis of the preceding sections, it has been shown that the stress field very near the crack tip has the same spatial distribution for the dynamic case as for the static case, the only difference being that the intensity of the field is a function of time.' [127]

Another dynamic case can also be calculated using analytical methods. However, this dynamic case relates to a crack that spreads at a constant speed. This corresponds to a steady-state considered in a moving coordinate system. Examples are in the work of Radok [109], Sih [126], Yang *et al.* [170] and Stroh [139], while Deng treated the case with a contact condition [41].

It is worth mentioning that the analytical solution of the Helmholtz equation for a dynamic crack-like coordinate system (Figure 3.1) is known. The Helmholtz equation has resemblances with the dynamic elastic wave equation in the frequency domain. For the Helmholtz equation, the solution is a frequency-dependent Bessel function which depends on the radius r [133].

3.2 Semi-analytical Methods for the Computation of Stress Singularities

One of the first approaches to calculate stress singularities using the Finite Element Method was published by Yamada & Okumura in 1981 [168]. Yeh & Tadjbakhsh refer to the work from 1986 [177]. The work of Yeh & Tadjbakhsh is based on polar coordinates and a one-dimensional FE-approximation on a circular boundary which is scaled to the origin. The method leads to a quadratic eigenvalue problem.

Another approach is developed by Yosibash & Szabó [178]. A polar grid is used in two dimensions, and the inner nodes are then eliminated by static condensation. The polar grid must be particularly suitable for singularities. The grid is locally refined around the origin with a strong grading. Finally, this method also leads to a quadratic eigenvalue problem.

In 1996 Pageau & Biggers used an FE-eigenanalysis very similar to the approach by Yeh & Tadjbakhsh [104–106]. In a different context, but the same year, Song and Wolf developed an FE-eigenanalysis based on a more general coordinate transformation [137]. Their transformation scales a boundary parametrization of a sub-domain towards a point – a feature which initiated the development of a more general semi-analytical approach, nowadays termed Scaled Boundary Finite Element Method (SBFEM).

All these FE-approaches have in common that the material parameters can change depending on the angle, and a general anisotropic material can be considered. All methods mentioned above

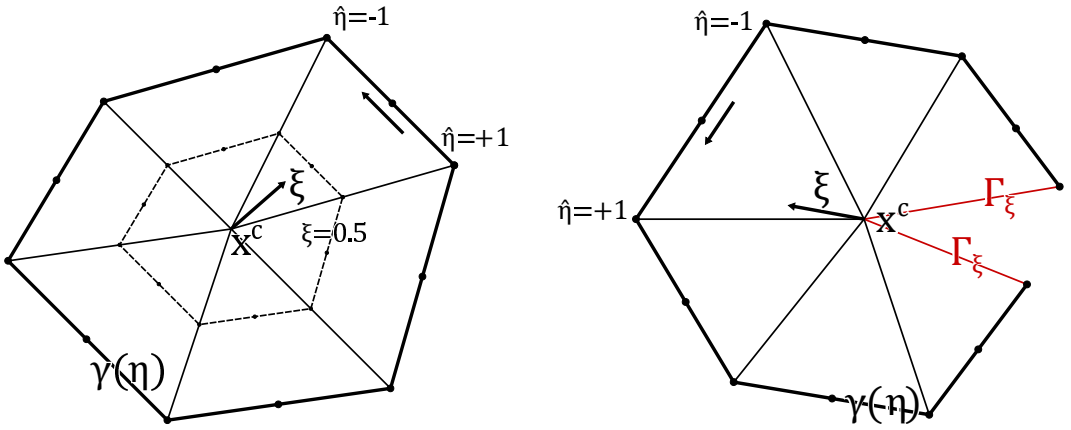

(a) Example for a closed polygon

(b) Example for an open polygon

Figure 3.5: The scaled boundary coordinate system

for determining singular stress are based on linear elasticity.

3.3 The Scaled Boundary Shape Functions for a Single Super-element

The previous sections contain several statements about singularities and contact. The following section is intended to confirm some of these results using the SBFEM. We assume at first that a single super-element can model the problem, i.e., a single polygon as in Figure 3.5. The SBFEM is originated in the context of dynamic soil-structure interaction [132, 137, 160]. The classic approach is based on modal decomposition for homogeneous linear elastic problems. Below, a particular version of the SBFEM - the SBFEM with Scaled Boundary (SB) shape functions [98] - is utilized for the approximation of the static and dynamic elastic equations on polygonal meshes [99]. On polygonal meshes, multiple super-elements are connected, but in this section, we focus on a single super-element.

The derivation starts with the weak form for the static problem (Equation (2.10) with $\partial_{tt} = \mathbf{0}$):

$$-\int (\mathcal{L}\boldsymbol{\delta u})^{\mathsf{T}} \mathbf{D} \mathcal{L}\boldsymbol{u} \, \mathrm{d}\Omega + \int \boldsymbol{\delta u}^{\mathsf{T}} \boldsymbol{f} \, \mathrm{d}\Omega + \int \boldsymbol{\delta u}^{\mathsf{T}} \boldsymbol{\tau} \, \mathrm{d}\Gamma = \mathbf{0}, \tag{3.29}$$

where $\boldsymbol{\delta u}$ is the virtual displacement, $\boldsymbol{u}$ is the displacement, $\boldsymbol{f}$ the body load and $\boldsymbol{\tau}$ the traction. Recall that $\mathcal{L}$ is the differential operator and $\mathbf{D}$ the elasticity material matrix. This equation will be solved for the scaled boundary coordinate system. The scaled boundary coordinates are

$$\mathbf{x}(\xi, \eta) = \xi\big(\boldsymbol{\gamma}(\eta) - \mathbf{x}^c\big) + \mathbf{x}^c, \tag{3.30}$$

where $\boldsymbol{\gamma}(\eta)$ is a boundary curve, defined by one-dimensional finite elements (see Figure 3.5). The point $\mathbf{x}^c = (x_c, y_c)^{\mathsf{T}}$ is the so-called scaling center and must be 'visible' from the whole curve. This means the scaling center has to be connectable with each point on the curve $\boldsymbol{\gamma}(\eta)$ by a straight line, or in other words, the polygon is star-convex. The scaling parameter ξ is between zero and one. It is one for the points on the curve $\boldsymbol{\gamma}$. The curve $\boldsymbol{\gamma}$ can be open as in Figure 3.5b. In the limiting case, where both sides of the curve $\boldsymbol{\gamma}$ are touching, this leads to a zero-thickness crack model.

In general, different types of one-dimensional shape functions with a different polynomial degree can be utilized for the boundary finite elements [62, 64]. Different kinds of mappings can be applied, including the iso-parametric concept. In this thesis, we will use nodal shape functions with global degree p as presented in Section 2.2.1. In most cases, the elements will be straight, with rare exceptions.

To derive the SBFEM formulation, one of the key aspects of the coordinate system is that the

JACOBIAN matrix is separable for each boundary finite element:

$$\mathbf{J}_{\mathbf{x}} = \begin{pmatrix} 1 & 0 \\ 0 & \xi \end{pmatrix} \mathbf{J}_{\eta} \tag{3.31}$$

with

$$\mathbf{J}_{\eta} = \begin{pmatrix} (\boldsymbol{\gamma}(\eta) - \mathbf{x}^c) & \partial_{\eta}\boldsymbol{\gamma}(\eta) \end{pmatrix}. \tag{3.32}$$

With a separable JACOBIAN matrix, also the inverse JACOBIAN matrix

$$\mathbf{J}_{\mathbf{x}}^{-1} = \mathbf{J}_{\eta}^{-1} \begin{pmatrix} 1 & 0 \\ 0 & \xi^{-1} \end{pmatrix} \tag{3.33}$$

and the JACOBIAN determinate

$$\det(\mathbf{J}_{\mathbf{x}}) = \xi \det(\mathbf{J}_{\eta}) \tag{3.34}$$

$$= \xi j(\hat{\eta}) \tag{3.35}$$

are separable. The JACOBIAN matrix and JACOBIAN determinate are required to transfer integrals and derivatives.

Assume that the virtual displacement, as well as the displacement, is separable in the scaled boundary coordinate system:

$$\boldsymbol{u}\big(\mathbf{x}(\xi,\eta)\big) = \boldsymbol{M}(\eta)\mathbf{u}(\xi) \qquad\qquad \boldsymbol{\delta u}\big(\mathbf{x}(\xi,\eta)\big) = \boldsymbol{M}(\eta)\boldsymbol{\delta}\mathbf{u}(\xi), \tag{3.36}$$

where $\boldsymbol{M}$ is the matrix of the assembled finite element shape functions of the boundary curve $\boldsymbol{\gamma}$. After substituting this ansatz into Equation (3.29), transforming the derivatives and integrals, separating all ξ-dependent parts, integrating by parts, and considering the arbitrariness of the virtual displacement, the equilibrium equation becomes the SBFEM equation in displacement for a single sub-domain [134, 136, 162]:

$$\xi^2 \mathbf{E}_0 \partial_{\xi\xi}\boldsymbol{u}(\xi) + \xi(\mathbf{E}_0 + \mathbf{E}_1^{\mathsf{T}} - \mathbf{E}_1)\partial_{\xi}\boldsymbol{u}(\xi) - \mathbf{E}_2\boldsymbol{u}(\xi) + \boldsymbol{f}(\xi) = \mathbf{0}, \tag{3.37}$$

where $\boldsymbol{f}(\xi)$ is the sum of the body load term $\boldsymbol{f}_b$ and traction term $\boldsymbol{f}_\tau$ in ξ-direction, i.e.,

$$\boldsymbol{f}(\xi) = \xi^2 \boldsymbol{f}_b(\xi) + \xi \boldsymbol{f}_\tau(\xi). \tag{3.38}$$

The detailed derivation can be found in [134, 136, 162].

All matrices and vectors are assembled over the elements:

$$\mathbf{E}_i = \mathop{\mathrm{A}}_{e\in\boldsymbol{\gamma}} \mathbf{E}_i^e, \qquad i \in \{0,1,2\}, \tag{3.39}$$

$$\boldsymbol{f}_\alpha = \mathop{\mathrm{A}}_{e\in\boldsymbol{\gamma}} \boldsymbol{f}_\alpha^e, \qquad \alpha \in \{b,\tau\}. \tag{3.40}$$

For a more convenient notation, we introduce the traction in ξ-direction on the boundary Γ_ξ in scaling direction (see Figure 3.5b). The traction is formally extended by zero inside the domain:

$$\bar{\boldsymbol{\tau}}(\mathbf{x}) = \begin{cases} \boldsymbol{\tau}(\mathbf{x}) & \mathbf{x} \in \Gamma_\xi \\ \mathbf{0} & \mathbf{x} \in \Omega \end{cases}. \tag{3.41}$$

The element matrices and vectors are computed by

$$\begin{aligned} \mathbf{E}_0^e &= \int_{-1}^{+1} \hat{\boldsymbol{B}}_1(\hat{\eta})^{\mathsf{T}} \mathbf{D}(\hat{\eta}) \hat{\boldsymbol{B}}_1(\hat{\eta}) \, |j(\hat{\eta})| \, \mathrm{d}\hat{\eta}, \\ \mathbf{E}_1^e &= \int_{-1}^{+1} \hat{\boldsymbol{B}}_2(\hat{\eta})^{\mathsf{T}} \mathbf{D}(\hat{\eta}) \hat{\boldsymbol{B}}_1(\hat{\eta}) \, |j(\hat{\eta})| \, \mathrm{d}\hat{\eta}, , \\ \mathbf{E}_2^e &= \int_{-1}^{+1} \hat{\boldsymbol{B}}_2(\hat{\eta})^{\mathsf{T}} \mathbf{D}(\hat{\eta}) \hat{\boldsymbol{B}}_2(\hat{\eta}) \, |j(\hat{\eta})| \, \mathrm{d}\hat{\eta}, \end{aligned} \tag{3.42}$$

where $\hat{\eta}$ is the local element-wise circumferential coordinate between -1 and $+1$. The force contributions are given by

$$\boldsymbol{f}_b^e = \int_{-1}^{+1} \hat{\boldsymbol{M}}(\hat{\eta})^\mathsf{T} \boldsymbol{f}_b(\boldsymbol{\gamma}^e(\hat{\eta}))\, |j(\hat{\eta})|\, \mathrm{d}\hat{\eta} \tag{3.43}$$

$$\boldsymbol{f}_\tau^e = \hat{\boldsymbol{M}}(-1)L(-1)\bar{\boldsymbol{\tau}}\big(\boldsymbol{\gamma}^e(-1)\big) + \hat{\boldsymbol{M}}(+1)L(+1)\bar{\boldsymbol{\tau}}\big(\boldsymbol{\gamma}^e(+1)\big), \tag{3.44}$$

where $\hat{\boldsymbol{M}}(\hat{\eta})$ is the matrix containing the local shape functions and $L(\hat{\eta}) = \|\boldsymbol{\gamma}^e(\hat{\eta}) - \mathbf{x}^c\|$ is the length between the boundary point and the scaling center. Note that only the nodes at the end of the curve $\boldsymbol{\gamma}$ have a contribution to $\boldsymbol{f}_\tau$. For all other points $\bar{\boldsymbol{\tau}}$ is vanishing. Additionally, it is

$$\hat{\boldsymbol{B}}_1(\hat{\eta}) = \hat{\boldsymbol{b}}_1(\hat{\eta})\hat{\boldsymbol{M}}(\hat{\eta}), \qquad \hat{\boldsymbol{B}}_2(\hat{\eta}) = \hat{\boldsymbol{b}}_2(\hat{\eta})\partial_{\hat{\eta}}\hat{\boldsymbol{M}}(\hat{\eta}), \tag{3.45}$$

with

$$j(\hat{\eta}) = (\gamma_x^e(\hat{\eta}) - x_c)\partial_{\hat{\eta}}\gamma_y^e - (\gamma_y^e(\hat{\eta}) - y_c)\partial_{\hat{\eta}}\gamma_x^e \tag{3.46}$$

and

$$\hat{\boldsymbol{b}}_1(\hat{\eta}) = \frac{1}{j(\hat{\eta})}\begin{pmatrix} +\partial_{\hat{\eta}}\gamma_y^e & 0 \\ 0 & -\partial_{\hat{\eta}}\gamma_x^e \\ -\partial_{\hat{\eta}}\gamma_x^e & +\partial_{\hat{\eta}}\gamma_y^e \end{pmatrix}, \quad \hat{\boldsymbol{b}}_2(\hat{\eta}) = \frac{1}{j(\hat{\eta})}\begin{pmatrix} -(\gamma_y^e(\hat{\eta}) - y_c) & 0 \\ 0 & +(\gamma_x^e(\hat{\eta}) - x_c) \\ +(\gamma_x^e(\hat{\eta}) - x_c) & -(\gamma_y^e(\hat{\eta}) - y_c) \end{pmatrix}, \tag{3.47}$$

where $\boldsymbol{\gamma}^e = (\gamma_x^e, \gamma_y^e)^\mathsf{T}$ is the element part of $\boldsymbol{\gamma}$.

The second-order ordinary differential equation (ODE) (3.37) can be transferred into a first-order ODE by defining the inner nodal forces

$$\boldsymbol{q}(\xi) = (\xi\mathbf{E}_0\partial_\xi + \mathbf{E}_1^\mathsf{T})\boldsymbol{u}(\xi). \tag{3.48}$$

Equations (3.37) and (3.48) lead to a first order ODE

$$\xi\partial_\xi \boldsymbol{v}(\xi) = -\mathbf{Z}\boldsymbol{v}(\xi) - \boldsymbol{v}^*(\xi) \tag{3.49}$$

with

$$\boldsymbol{v}(\xi) = \begin{bmatrix}\boldsymbol{u}(\xi)\\ \boldsymbol{q}(\xi)\end{bmatrix} \quad \text{and } \mathbf{Z} = \begin{bmatrix}\mathbf{E}_0^{-1}\mathbf{E}_1^\mathsf{T} & -\mathbf{E}_1^{-1} \\ \mathbf{E}_1\mathbf{E}_0^{-1}\mathbf{E}_1^\mathsf{T} - \mathbf{E}_2 & -\mathbf{E}_1^\mathsf{T}\mathbf{E}_0^{-1}\end{bmatrix} \quad \text{and } \boldsymbol{v}^*(\xi) = \begin{bmatrix}\mathbf{0}\\ \boldsymbol{f}(\xi)\end{bmatrix}. \tag{3.50}$$

In this section, the first order ODE is solved by Schur decomposition (Appendix A.2). Let the matrix $\mathbf{Z}$ be decomposed as

$$\mathbf{Z} = \begin{bmatrix}\boldsymbol{\Psi}_q & -\boldsymbol{\Psi}_q \\ \boldsymbol{\Psi}_u & -\boldsymbol{\Psi}_u\end{bmatrix}\begin{bmatrix}\mathbf{S}_n & \mathbf{0} \\ \mathbf{0} & \mathbf{S}_p\end{bmatrix}\begin{bmatrix}\boldsymbol{\Psi}_q & -\boldsymbol{\Psi}_q \\ \boldsymbol{\Psi}_u & -\boldsymbol{\Psi}_u\end{bmatrix}^{-1}, \tag{3.51}$$

where $\mathbf{S}_n$ and $\mathbf{S}_p$ are block-diagonal matrices. The blocks $\boldsymbol{\Psi}_q$ and $\boldsymbol{\Psi}_u$ build the unitarian matrix, and its columns define the modes in the SBFEM. The matrix $\mathbf{Z}$ is a Hamiltonian matrix. Therefore, its decomposition contains positive and negative blocks [134]. These blocks are linked to the eigenvalues of the matrix $\mathbf{Z}$ (Appendix A.2). The matrix $\mathbf{S}_n$ is associated with the non-positive eigenvalues, and $\mathbf{S}_p$ corresponds to the non-negative eigenvalues. An additional sorting step has to be made for splitting the block associated with the zero eigenvalues. The details can be found in [134]. The solution of Equation (3.37) is

$$\boldsymbol{u}(\xi) = \boldsymbol{\Psi}_u\xi^{-\mathbf{S}_n}\mathbf{c}_1 - \boldsymbol{\Psi}_u\xi^{-\mathbf{S}_p}\mathbf{c}_2 + \boldsymbol{\phi}(\xi), \tag{3.52}$$

where the coefficient vector $\mathbf{c}_2$ is zero because the displacements at the origin have to be finite for bounded domains. The boundary conditions and body loads determine the coefficient vector $\mathbf{c}_1$ and a particular solution $\boldsymbol{\phi}$ is gained by tractions and body loads. Equation (3.52) represents a modal decomposition of the displacement field. This is similar to Equation (3.2), but in a different coordinate system.

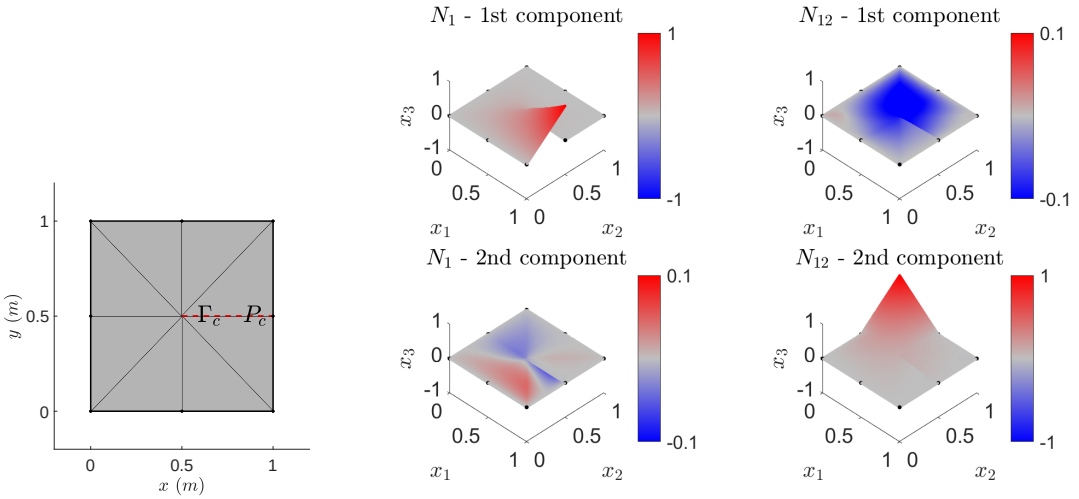

(a) Rectangular domain with crack

(b) Crack side SB shape functions with p=1 for u_x

(c) Corner side SB shape functions with p=1 for u_y

Figure 3.6: Example of SB shape functions with vanishing traction

Remark 3.3.1 (Eigenvalue Problem)**.** *As an alternative to* SCHUR *decomposition, Equation* (3.51) *can also be solved by an eigenvalue decomposition. The matrix* $\mathbf{Z}$ *and*

$$\begin{bmatrix} \mathbf{S}_n & \mathbf{0} \\ \mathbf{0} & \mathbf{S}_p \end{bmatrix} \tag{3.53}$$

have the same eigenvalues because both are mathematically 'similar'. In addition, let $(\boldsymbol{\psi}_q^\mathsf{T}, \boldsymbol{\psi}_u^\mathsf{T})^\mathsf{T}$ *be an eigenvector and* λ *its eigenvalue of the matrix* $\mathbf{Z}$*, then from Equation* (3.37) *follows*

$$\lambda^2 \mathbf{E}_0 \boldsymbol{\psi}_u + \lambda(\mathbf{E}_1^\mathsf{T} - \mathbf{E}_1)\boldsymbol{\psi}_u - \mathbf{E}_2 \boldsymbol{\psi}_u = \mathbf{0}. \tag{3.54}$$

3.3.1 SBFEM Solution by Case-by-Case Analysis for Frictionless Contact

As described in Section 3.1.2, contact boundary conditions can change on different zones of the boundary. Consider for example the geometry in Figure 3.6a. The possible contact boundary Γ_c is approximated with a double node at P_c. It is generally unknown if the gap is positive or zero because the gap depends on the displacement itself. As a result, it is also unclear which type of contact zone is present. For the analysis, we first assume that there is only one type of zone, and we solve the two cases, i.e., the separation case ($g > 0$) and the slip case ($g = 0$), separately (see Section 3.1.2).

3.3.1.1 SB Shape Functions of the Separation Case for a Polygonal Element

For the separation case, we consider the boundary conditions in Equation (3.21)

$$g(x) > 0, \quad \tau_{\mathbf{n}}(x) = 0, \quad \tau_{\mathbf{t}}(x) = 0, \tag{3.55}$$

where $g(x) > 0$ is ensured by the contact detection. Note that boundary conditions for this case are traction-free. If there is a double node at P_c, all the traction-free boundary conditions ($\tau_{\mathbf{n}} = \tau_{\mathbf{t}} = 0$) are natural and do not require additional consideration. As an alternative to the solution in Equation (3.52), SB shape functions for a polygonal element are constructed, which can represent the complete solution space. The SB shape functions $\boldsymbol{N}(\xi, \eta)$ are defined as [98]

$$\boldsymbol{N}(\xi, \eta) = \boldsymbol{M}(\eta)\mathbf{P}\xi^{-\mathbf{S}}\mathbf{T}. \tag{3.56}$$

For vanishing body loads and traction-free boundary conditions, i.e., $\boldsymbol{f} = \mathbf{0}$, the matrices $\mathbf{P}, \mathbf{S}, \mathbf{T}$ are defined as

$$\begin{aligned} \mathbf{P} &= \boldsymbol{\Psi}_u \\ \mathbf{S} &= \mathbf{S}_n \\ \mathbf{T} &= \boldsymbol{\Psi}_u^{-1}. \end{aligned} \tag{3.57}$$

Remark 3.3.2 (Properties of the traction-free SB shape functions)**.**

- *By construction, the traction-free SB shape functions fulfill the* Kronecker*-delta property. Only one SB shape function has a unit value in one of its components for every boundary node, and the other shape functions are zero.*
- *The traction-free SB shape functions form a partition of unity because they can represent the rigid body modes.*
- *The SB shape functions are compatible with the common finite element shape functions on the boundary with $\xi = 1$. Both types of shape functions can be utilized in the same approximation by a usual assembly process.*

Remark 3.3.3 (Traction-free)**.** *The traction-free boundary condition does not take into account contact forces. Consequently, the SB shape functions cannot represent any energy transfer over these boundaries and are not suitable for modeling the state of contact.*

Figure 3.6 shows two examples of SB shape functions for p = 1 for a cracked rectangle, which is depicted on the left-hand side. Note that these shape functions are naturally vector-valued, but only either the x- or the y-component is one at a specific node on the boundary.

3.3.1.2 SB Shape Functions of the Slip Case for a Polygonal Element

For the slip case, we consider the boundary conditions in Equation (3.22)

$$g(x) = 0, \quad \tau_{\mathbf{n}}(x) \leq 0, \quad \tau_{\mathbf{t}}(x) = 0, \tag{3.58}$$

where $\tau_{\mathbf{n}}(x) \leq 0$ is ensured by closed contact. This section presents a direct elimination of the constraint ($g = 0$). Similar to finite elements, natural boundary conditions need no special treatment, while for constraints, the finite element space requires adjustment.

For the slip state, the elimination of the constraint can be written with a transformation matrix $\mathbf{H} \in \mathbb{R}^{K \times L}$ with $L < K$ and the assumption

$$\boldsymbol{M}(\eta)\boldsymbol{u}(\xi) = \boldsymbol{M}(\eta)\mathbf{H}\tilde{\boldsymbol{u}}(\xi) = \tilde{\boldsymbol{M}}(\eta)\tilde{\boldsymbol{u}}(\xi) \qquad \text{with } \tilde{\boldsymbol{u}}(\xi) \in \mathbb{C}^L. \tag{3.59}$$

Recall that $\boldsymbol{M}$ contains the assembled finite element shape functions of the boundary curve $\boldsymbol{\gamma}$. A transformation matrix allows to first use the standard derivation of the SBFEM-equation in displacement with traction-free boundary conditions and a double node in the slip zone. Then, we use the basis transformation $\mathbf{H}$ to alter the equation and incorporate constraints. Section 4.11.2 describes the direct elimination for a more general case for the Galerkin Method. For vanishing loads $\boldsymbol{f}(\xi) = \mathbf{0}$, the Equation (3.37) can be altered to

$$\xi^2 \tilde{\mathbf{E}}_0 \partial_{\xi\xi} \tilde{\boldsymbol{u}}(\xi) + \xi(\tilde{\mathbf{E}}_0 + \tilde{\mathbf{E}}_1^{\mathsf{T}} - \tilde{\mathbf{E}}_1)\partial_\xi \tilde{\boldsymbol{u}}(\xi) - \tilde{\mathbf{E}}_2 \tilde{\boldsymbol{u}}(\xi) = \mathbf{0}, \tag{3.60}$$

with

$$\tilde{\mathbf{E}}_i = \mathbf{H}^{\mathsf{T}} \mathbf{E}_i \mathbf{H} \in \mathbb{R}^{L \times L}. \tag{3.61}$$

The exact transformation matrix $\mathbf{H}$ depends on the considered example. Section 3.4.1 gives a specific implementation.

The equation can be solved using the known methods from the SBFEM. Denote by $\tilde{\boldsymbol{\Psi}}_u$ and $\tilde{\mathbf{S}}_n$ the matrices obtained from decomposing the matrix $\mathbf{Z}$ (Equation (3.51)), where all $\mathbf{E}_i$ are replaced by $\tilde{\mathbf{E}}_i$. The matrices of the SB shape functions (Equation (3.56)) are defined by

$$\begin{aligned} \mathbf{P} &= \tilde{\boldsymbol{\Psi}}_u \in \mathbb{R}^{L \times L}, \\ \mathbf{S} &= \tilde{\mathbf{S}}_n \in \mathbb{R}^{L \times L}, \\ \mathbf{T} &= \tilde{\boldsymbol{\Psi}}_u^{-1} \in \mathbb{R}^{L \times L}. \end{aligned} \tag{3.62}$$

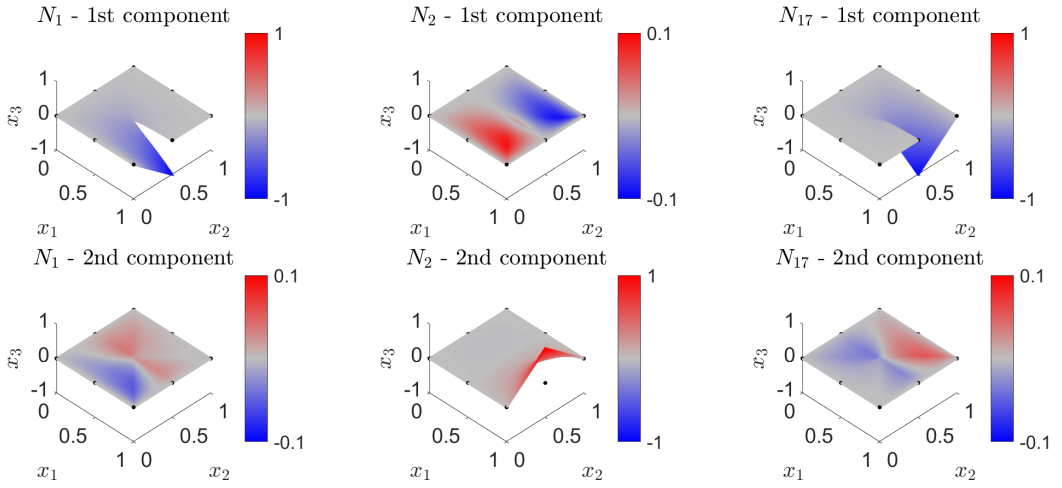

(a) Single SB shape functions with p=1

(b) Single SB shape functions with p=1

(c) Single SB shape functions with p=1

Figure 3.7: Example for the three modified SB shape functions gained by direct elimination

The matrices are different from those in Equation (3.57) and lead to different shape functions of the super-element.

Remark 3.3.4 (Advantage of direct elimination)**.** *The direct elimination of constraints considers an entirely new set of modes for the state of contact. This also allows for the change of singular behavior. The contact pressure and displacement are solved as a coupled system. The modification of the equation by the transformation matrix* $\mathbf{H}$ *enables the reuse of the matrices* $\mathbf{E}_i$*, which are already calculated for a crack tip without contact (see Section 3.5).*

Remark 3.3.5 (Disadvantages of direct elimination)**.** *Direct elimination of the constraint leads to a smaller stiffness matrix, and the SB shape functions on the boundary are modified. This can lead to difficulties in assembling multiple super-elements. Our target is a dynamic simulation, where the shape functions usually are time-independent. The direct elimination leads to time-dependent shape functions. For time-dependent shape functions, a new projection step has to be introduced to map between the two sets of shape functions. In numerical experiments, a projection based only on the nodal values was unstable.*

3.4 Numerical Experiments for the Eigenvalues

The following two numerical examples demonstrate the computation of singular orders with the SBFEM in the state of contact. The first example validates the approach by comparing it to literature values, while the second example presents a more general case.

3.4.1 Transition between a Frictionless Contact Zone and a Separation Zone by Direct Elimination

As in the theoretical part, we first consider the transition in a sliding problem. The problem was originally investigated by Dundurs and Comninou [48]. Two bodies with different isotropic materials are involved. The sliding is friction-free.

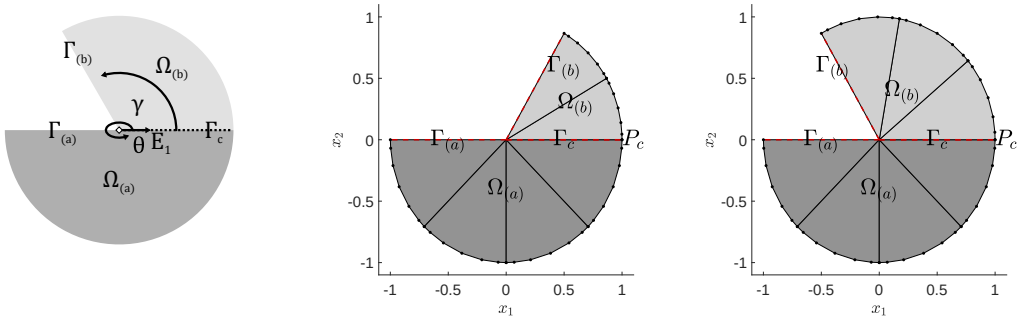

(a) Overview of the contact transition for different wedges

(b) SBFEM-mesh for $\gamma = \frac{1}{3}\pi$

(c) SBFEM-mesh for $\gamma = \frac{2}{3}\pi$

Figure 3.8: Domain and SBFEM-mesh for the transition problem between a frictionless contact zone and a separation zone

Assume the following boundary conditions [48, 49] for the domain depicted in Figure 3.8:

$$u_n^{(a)} = u_n^{(b)} \qquad \text{for } x \in \Gamma_c, \tag{3.63}$$

$$\sigma_{nt}^{(a)} = \sigma_{nt}^{(b)} = 0 \quad \text{for } x \in \Gamma_c, \tag{3.64}$$

$$\sigma_{nn}^{(a)} = \sigma_{nn}^{(b)} \leq 0 \quad \text{for } x \in \Gamma_c, \tag{3.65}$$

$$\sigma_{nt}^{(a)} = \sigma_{tt}^{(a)} = 0 \quad \text{for } x \in \Gamma_{(a)}, \tag{3.66}$$

$$\sigma_{nt}^{(b)} = \sigma_{tt}^{(b)} = 0 \quad \text{for } x \in \Gamma_{(b)} \tag{3.67}$$

with

$$u_n = \mathbf{n}^\mathsf{T}\mathbf{u}, \qquad \sigma_{nn} = \mathbf{n}^\mathsf{T}\underline{\underline{\boldsymbol{\sigma}}}\mathbf{n}, \qquad \sigma_{nt} = \mathbf{n}^\mathsf{T}\underline{\underline{\boldsymbol{\sigma}}}\mathbf{t}, \qquad \sigma_{tt} = \mathbf{t}^\mathsf{T}\underline{\underline{\boldsymbol{\sigma}}}\mathbf{t}, \tag{3.68}$$

where $\mathbf{n}$ is one of the two normal vectors of the surface Γ_c and $\mathbf{t} = (t_x, t_y)^\mathsf{T} = (-n_y, n_x)^\mathsf{T}$ is its tangential vector. Note that the normal stress σ_{nn} is the contact pressure.

Remark 3.4.1 (Simplification)**.** *As a first step, we neglect the inequality in Equation* (3.65) *and solve the system for the more general case of* $\sigma_{nn}^{(a)} = \sigma_{nn}^{(b)}$*.*

Assume there is a double node at the boundary Γ_c with coordinates P_c. Then, it is possible to construct a suitable finite element space from the standard shape function with non-traction boundary conditions (i.e. $\underline{\underline{\boldsymbol{\sigma}}}\mathbf{n} = \mathbf{0}$ on Γ_c). Let $\boldsymbol{M}$ be the vector-valued SB matrix of shape functions with

$$\boldsymbol{M} = \begin{pmatrix} M_1 & \dots & M_{K/2} \end{pmatrix} \otimes \mathbf{I}_2 \in \mathbb{R}^{2\times K}, \tag{3.69}$$

where $M_1, \dots, M_{K/2}$ are the scalar shape functions and $\mathbf{I}_m$ is the identity matrix of size m. Without loss of generality, we assume that the degrees associated with the double node on Γ_c are consecutive indices. Let k_P be the index of the first node on the interface Γ_c. The new shape functions must eliminate one degree of freedom because there is one constraint on Γ_c. One possible choice for a transformation matrix is

$$\mathbf{H} = \begin{pmatrix} \mathbf{I}_{2(k_\mathrm{P}-1)} & \mathbf{0} & \mathbf{0} \\ \mathbf{0} & \mathbf{H}_c & \mathbf{0} \\ \mathbf{0} & \mathbf{0} & \mathbf{I}_{K-2(k_\mathrm{P}-1)-3} \end{pmatrix} \qquad \text{with } \mathbf{H}_c = \begin{pmatrix} +n_x & t_x & 0 \\ +n_y & t_y & 0 \\ +n_x & 0 & t_x \\ +n_y & 0 & t_y \end{pmatrix}. \tag{3.70}$$

The transformed matrix of shape functions $\tilde{\boldsymbol{M}}$ expressed in scalar shape functions is

$$\tilde{\boldsymbol{M}} = \begin{pmatrix} M_1 & \dots & 0 & n_x(M_{k_\mathrm{P}} + M_{k_\mathrm{P}+1}) & t_x M_{k_\mathrm{P}} & t_x M_{k_\mathrm{P}+1} & M_{k_\mathrm{P}+2} & \dots & 0 \\ 0 & \dots & M_{k_\mathrm{P}-1} & n_y(M_{k_\mathrm{P}} + M_{k_\mathrm{P}+1}) & t_y M_{k_\mathrm{P}} & t_y M_{k_\mathrm{P}+1} & 0 & \dots & M_{K/2} \end{pmatrix} \tag{3.71}$$

$$\in \mathbb{R}^{2\times K-1}. \tag{3.72}$$

The three modified one-dimensional shape functions all satisfy Equation (3.63) independent of $\tilde{\boldsymbol{u}}(\xi)$. The first transformed shape function is continuous in the normal direction, while for the other directions, the transformed shape functions describe a displacement in the direction of the interface Γ_c. Since the shape functions satisfy Equation (3.63), also all linear combinations satisfy Equation (3.63). All other boundary conditions are natural and will not lead to additional terms in the derivation.

Figure 3.7 shows the three modified shape functions for the cracked rectangle in Figure 3.6a. The x-direction is discontinuous, while the y-direction is continuous.

For comparison with the theoretical results, the minimal non-zero order $\lambda_{\min}$ (Equation (3.4)) can be approximated by

$$\lambda_{\min}^h = \min\{\lambda | -\lambda \text{ is an eigenvalue of } \tilde{\mathbf{S}}_n \text{ and } \lambda > 0\}. \tag{3.73}$$

The approximation quality depends on the boundary mesh and the polynomial degree of the shape functions.

3.4.2 Isotropic Case

We first consider a problem, where both domains $\Omega_{(a)}$ and $\Omega_{(b)}$ consist of isotropic materials. Figure 3.8 shows the SBFEM grid. The number of boundary elements varies for the upper part of the domain depending on the angle γ. Shape functions of degree 10 are used. This case was investigated in detail by Dundurs *et al.* [48]. The problem is solved with the plane strain condition. The material properties are listed in Table A.1b (see Appendix A.1.5). Here, the material of the second domain is dependent on α, such that α is the mismatch parameter (Equation (3.25)). Figure 3.9 shows the first non-zero eigenvalue $\lambda_{\min}$ for varied normalized angle γ/π and varied mismatch parameter α, see Equation (3.25). Results from Dundurs *et al.* [48] (solid black lines) by root finding are overlaid with the results of the SBFEM (colored dashed lines). We observe a good agreement between root finding by Dundurs *et al.* and the SBFEM.

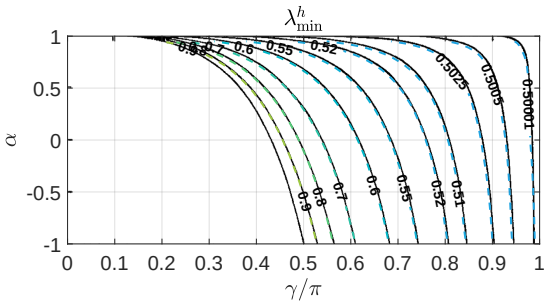

Figure 3.9: $\lambda_{\min}$ in the transition problem for isotropic materials (Table A.1b). Overlay between the SBFEM results (colored dashed lines) and the results from Dundurs *et al.* [48] (solid black lines) by root finding

The geometry can be interpreted as an interface crack for a value of $\gamma = \pi$, and the problem models the transition between a frictionless contact zone and a separation zone. Interestingly, all material variants tend to have a value of $\lambda_{\min}^h = 0.5$ for a crack. Nevertheless, the mode associated with $\lambda_{\min}^h = 0.5$ is not physically feasible. The singular mode only appears because we solved a more general problem (see Remark 3.4.1). By construction, the origin is the point where the transition of the frictionless contact zone and the separation zone occurs. Without loss of generality for this case, the singular mode can be normalized such that the gap $g(-1)$ takes the unit value. The singular mode describes a transition between a crack opening ($g(-1) > 0$) and a slip zone due to this normalization. Figure 3.10a shows that the normal stress of the singular mode at point P_c is positive. Consequently, the normal stress of the singular mode is greater than zero on Γ_c. Near the origin, the singular mode will always dominate the stress. A positive normal stress, however, means that the slip zone should separate (Equation (3.65)). This contradicts the fact that the

origin is defined as the point of transition. Consequently, the singular mode can not exist in this configuration.

Figure 3.10a shows a linear relationship between the normal stress and the mismatch parameter α. On the other hand, there is a non-linear relationship between the shear modulus ratio $G_{(b)}/G_{(a)}$ and the mismatch parameter α. Nevertheless, the range of the ratio $G_{(b)}/G_{(a)}$ covers all practical cases, and for all practical cases, a singular mode has not to be considered in this configuration.

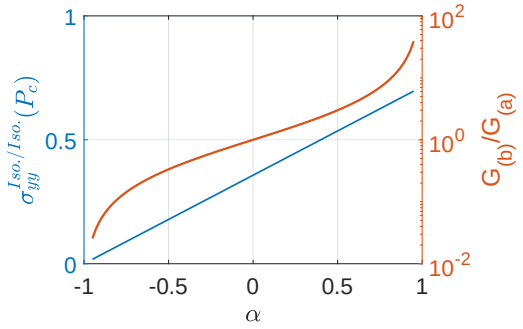

(a) Left axis: normal stress - right axis: shear modulus for material properties in Table A.1b

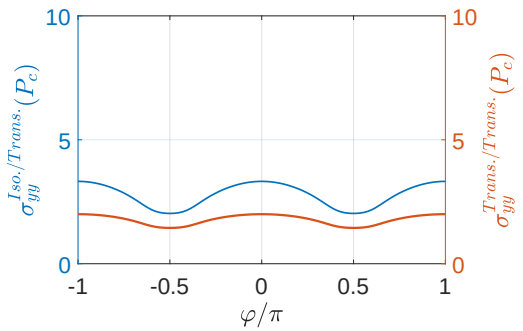

(b) Left axis: CFRP/aluminium (Table A.1e/Table A.1c) - right axis: CFRP/CFRP (Table A.1e/Table A.1e)

Figure 3.10: Normal stress at point P_c for the singular mode with $\gamma = \pi$ for the model in Figure 3.8

3.4.3 Transverse Isotropic Case

As a second problem, we consider transversely isotropic materials. The domains (Figure 3.8) and the plane strain assumption are the same as in the first example. We model two material combinations, which could appear in a modern NDT/SHM application [83]. However, another variation of the materials is used instead of examining a mismatch parameter. For the upper one, the principal material directions of carbon-fiber-reinforced polymers (CFRP) are rotated around the y-axis by the angle θ relative to the global coordinate system, see Appendix A.1.3 for more details. For the bottom material, aluminum and CFRP are considered. The results for the first non-zero eigenvalue are shown in Figure 3.11. The figure illustrates the periodicity of the material rotation in the θ-dependency.

As a second criterion, we again investigate the normal stress for the crack case $\gamma = \pi$. For the investigation, the singular mode is normalized such that $g(-1) = 1$. The normal stress is positive for all material directions as shown in Figure 3.10b. As in the previous case, there is no physically feasible singular mode. The shape of the stress curve is similar in both material combinations - the main differences are the magnitude and the offset.

3.4.4 Conclusion on the Transition Problem

In summary, the results of the SBFEM indicate that the transition between a frictionless contact zone and a separation zone inside an interface crack has no physically feasible singular mode. This result is consistent with Remark 3.1.2. All findings are consistent with the analytical results by Comninou, Dundurs, and others. The SBFEM can extend these findings by also considering different material configurations. In theory, the material properties in the circumferential direction can vary arbitrarily. Even functional graded materials can be considered.

3.5 The Galerkin Approach for SB Shape Functions

This section presents a model for a single super-element under a static load. For a problem under load, the type of contact zone is not given in advance and has to be determined by the algorithm.

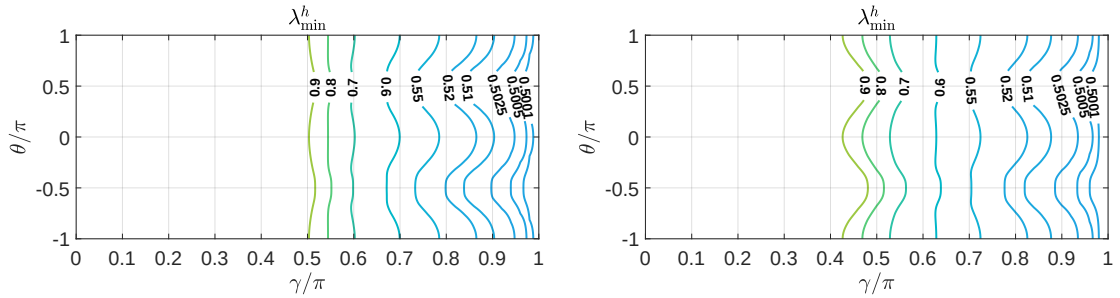

(a) Result for the SBFEM for CFRP/aluminium (Table A.1e/Table A.1c)

(b) Result for the SBFEM for CFRP/CFRP (Table A.1e/Table A.1e)

Figure 3.11: $\lambda_{\min}$ in the transition problem for transversally isotropic materials

For simplicity, we first consider vanishing body loads. The following simple detection method is proposed:

1. Solve the problem for the separated zone:
   The linear system of equations is

   $$\mathbf{K}\mathbf{u} = \mathbf{f}_\tau \tag{3.74}$$

   which follows from Equation (2.12) with $\partial_{tt}\mathbf{u} = \mathbf{0}$ and $\mathbf{f}_b = \mathbf{0}$. The static stiffness matrix $\mathbf{K}$ is calculated with the SB shape functions in Equation (3.57). Section 3.5.1 presents the computation of the static stiffness matrix by a semi-analytical integration, while $\mathbf{f}_\tau$ is computed as in the FEM.

2. Calculate the mean gap (see Section 3.5.2)

   $$\overline{g} = \frac{1}{|\Gamma_c|}\int g(\mathbf{x})\,\mathrm{d}\Gamma_c. \tag{3.75}$$

   - If $\overline{g} > 0$, the approximation is finished.
   - If $\overline{g} \leq 0$, then recalculate the solution with the slip case, i.e., with the SB shape functions given by Equation (3.62).

This is a segment-to-segment approach for contact detection [163]. We will call this approach the Direct Elimination Method (DEM) in the following.

Additionally, an alternative approach is derived in this section, which extends the SB shape functions with polynomial tractions terms to simulate cracks under contact conditions. This alternative approach is based on the Lagrange Multiplier Method.

3.5.1 Static Stiffness Matrix

This section presents the derivation of the static stiffness matrix $\mathbf{K}$ for SB shape functions (Equation (3.56)), which are defined by the matrices $\mathbf{P}$, $\mathbf{S}$ and $\mathbf{T}$. This static stiffness matrix is required for approximating the displacement in domains with a load applied to the boundary. The derivation follows in large parts [98].

The static stiffness matrix is defined as

$$\mathbf{K} = \int \boldsymbol{\varepsilon}(\xi,\eta)^{\mathsf{T}}\mathbf{D}(\eta)\boldsymbol{\varepsilon}(\xi,\eta)\,\mathrm{d}\Omega\,, \tag{3.76}$$

where the strain (in Voigt-notation) for the SB shape functions (Equation (3.56)) can be expressed by [181]

$$\boldsymbol{\varepsilon}(\xi,\eta) = \boldsymbol{\varepsilon}_\eta(\eta)\xi^{(-\mathbf{S}-\mathbf{I})}\mathbf{T}, \tag{3.77}$$

$$\boldsymbol{\varepsilon}_\eta(\eta) = \boldsymbol{B}_1(\eta)\mathbf{P}[-\mathbf{S}] + \boldsymbol{B}_2(\eta)\mathbf{P}, \tag{3.78}$$

where $\boldsymbol{B}_1$ and $\boldsymbol{B}_2$ are element-wise given by Equation (3.45). Equation (3.76) leads to

$$\mathbf{K} = \int (\boldsymbol{\varepsilon}_\eta(\eta)\xi^{(-\mathbf{S}-\mathbf{I})}\mathbf{T})^\mathsf{T}\mathbf{D}(\eta)\boldsymbol{\varepsilon}_\eta(\eta)\xi^{(-\mathbf{S}-\mathbf{I})}\mathbf{T}\,\mathrm{d}\Omega \tag{3.79}$$

$$= \int_0^1 \int (\boldsymbol{\varepsilon}_\eta(\eta)\xi^{(-\mathbf{S}-\mathbf{I})}\mathbf{T})^\mathsf{T}\mathbf{D}(\eta)(\boldsymbol{\varepsilon}_\eta(\eta)\xi^{(-\mathbf{S}-\mathbf{I})}\mathbf{T})|j(\hat{\eta})|\,\mathrm{d}\eta\,\xi\,\mathrm{d}\xi \tag{3.80}$$

$$= \mathbf{T}^\mathsf{T}\int_0^1 \xi^{(-\mathbf{S})^\mathsf{T}}\mathbf{Y}\xi^{(-\mathbf{S}-\mathbf{I})}\,\mathrm{d}\xi\,\mathbf{T} \tag{3.81}$$

with

$$\mathbf{Y} = \int \boldsymbol{\varepsilon}_\eta(\eta)^\mathsf{T}\mathbf{D}(\eta)\boldsymbol{\varepsilon}_\eta(\eta)|j(\hat{\eta})|\,\mathrm{d}\eta \tag{3.82}$$

$$= [-\mathbf{S}]^\mathsf{T}\mathbf{P}^\mathsf{T}\mathbf{E}_0\mathbf{P}[-\mathbf{S}] + \mathbf{P}^\mathsf{T}\mathbf{E}_1\mathbf{P}[-\mathbf{S}] + [-\mathbf{S}]^\mathsf{T}\mathbf{P}^\mathsf{T}\mathbf{E}_1^\mathsf{T}\mathbf{P} + \mathbf{P}^\mathsf{T}\mathbf{E}_2\mathbf{P}, \tag{3.83}$$

where Equations (3.39) and (3.42) are used. Here, the SBFEM coefficient matrices from Equation (3.37) appear again. We consider the following identity

$$\mathbf{Y} = \xi^{(-\mathbf{S})^\mathsf{T}}\mathbf{Y}\xi^{(-\mathbf{S})}\Big|_{\xi=0}^1. \tag{3.84}$$

Integration by parts leads to

$$\mathbf{Y} = \int_0^1 [-\mathbf{S}]^\mathsf{T}\xi^{(-\mathbf{S}-\mathbf{I})^\mathsf{T}}\mathbf{Y}\xi^{(-\mathbf{S})}\,\mathrm{d}\xi + \int_0^1 \xi^{(-\mathbf{S})^\mathsf{T}}\mathbf{Y}\xi^{(-\mathbf{S}-\mathbf{I})}[-\mathbf{S}]\,\mathrm{d}\xi \tag{3.85}$$

$$= [-\mathbf{S}]^\mathsf{T}\int_0^1 \xi^{(-\mathbf{S}-\mathbf{I})^\mathsf{T}}\mathbf{Y}\xi^{(-\mathbf{S})}\,\mathrm{d}\xi + \int_0^1 \xi^{(-\mathbf{S})^\mathsf{T}}\mathbf{Y}\xi^{(-\mathbf{S}-\mathbf{I})}\,\mathrm{d}\xi\,[-\mathbf{S}] \tag{3.86}$$

$$= [-\mathbf{S}]^\mathsf{T}\mathbf{X} + \mathbf{X}[-\mathbf{S}] \tag{3.87}$$

with

$$\mathbf{X} = \int_0^1 \xi^{(-\mathbf{S})^\mathsf{T}}\mathbf{Y}\xi^{(-\mathbf{S}-\mathbf{I})}\,\mathrm{d}\xi \tag{3.88}$$

$$= \int_0^1 \xi^{(-\mathbf{S}-\mathbf{I})^\mathsf{T}}\mathbf{Y}\xi^{(-\mathbf{S})}\,\mathrm{d}\xi\,. \tag{3.89}$$

The result is a LYAPUNOV-equation [98] for $\mathbf{X}$

$$\mathbf{Y} = [-\mathbf{S}]^\mathsf{T}\mathbf{X} + \mathbf{X}[-\mathbf{S}]. \tag{3.90}$$

Finally, substitute the integral in Equation (3.81) by $\mathbf{X}$ (Equation (3.89)) to get the static stiffness matrix

$$\mathbf{K} = \mathbf{T}^\mathsf{T}\mathbf{X}\mathbf{T}. \tag{3.91}$$

This concludes the derivation of the static stiffness matrix with an analytical integration with respect to ξ.

3.5.2 Mean Gap Matrix

Another key ingredient for solving the contact problems is an efficient evaluation of contact detection. This short section presents the evaluation of the mean gap integral (Equation (3.75)) as a matrix.

Recall that P_c is a double node, k_P is the index of the first node associated with P_c and without loss of generality, all four degrees of P_c are consecutive indices, and the first degree is associated with the boundary (a). Then, for the function g it holds

$$g(\mathbf{x}) = (\mathbf{n}^{(b)})^\mathsf{T}\boldsymbol{u}^{(b)}(\mathbf{x}) + (\mathbf{n}^{(a)})^\mathsf{T}\boldsymbol{u}^{(a)}(\mathbf{x}) \tag{3.92}$$

$$= \mathbf{n}^\mathsf{T}(\boldsymbol{u}^{(b)}(\mathbf{x}) - \boldsymbol{u}^{(a)}(\mathbf{x})) \tag{3.93}$$

with $\mathbf{n} = \mathbf{n}^{(b)} = -\mathbf{n}^{(a)}$. The nodal gap $\mathbf{g}$ is given by

$$\mathbf{g} = \mathbf{n}\big(\boldsymbol{M}(\eta_{(b)}) - \boldsymbol{M}(\eta_{(a)})\big), \tag{3.94}$$

where $\eta_{(a)}$, $\eta_{(b)}$ are the circumferential coordinates associated with the boundary Γ_c approaching from the respective sides, (a) or (b), and $\boldsymbol{M}$ is the boundary matrix of shape functions of Equation (3.36). The nodal gap can be calculated entry-wise by

$$(\mathbf{g})_i = \begin{cases} -n_x & i = 2(k_\mathrm{P} - 1) + 1 \\ -n_y & i = 2(k_\mathrm{P} - 1) + 2 \\ +n_x & i = 2(k_\mathrm{P} - 1) + 3 \\ +n_y & i = 2(k_\mathrm{P} - 1) + 4 \\ 0 & \text{otherwise} \end{cases}. \tag{3.95}$$

The mean gap from Equation (3.75) is calculated using Equation (3.56) by

$$\begin{aligned} \overline{g} &= \frac{1}{|\Gamma_c|} \int g(\mathbf{x}) \, \mathrm{d}\Gamma_c && (3.96)\\ &= \frac{1}{L_c} \int_0^1 \mathbf{g}^\mathsf{T} \mathbf{P} \xi^{-\mathbf{S}} \mathbf{T} \mathbf{u} L_c \, \mathrm{d}\xi && (3.97)\\ &= \mathbf{g}^\mathsf{T} \mathbf{P} \, (-\mathbf{S} + \mathbf{I})^{-1} \xi^{-\mathbf{S}+\mathbf{I}} \big|_{\xi=0}^1 \mathbf{T} \mathbf{u} && (3.98)\\ &= \mathbf{g}^\mathsf{T} \mathbf{P} (-\mathbf{S} + \mathbf{I})^{-1} \mathbf{T} \mathbf{u} && (3.99)\\ &= \mathbf{G} \mathbf{u}, && (3.100) \end{aligned}$$

where L_c is the distance between the scaling center and the double node P_c. The gap matrix $\mathbf{G}^{\star 1}$ is given by

$$\mathbf{G} = \mathbf{g}^\mathsf{T} \mathbf{P} (-\mathbf{S} + \mathbf{I})^{-1} \mathbf{T}. \tag{3.101}$$

The gap matrix allows an efficient evaluation of the mean gap.

3.5.3 SB Shape Function with Traction Bubble Functions

The direct elimination approach discussed in the previous section has disadvantages, which are summarized in Remark 3.3.5. Furthermore, the shape functions of the traction-free boundary condition are not able to represent contact forces (Remark 3.3.3). To overcome these disadvantages, a new approach is considered in this section. The basic idea is to divide the displacement formally into a sum

$$\boldsymbol{u} = \boldsymbol{u}_{\boldsymbol{\tau}=\mathbf{0}} + \boldsymbol{u}_{\boldsymbol{\tau}\in\mathcal{P}}, \tag{3.102}$$

where $\boldsymbol{u}_{\boldsymbol{\tau}=\mathbf{0}}$ is a displacement with zero-tractions and $\boldsymbol{u}_{\boldsymbol{\tau}\in\mathcal{P}}$ is a displacement with a polynomial traction. This leads to additional terms in the traction-free shape functions so that polynomial tractions are also incorporated in the shape functions. However, this approach neglects the displacement and contact pressure dependency, which can lead to a change in the singular order. Nevertheless, we will see that the contact pressure can be represented polynomially in an important case - a crack in an isotropic material. The approach is inspired by [181]. The shape functions are not continuous in the normal direction. For the state of contact, additionally, Lagrange multipliers are used [181] to weakly enforce continuity. In contrast to [181], the additional term presented here is based on the traction on both boundaries being non-zero. While the solution process for $\boldsymbol{u}_{\boldsymbol{\tau}=\mathbf{0}}$ is the same as in Section 3.3.1.1, this section will present only the solution process for $\boldsymbol{u}_{\boldsymbol{\tau}\in\mathcal{P}}$ and the coupling of both. In the following, we will call this approach the Lagrange Multiplier Method (LMM).

[⋆1] Technically, $\mathbf{G}$ is here only a vector. In other methods, there is a gap matrix with multiple columns.

For nodal shape functions of degree p (p + 1 nodes), let an extended traction $\bar{\boldsymbol{\tau}}$ be expressed as a TAYLOR-series up to degree p − 1 multiplied by a normal vector according to the sides, i.e.,

$$\bar{\boldsymbol{\tau}}(\mathbf{x}) = \begin{cases} \mathbf{n}^{(a)} \sum_{\ell=1}^{\mathrm{p}} c_\ell \xi^{\ell-1} & \mathbf{x} \in \Gamma_c^{(a)} \\ \mathbf{n}^{(b)} \sum_{\ell=1}^{\mathrm{p}} c_\ell \xi^{\ell-1} & \mathbf{x} \in \Gamma_c^{(b)} \\ \mathbf{0} & \mathbf{x} \in \Omega \end{cases}, \tag{3.103}$$

where c_ℓ are arbitrary coefficients, and an index shift is introduced for a more straightforward result at the end. Figure 3.12a shows an exemplary domain for the SB shape functions. The arrows in this figure indicate the traction for the constant term. Then, the nodal traction $\boldsymbol{f}_\tau$ in Equation (3.38) can be written as

$$\boldsymbol{f}_\tau = \sum_{\ell=1}^{\mathrm{p}} c_\ell \xi^{\ell-1} \mathbf{w}_\ell \tag{3.104}$$

$$= \mathbf{W} \xi^{(\boldsymbol{\Theta}_\tau - \mathbf{I})} \mathbf{c}, \tag{3.105}$$

where $\boldsymbol{\Theta}_\tau = \mathrm{diag}(1, \ldots, \mathrm{p})$ is a diagonal matrix, the vector $\mathbf{c}$ contains the coefficients, and $\mathbf{W}$ is a matrix with the columns $\mathbf{w}_\ell$.

The traction in Equation (3.103) is defined by the normal vector and has a non-zero contribution only at the double node. The definition is similar to the gap g, except for the gap being formulated for the displacement, while the traction is a boundary force. Nevertheless, from a purely algebraic point of view, the nodal traction $\mathbf{w}_\ell$ of each TAYLOR-term can be expressed by the nodal gap $\mathbf{g}$ (see Equation (3.95)), i.e.,

$$\mathbf{w}_\ell = \mathbf{g}. \tag{3.106}$$

The particular solution $\boldsymbol{\phi}(\xi)$ (see Equation (3.52)) for each ℓ is calculated separately by the ansatz $\boldsymbol{\phi}_\ell \xi^\ell$. Substituting $\boldsymbol{f}_\tau = \mathbf{w}_\ell \xi^{\ell-1}$ and Equations (3.38) in Equation (3.37), the ansatz for $\mathbf{u}$ leads to the following linear system for each TAYLOR-term ℓ [181]

$$\boldsymbol{\phi}_\ell = -\mathbf{E}_\theta(\ell)^{-1} \mathbf{w}_\ell, \tag{3.107}$$

$$\mathbf{E}_\theta(\ell) = \ell^2 \mathbf{E}_0 + \ell(\mathbf{E}_1^\mathsf{T} - \mathbf{E}_1) - \mathbf{E}_2. \tag{3.108}$$

Remark 3.5.1 (Stabilization of $\mathbf{E}_\theta$)**.** *Let $(\boldsymbol{\psi}_\mathbf{u}, \lambda)$ be an eigenpair of the matrix $\mathbf{Z}$ (Equation (3.50)), then $\mathbf{E}_\theta(\lambda)$ is singular because $\boldsymbol{\psi}_\mathbf{u}$ is a non-trivial vector which lies in the kernel (see Equation (3.54)). It is well known that the matrix $\mathbf{Z}$ has integers as eigenvalues, e.g., [72]. To invert $\mathbf{E}_\theta$, the following stabilization is proposed:*
Compute the eigenvalues λ_i of $\mathbf{S}_p$ in an ordered fashion so that the SCHUR *block can be traced back. Check if there is an eigenvalue λ^*, such that $\|\ell - \lambda^*\| <$ tol for a given tolerance* tol.

- *If not, solve Equation* (3.107)

$$\tilde{\boldsymbol{\phi}}_\ell = -\mathbf{E}_\theta(\ell)^{-1} \mathbf{w}_\ell, \tag{3.109}$$

  to get a preliminary vector $\tilde{\boldsymbol{\phi}}_\ell$.

- *If there is an eigenvalue λ^*, then let $\boldsymbol{\Psi}_u^*$ be the columns of $\boldsymbol{\Psi}_u$ corresponding to the* SCHUR *block of λ^* and n^* the size of the* SCHUR *block. Introduce a vector $\mathbf{w}^*$ of n^* auxiliary variables and solve*

$$\tilde{\boldsymbol{\phi}}_\ell = -\begin{pmatrix} \mathbf{E}_\theta(\ell) \\ (\boldsymbol{\Psi}_u^*)^\mathsf{T} \end{pmatrix}^\dagger \begin{pmatrix} \mathbf{w}_\ell \\ \mathbf{w}^* \end{pmatrix}, \tag{3.110}$$

  where † denotes the pseudo-inverse and $\tilde{\boldsymbol{\phi}}_\ell$ is the preliminary vector.

The reasoning behind this stabilization is that we prefer modes where the nodal vectors are orthogonal. The auxiliary equations enforce the nodal orthogonality. Afterward, normalize the preliminary vector

$$\boldsymbol{\phi}_\ell = \frac{\tilde{\boldsymbol{\phi}}_\ell}{\|\tilde{\boldsymbol{\phi}}_\ell\|}. \tag{3.111}$$

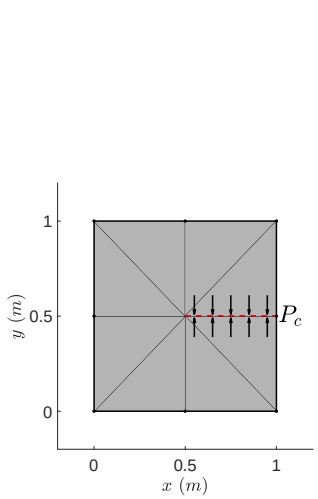

(a) Rectangular domain with crack and traction

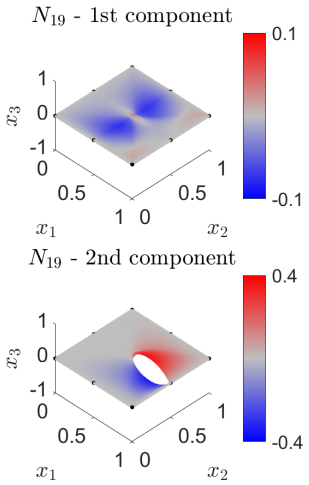

(b) Traction SB shape functions with p=1

Figure 3.12: Example of the SB shape function associated with a constant traction

The matrices for the SB shape functions (Equation (3.56)) are defined by [98, 181]

$$\begin{aligned}\mathbf{P} &= \begin{bmatrix}\boldsymbol{\Psi}_u & \boldsymbol{\Phi}_\tau\end{bmatrix},\\ \mathbf{S} &= \begin{bmatrix}\mathbf{S}_p & \mathbf{0}\\ \mathbf{0} & -\boldsymbol{\Theta}_\tau\end{bmatrix},\\ \mathbf{T} &= \begin{bmatrix}\boldsymbol{\Psi}_u^{-1} & \boldsymbol{\Psi}_u^{-1}\boldsymbol{\Phi}_\tau\\ \mathbf{0} & \mathbf{I}\end{bmatrix},\end{aligned} \tag{3.112}$$

where $\boldsymbol{\Phi}_\tau$ is a matrix with the columns $\boldsymbol{\phi}_\ell$ with the steps of Remark 3.5.1. Figure 3.12b shows the SB shape functions for $\mathrm{p} = 1$ and $\ell = 1$. Note that due to the definition of $\mathbf{T}$ this shape function is a so-called bubble function. Bubble functions are zero on the boundary of a super-element. This leads to a simplified assembly process because the degree of freedom is independent of neighboring super-elements.

3.5.4 Lagrange Multiplier Matrix for Domains with Common Scaling Center

As mentioned above, it is not enough to add the bubble functions to the traction-free shape functions. Additionally, the traction has to be added as degrees of freedom in the form of Lagrange multipliers (see [181]). A general summary of the Lagrange Multiplier Method for the enforcement of continuity conditions can be found in Section 4.11.1 The Lagrange multiplier matrix is defined as

$$\mathbf{L} = \int (\boldsymbol{\delta}\mathbf{u}^{(a)} - \boldsymbol{\delta}\mathbf{u}^{(b)})^\mathsf{T}\mathbf{n}\lambda \, \mathrm{d}\Gamma_c, \tag{3.113}$$

where $\boldsymbol{\delta}\mathbf{u}$ is the virtual displacement and λ is the Lagrange multiplier. Denote the shape functions of the Lagrange multiplier by $\boldsymbol{N}^\lambda(\xi)$. The Lagrange multiplier shape functions are only associated with the boundary and therefore one-dimensional shape functions. For the sake of simplicity, we use Lagrange shape functions that are represented as monomials

$$\boldsymbol{N}^\lambda(\xi) = \mathbf{P}_\lambda \xi^{\mathbf{S}_\lambda}\mathbf{T}_\lambda \tag{3.114}$$

with

$$\mathbf{P}_\lambda = (1, \ldots, 1), \tag{3.115}$$

$$\mathbf{S}_\lambda = \mathrm{diag}(\mathrm{p}-1, \ldots, 0) \tag{3.116}$$

and a matrix $\mathbf{T}_\lambda$ which contains the coefficients of the LAGRANGE polynomials as columns. Note that the degree matches with the traction bubble functions.

Analogous to the static stiffness matrix (see Section 3.5.1), this leads to

$$\mathbf{L} = \mathbf{T}^\mathsf{T} \int [\xi^{-\mathbf{S}}]^\mathsf{T} \mathbf{Y}^\lambda [\xi^{-\mathbf{S}_\lambda}] \, \mathrm{d}\xi \, \mathbf{T}_\lambda \tag{3.117}$$

$$= \mathbf{T}^\mathsf{T} \int [\xi^{-\mathbf{S}+0.5\mathbf{I}-\mathbf{I}}]^\mathsf{T} \mathbf{Y}^\lambda [\xi^{-\mathbf{S}_\lambda+0.5\mathbf{I}}] \, \mathrm{d}\xi \, \mathbf{T}_\lambda \tag{3.118}$$

with $\mathbf{P}$, $\mathbf{S}$, $\mathbf{T}$ from Equation (3.112) for the displacement SB shape functions and

$$\mathbf{Y}^\lambda = \mathbf{P}^\mathsf{T} \mathbf{g}^\mathsf{T} L_c \mathbf{P}_\lambda, \tag{3.119}$$

where $\mathbf{g}$ is the nodal gap (see Equation (3.95)) and L_c is the distance between the scaling center and the double node P_c. Defining

$$\mathbf{X}^\lambda = \int [\xi^{-\mathbf{S}+0.5\mathbf{I}-\mathbf{I}}]^\mathsf{T} \mathbf{Y}^\lambda [\xi^{-\mathbf{S}_\lambda+0.5\mathbf{I}}] \, \mathrm{d}\xi \tag{3.120}$$

$$= \int [\xi^{-\mathbf{S}+0.5\mathbf{I}}]^\mathsf{T} \mathbf{Y}^\lambda [\xi^{-\mathbf{S}_\lambda+0.5\mathbf{I}-\mathbf{I}}] \, \mathrm{d}\xi \tag{3.121}$$

and integrating by parts leads to a LYAPUNOV-equation

$$[-\mathbf{S}+0.5\mathbf{I}]^\mathsf{T} \mathbf{X}^\lambda + \mathbf{X}^\lambda [-\mathbf{S}_\lambda + 0.5\mathbf{I}] = \mathbf{Y}^\lambda. \tag{3.122}$$

Substituting Equation (3.120) in Equation (3.118) results finally in

$$\mathbf{L} = \mathbf{T}^\mathsf{T} \mathbf{X}^\lambda \mathbf{T}_\lambda. \tag{3.123}$$

This concludes the derivation of the LAGRANGE multiplier matrix $\mathbf{L}$ with an analytical integration technique.

3.5.5 LAGRANGE Multiplier Method for a Single Super-element

For the LAGRANGE Multiplier Method, the overall solution process for a segment-to-segment approach is similar to Section 3.5. The algorithms must determine the state of contact via the mean gap. First, solve

$$\mathbf{K}\mathbf{u} = \mathbf{f}_\tau, \tag{3.124}$$

with the static stiffness matrix $\mathbf{K}$ computed with the SB shape functions defined by Equation (3.112). If $\mathbf{G}\mathbf{u} < 0$ activate the contact segment and resolve the problem. As usual for LAGRANGE multipliers, the force-displacement relationship matrix for an active contact segment takes the form of a saddle point problem, i.e.,

$$\begin{pmatrix} \mathbf{K} & \mathbf{L} \\ \mathbf{L}^\mathsf{T} & \mathbf{0} \end{pmatrix} \begin{pmatrix} \mathbf{u} \\ \boldsymbol{\lambda} \end{pmatrix} = \begin{pmatrix} \mathbf{f}_\tau \\ \mathbf{0} \end{pmatrix}. \tag{3.125}$$

For saddle point problems, Remark 4.11.1 has to be considered.

3.6 Numerical Experiments for Loaded Structures

This section presents two cracked rectangles. The first one is homogeneous, and the second consists of two materials. For these domains, the direct elimination approach (Section 3.3.1) and the LAGRANGE multiplier approach (Section 3.5.4) of the previous sections are compared with each other.

3.6.1 Patch Test of a Domain with a Crack

As a first example, we consider a patch test. Figure 3.13a shows an overview of the problem. At the top of a rectangular domain with a single straight crack, a uniform load of τ_0 is applied, while the y-direction of the lower edge is fixed, and the lower-left corner is fixed in both directions. We first consider a negative τ_0. For a horizontal crack, the analytical solution for the material parameters given in Table A.1a is well known:

$$\mathbf{u}(x,y) = \tau_0 \begin{pmatrix} \frac{x}{6} \\ \frac{-y}{3} \end{pmatrix}. \tag{3.126}$$

Note that in this case, the contact pressure $\mathbf{n}^\mathsf{T}\underline{\underline{\boldsymbol{\sigma}}}\mathbf{n}$ equals τ_0, while the tangential pressure is zero. Both methods, the Direct Elimination Method (DEM) of Section 3.3.1.2 and the LAGRANGE Multiplier Method (LMM) of Section 3.5.3, are applied. The contact detection of Section 3.5 is used. Figure 3.13a also shows the deformed body as a dashed line for $\tau_0 = -0.5\,\mathrm{GPa}$. Figure 3.14a and Figure 3.14b show the eigenvalues of the matrix $\mathbf{S}$ in the complex plane for both methods together with their multiplicity as a number. The eigenvalues of the traction-free solution are shown in blue, and the additional eigenvalues due to the TAYLOR-series in red (see Figure 3.14b). The traction-free solution has one mode less than the Direct Elimination Method for every integer. The additional eigenvalues compensate for this. The same eigenvalues are required for being able to represent the same displacements. However, the numerical solution of higher modes with an eigenvalue smaller than 0.5 does not coincide.

In the case of low degrees, both methods result in the same nodal values because the relative nodal difference

$$\text{max. nodal difference} = \max_{\text{P is a node}} \frac{|\mathbf{u}^{\mathrm{DEM}}(\mathrm{P}) - \mathbf{u}^{\mathrm{LMM}}(\mathrm{P})|}{|\mathbf{u}^{\mathrm{DEM}}(\mathrm{P})|} \tag{3.127}$$

is close to the machine precision (see Figure 3.16a) for $\tau_0 = -0.5\,\mathrm{GPa}$. At higher degrees, the difference increases. The increasing value of the condition number of the LMM could lead to larger errors. The DEM fulfills the patch test for every degree within the machine accuracy ($< 10^{-15}$), while the LMM results in a maximal nodal difference below 10^{-9}. The higher condition number for the LMM results in this larger difference.

In the case of a positive load, the described setting is a typical fracture test. Figure 3.13b shows the approximation for 0.05 GPa. Comparing the shape of both approximations in Figure 3.13a and Figure 3.13b, the non-linearity of a contact problem is visible. Figure 3.13c additionally shows the displacement of the right/top $\mathrm{P} = (1\,\mathrm{m}, 1\,\mathrm{m})$ corner and the mean gap as a function of τ_0. Here, the non-differentiable behavior at $\tau_0 = 0\,\mathrm{GPa}$ can be observed.

3.6.2 Test with a Non-polynomial Traction of a Domain with a Crack

As a second example, the same geometry is loaded with a non-polynomial traction $\boldsymbol{\tau}$ with

$$\boldsymbol{\tau}(\mathbf{x}) = \begin{pmatrix} 0 \\ -0.5\sin(\pi x) \end{pmatrix} \mathrm{GPa}. \tag{3.128}$$

The negative sign of the traction leads to an active contact area. Figure 3.15 shows the displacement as a dashed line for both methods - DEM and LMM. For further comparison, Figure 3.16b depicts the maximal nodal difference. The difference compared to a constant load is more significant (Figure 3.16a), but the difference decreases rapidly under p-refinement, so it can be assumed that both methods have the same displacement as a limit.

3.6.3 Test of a Domain with an Interface Crack between two Materials

As the last example, we investigate a test for an interface crack. Figure 3.17a for DEM and Figure 3.17b for LMM give an overview. We consider a uniform load of $-0.5\,\mathrm{GPa}$ at the top edge. To investigate the behavior of many material ratios, the material parameters from Table A.1b are used again because they depend on the mismatch parameter α which is varied.

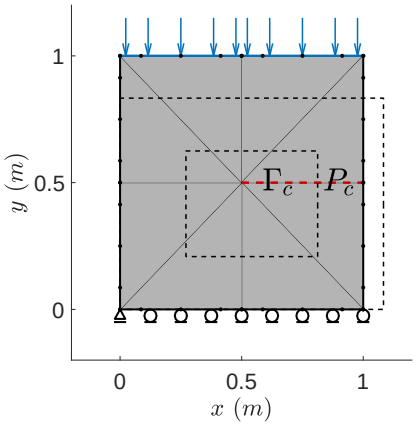

(a) Domain with solution with LMM for $\tau_0 = -0.5\,\mathrm{GPa}$

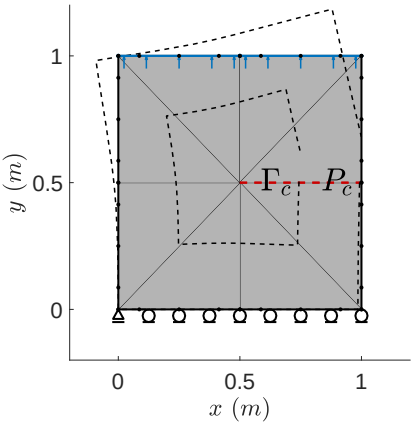

(b) Domain with solution with LMM for $\tau_0 = 0.05\,\mathrm{GPa}$

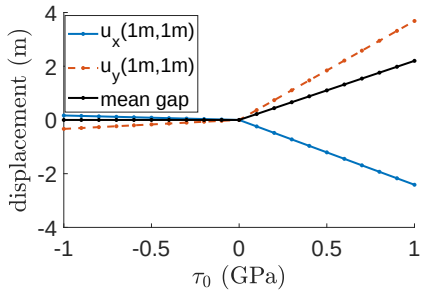

(c) Displacement at P = (1 m, 1 m) and mean gap for LMM

Figure 3.13: Test for a single super-element with a crack; constant traction and one material

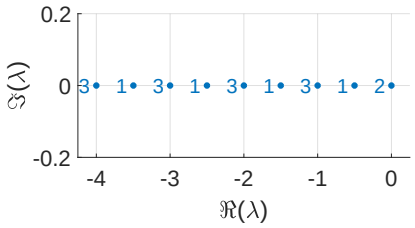

(a) Eigenvalues of **S** with the DEM

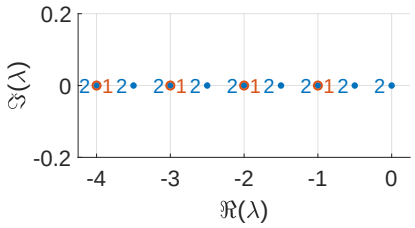

(b) Eigenvalues of **S** with the LMM

Figure 3.14: Eigenvalues of a single super-element with a crack; one material

The approximation of the displacements for $\alpha = 0.5$ and $\mathrm{p} = 4$ is displayed as a dashed line in Figure 3.17a and Figure 3.17b for DEM and LMM, respectively. As a result of the two materials, the eigenvalues of both systems do no longer match for $\alpha = 0.5$, compare Figures 3.18a and 3.18b. This leads to a difference in the nodal displacements, as Figure 3.19a shows. The difference is nearly independent of the polynomial degree, which indicates a fundamentally different behavior because of the differences in the modes, while a numerical reason is unlikely. To illustrate the difference between an interface crack and a crack in a uniform material, the α-dependency is depicted in Figure 3.19b. Only for a very narrow peak, both methods lead to numerically identical results for $\alpha = 0$, where both materials are the same. The figure only shows the case $p = 2$, but this behavior is the same for all polynomial degrees.

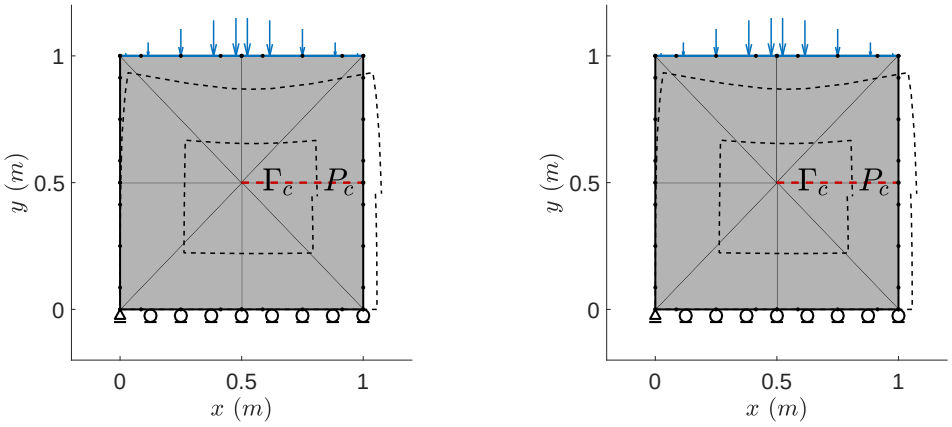

(a) Domain with the solution for DEM

(b) Domain with the solution for LMM

Figure 3.15: Test for a single super-element with a crack; non-polynomial traction and one material

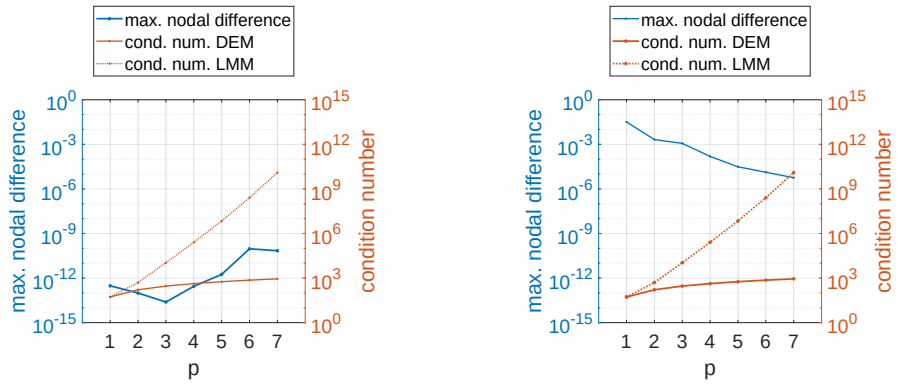

(a) p-refinement for the test in Figure 3.13

(b) p-refinement for the test with non-polynomial traction in Figure 3.15

Figure 3.16: Nodal comparison between Direct Elimination Method and LAGRANGE Multiplier Method

3.6.4 Conclusion for Loaded Structures

In general, both models - the direct elimination approach (Section 3.3.1) and the LAGRANGE multiplier approach (Section 3.5.4) - for cracks under contact conditions lead to different results. The direct elimination approach implements the boundary conditions exactly by considering both limiting cases - contact and non-contact. However, direct elimination is not very practical for dynamic simulation because the shape functions change for a transition from contact to non-contact. Changing shape functions require an additional projection step in dynamic analysis.

The LAGRANGE multiplier approach requires the additional assumption that a polynomial can approximate the contact pressure. The following investigations on general material configurations will show that this assumption can indeed be questioned. However, for cracks in a single material, both models show similar results, justifying the polynomial pressure assumption. If this additional assumption holds, the same set of shape functions can be used for both contact and non-contact states. The use of traction bubble functions provides a straightforward implementation for dynamic analysis. Therefore, the LAGRANGE multiplier approach is extended to dynamic problems in Section 4.

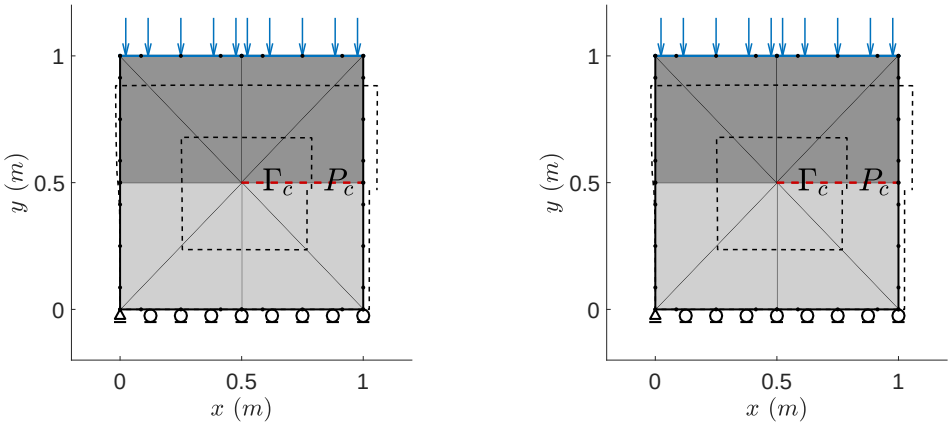

(a) Domain with the solution for DEM

(b) Domain with the solution for LMM

Figure 3.17: Test for a single super-element with a crack; constant traction and two materials

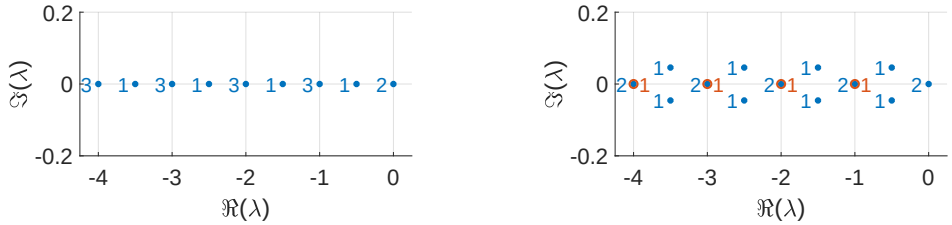

(a) Eigenvalues of **S** with DEM

(b) Eigenvalues of **S** with LMM

Figure 3.18: Eigenvalues of a single super-element with a crack; two materials

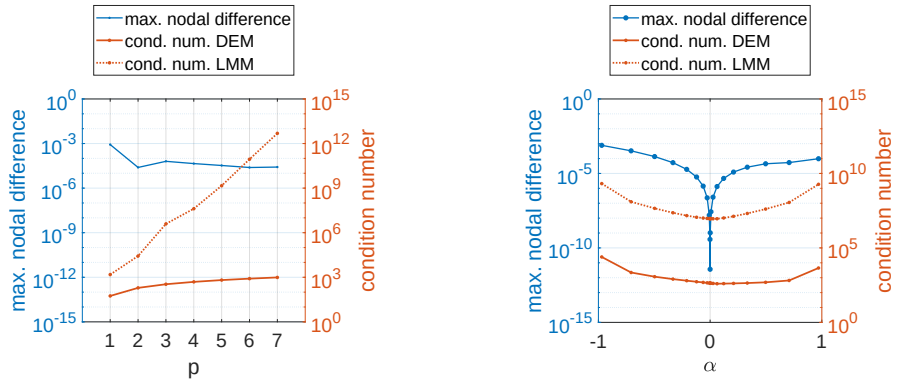

(a) p-refinement for the patch test in Figure 3.17

(b) α-dependency for p = 2 for the patch test in Figure 3.17

Figure 3.19: Nodal comparison between Direct Elimination Method and Lagrange Multiplier Method for the tests of a crack between two materials

3.7 Introduction to the Construction of the Enrichment Functions

The SB shape functions approach for the simulation of contact and singular behavior is to add polynomial traction bubble functions to a super-element that can already represent the singular stress. In this section, we follow the opposite approach: adding singular bubble functions to the

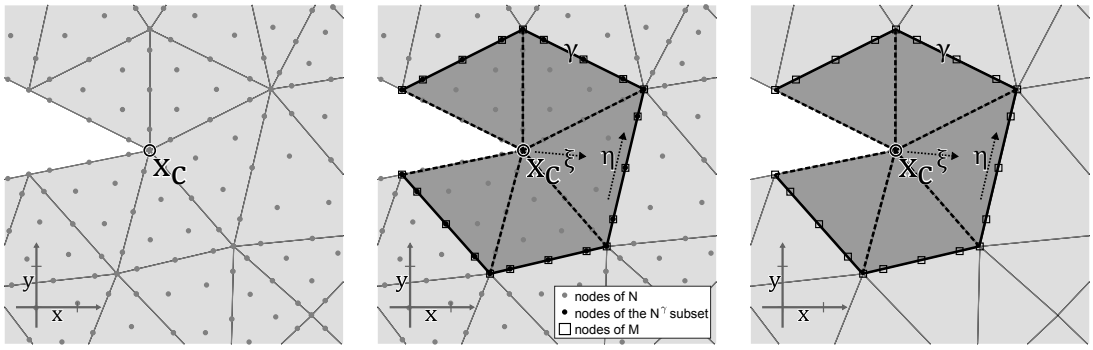

(a) FE-mesh [23] (b) SBFE-polygon in FE-mesh [23] (c) SBFE-mesh [23]

Figure 3.20: Definition of an SBFE-polygon within a triangular finite element mesh [23]

FEM on a triangular mesh. The FEM can represent the polynomial traction, but an accurate representation of the singular field is missing. These studies allow the comparison of different methods for simulating breathing cracks, since the most effective method is difficult to predict for nonlinear problems. Since the FEM is a very effective method for simulating wave propagation problems in the time domain, an extension of the FEM seems to be a competitive alternative to the SBFEM approach presented in the previous sections. One of the main features of the proposed approach, originally presented in [23] and further investigated in [22], is that it requires only information that is readily available in a standard triangulation and that it can be automatized.

In general, to develop an automated procedure, a method that provides the local behavior of the stress singularity is required. In principle, this can be every analytical or numerical procedure mentioned previously if it fits the problem. Yeh and Tadjbakhsh [176] investigate multi-material corners by employing an FE-eigenanalysis on a radial mesh with a polar coordinate transformation. Pageua and Biggers [102, 103] used an enrichment for linear elements by an FE-eigenanalysis, also based on polar coordinates. Similarly, Duarte *et al.* [46] used a root-finding algorithm in combination with the XFEM for isotropic solids. The polar coordinates lead to a simple transformation but at the same time require a layer of transitional elements. Bi-material wedges were investigated by Chen *et al.* [30] by extending the Hybrid Crack Element with the polar FE-eigenanalysis by Sze and Wang [149].

3.8 Construction of the Enrichment Functions

Consider an arbitrary triangular finite element mesh (Figure 3.20a). For the Galerkin Method, the displacement is approximated with enriched finite element shape functions, i.e.,

$$\boldsymbol{u}(\mathbf{x}) = \sum_{m=1}^{M} c_m \boldsymbol{N}_m(\mathbf{x}) + \sum_{n=1}^{M^*} c_n^* \boldsymbol{N}_n^*(\mathbf{x}), \tag{3.129}$$

where $\boldsymbol{N}_m \colon \mathbb{R}^2 \to \mathbb{R}^2$ are the M two-dimensional, vector-valued shape functions of degree p (see Section 2.2.1) and $\boldsymbol{N}_n^* \colon \mathbb{R}^2 \to \mathbb{R}^2$ are M^* special enrichment functions. These special enrichment functions incorporate the scaled boundary modes in the approximation in an automatic way. We follow similar steps as in [102].

The procedure for the construction is divided into three sub-steps:

1. Defining the SBFE-polygon,

2. Computing modes based on the SBFEM procedure,

3. Constructing the enrichment functions based on the singular modes.

Defining the SBFE-polygon We can identify vertices that potentially exhibit stress singularities based on the geometry, material distribution, and boundary conditions. We assume that the elements have straight lines. Elements containing the vertex build the support for the enrichment function. We define a scaled boundary coordinate system to determine the potentially existing singular modes. The vertex is chosen as the scaling center $\mathbf{x}^c$ (see Figure 3.20a), while the curve $\boldsymbol{\gamma}$ consists of the boundary edges which do not contain the scaling center. The scaled boundary coordinate system

$$\mathbf{x}(\xi,\eta) = \xi\big(\boldsymbol{\gamma}(\eta) - \mathbf{x}^c\big) + \mathbf{x}^c, \tag{3.130}$$

with $0 \leq \xi \leq 1$ can express every point inside the SBFE-polygon marked in Figure 3.20b by a darker area. Figure 3.20b shows the curve $\boldsymbol{\gamma}$ as a thick line, but note that the two dashed lines that are part of the boundary are not included.

Computing modes based on the SBFEM procedure For the curve $\boldsymbol{\gamma}$, we define a matrix of shape functions $\boldsymbol{M}\colon \mathbb{R} \to \mathbb{R}^{2\times 2\,\mathrm{n_{node}}}$, which is directly computed with the nodes from the FE-mesh. $\mathrm{n_{node}}$ is the number of active nodes of the FE-mesh. If DIRICHLET boundary conditions fix a node, the node gets no associated shape functions. The matrix of shape functions $\boldsymbol{M}$ is used for the SBFEM approach, which is presented in Section 3.3, leading to the SBFEM equation in displacement

$$\xi^2\mathbf{E}_0\partial_{\xi\xi}\tilde{\boldsymbol{u}}(\xi) + \xi(\mathbf{E}_0 + \mathbf{E}_1^{\mathsf{T}} - \mathbf{E}_1)\partial_\xi\tilde{\boldsymbol{u}}(\xi) - \mathbf{E}_2\tilde{\boldsymbol{u}}(\xi) = \mathbf{0}. \tag{3.131}$$

with vanishing tractions and body load (compare with Equation (3.37)). Here, $\tilde{\boldsymbol{u}}$ is a temporary ansatz for the displacement, which will not be used for the GALERKIN approach. It is sufficient to consider only the unloaded modes because the shape functions of the FE-mesh can already represent tractions and the body load well enough. In rare cases, the body load can lead to additional singular modes - the interested reader is referred to [129, 131, 171]. Figure 3.20c shows this substep. Here, the nodes of the SBFE-polygon are marked with squares (□). If NEUMANNboundary conditions hold for both boundary edges along the scaling direction, $\mathrm{n_{node}}$ is 21. The element-wise computation of the matrices $\mathbf{E}_0, \mathbf{E}_1$ and $\mathbf{E}_2$ follows Equation (3.42). In the computation, there is the additional assumption that the elasticity matrix $\mathbf{D}$ is independent of the scaling direction ξ. Crucially, the elasticity matrix $\mathbf{D}$ can change in the circumferential direction η and can incorporate anisotropic material behavior.

In the previous sections, the solution of Equation (3.131) is derived with SCHUR decomposition. Now, it is solved with the ansatz for the EULER matrix equation:

$$\tilde{\boldsymbol{u}}(\xi) = \sum_{i=1}^{I} \xi^{-\lambda_i}\boldsymbol{\phi}_i \qquad \text{with } \lambda_i \in \mathbb{C},\ \boldsymbol{\phi}_i \in \mathbb{C}^{2\,\mathrm{n_{node}}}, \tag{3.132}$$

where $\xi^{-\lambda_i}\boldsymbol{\phi}_i$ is referred to as a mode of the SBFE-polygon. A quadratic eigenvalue problem for every single mode follows:

$$\lambda_i^2\mathbf{E}_0\boldsymbol{\phi}_i - \lambda_i(\mathbf{E}_1^{\mathsf{T}} - \mathbf{E}_1)\boldsymbol{\phi}_i - \mathbf{E}_2\boldsymbol{\phi}_i = \mathbf{0}. \tag{3.133}$$

The quadratic eigenvalue problem has $4\,\mathrm{n_{node}}$ solutions. The modes with eigenvalues having a positive real part can be discarded, since the displacement must be finite at $\xi = 0$. We are interested in the modes which correspond to modes with singular stresses. The stress is related, among other things, to the displacement in the scaled boundary coordinate system through differentiation with respect to ξ:

$$\partial_\xi\xi^{-(a+\mathrm{i}\,b)} = -(a+\mathrm{i}\,b)\xi^{-(a+1)}\Big(\cos\big(b\log(\xi)\big) - \mathrm{i}\sin\big(b\log(\xi)\big)\Big). \tag{3.134}$$

Thus, the singular modes are characterized by $-1 + \mathrm{tol} < \Re(\lambda_i) < 0 - \mathrm{tol}$, where $\Re$ is the real part of the argument and $\mathrm{tol} = 10^{-5}$ is a small number which is necessary due to numerical errors. The value of tol was chosen by experience. Since the modes are only once weakly differentiable, the FE-approximation without enrichment shows an impaired convergence rate if the displacement contains those modes. Figure 3.21 depicts the eigenvalues corresponding to the geometry given in Figure 3.20b in the complex plane. For the rest of this section, the index i refers only to singular modes within the area of interest. This area is marked in gray in Figure 3.21.

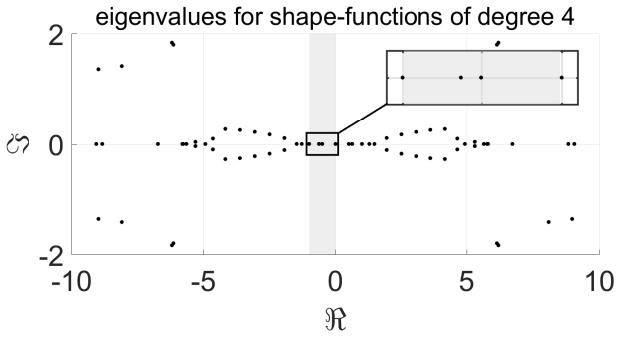

Figure 3.21: Eigenvalues of the SBFE-polygon given in Figure 3.20b for an isotropic material (plane strain, $\nu = 1/3$) [23]

In global coordinates, a single mode is

$$\boldsymbol{\Phi}_i(\mathbf{x}(\xi,\eta)) = \boldsymbol{M}(\eta)\boldsymbol{\phi}_i\xi^{-\lambda_i}. \tag{3.135}$$

As usual, these modes are finite element approximations on the curve $\boldsymbol{\gamma}$.

Constructing the enrichment functions The enrichment functions can be written as

$$\boldsymbol{N}^*_{n(i)}(\mathbf{x}) = \begin{cases} \boldsymbol{\Phi}_i(\mathbf{x}) - \sum_{k=1} N^K_k(\mathbf{x}_k)\boldsymbol{\Phi}_i(\mathbf{x}_k) & \text{if } \mathbf{x} \text{ is inside the SBFE-polygon} \\ \mathbf{0} & \text{if } \mathbf{x} \text{ is outside the SBFE-polygon} \end{cases}, \tag{3.136}$$

where N_k is the scalar shape function of the node $\mathbf{x}_k$ in global coordinates. For the original approach in [23], the nodes $\mathbf{x}_k$ on the curve $\boldsymbol{\gamma}$ are chosen to reach a conforming enrichment.

As mentioned before, this process is fully automated because it relies only on the underlying FE-mesh and does not require additional meshing routines. To further simplify the construction, an element-based calculation is presented. The boundaries of most inner triangles are straight lines. If the lines are straight, it is possible to map between the SBFEM coordinates and the local FEM coordinates directly - without a detour to the global coordinates. This is illustrated in Figure 3.22. We will denote the reference coordinates with a circumflex symbol ($\hat{}$). The coordinates of the FE-triangle are $(\hat{\alpha},\hat{\beta})^\mathsf{T}$ and the linear triangle map is

$$\mathfrak{t}(\hat{\alpha},\hat{\beta}) = \begin{pmatrix} \mathbf{x}_1 - \mathbf{x}^c & \mathbf{x}_2 - \mathbf{x}^c \end{pmatrix} \begin{pmatrix} \hat{\alpha} \\ \hat{\beta} \end{pmatrix} + \mathbf{x}^c. \tag{3.137}$$

The coordinates of the triangular sector from the scaled boundary coordinates are $(\hat{\xi},\hat{\eta})^\mathsf{T}$ and the corresponding map is

$$\mathfrak{s}(\hat{\xi},\hat{\eta}) = \hat{\xi}\left(\mathbf{x}_1\frac{(1-\hat{\eta})}{2} + \mathbf{x}_2\frac{(1+\hat{\eta})}{2} - \mathbf{x}^c\right) + \mathbf{x}^c, \tag{3.138}$$

where the local $\hat{\xi}$ and the global ξ are equal. There is a connection between both coordinate systems such that

$$\mathfrak{t}(\hat{\alpha},\hat{\beta}) = \mathfrak{s}\big(\mathfrak{d}(\hat{\alpha},\hat{\beta})\big). \tag{3.139}$$

This map is given by

$$\mathfrak{d}\colon (\hat{\alpha},\hat{\beta}) \mapsto (\hat{\xi},\hat{\eta}) = \left(\hat{\alpha}+\hat{\beta}, \frac{2\hat{\beta}}{\hat{\alpha}+\hat{\beta}} - 1\right), \tag{3.140}$$

and is referred to either as Duffy's-map or collapsed edge mapping.

With the help of Duffy's-map, the enrichment functions (Equation (3.136)) can be defined over each triangle T of the SBFE-polygon by

$$\begin{aligned} \boldsymbol{N}^*_{n(i)}\big(\mathfrak{t}(\hat{\alpha},\hat{\beta})\big)\big|_T &= \left(\hat{\xi}^{-\lambda_i}\hat{\boldsymbol{M}}^e(\hat{\eta}) - \hat{\boldsymbol{N}}^e(\hat{\alpha},\hat{\beta})\right)\boldsymbol{\phi}^e_i \\ &= \left((\hat{\alpha}+\hat{\beta})^{-\lambda_i}\hat{\boldsymbol{M}}^e\left(\frac{2\hat{\beta}}{\hat{\alpha}+\hat{\beta}} - 1\right) - \hat{\boldsymbol{N}}^e(\hat{\alpha},\hat{\beta})\right)\boldsymbol{\phi}^e_i, \end{aligned} \tag{3.141}$$

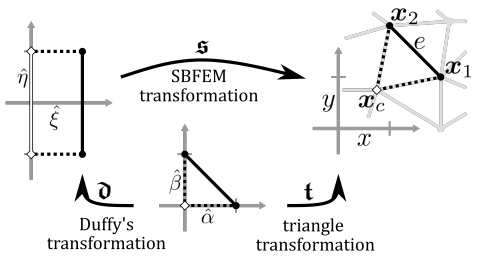

Figure 3.22: Transformation maps between different coordinate systems [23]

where the matrices $\hat{\boldsymbol{M}}^e(\hat{\eta})$, $\hat{\boldsymbol{N}}^e(\hat{\alpha},\hat{\beta})$, and the vector $\boldsymbol{\phi}_i^e$ are the part of the matrices $\boldsymbol{M}$, $\boldsymbol{N}$ and the vector $\boldsymbol{\phi}_i$ that corresponds to the edge e, respectively. The global degree $n(i)$ is for the enrichment function associated with the singular mode i.

For an arbitrary edge in Figure 3.20b, it is $\hat{\boldsymbol{M}}^e(\hat{\eta}), \hat{\boldsymbol{N}}^e(\hat{\alpha},\hat{\beta}) \in \mathbb{R}^{2\times 10}$ and $\boldsymbol{\phi}_i^e \in \mathbb{C}^{10\times 1}$. The support of the proposed enrichment function is restricted to the SBFE-polygon as shown in Figure 3.23 because the one-dimensional shape functions have the same shape as the two-dimensional shape functions everywhere on the edge e. Additionally, the FE-shape functions cannot represent the enrichment and vice versa, so both parts of the solution are linearly independent.

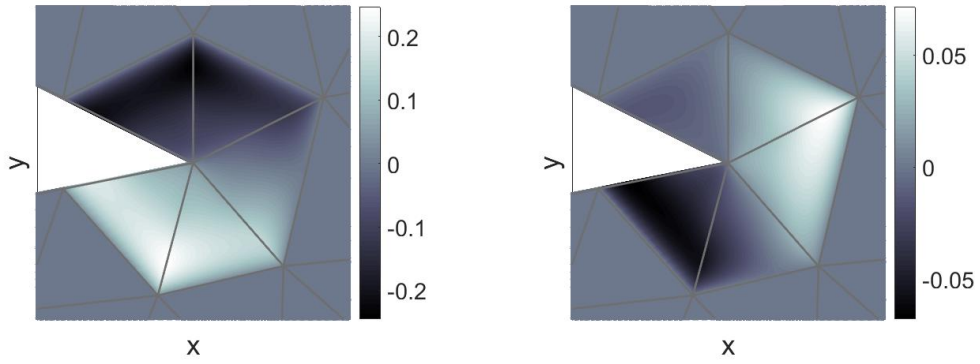

(a) Enrichment for u_x [23].

(b) Enrichment for u_y [23].

Figure 3.23: Example of an enrichment function according to Equation (3.141) for the grid in Figure 3.20b with $\lambda_i = -0.62$ [23]

.

As an overall procedure, all vertices can be first analyzed and, if a singular mode is present, can be enriched with it. The number of singular modes lies between 0 and 2 for plane elasticity problems. Each singular mode adds a new shape function to Equation (3.129) and with it a new degree of freedom to the final stiffness matrix.

Remark 3.8.1 (Eigenpair)**.** *The eigenpairs of the quadratic eigenvalue problem fulfill the following: If* $(\lambda,\boldsymbol{\phi})$ *is an eigenpair,* $(-\lambda,-\boldsymbol{\phi})$ *is also an eigenpair. If* $(\lambda,\boldsymbol{\phi})$ *is a complex eigenpair,* $(\bar{\lambda},\bar{\boldsymbol{\phi}})$ *is also an eigenpair, where* $(\bar{\cdot})$ *denotes the complex conjugate.*

Remark 3.8.2 (Later improvements)**.** *For the approach presented in [22], all nodes* $\mathbf{x}_k$ *in Equation* (3.136) *inside the SBFE-polygon are chosen as it is common in the context of the XFEM [56]. This leads to enrichment functions, which are zero at the nodes. Also, instead of adding two modes with complex eigenvalues and the relationship* $(\lambda_i,\boldsymbol{\phi}_i) = (\bar{\lambda}_j,\bar{\boldsymbol{\phi}}_j)$ *(Remark 3.8.1), two real functions are added*

$$\tilde{\boldsymbol{N}^*}_{n(i)} = \Re\left(\boldsymbol{N}^*_{n(i)}\right), \qquad \tilde{\boldsymbol{N}^*}_{n(j)} = \Im\left(\boldsymbol{N}^*_{n(i)}\right). \tag{3.142}$$

Remark 3.8.3 (Higher non-integer modes)**.** *In general, also higher non-integer orders* λ_i *can lead to a deteriorated convergence rate because there is a maximal* k*, such that the mode* $\boldsymbol{M}(\eta)\boldsymbol{\phi}_i\xi^{-\lambda_i}$

is in $\mathrm{H}^k(\Omega)$*. Only the singular modes are investigated in this thesis, but the algorithm could be extended straightforwardly.*

3.9 Numerical Treatment of the Singular Behavior

This section defines the numerical quadrature and the evaluation of stress intensity factors.

3.9.1 Graded hp-refined Gauss Quadrature

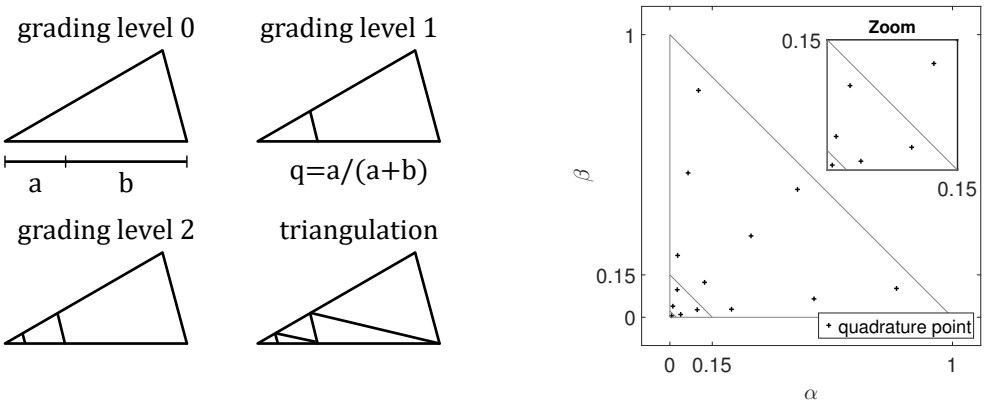

(a) Grading process

(b) hp-refined Gauss quadrature with $K = 3$ cells [23]

Figure 3.24: Grading for singular points

Standard numerical quadrature has its limitations [27, 89, 90] for singular functions. However, both singular and polynomial shape functions must be integrated to obtain the static stiffness matrix. For each triangle of the SBFE-polygon, a non-uniform, hp-refined Gauss quadrature [120] with a strong geometrically grading (grading factor of $\mathrm{q} = 0.15$) is utilized. Figure 3.24a illustrates the grading process. Exponential decay of the integration error for a singular integrand [120] outweighs a small error for the polynomials. Figure 3.24b shows the quadrature points for three integration cells. The formula is given in Appendix A.3. An exact quadrature is employed for all triangles without enrichment.

3.9.2 Computation of Stress Intensity Factors (SIFs)

Stress intensity factors indicate the strength of the singular mode [93, 132]. They are usually employed in Linear Fracture Mechanics. The SIFs are evaluated after the displacement is determined. The first step is to recover the singular field $\boldsymbol{u}^{\tilde{s}}(\mathbf{x})$ from the shifted enrichment function

$$\begin{aligned}\boldsymbol{u}^{\tilde{s}}(\mathbf{x}) = \begin{pmatrix} u_x^{\tilde{s}}(\mathbf{x}) \\ u_y^{\tilde{s}}(\mathbf{x}) \end{pmatrix} &= \sum_{i=1}^{\ell} \boldsymbol{\Phi}_i c^*_{n(i)} \\ &= \sum_{i=1}^{\ell} \left(\boldsymbol{N}^*_{n(i)}(\mathbf{x}) + \boldsymbol{N}^{\boldsymbol{\gamma}}(\mathbf{x}) \boldsymbol{\phi}_i \right) c^*_{n(i)},\end{aligned} \tag{3.143}$$

where $c^*_{n(i)}$ is the coefficient of the enrichment function corresponding to the mode i – see Equations (3.129) and (3.135), ℓ is the number of singular modes, and $\boldsymbol{\phi}_i$ is the mode shape. $\boldsymbol{N}^{\boldsymbol{\gamma}}(\mathbf{x})$ is the matrix that contains the shape functions corresponding to the standard degrees of freedom of the curve $\boldsymbol{\gamma}$ (see Figure 3.20b), and the enrichment function $\boldsymbol{N}^*_{n(i)}(\mathbf{x})$ is given in Equation (3.141).

Singular modes are usually defined in polar coordinates (see Equation (3.3)). By convention, a local crack coordinate system (r, θ) as in Figure 3.25a is used, where θ equals zero in the extension

of the crack. With a slight abuse of notation, $\boldsymbol{u}^{\tilde{s}}$ will be expressed directly in this coordinate system.

3.9.2.1 Stress-based Evaluation of the Stress Intensity Factors

Modes are eigenfunctions. Thus, their shape is determined, but not their magnitude. To identify the magnitude of the singular stress field, the field is evaluated at a characteristic length in the extension of the crack and normalized as the generalized SIFs proposed by Song *et al.* [117, 130]. The dimensionless SIFs K_I, K_{II} can be computed directly without a transformation to the local polar coordinates if the crack and the x-axis have the same orientation:

$$\begin{aligned}\begin{pmatrix} K_I \\ K_{II} \end{pmatrix} &= \frac{\sqrt{2\pi L_0}}{\tau_0\sqrt{\pi a}} \begin{pmatrix} \sigma_{yy}^{\tilde{s}}(L_0, \theta = 0) \\ \sigma_{yx}^{\tilde{s}}(L_0, \theta = 0) \end{pmatrix} \\ &= \frac{\sqrt{2\pi L_0}}{\tau_0\sqrt{\pi a}} \sum_{i=1}^{\ell} \begin{pmatrix} \sigma_{yy}^{\boldsymbol{\Phi}_i}(r_\sigma, \theta = 0) \\ \sigma_{yx}^{\boldsymbol{\Phi}_i}(r_\sigma, \theta = 0) \end{pmatrix} \left(\frac{L_0}{r_\sigma}\right)^{-\lambda_i - 1} c_{n(i)}^*\end{aligned} \tag{3.144}$$

with the stress of a mode

$$(\sigma_{xx}^{\boldsymbol{\Phi}_i} \sigma_{yy}^{\boldsymbol{\Phi}_i} \sigma_{yx}^{\boldsymbol{\Phi}_i})^\mathsf{T} = \mathbf{D}\mathcal{L}\boldsymbol{\Phi}_i, \tag{3.145}$$

the crack length a, an arbitrary radius r_σ inside the SBFE-polygon, a characteristic length L_0, a characteristic pressure τ_0 and the elasticity matrix $\mathbf{D}$. Half the distance between the scaling center $\mathbf{x}^c$ and the point between the crack and the curve $\boldsymbol{\gamma}$ (see Figure 3.25a) is chosen for r_σ. The stress is averaged if the point $\mathbf{x}(r_\sigma, 0)$ lies at an edge between two triangles. In the following paragraphs, evaluation based on Equation (3.144) is referred to as *stress-based*.

3.9.2.2 Displacement-based Evaluation of the Stress Intensity Factors

Alternatively to a stress-based evaluation, it is possible to evaluate the dimensionless SIFs based on the displacement. As in [132], the complex stress intensity factors can be evaluated as

$$\begin{aligned} K_c &= K_I + \mathrm{i}\, K_{II} \\ &= C_K \cdot \left(\Delta_y^{\tilde{s}} + \mathrm{i}\, \Delta_x^{\tilde{s}}\right) \end{aligned} \tag{3.146}$$

with

$$\Delta_y^{\tilde{s}} = u_y^{\tilde{s}}(r_u, +\pi) - u_y^{\tilde{s}}(r_u, -\pi), \tag{3.147}$$

$$\Delta_x^{\tilde{s}} = u_x^{\tilde{s}}(r_u, +\pi) - u_x^{\tilde{s}}(r_u, -\pi), \tag{3.148}$$

where r_u is the distance between the scaling center $\mathbf{x}^c$ and the endpoints of the curve $\boldsymbol{\gamma}$ – see Figure 3.25a. The coefficient C_K is case-dependent; for isotropic materials, it is given by [132]

$$C_K = \frac{G}{\kappa + 1} \sqrt{\frac{2\pi L_0}{r_u}} \frac{1}{\tau_0\sqrt{\pi a}} \tag{3.149}$$

with Poisson's ratio ν, shear modulus $G = E/\big(2(1+\nu)\big)$, Young's modulus E and Kolosov's constant κ (Equation (3.27)). Again, a denotes the crack length. In the case of a bi-material crack on an isotropic-isotropic interface (as in Figure 3.31) with plane stress condition and a dimensionless SIF, the coefficient C_K is given as [132]

$$C_K = \frac{E_1 E_2 (1 + 2\,\mathrm{i}\,\varepsilon)\cosh(\pi\varepsilon)}{4(E_1 + E_2)} \sqrt{\frac{2\pi}{r_u}} \left(\frac{L_0}{r_u}\right)^{\mathrm{i}\,\varepsilon} \left(\frac{1}{\tau_0\sqrt{\pi a}}\right) \tag{3.150}$$

with

$$\varepsilon = \frac{1}{2\pi} \ln \frac{\frac{3-\nu_1}{1+\nu_1}\frac{G_2}{G_1} + 1}{\frac{3-\nu_2}{1+\nu_2}\frac{G_2}{G_1}}, \tag{3.151}$$

where E_1, G_1, ν_1 are the material properties in the part of the geometry with positive angle θ, while E_2, G_2, ν_2 are the material properties in the part with negative θ. Below, we will refer to the evaluation based on Equation (3.146) as *displacement-based*.

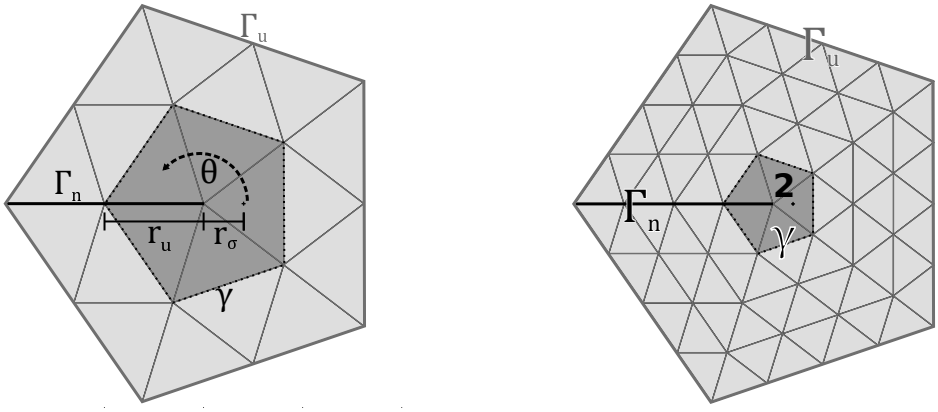

(a) h-refinement, level 1 [23]

(b) h-refinement, level 2 [23]

Figure 3.25: Domain with DIRICHLET boundary conditions [23]

3.10 Numerical Examples for the Enrichment Approach

The performance of the enrichment is studied in five different examples. For the first two examples, errors in the energy norm can be calculated because the analytical solutions are given. The first case studies a singular stress field and the second a non-singular, trigonometric stress. The following three examples are typical benchmark problems of Linear Fracture Mechanics. These examples cover different types of singularities, geometries, materials, and boundary conditions. The last example gives an impression of the automatized application. It contains multiple points with singular stress and different boundary conditions.

3.10.1 Polygonal Domain with DIRICHLET Boundary Conditions

The first example considers a straight crack in a homogeneous, isotropic, elastic medium in the form of a regular, cracked pentagon. Figure 3.25a shows the domain where the crack marked in black is located between the center and the left corner of the pentagon. The displacement and stress are given by the first two terms of WILLIAM' expansion (Equation (3.153)). While the complete WILLIAM's expansion (Equation (3.2)), typically describes a crack in an infinite medium, we can mimic this behavior by applying the two terms as a DIRICHLET boundary condition on the outer boundary of the pentagon. Additionally, due to the knowledge of the singular field, the SIFs are also known. Both sides have distinct degrees of freedom for the crack or expressed differently: the crack has double nodes. With the notation of Figure 3.25a, the problem is given by

$$\begin{aligned} \boldsymbol{\nabla} \cdot \underline{\underline{\boldsymbol{\sigma}}}(\boldsymbol{u}) &= \mathbf{0} && \text{in } \Omega, \\ \boldsymbol{u} &= (u_x^s, u_y^s)^\mathsf{T} && \text{on } \Gamma_{\boldsymbol{u}}, \\ \underline{\underline{\boldsymbol{\sigma}}}\mathbf{n} &= \mathbf{0} && \text{on } \Gamma_{\mathbf{n}}. \end{aligned} \tag{3.152}$$

We study an isotropic material under plane strain condition. YOUNG's modulus E and the POISSON's ratio ν are 8/3 GPa and 1/3, respectively. The first two terms of WILLIAM's expansion are

$$\begin{aligned} u_x^s(r,\theta) &= K_I \frac{\tau_0}{2G}\sqrt{\frac{r}{2L_0}}\cos\left(\frac{\theta}{2}\right)\left[\kappa - 1 + 2\sin^2\left(\frac{\theta}{2}\right)\right] \\ &\quad + K_{II}\frac{\tau_0}{2G}\sqrt{\frac{r}{2L_0}}\sin\left(\frac{\theta}{2}\right)\left[\kappa + 1 + 2\cos^2\left(\frac{\theta}{2}\right)\right] \\ u_y^s(r,\theta) &= K_I \frac{\tau_0}{2G}\sqrt{\frac{r}{2L_0}}\sin\left(\frac{\theta}{2}\right)\left[\kappa + 1 - 2\cos^2\left(\frac{\theta}{2}\right)\right] \\ &\quad - K_{II}\frac{\tau_0}{2G}\sqrt{\frac{r}{2L_0}}\cos\left(\frac{\theta}{2}\right)\left[\kappa - 1 - 2\sin^2\left(\frac{\theta}{2}\right)\right] \end{aligned} \tag{3.153}$$

Both stress intensity factors K_I and K_{II} are free variables. For our test, we choose one and two, respectively. Since this is not a physical problem, the choice of the characteristic length $L_0 = \pi\,\mathrm{mm}$ and the pressure $\tau_0 = 1\,\mathrm{MPa}$ is only made to get simple values for the SIFs.

To investigate the convergence behavior, a uniform h-refinement is performed. For triangles, each element is split into four smaller triangles (compare level 1 and level 2 in Figure 3.25). The element size is computed as the square root of the element area, and $h_{\min}$ is the minimum over all elements. The element size is halved in every refinement level. After the h-refinement step, the SBFE-polygon is enriched with two modes indicated by the black number in Figure 3.25b. Figure 3.26 shows the error in the energy-(semi)-norm, which is given by

$$\|\mathbf{v}\|_{\mathcal{E}} = \sqrt{\frac{1}{2}\int_{\Omega} (\mathcal{L}\mathbf{v})^{\mathsf{T}}\mathbf{D}\mathcal{L}\mathbf{v}\,\mathrm{d}\Omega}. \tag{3.154}$$

The results of the standard FEM and the enriched version (current) are plotted next to each other allowing a direct comparison. Here, the reference solution $\mathbf{u}^{\mathrm{ref}}$ is the singular field $\mathbf{u}^s$. A more precise quadrature is utilized at the crack tip for the error calculation. The triangles inside the SBFE-polygon are split into 9 integration cells, resulting in 285 quadrature points. The theoretical convergence behavior is of type $\mathcal{C}h_{\min}^{\lambda}$, where the *rate* $\lambda = 0.5$ is the order of the singularity. The convergence rate stays unchanged by the enrichment, but the coefficient $\mathcal{C}$ is significantly improved (Figure 3.26). This is particularly visible if p-refinement is considered, where the coefficient $\mathcal{C}$ is crucial. In the literature, some methods reach higher-order convergence under h-refinement

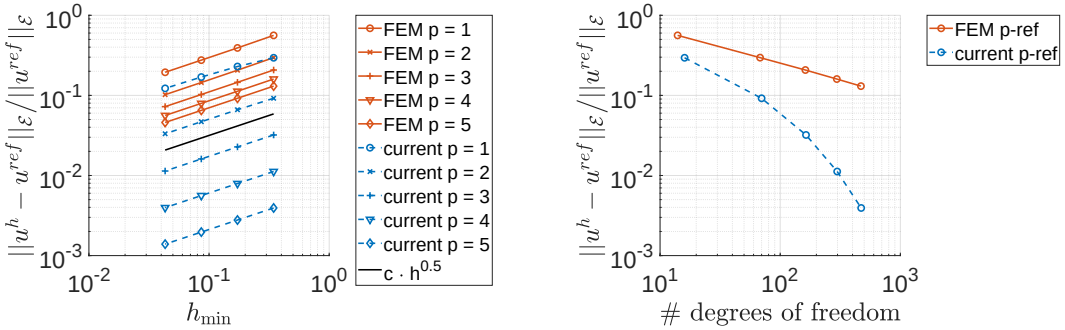

(a) h-refinement [23]

(b) p-refinement [23]

Figure 3.26: Comparison of energy-errors between the standard FEM and the current approach for the problem defined by Equations (3.152) [23]

with an enrichment approach. There are two possibilities: a non-conforming transition between the elements or a geometrical enrichment, where the enriched area is held constant under h-refinement [3, 78, 116]. Other methods are non-uniform refinements such as graded refinement or hp-refinement [27, 148].

Besides the convergence, the evaluation of the SIFs is investigated. For this purpose, the previously introduced nomenclature is used: stress-based method 3.9.2.1 and displacement-based method 3.9.2.2. Additionally, the SBFE-polygon is replaced with a classic SBFEM super-element, which is based on modal decomposition and not based on SB shape functions (see [135]). This method is abbreviated with 'SBFEM'. The SIFs with the SBFEM super-element are evaluated with the displacement-based approach. Figure 3.27 shows the relative error of the complex SIFs under p-refinement for $\mathrm{p} = 1, \ldots, 8$. For the p-refinement, the coarse grid in Figure 3.25a is utilized. In general, the displacement is approximated with a higher order than the stress, leading to a smaller error. Similarly, the displacement-based method leads to smaller errors.

For h-refinement, the observations are quite different. While the displacement converges, the SIFs do not converge. Here, we assume the reason is the constant resolution of the singular modes. The number of degrees of freedom to approximate the singular mode is the same for each h-refinement step. Therefore, the approximation error for these modes remains the same. Due to the DIRICHLET boundary conditions, only the singular modes contribute to the solution. The

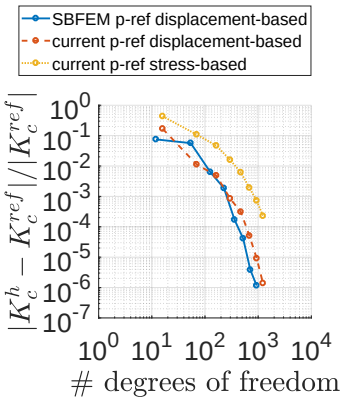

Figure 3.27: Relative error in K_c obtained using method 3.9.2.1, method 3.9.2.2, and replacing the polygon around the crack tip with an SBFEM-polygonal element for $p = 1, \dots, 8$ [23]

calculation of SIFs does not benefit from a more precise solution of the area outside the SBFE-polygon. However, later examples show that a good approximation of the SIFs can be gained for practical applications, even with lower-order shape functions. The observations show similarities with the literature. For example, the SIFs computed with a flat top enrichment converge only with the geometric approach, where the area stays the same with the h-refinement [56]. In [102], also the influence of the enrichment area on the calculation of SIFs is studied.

As a second test, we use the same geometry and material properties, but the body force and traction are chosen, such that a non-singular trigonometric solution is taken. The modified problem is

$$\begin{aligned} \boldsymbol{\nabla} \cdot \underline{\underline{\boldsymbol{\sigma}}}(\boldsymbol{u}) &= \mathbf{f} && \text{at } \Omega, \\ \boldsymbol{u} &= (u_x^{\text{ref}}, u_y^{\text{ref}})^{\mathsf{T}} && \text{at } \Gamma_{\boldsymbol{u}}, \\ \underline{\underline{\boldsymbol{\sigma}}}\mathbf{n} &= \boldsymbol{\tau} && \text{at } \Gamma_{\mathbf{n}}, \end{aligned} \tag{3.155}$$

where the body force $\mathbf{f} = \boldsymbol{\nabla} \cdot \underline{\underline{\boldsymbol{\sigma}}}(\boldsymbol{u}^{\text{ref}})$ and the traction $\boldsymbol{\tau} = \underline{\underline{\boldsymbol{\sigma}}}(\boldsymbol{u}^{\text{ref}})\mathbf{n}$ are applied to get the following solution

$$\boldsymbol{u}^{\text{ref}}(x, y) = \begin{pmatrix} \sin(k_x^x x) \cdot \sin(k_x^y y) \\ \sin(k_y^x x) \cdot \sin(k_y^y y) \end{pmatrix} \mu\text{m} \tag{3.156}$$

with $k_x^x = 4\pi\,\text{mm}^{-1}$, $k_x^y = 2\pi\,\text{mm}^{-1}$, $k_y^x = 2\pi\,\text{mm}^{-1}$, and $k_y^y = 6\pi\,\text{mm}^{-1}$.

This example already hints towards wave propagation. As we expect, the error for a non-singular case is the same comparing the FEM with the enriched version, as illustrated in Figure 3.28. The usual convergence rates are reached, indicating higher-order completeness. This is expected as the finite element space is still a subspace of the enriched space. However, we observe a deteriorated convergence rate if the quadrature is not accurate enough. Hence, Figure 3.28 shows that the proposed quadrature is sufficient.

1. In the singular case, the enrichment yields a significant improvement of the error in comparison to a conventional finite element basis;
2. For the SIFs to converge, a sufficient number of nodes around the singularity has to be introduced;
3. For non-singular problems, the enriched approach and the conventional high-order finite element basis lead to the same results.

3.10.2 Crack under Shear

A typical example from fracture mechanics follows. A uniform shear with $\boldsymbol{\tau}_0 = (1, 0)^{\mathsf{T}}$MPa is applied to the upper boundary of a rectangular domain with a horizontal crack and a vanishing

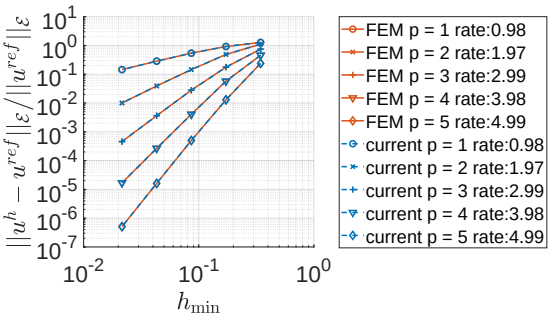

Figure 3.28: Comparison of energy-errors between the standard FEM and the current work for the problem defined by Equations (3.155) – the lines coincide [23]

polyn. degree p / reference	2	4	6	[82, 93]
coarse grid				
stress-based 3.9.2.1	$34.54 + 4.37\,\mathrm{i}$	$33.96 + 4.51\,\mathrm{i}$	$33.99 + 4.53\,\mathrm{i}$	$34 + 4.55\,\mathrm{i}$
displacement-based 3.9.2.2	$33.42 + 4.36\,\mathrm{i}$	$33.94 + 4.51\,\mathrm{i}$	$33.99 + 4.53\,\mathrm{i}$	$34 + 4.55\,\mathrm{i}$
degrees of freedom	476	1796	3964	-
fine grid				
stress-based 3.9.2.1	$34.97 + 4.50\,\mathrm{i}$	$34.04 + 4.53\,\mathrm{i}$	$34.07 + 4.54\,\mathrm{i}$	$34 + 4.55\,\mathrm{i}$
displacement-based 3.9.2.2	$33.83 + 4.49\,\mathrm{i}$	$34.02 + 4.53\,\mathrm{i}$	$34.07 + 4.54\,\mathrm{i}$	$34 + 4.55\,\mathrm{i}$
degrees of freedom	6980	27524	61636	-

Table 3.1: Results of the complex stress intensity factor K_c for the cracked domain under shear load [23]

body load. As depicted in Figure 3.29a, the bottom side is fixed. The characteristic values are $\tau_0 = \|\boldsymbol{\tau}_0\|$ and $L_0 = \pi a$. The material is isotropic with YOUNG's modulus $E = 100\,\mathrm{GPa}$, and POISSON's ratio $\nu = 0.3$. It is in a state of plane strain.

The black numbers in Figure 3.29b show that the algorithm finds three points with singular modes: the two bottom corners $(-3.5\,\mathrm{mm}, -8\,\mathrm{mm})$, $(3.5\,\mathrm{mm}, -8\,\mathrm{mm})$ as well as the crack tip at $(0\,\mathrm{mm}, 0\,\mathrm{mm})$. The singular modes appear for the two bottom corners because of the DIRICHLET boundary condition. For the DIRICHLET boundary condition, it is critical to utilize the reduced number of shape functions leading to smaller matrices $\mathbf{E}_0$, $\mathbf{E}_1$, and $\mathbf{E}_2$ in Equation (3.37). Only the fixed boundary condition results in singular modes, while the traction edge at the top does not result in singular modes. In total, four enrichment functions are added. According to the literature, e.g., [82, 93], reference values for the SIFs at the crack tip are $K_I^{\mathrm{ref}} = 34$ and $K_{II}^{\mathrm{ref}} = 4.55$. Table 3.1 summarizes the complex SIFs for varying polynomial degrees and two h-refinement levels. The values approach the reference solutions as the degree increases.

The square root of the energy $\|\boldsymbol{u}\|_\mathcal{E}$ is studied as a second measurement of the approximation quality. The convenient matrix expression is

$$\|\mathbf{u}\|_\mathcal{E} = \sqrt{0.5\,\mathbf{uKu}}, \tag{3.157}$$

where $\mathbf{K}$ is the stiffness matrix. A reference energy is computed with a highly refined approximation using the proposed approach with a polynomial degree of 7 and 1 332 356 degrees of freedom. Figure 3.30 shows the relative deviation from a reference $\|\mathbf{u}^{\mathrm{ref}}\|_\mathcal{E}$ for the FEM and the current approach. The rates of convergence for the higher-order approximations of the current approach may be slightly affected by the fact that the same approach is used to compute the reference solution.

3.10.3 Bi-material Crack under Tension

After the shear case, we study tension. While Figure 3.31a shows the idealized fracture problem, the numerical problem is solved with a bottom edge with $u_y = 0$. The lower/left corner is fixed in

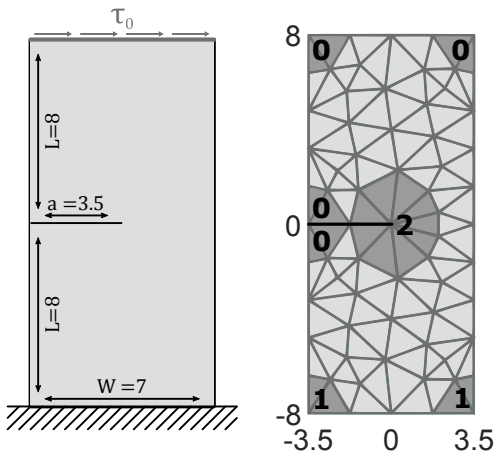

(a) Boundary conditions [23] (b) Coarse grid [23]

Figure 3.29: Crack under shear load (dimensions in mm) [23]

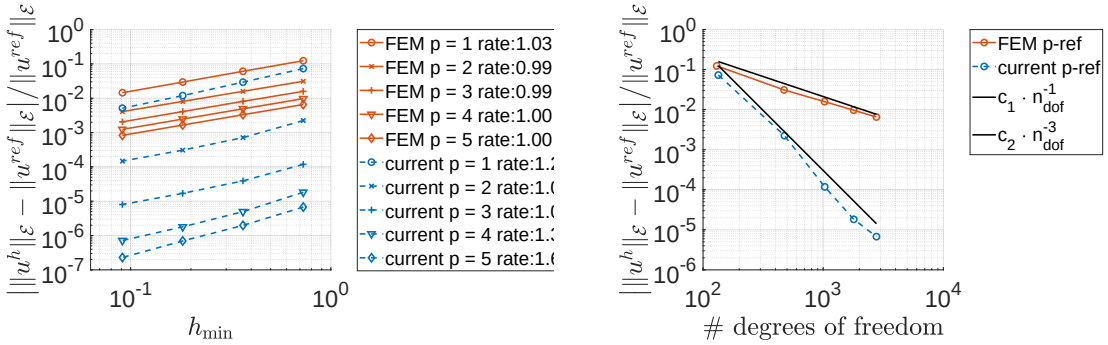

(a) h-refinement [23] (b) p-refinement [23]

Figure 3.30: Relative deviation from the reference $\|\mathbf{u}^{\text{ref}}\|_{\mathcal{E}} = 4.967356034022807$ for the crack under shear [23]

both directions. The pressure $\boldsymbol{\tau}_0 = (0,1)^{\mathsf{T}}$MPa on the top edge leads to the characteristic pressure $\tau_0 = \|\boldsymbol{\tau}_0\|$, while the characteristic length L_0 is $2a$, where the crack length a is varied. We consider a vanishing body load. The material in the lower half (material 2) is chosen to have a Young's modulus $E = 1\,\text{GPa}$. Young's modulus in the upper half of the geometry (material 1) has been varied between 1 GPa and 10 GPa, according to Table 3.2. For both materials, Poisson's ratio is $\nu = 0.3$, and plane stress is assumed. Besides the change in the material parameters, different crack lengths a of 0.4 mm, 0.5 mm, and 0.6 mm are studied. Figure 3.31b shows the mesh for a crack length of 0.4 mm. As before, SBFE-polygons are indicated by darker areas, and the black numbers indicate the number of singular modes. The point $(1-a, 0)$ is special because the number of singular modes is material-dependent. A singularity only appears if both materials are different from each other. Table 3.2 contains the results for the SIFs at the crack tip in the origin with the displacement-based method 3.9.2.2. The values for degree 4 and 6 are in good agreement with the literature values, while the coarse grid is insufficient for p = 2.

3.10.4 Crack under Tension at an Anisotropic-Isotropic Interface

The fourth example demonstrates that anisotropic materials can be treated with the proposed method. A crack at an anisotropic-isotropic interface is considered. The orthotropic material in the upper part of the geometry (material 1) has the material parameters $E_{11} = 100\,\text{GPa}$, $E_{22} = 30\,\text{GPa}$,

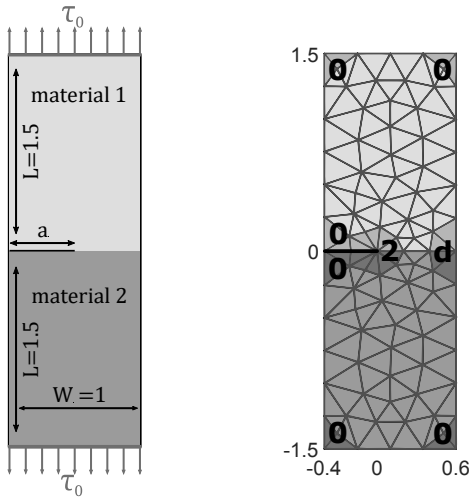

(a) Boundary conditions [23]

(b) Coarse grid, $a = 0.4\,\text{mm}$ [23]

Figure 3.31: Bi-material crack under tension (dimensions in mm) [23]

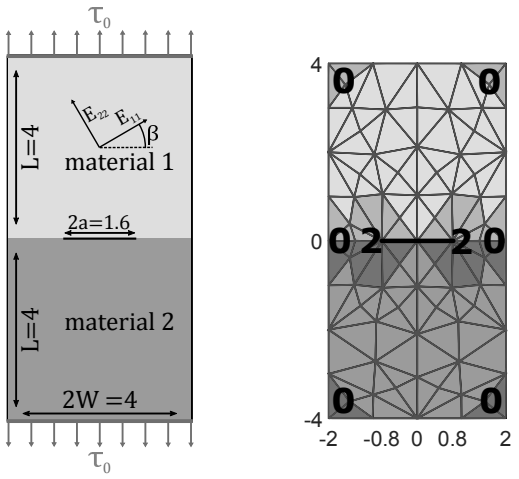

(a) Boundary conditions [23]

(b) Grid [23]

Figure 3.32: Isotropic-anisotropic crack under tension (dimensions in mm)

$G_{12} = 23.5212\,\text{GPa}$ and $\nu_{12} = 0.3$, while the isotropic material in the lower part (material 2) has the material parameters $E = 100\,\text{GPa}$ and $\nu = 0.3$. Plane stress is assumed. Additionally, material 1 is modeled using four different rotation angles of the stiffness matrix. The first case corresponds to the elastic coefficient E_{11} being aligned parallel to the crack, and the three other cases are modeled using 30° steps in the counter-clockwise direction as depicted in Figure 3.32a. The figure shows the geometrical dimensions and boundary conditions. The uniform pressure is applied with the characteristic value of $\tau_0 = 1\,\text{MPa}$, while the characteristic length L_0 for the calculation of stress intensity factors is chosen as $2a$. Only the right crack tip is studied. The grid is shown in Figure 3.32b, where two singular points are surrounded by two SBFE-polygons marked with the darkest shade of gray. For all angles, there are two singular modes per crack tip. As before, this is indicated by the black numbers in Figure 3.32b. The results for both SIFs presented in Figure 3.33 demonstrate that the SIFs tend to the reference values computed using pure SBFEM [130] of degree 10. The angle β has a negligible impact on the error of K_I, while the error of K_{II} is influenced to

polyn. degree / reference	$E_1 = 1\,\mathrm{GPa}$	$E_1 = 2\,\mathrm{GPa}$	$E_1 = 4\,\mathrm{GPa}$	$E_1 = 10\,\mathrm{GPa}$
$a = 0.4\,\mathrm{mm}$				
p = 2	2.110	$2.107 - 0.195\,\mathrm{i}$	$2.100 - 0.354\,\mathrm{i}$	$2.090 - 0.488\,\mathrm{i}$
p = 4	2.110	$2.107 - 0.197\,\mathrm{i}$	$2.099 - 0.357\,\mathrm{i}$	$2.089 - 0.492\,\mathrm{i}$
p = 6	2.111	$2.107 - 0.197\,\mathrm{i}$	$2.100 - 0.358\,\mathrm{i}$	$2.089 - 0.494\,\mathrm{i}$
[132]	2.111	$2.108 - 0.198\,\mathrm{i}$	$2.100 - 0.359\,\mathrm{i}$	$2.089 - 0.495\,\mathrm{i}$
[87]	2.113	$2.109 - 0.197\,\mathrm{i}$	$2.100 - 0.358\,\mathrm{i}$	$2.089 - 0.493\,\mathrm{i}$
$a = 0.5\,\mathrm{mm}$				
p = 2	$2.808 - 0.011\,\mathrm{i}$	$2.803 - 0.270\,\mathrm{i}$	$2.789 - 0.478\,\mathrm{i}$	$2.771 - 0.649\,\mathrm{i}$
p = 4	2.824	$2.818 - 0.264\,\mathrm{i}$	$2.805 - 0.478\,\mathrm{i}$	$2.788 - 0.655\,\mathrm{i}$
p = 6	2.824	$2.818 - 0.266\,\mathrm{i}$	$2.805 - 0.481\,\mathrm{i}$	$2.788 - 0.660\,\mathrm{i}$
[132]	2.824	$2.818 - 0.267\,\mathrm{i}$	$2.805-$	$2.787 - 0.664\,\mathrm{i}$
[87]	2.836	$2.819 - 0.267\,\mathrm{i}$	$2.806 - 0.483\,\mathrm{i}$	$2.787 - 0.661\,\mathrm{i}$
$a = 0.6\,\mathrm{mm}$				
p = 2	4.002	$3.995 - 0.366\,\mathrm{i}$	$3.981 - 0.661\,\mathrm{i}$	$3.961 - 0.905\,\mathrm{i}$
p = 4	4.029	$4.020 - 0.388\,\mathrm{i}$	$4.000 - 0.700\,\mathrm{i}$	$3.973 - 0.958\,\mathrm{i}$
p = 6	4.031	$4.022 - 0.392\,\mathrm{i}$	$4.001 - 0.708\,\mathrm{i}$	$3.973 - 0.969\,\mathrm{i}$
[132]	4.032	$4.022 - 0.397\,\mathrm{i}$	$3.998 - 0.716\,\mathrm{i}$	$3.967 - 0.979\,\mathrm{i}$
[87]	4.037	$4.027 - 0.396\,\mathrm{i}$	$4.001 - 0.714\,\mathrm{i}$	$3.971 - 0.974\,\mathrm{i}$

Table 3.2: K_c results for the bi-material crack under tension with the displacement-based method 3.9.2.2

coordinates in mm	$(0.0, 0.0)$	$(1.0, 2.0)$	$(2.0, 2.5)$	$(3.0, 2.0)$	$(4.0, 0.0)$	$(0.0, 3.0)$
eigenvalues	-0.839	-0.684	-0.893	$-0.577 - 0.051\,\mathrm{i}$	-0.839	-0.919
		-0.985	-0.927	$-0.577 + 0.051\,\mathrm{i}$		

Table 3.3: Eigenvalues for the singular points (cf. Figure 3.34b)

a greater extent by the material angle.

3.10.5 Multiple Singularities

Finally, the last example shows the automatization capability of the proposed method. The method can handle a domain with multiple critical points by automatically analyzing them. Such a domain is presented in Figure 3.34a. Various singular modes appear through different boundary conditions, material interfaces, and a re-entrant wedge. Table 3.3 lists the corresponding eigenvalues of the critical points, which are analyzed by the proposed method. Apparent differences are visible with single, double, and complex eigenvalues. The diversity of the enrichment functions is shown by the black numbers in Figure 3.34b, where also the SBFE-polygons are colored. Additionally to the uniform shear of $\boldsymbol{\tau}_0 = (1, 0)^\mathsf{T}\mathrm{MPa}$, a quadratic body load $\mathbf{f}(x, y) = (y^2, 0)^\mathsf{T}$ is applied. The upper orthotropic material has the material parameters $E_{11} = 10\,\mathrm{GPa}$, $E_{22} = 3\,\mathrm{GPa}$, $G_{12} = 1\,\mathrm{GPa}$, $\nu_{12} = 0.25$, while the lower isotropic material has the material parameters $E = 1\,\mathrm{GPa}$, $\nu = 0.3$. Plane stress is assumed. Some of the points clearly show up as bright spots in the visualization of shear stress presented in Figure 3.34c. A comparison between the energy $\|\mathbf{u}^h\|_\mathcal{E}$ and the reference energy $\|\mathbf{u}^\mathrm{ref}\|_\mathcal{E}$ of the current approach on a highly refined grid with 1 657 832 degrees of freedom and a polynomial degree of 7 shows the significance of the singular modes as Figure 3.35 indicates.

3.11 Conclusion for the Enrichment Approach

We proposed an automatic pre-processing for treating critical points in a triangular finite element mesh. The algorithm automatically decides if an enrichment function, which captures the possible singular stress, is required. The decision is based on the SBFEM, and the final enriched basis combines the advantages of the FEM and the SBFEM. This leads to a minimal increase in the number

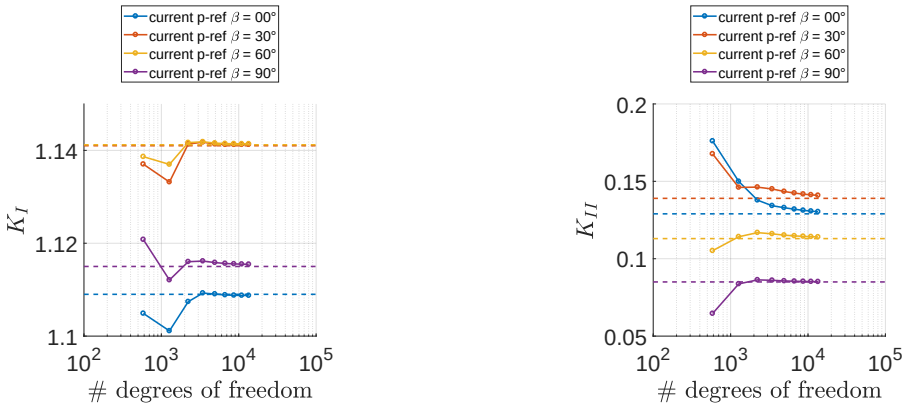

(a) K_I [23] (b) K_{II} [23]

Figure 3.33: SIFs computed with the stress-based method 3.9.2.1 for the anisotropic-isotropic crack under tension for p-refinement with $p = 2, \ldots, 10$. The dashed lines correspond to reference values from [130]

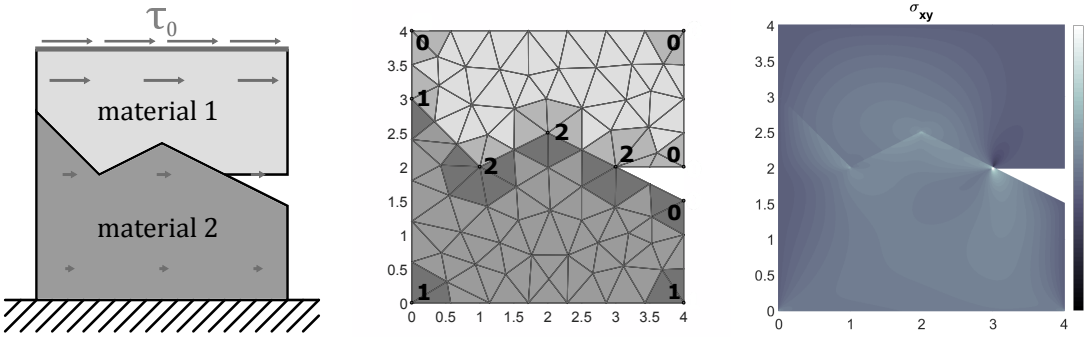

(a) Boundary conditions [23] (b) Grid and singular modes [23] (c) Shear stress [23]

Figure 3.34: Example involving multiple stress concentrations (dimensions in mm) [23]

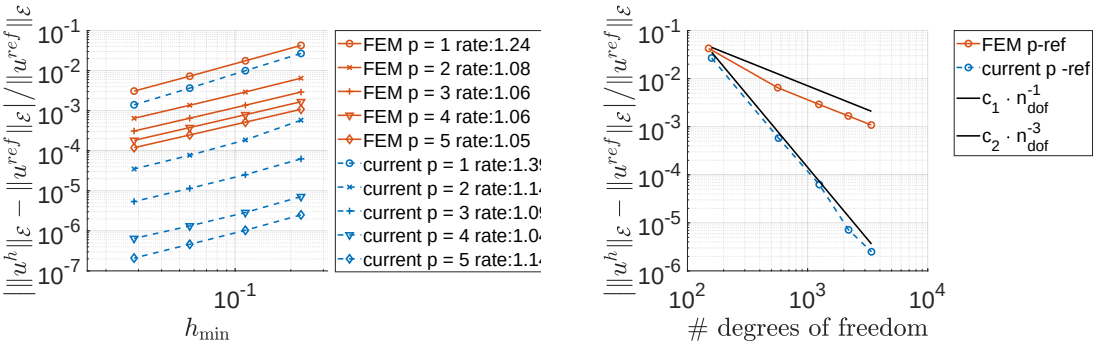

(a) h-refinement [23] (b) p-refinement [23]

Figure 3.35: Relative deviation from the reference $\|\mathbf{u}^{\text{ref}}\|_{\mathcal{E}} = 89.264095354384537$ for the example with multiple singularities [23]

of degrees of freedom but significantly reduces the approximation error compared to the standard finite element basis. Especially under p-refinement, we observe a rapid convergence. The method utilizes only information of the underlying FE mesh and has a straightforward implementation as

a pre-processing routine. The approach yields optimal convergence rates for non-singular problems with the proposed quadrature because of the finite element basis. Additionally, two direct evaluation methods for the evaluation of SIFs are investigated. Overall, the displacement-based approach performed better but needs some knowledge of the analytical solution. On the other hand, the stress-based version is fully automatable, even for complicated material setups.

Chapter 4

Linear Dynamic Problems

The methods proposed in the previous sections are extended in this section for simulating ultrasonic wave propagation and its interaction with cracks. Moreover, continuity conditions are introduced as a preliminary step for modeling contact. It is shown that the mortar method with the LAGRANGE Multiplier Method reaches higher-order convergences and is appropriate for an extension to dynamically changing continuity conditions, e.g., contact conditions. Further, tests are performed to clarify details around crack tips. In the following, the general overview of the simulation of ultrasonic waves is given.

Dynamic problems, such as the simulation of ultrasonic waves, can be solved in the time or frequency domain. However, the non-linearity of the contact problem depends on the current displacement for each point in time. Therefore, this non-linear dependency makes a separation into frequencies impossible because the superposition principle is violated. Thus, this section focuses only on the time domain simulation, and the available methods are reviewed.

In general, a large variety of methods can simulate ultrasonic guided waves with the most prominent being Finite Differences, Finite Elements, and Finite Volumes. Here, the discussion is limited to the methods which use polygonal elements in the time domain because a review of all available methods is out of the scope of the work presented in this section.

One important point to consider while modeling ultrasonic guided waves is that these waves have short wavelengths compared to the thickness of the domain and typically very long waveguides are of interest. The following rule of thumb holds: ten to twenty linear elements per wavelength are required to get physically meaningful results, e.g., [155]. However, such a fine resolution would lead to a significant number of degrees of freedom. This effect will even be more critical for a breathing crack because these cracks introduce higher harmonics which lie at the multiples of the frequency of the original wave. Therefore, even smaller elements are necessary to resolve them requiring more elements for the simulation [*1].

A better option to h-refinement is to use higher-order shape functions which are significantly more effective for the simulation of waves with small wavelengths [62]. This section extends the approaches presented in the static analysis (Section 3) such that higher-order convergence is reached for dynamic problems. For the scaled boundary shape functions, this means that a second type of bubble functions associated with the body loads, which were first introduced in [98], must be added. Here, it is important to note that this approach does not solve the dynamic wave Equation (2.8) directly. Instead, the idea of reaching a higher order completeness by representing polynomial body loads [72, 98, 182] is tested in this section. Moreover, it is shown that the extension with these additional bubble functions yields a higher-order convergence of the SB shape functions' method on polygonal meshes.

In recent years, interest in polygonal meshes has risen as they have the same flexibility as triangular elements for meshing of the domain while offering additional benefits. One benefit is a more effective approximation with the same number of degrees of freedom; another benefit is a higher resistance to distortions inside the element [86, 181]. Methods for polygonal elements include finite element formulations based on the generalized barycentric coordinates [55, 143, 144], the Voronoi Cell Finite Element Method [60] and the Virtual Element Method (VEM) [11, 37, 86].

[*1] The exceptions are the areas with a negative group velocity.

The generalized barycentric coordinates are an extension of standard Finite Elements to polygons. Nowadays, the VEM is also framed in a similar setup as the Finite Element Method, with the distinguishing feature that the shape function is not directly computed. The shape functions are only 'virtual', and all quantities are expressed in terms of the boundary-dependent calculations. For the Voronoi Cell Finite Element Method, the shape functions are explicit stress functions to calculate the polygons' stiffness matrix.

Alternatively to the SB shape functions extended with bubble functions, there are approaches within the SBFEM, which solve the elastic wave equation in a direct way [9, 171]. The most prominent approach is a continued-fraction method which reaches higher-order convergences and is well suited for dynamic problems with singular points [9, 29, 62, 63]. The drawback of this method is that an extension to include contact forces at the crack seems out of reach due to the sophisticated continued-fraction algorithm. However, the lack of contact forces can be simply neglected to get a rough approximation [121].

Another way to handle small wavelengths and singular points is to increase the efficiency of existing approaches, e.g., using mesh adaptivity [183, 184] and parallelization [180] approaches. Mesh adaptivity tries to reduce the necessary resources by only discretizing those parts of the domain densely, where it is required. An adaptive approach is iterative, and due to the iterations, not necessarily faster. As for the parallelization, it distributes the computation on multiple computers to treat complicated problems through massive resources. To allow for parallelization, one possibility is to introduce continuity conditions. Besides parallelization, the continuity conditions were investigated in different situations for the SBFEM. Yang *et al.* used a non-conforming penalty coupling for a scaled boundary super-element [172]. This super-element is used in a crack growth algorithm. Schauer *et al.* coupled a near-field FEM-approximation with an SBFEM far-field approximation on non-matching meshes [119]. Bulling *et al.* showed a tying of different domains with the continued-fraction approach of the SBFEM [20].

In this section, the SB shape functions are tested on meshes with multiple polygonal super-elements. Therefore, polygonal meshes and the uniform refinement of such are presented. Further, the section investigates the performance of the SB shape functions in problems with singularities and compares it with the enrichment approach from the previous section. Here, a graded refinement strategy for the FEM serves as a reference method for an independent comparison. Additionally, continuity conditions are studied. These conditions represent a simpler form of contact conditions which are necessary for the non-linear relations presented in Section 5.

4.1 SB Shape Functions with Body Loads

In this section, the scaled boundary shape functions associated with the body load terms are derived. The body load shape functions are originally proposed in [98]. The computation, however, is strongly influenced by [181] and [72].

We will start with the derivation for a single closed super-element (without traction). Like in Equation (3.102), the displacement $\boldsymbol{u}$ is separated into two parts

$$\boldsymbol{u} = \boldsymbol{u}_{\boldsymbol{f}=\boldsymbol{0}} + \boldsymbol{u}_{\boldsymbol{\tau}=\boldsymbol{0},\boldsymbol{f}\in\mathcal{P}}, \tag{4.1}$$

where $\boldsymbol{u}_{\boldsymbol{f}=\boldsymbol{0}}$ is the part without body loads and $\boldsymbol{u}_{\boldsymbol{\tau}=\boldsymbol{0},\boldsymbol{f}\in\mathcal{P}}$ is the part with polynomial body loads. The part $\boldsymbol{u}_{\boldsymbol{f}=\boldsymbol{0}}$ is defined in Section 3.3.1.1, while the current section focuses on the computations of $\boldsymbol{u}_{\boldsymbol{\tau}=\boldsymbol{0},\boldsymbol{f}\in\mathcal{P}}$ and its coupling with the term $\boldsymbol{u}_{\boldsymbol{f}=\boldsymbol{0}}$.

The body load bubble shape functions are only defined for nodal shape functions of degree $p > 1$. For linear shape functions, a body load term is not necessary. Let the body loads $\boldsymbol{f}$ be expressed as a Taylor-series up to degree $\mathrm{p}-2$ for each direction, i.e.,

$$\boldsymbol{f}(\mathbf{x}) = \sum_{i=1}^{\mathrm{d}} \sum_{j=0}^{\mathrm{p}-2} \sum_{k=0}^{j} c_{ijk}\, \mathbf{e}_i \hat{x}^{j-k} \hat{y}^{k}, \tag{4.2}$$

where $\hat{x} = (x - x_c)/L, \hat{y} = (y - y_c)/L$ are super-element coordinates, L is the greatest distance between the scaling center and the nodes, $\mathbf{e}_i$ is the i-th unit vector, and $d = 2$ is the number

of displacement dimensions. These local coordinates are introduced for better stability and are similar to the local coordinates utilized by the VEM [11, 86]. For a single term, it is

$$\begin{aligned}\mathbf{e}_i\hat{x}^{j-k}\hat{y}^k &= \mathbf{e}_i\big((x-x_c)/L\big)^{j-k}\big((y-y_c)/L\big)^k && (4.3)\\ &= \mathbf{e}_i\xi^j\big((\gamma_x(\eta)-x_c)/L\big)^{j-k}\big((\gamma_y(\eta)-y_c)/L\big)^k && (4.4)\\ &= \xi^j\tilde{\boldsymbol{w}}_{ijk}(\eta), && (4.5)\end{aligned}$$

where $\tilde{\boldsymbol{w}}_{ijk}(\eta) = \mathbf{e}_i\big((\gamma_x(\eta)-x_c)/L\big)^{j-k}\big((\gamma_y(\eta)-y_c)/L\big)^k$ is the η-dependent part of the TAYLOR-term. Use the PASCAL-triangle for monomials to define a linear index ℓ

$$\begin{aligned}&&\mathbf{e}_1x^0y^0 = \xi^{\theta_1-2}\boldsymbol{w}_1(\eta) \quad \mathbf{e}_2x^0y^0 = \xi^{\theta_2-2}\boldsymbol{w}_2(\eta) && (4.6)\\ \mathbf{e}_1x^1y^0 = \xi^{\theta_3-2}\boldsymbol{w}_3(\eta) \quad \mathbf{e}_2x^1y^0 = \xi^{\theta_4-2}\boldsymbol{w}_4(\eta) &\quad \mathbf{e}_1x^0y^1 = \xi^{\theta_5-2}\boldsymbol{w}_5(\eta) &\quad \mathbf{e}_2x^0y^1 = \xi^{\theta_6-2}\boldsymbol{w}_6(\eta)\\ \vdots \qquad\qquad \vdots &\quad \vdots \qquad\qquad \vdots &\quad \vdots,\end{aligned}$$

where the -2 term is added for a simpler final result and it is $\theta_\ell = 2, 2, 3, 3, 3, 3, 4, 4, 4, 4, 4, 4, 5 \ldots, p$. Then, the nodal body load $\boldsymbol{f}_b$ in Equation (3.38) can be written as

$$\begin{aligned}\boldsymbol{f}_b &= \sum_{\ell=1}^{n} c_\ell\xi^{\theta_\ell-2}\mathbf{w}_\ell && (4.7)\\ &= \mathbf{W}\xi^{(\boldsymbol{\Theta}_b-2\mathbf{I})}\mathbf{c}, && (4.8)\end{aligned}$$

where $\boldsymbol{\Theta}_b = \operatorname{diag}(\theta_1, \ldots, \theta_n)$ is a diagonal matrix, $\mathbf{W}$ is a matrix with the columns $\mathbf{w}_\ell$, and the columns $\mathbf{w}_\ell$ are assembled over the elements

$$\mathbf{w}_\ell^e = \int_{-1}^{+1} \hat{\boldsymbol{M}}(\hat{\eta})^\mathsf{T}\boldsymbol{w}_\ell(\hat{\eta})\,|j(\hat{\eta})|\,\mathrm{d}\hat{\eta}, \tag{4.9}$$

where $\boldsymbol{w}_\ell(\hat{\eta})$ is the element-wise version of $\tilde{\boldsymbol{w}}_{ijk}(\eta)$ with a linear index $\ell(i,j,k)$. The one-dimensional matrix of shape functions $\hat{\boldsymbol{M}}$ and the JACOBIAN determinate $j(\hat{\eta})$ depend on the element-wise circumferential coordinate $\hat{\eta}$ (Figure 3.5). The assembling process is analog to the assembling of the matrices $\mathbf{E}_i$ in Equation (3.39).

Analogously to the traction case (Section 3.5.3), the particular solution for each ℓ is calculated by the ansatz $\boldsymbol{\phi}_\ell\xi^{\theta_\ell}$. Substituting $\boldsymbol{f}_b = \mathbf{w}_\ell\xi^{\theta_\ell-2}$ and Equation (3.38) in Equation (3.37), the ansatz for $\mathbf{u}$ leads to the following linear system for each TAYLOR-term ℓ [181]

$$\begin{aligned}\mathbf{E}_\theta(\theta_\ell) &= \theta_\ell^2\mathbf{E}_0 + \theta_\ell(\mathbf{E}_1 - \mathbf{E}_1^\mathsf{T}) - \mathbf{E}_2 && (4.10)\\ \boldsymbol{\phi}_\ell &= -\mathbf{E}_\theta(\ell)^{-1}\mathbf{w}_\ell. && (4.11)\end{aligned}$$

Here, the same stabilization as introduced in Remark 3.5.1 is utilized. The matrices for the polygonal shape functions (Equation (3.56)) are defined by [98]

$$\begin{aligned}\mathbf{P} &= \begin{bmatrix}\boldsymbol{\Psi}_u & \boldsymbol{\Phi}_b\end{bmatrix}, && (4.12)\\ \mathbf{S} &= \begin{bmatrix}\mathbf{S}_p & \mathbf{0}\\ \mathbf{0} & -\boldsymbol{\Theta}_b\end{bmatrix}, && (4.13)\\ \mathbf{T} &= \begin{bmatrix}\boldsymbol{\Psi}_u^{-1} & \boldsymbol{\Psi}_u^{-1}\boldsymbol{\Phi}_b\\ \mathbf{0} & \mathbf{I}\end{bmatrix}, && (4.14)\end{aligned}$$

where $\boldsymbol{\Phi}_b$ is a matrix with the columns $\boldsymbol{\phi}_\ell$.

Figure 4.1 shows the two body load shape functions for the rectangular mesh on the left-hand side. Quadratic shape functions are used on the boundary. The functions are also bubble functions by definition as the values on the boundary are zeros.

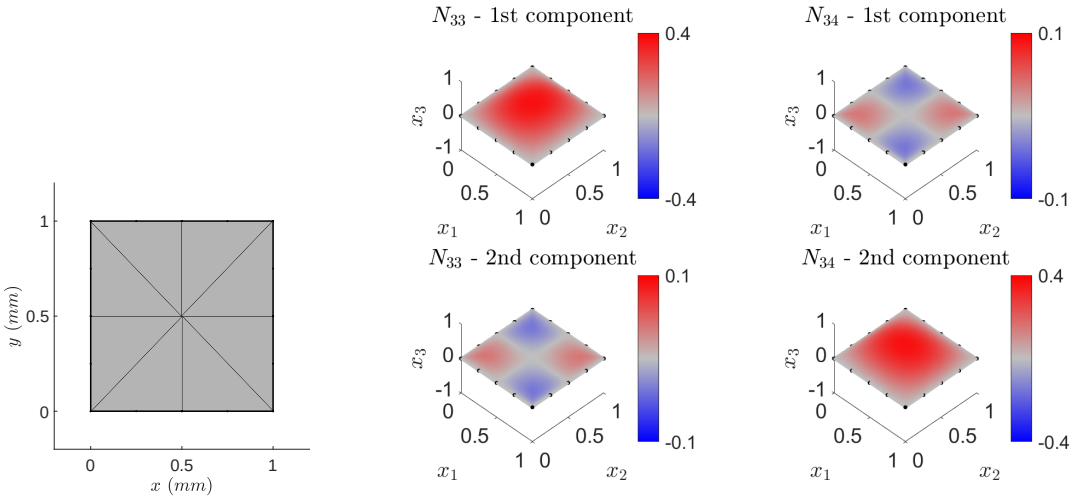

(a) Rectangular domain

(b) Body load shape functions for $\boldsymbol{f} = (1,0)^t r$ with p=2

(c) Body load shape functions for $\boldsymbol{f} = (0,1)^t r$ with p=2

Figure 4.1: Example of SB shape functions associated with a constant body load

4.2 SB Shape Functions with Body Loads and Traction Functions

To the best of the authors' knowledge, a combination of the traction and body load shape functions is proposed for the first time. These shape functions are utilized for domains containing cracks. The displacement is formally separated into three parts.

$$\boldsymbol{u} = \boldsymbol{u}_{\boldsymbol{\tau}=\boldsymbol{0},\boldsymbol{f}=\boldsymbol{0}} + \boldsymbol{u}_{\boldsymbol{\tau}\in\mathcal{P},\boldsymbol{f}=\boldsymbol{0}} + \boldsymbol{u}_{\boldsymbol{\tau}=\boldsymbol{0},\boldsymbol{f}\in\mathcal{P}}, \tag{4.15}$$

where $\boldsymbol{u}_{\boldsymbol{\tau}=\boldsymbol{0},\boldsymbol{f}=\boldsymbol{0}}$ is the displacement without body loads and traction, $\boldsymbol{u}_{\boldsymbol{\tau}\in\mathcal{P},\boldsymbol{f}=\boldsymbol{0}}$ is the part due to polynomial traction but without any body loads, and $\boldsymbol{u}_{\boldsymbol{\tau}=\boldsymbol{0},\boldsymbol{f}\in\mathcal{P}}$ is the displacement due to polynomial body loads. The part $\boldsymbol{u}_{\boldsymbol{\tau}=\boldsymbol{0},\boldsymbol{f}=\boldsymbol{0}}$ is defined in Section 3.3.1.1, the part $\boldsymbol{u}_{\boldsymbol{\tau}\in\mathcal{P},\boldsymbol{f}=\boldsymbol{0}}$ is defined in Section 3.5.3, and the part $\boldsymbol{u}_{\boldsymbol{\tau}=\boldsymbol{0},\boldsymbol{f}\in\mathcal{P}}$ is defined in Section 4.1.

Finally, the matrices for the polygonal shape functions (Equation (3.56)) are given by

$$\mathbf{P} = \begin{bmatrix} \boldsymbol{\Psi}_u & \boldsymbol{\Phi}_b & \boldsymbol{\Phi}_\tau \end{bmatrix}, \tag{4.16}$$

$$\mathbf{S} = \begin{bmatrix} \mathbf{S}_p & \mathbf{0} & \mathbf{0} \\ \mathbf{0} & -\boldsymbol{\Theta}_b & \mathbf{0} \\ \mathbf{0} & \mathbf{0} & -\boldsymbol{\Theta}_\tau \end{bmatrix}, \tag{4.17}$$

$$\mathbf{T} = \begin{bmatrix} \boldsymbol{\Psi}_u^{-1} & \boldsymbol{\Psi}_u^{-1}\boldsymbol{\Phi}_b & \boldsymbol{\Psi}_u^{-1}\boldsymbol{\Phi}_\tau \\ \mathbf{0} & \mathbf{I} & \mathbf{0} \\ \mathbf{0} & \mathbf{0} & \mathbf{I} \end{bmatrix}. \tag{4.18}$$

By definition, all SB shape functions associated with the traction or the body load terms are bubble functions.

4.3 Derivation of the Mass Matrix

This section presents the derivation of the mass matrix $\mathbf{M}$ for SB shape functions which are defined by the matrices $\mathbf{P}$, $\mathbf{S}$, and $\mathbf{T}$. This mass matrix is required for approximating the displacement for dynamic problems (see Equation (2.12)). The derivation follows in large parts [98].

The mass matrix is defined as

$$\mathbf{M} = \int \rho(\eta) \boldsymbol{N}(\xi,\eta)^{\mathsf{T}} \boldsymbol{N}(\xi,\eta)\, \mathrm{d}\Omega\,, \tag{4.19}$$

where the SB shape functions can be expressed by [181]

$$\boldsymbol{N}(\xi,\eta) = \boldsymbol{M}(\eta)\mathbf{P}\xi^{(-\mathbf{S})}\mathbf{T}. \tag{4.20}$$

Equation (4.19) leads to

$$\mathbf{M} = \int (\boldsymbol{M}(\eta)\mathbf{P}\xi^{(-\mathbf{S})}\mathbf{T})^{\mathsf{T}}\rho(\eta)\boldsymbol{M}(\eta)\mathbf{P}\xi^{(-\mathbf{S})}\mathbf{T}\,\mathrm{d}\Omega \tag{4.21}$$

$$= \int_0^1 \int (\boldsymbol{M}(\eta)\mathbf{P}\xi^{(-\mathbf{S})}\mathbf{T})^{\mathsf{T}}\rho(\eta)(\boldsymbol{M}(\eta)\mathbf{P}\xi^{(-\mathbf{S})}\mathbf{T})|j(\hat{\eta})|\,\mathrm{d}\eta\,\xi\,\mathrm{d}\xi \tag{4.22}$$

$$= \mathbf{T}^{\mathsf{T}} \int_0^1 \xi^{(-\mathbf{S})^{\mathsf{T}}}\mathbf{Y}\xi^{(-\mathbf{S}+\mathbf{I})}\,\mathrm{d}\xi\,\mathbf{T} \tag{4.23}$$

with

$$\mathbf{Y} = \mathbf{P}^{\mathsf{T}}\mathbf{M}_0\mathbf{P}. \tag{4.24}$$

Analogously to Equation (3.39), the boundary mass matrix is assembled over the elements

$$\mathbf{M}_0 = \underset{e}{\mathrm{A}}\,\mathbf{M}_0^e \tag{4.25}$$

with

$$\mathbf{M}_0^e = \int_{-1}^{+1} \hat{\boldsymbol{M}}(\hat{\eta})^{\mathsf{T}}\rho(\hat{\eta})\hat{\boldsymbol{M}}(\hat{\eta})\,|j(\hat{\eta})|\,\mathrm{d}\hat{\eta}. \tag{4.26}$$

We consider the following identity

$$\mathbf{Y} = \left.\xi^{(-\mathbf{S}+\mathbf{I})^{\mathsf{T}}}\mathbf{Y}\xi^{(-\mathbf{S}+\mathbf{I})}\right|_{\xi=0}^{1}. \tag{4.27}$$

Integration by parts leads to

$$\mathbf{Y} = \int_0^1 [-\mathbf{S}+\mathbf{I}]^{\mathsf{T}}\xi^{(-\mathbf{S})^{\mathsf{T}}}\mathbf{Y}\xi^{(-\mathbf{S}+\mathbf{I})}\,\mathrm{d}\xi + \int_0^1 \xi^{(-\mathbf{S}+\mathbf{I})^{\mathsf{T}}}\mathbf{Y}\xi^{(-\mathbf{S})}[-\mathbf{S}+\mathbf{I}]\,\mathrm{d}\xi \tag{4.28}$$

$$= [-\mathbf{S}+\mathbf{I}]^{\mathsf{T}}\mathbf{X} + \mathbf{X}[-\mathbf{S}+\mathbf{I}] \tag{4.29}$$

with

$$\mathbf{X} = \int_0^1 \xi^{(-\mathbf{S})^{\mathsf{T}}}\mathbf{Y}\xi^{(-\mathbf{S}+\mathbf{I})}\,\mathrm{d}\xi \tag{4.30}$$

$$= \int_0^1 \xi^{(-\mathbf{S}+\mathbf{I})^{\mathsf{T}}}\mathbf{Y}\xi^{(-\mathbf{S})}\,\mathrm{d}\xi\,. \tag{4.31}$$

The result is a LYAPUNOV-equation [98] for $\mathbf{X}$

$$\mathbf{Y} = [-\mathbf{S}+\mathbf{I}]^{\mathsf{T}}\mathbf{X} + \mathbf{X}[-\mathbf{S}+\mathbf{I}]. \tag{4.32}$$

Finally, substitute the definition of $\mathbf{X}$ (Equation (4.30)) in Equation (4.23) to get the mass matrix

$$\mathbf{M} = \mathbf{T}^{\mathsf{T}}\mathbf{X}\mathbf{T}. \tag{4.33}$$

This concludes the derivation of the mass matrix with an analytical integration with respect to ξ.

4.4 Summary of the Matrices Analysis for the SB Shape Functions

Before the assembling of multiple super-elements is described, the properties of a single super-element are summarized. Let p be the polynomial degree of the boundary shape functions, and $\mathrm{n}_{\mathrm{node}}$ the number of nodes on the boundary of an SBFEM-polygon. Then, the shape functions have the following degrees of freedom:

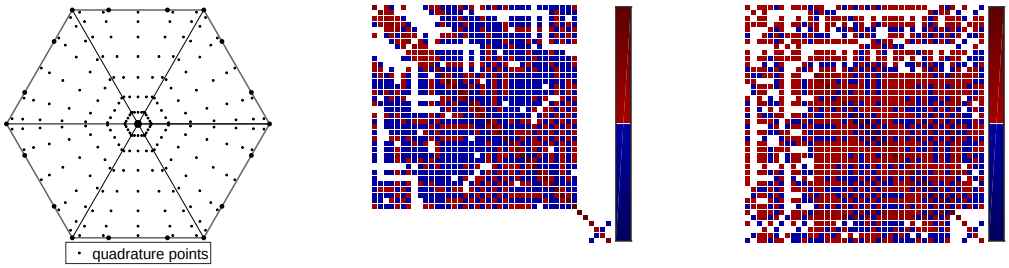

(a) SBFEM-mesh with displayed quadrature points (b) Matrix plot for $\mathbf{K}$ (c) Matrix plot for $\mathbf{M}$

Figure 4.2: Example polygon and matrix plots

- $2 \cdot \mathrm{n}_{\mathrm{node}}$ DIRICHLET degrees of freedom,
- depending on the shape:
  - for a crack tip element, p traction degrees of freedom on the scaling lines
  - for a closed super-element, zero traction degrees of freedom
- $2 \cdot \binom{p}{2}$ body load degrees, where $\binom{1}{2}$ is defined as 0.

For closed super-elements, the number of degrees of freedom is equal to the number of degrees of freedom in the VEM [37].

The SB shape functions for computing the matrices and vectors are integrated as follows:

- The mass matrix $\mathbf{M}$ is semi-analytically integrated in ξ-direction with a consistent numerical part for the η-direction (Section 4.3).
- The static stiffness matrix $\mathbf{K}$ is semi-analytically integrated in ξ-direction with a consistent numerical part for the η-direction (Section 3.5.1).
- The force vector $\mathbf{f}$ is numerically integrated over the different wedges of the polygon (see Figure 4.2a).

Figure 4.2a shows an example polygon for linear elasticity with $p = 3$, as well as the static stiffness and mass matrix. We observe the block structure in the static stiffness matrix (Figure 4.2b) because of the orthogonality of the SB shape functions to the polynomial functions in ξ-direction, which disappear at the boundary and scaling center [32]. The small 6×6 block on the right-hand side is associated with the body load degrees of freedom. In contrast, the mass matrix is dense (Figure 4.2c) and the body load degrees of freedom are coupled to the other ones.

4.5 Polygonal Meshes and their h-refinement

For a more complicated domain, a sub-division into several super-elements is necessary. As these super-elements take the form of polygons, an effective procedure for their definition is required. Standard meshing tools can provide a triangular mesh and its refinement but rarely generate polygonal meshes. Additionally, for convergence studies, the element size must decrease uniformly. For this purpose, a meshing routine with a uniform refinement is implemented. For this thesis, the triangular meshes are created by GMSH [58]. The triangular mesh can be afterward converted into a polygonal mesh by the dual-mesh approach [99]. The concept is depicted in the first row of Figure 4.3.

The following steps create the dual-mesh:

- Introduce the old nodes as possible nodes or scaling centers.
- For each triangle, introduce the center as a new node.
- For each boundary edge, introduce the center as a new node.
- Each old node leads to a new polygon:

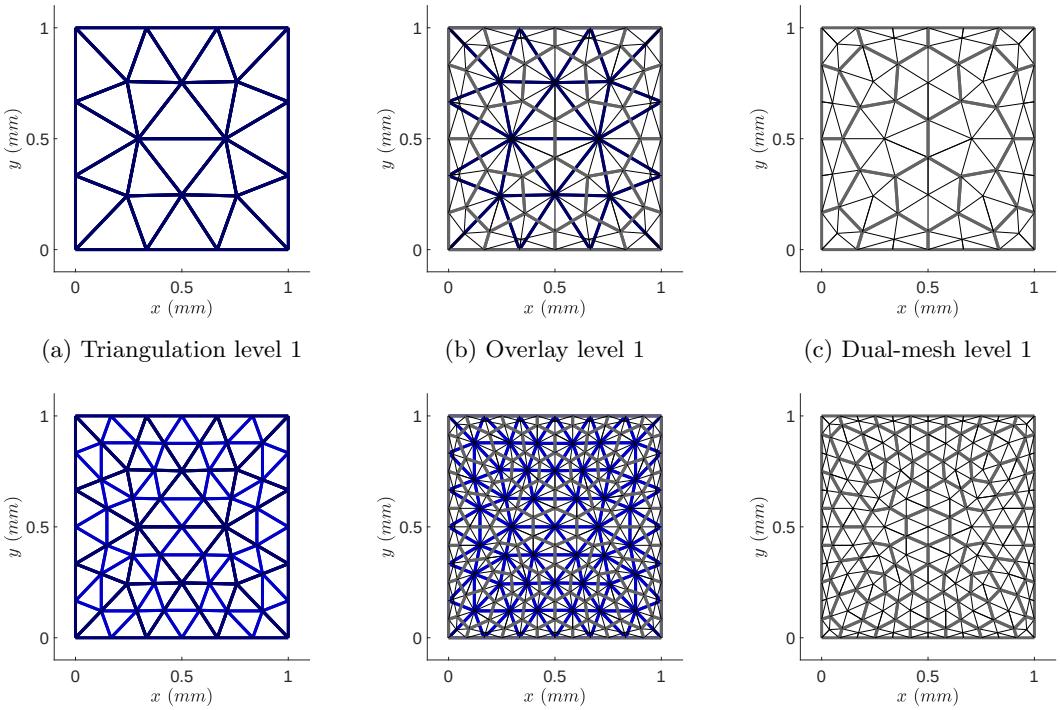

(a) Triangulation level 1 (b) Overlay level 1 (c) Dual-mesh level 1

(d) Triangulation level 2 (e) Overlay level 2 (f) Dual-mesh level 2

Figure 4.3: Dual meshes and h-refinement for polygonal meshes

- If the old node is an inner node, connect all centers of the adjacent triangles to define the new polygon boundary. The scaling center is the old node.
- If the old node is a boundary node, connect this node with the center of the adjacent boundary edges and all centers of the adjacent triangles to define the new polygon boundary. The scaling center is a new point located at the mean value of the nodes of the new polygonal boundary.

Figure 4.3a shows the underlying triangular mesh in blue. Figure 4.3b overlays the triangular mesh in blue with the polygonal mesh in black. Finally, Figure 4.3c shows only the polygonal mesh, where the polygons are drawn in thick lines, and the thin lines mark the scaling towards the scaling center. For polygonal elements, the h-refinement is not canonically given in every element. Instead, the dual-mesh is used to define the h-refinement. In all examples, first, a coarse triangulation is created. This coarse triangulation is level-wise refined. In each refinement level, all triangles in each triangulation are canonically h-refined by splitting each triangle into four smaller triangles. Afterward, the dual-mesh is created with the steps described above.

Figure 4.3 also illustrates the h-refinement process. The second row shows the second refinement level. Compare Figure 4.3d to Figure 4.3a to observe that the dark blue triangles are split into four, where the new lines are drawn in light blue. From Figure 4.3d to Figure 4.3f, the dual-mesh is created for the second level.

For a crack, Gmsh [58] can introduce an embedded boundary in the domain. The endpoints of the embedded boundary of the triangular mesh, which represent the crack tip, are marked. For the inner nodes of the embedded boundary, the double nodes are added. For a polygonal mesh, the dual-mesh is constructed with the following modification: For the marked crack tip, the polygon definition is modified such that the crack tip is the scaling center. It is worth mentioning that the meshing process is fully automatized and can be utilized in parametric studies as presented in Sections 5.3.2 and 5.3.3.

The Galerkin approach for polygonal meshes has two different assembly stages. First, the matrices $\mathbf{E}_0$, $\mathbf{E}_1$, $\mathbf{E}_2$, and $\mathbf{M}_0$ are assembled in each polygon to calculate the SB shape functions and the associated static stiffness matrix, mass matrix, and force vector. Afterward, these are

assembled in the global static stiffness matrix (Equation (2.38)), mass matrix (Equation (2.37)), and force vector (Equation (2.39)), respectively. This leads to the ODE in Equation (2.12) for simulating linear dynamic problems with the SB shape functions on polygonal meshes.

4.6 Numerical Experiments for the SB Shape Functions

This section presents selected examples to show the higher-order convergence of the SB shape functions. Initially, the higher-order convergence was disputed because the first publication also included an example with deteriorated convergence rates [98]. Further investigations indicated that the deteriorated convergence rates are observed because the solution is not sufficiently regular in the analysed example with deteriorated convergence rates. These discussions, however, inspired the following examination.

The first example is a standard convergence test in the frequency domain. The second example tests the calculation of eigenfrequencies with many practical application areas - including techniques of NDT and SHM [141]. The third example compares the SB shape functions with higher-order FEM and shows the suitability for the simulation of ultrasonic waves.

4.6.1 Error Analysis for an Analytical Case in the Trapezoidal Domain

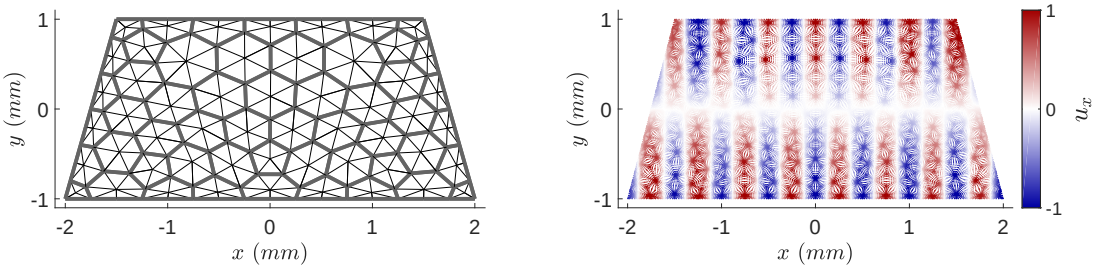

(a) SBFEM-mesh

(b) Approximation of u_x^{ref} (in µm) for p = 4

Figure 4.4: Domain and approximation of Equation (4.36) for a trapezoidal domain

As a first problem, we investigate the convergence in the frequency domain. A single frequency reduces the computation to solving a single matrix system. This is in contrast to the time domain where multiple time steps have to be solved. Figure 4.4a shows the trapezoidal domain with a polygonal mesh, which is the third level in the h-refinement (see Section 4.5). The error can be analyzed with an artificial analytical example.

The problem can be stated formally as: Find the displacement $\boldsymbol{u}(\mathbf{x})$, such that

$$(\mathrm{i}\,\omega)^2\rho\boldsymbol{u} = \boldsymbol{\nabla}\cdot\underline{\underline{\boldsymbol{\sigma}}}(\boldsymbol{u}) + \boldsymbol{f} \qquad \mathbf{x}\in\Omega \tag{4.34}$$

$$\underline{\underline{\boldsymbol{\sigma}}}(\boldsymbol{u})\mathbf{n} = \boldsymbol{\tau} \qquad \mathbf{x}\in\Gamma \tag{4.35}$$

with $\omega = 2\pi\,\mathrm{s}^{-1}$ and $\Omega\subset\mathbb{R}^2$.

Consider a body force $\boldsymbol{f} = -\boldsymbol{\nabla}\cdot\underline{\underline{\boldsymbol{\sigma}}}(\boldsymbol{u}^{\mathrm{ref}}) + (\mathrm{i}\,\omega)^2\rho\boldsymbol{u}^{\mathrm{ref}}$ and a traction $\boldsymbol{\tau} = \underline{\underline{\boldsymbol{\sigma}}}(\boldsymbol{u}^{\mathrm{ref}})\mathbf{n}$ such that the following analytical solution $\boldsymbol{u}^{\mathrm{ref}}$ is taken

$$\boldsymbol{u}^{\mathrm{ref}}(x,y) = \begin{pmatrix}\cos(k_x^u x)\sin(k_y^u y)\\ \cos(k_x^v x)\sin(k_y^v y)\end{pmatrix}\,\mu\mathrm{m} \tag{4.36}$$

with $k_x^u = 4\pi\,\mathrm{mm}^{-1}$, $k_y^u = \pi\,\mathrm{mm}^{-1}$, $k_x^v = 2\pi\,\mathrm{mm}^{-1}$, and $k_y^v = \pi\,\mathrm{mm}^{-1}$. Figure 4.4b shows the approximation of u_x^{ref} for p = 4. The material parameters are given in Table A.1d and plane strain is assumed.

The L^2-error between the reference solution and the solution obtained using SB shape functions is computed as follows

$$L^2\text{-error} = \frac{||\boldsymbol{u}^{\mathrm{h}} - \boldsymbol{u}^{\mathrm{ref}}||_2}{||\boldsymbol{u}^{\mathrm{ref}}||_2} \tag{4.37}$$

with the L^2-norm for complex functions

$$||\boldsymbol{u}||_2 = \sqrt{\int \boldsymbol{u}^{\mathrm{H}}\boldsymbol{u}\,\mathrm{d}\Omega}. \tag{4.38}$$

Error analysis for the SB shape functions is performed in [32, 72]. It is generally expected that the estimations obtained for FEM or VEM [37] are applicable. We follow the tradition in the SBFEM community to estimate the convergence rate in terms of degrees of freedom. It is expected that:

Remark 4.6.1 (L^2-error)**.** *If* $\boldsymbol{u}^{\mathrm{ref}}$ *is sufficiently regular, then there exists a constant* $\mathcal{C}$ *independent of* h *and a mesh size* h^**, such that for all* $\mathrm{h} < \mathrm{h}^*$ *it is*

$$L^2\text{-error} < \mathcal{C}\mathrm{h}^{\mathrm{p}+1}. \tag{4.39}$$

Since this inequality is sharp, it follows

$$\log_{10}(L^2\text{-error}) \approx \mathrm{r}\log_{10}(\#\,\mathrm{DoF}) + \log_{10}(\mathcal{C}) \tag{4.40}$$

with the rate $\mathrm{r} = -\frac{p+1}{2}$ *because it holds* $\mathrm{h} \approx (\#\,\mathrm{DoF})^{-\frac{1}{2}}$.

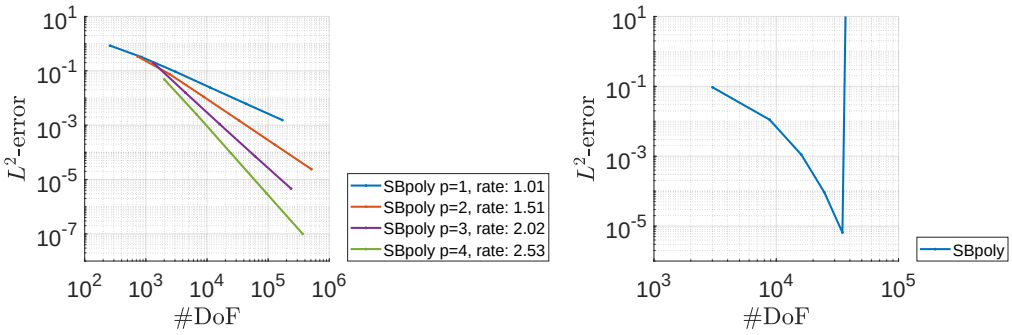

(a) L^2-error for h-refinement

(b) L^2-error for p-refinement

Figure 4.5: L^2-error with respect to Equation (4.36) for the trapezoidal domain (Figure 4.4a)

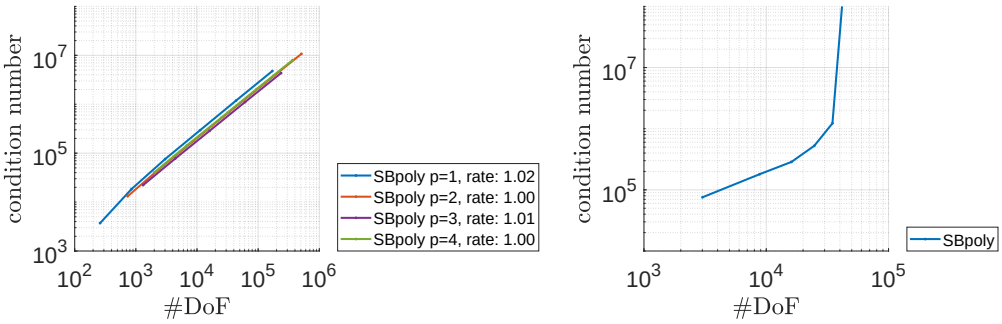

(a) Condition number for h-refinement

(b) Condition number for p-refinement with $\mathrm{p} = 1, \ldots, 9$

Figure 4.6: Condition number for the trapezoidal domain (Figure 4.4a)

Figure 4.5 shows the L^2-error for h- and p-refinement. The rates of h-refinement, given in the legend of the figure, are in good agreement with the theoretical values from Remark 4.6.1. The

p-refinement shows a curve of exponential convergences until the solution blows up for the last step (p = 9). Figure 4.6 depicts the condition number for both refinement strategies. Here, it can be observed that the condition number rapidly increases under p-refinement, which might explain the unstable last solution. Overall, such high degrees are rather uncommon in practical applications. The results for smaller degrees (p < 5) show a stable, optimal convergence behavior.

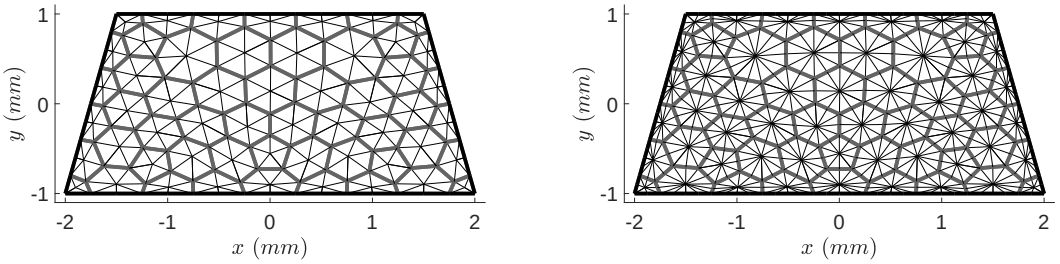

(a) SBFEM-mesh level 1

(b) SBFEM-mesh level 2

Figure 4.7: Meshes with sb-refinement of a trapezoidal domain

sb-refinement This numerical experiment is driven by curiosity. To the best of the author's knowledge, there is no mathematical theory about the studied refinement for shape functions. Besides h-refinement of a polygonal mesh (see Section 4.5), another refinement method is known in the SBFEM-literature. If we have a polygonal mesh with 1D boundary elements, we can refine this mesh by splitting each boundary element into two segments. The reader is referred to Figure 4.7 for a better understanding of this level-wise refinement. We will refer to this as sb-refinement. An investigation is interesting because an sb-refinement step leads to fewer degrees of freedom than an h-refinement step.

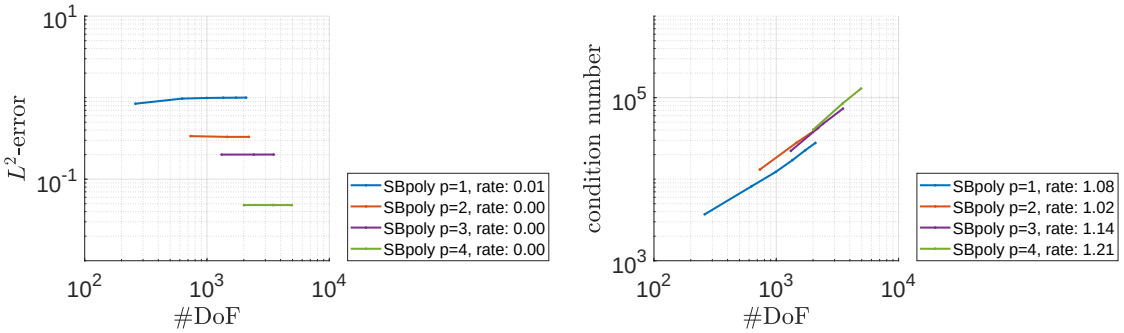

(a) L^2-error for sb-refinement

(b) Condition number for sb-refinement

Figure 4.8: Analysis with sb-refinement for a trapezoidal domain

The investigated problem is the same as presented in the previous subsection. Figure 4.8a shows the behavior under sb-refinement - no convergence can be observed. Additionally, Figure 4.8b even shows that the condition number is rising. In conclusion, sb-refinement is not appropriate for SB shape functions for problems with a body load. A heuristic explanation is that the number of bubble functions does not increase with sb-refinement. So, the same number of shape functions has to approximate the part of the solution associated with the body loads in each refinement step. It is worth mentioning that this refinement method is applicable to the classic SBFEM for homogeneous problems [134].

4.6.2 Convergence Analysis for the Eigenfrequencies

The second problem, for which the convergence behavior of the SB shape functions is tested, is the computation of eigenfrequencies. Figure 4.9a shows the quadratic domain as the coarsest polygonal mesh. The problem is: Find the displacement eigenpair $(\boldsymbol{u}(\mathbf{x}), \tilde{\omega})$, such that for $\tilde{\omega} = \omega^2$

$$-\tilde{\omega}\rho\boldsymbol{u} = \boldsymbol{\nabla}\cdot\underline{\underline{\boldsymbol{\sigma}}}(\boldsymbol{u}) \qquad \mathbf{x}\in\Omega \tag{4.41}$$

$$\mathbf{n}\cdot\boldsymbol{u} = 0 \qquad \mathbf{x}\in\Gamma. \tag{4.42}$$

Note that the normal direction $\mathbf{n}\cdot\boldsymbol{u}$ is fixed for the whole boundary, and both directions are fixed for the corners. For these boundary conditions, the analytical solution of the eigenfrequencies is known [66]. This naturally leads to a generalized eigenvalue problem for matrices:

$$-\tilde{\omega}\mathbf{M}\mathbf{u} = \mathbf{K}\mathbf{u} \tag{4.43}$$

for the eigenpair $(\mathbf{u}, \tilde{\omega})$, where the degrees of freedom for the normal direction of the boundary are removed from the system.

The eigenfrequency error between the reference solution and the SBFEM is computed as follows

$$\text{eigenfrequency error} = \frac{||\tilde{\boldsymbol{\omega}}^{\mathrm{h}} - \tilde{\boldsymbol{\omega}}^{\mathrm{ref}}||_2}{||\tilde{\boldsymbol{\omega}}^{\mathrm{ref}}||_2}, \tag{4.44}$$

where $\tilde{\boldsymbol{\omega}}^{\mathrm{ref}}$ is a vector with the first 40 analytical eigenfrequencies, which can be found in [66] for the material in Table A.1f under the plane stress assumption. It is important to notes that the eigenfunctions are smooth and consist of trigonometric functions. Hence, the problem is appropriate for convergence tests.

To the best of the author's knowledge, there is no particular publication handling the theoretical convergence of the SB shape functions for the eigenfrequencies, but due to the work in [72], it can be expected that convergence rates for the FEM [112] are applicable. We follow, again, the tradition in the SBFEM community to express the convergence rates in terms of degrees of freedom. If the eigenfunctions are sufficiently regular, then there exists a constant $\mathcal{C}$ independent of h and a mesh size h^*, such that for $\mathrm{h} < \mathrm{h}^*$ it is

$$\text{eigenfrequency error} < \mathcal{C}\mathrm{h}^{2\mathrm{p}}. \tag{4.45}$$

Since this inequality is sharp, it follows

$$\log_{10}(\text{eigenfrequency error}) \approx \mathrm{r}\log_{10}(\#\,\mathrm{DoF}) + \log_{10}(\mathcal{C}) \tag{4.46}$$

with $\mathrm{r} = -\mathrm{p}$ because it is $\mathrm{h} \approx (\#\,\mathrm{DoF})^{-\frac{1}{2}}$. Figure 4.9b shows the domain and the eigenfrequency error for h-refinement. The computed rates are in good agreement with the theoretical ones.

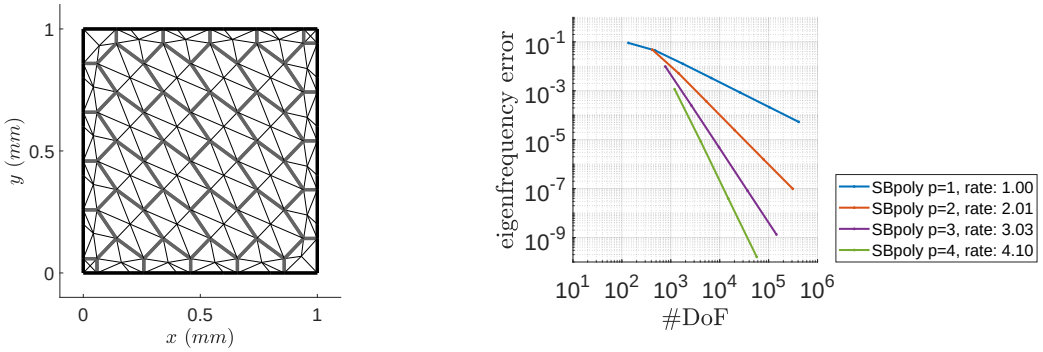

(a) SBFEM-mesh

(b) Eigenfrequency error for h-refinement

Figure 4.9: Analysis of the eigenfrequencies of a unit square

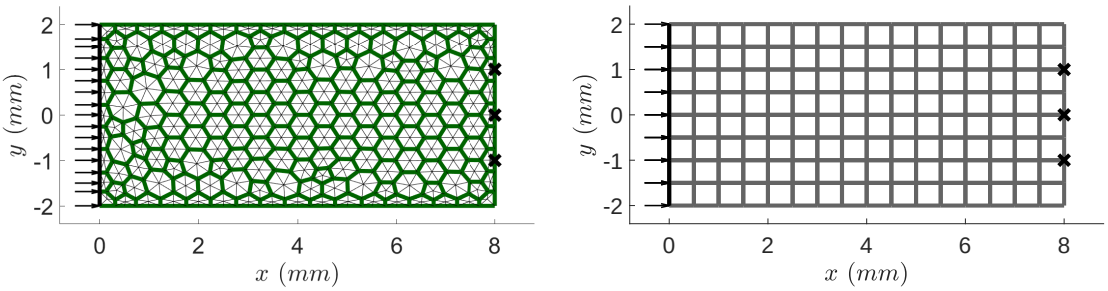

(a) SBFEM-mesh (b) FEM-mesh

Figure 4.10: Comparison of rectangular domains

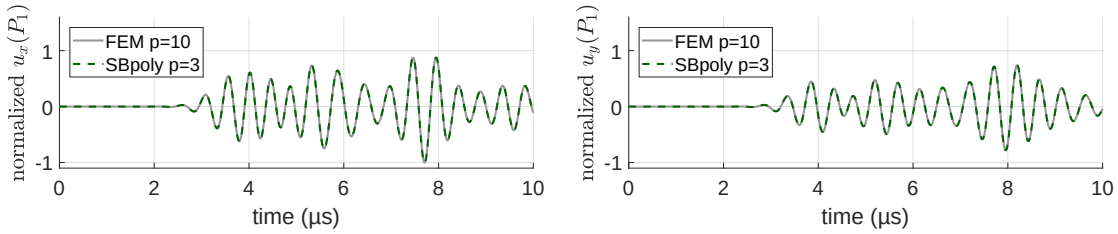

(a) Signal $\boldsymbol{u}_x(\mathrm{P}_1)$ (b) Signal $\boldsymbol{u}_y(\mathrm{P}_1)$

Figure 4.11: Signal for the point $\mathrm{P}_1 = (8\,\mathrm{mm}, 1\,\mathrm{mm})^\mathsf{T}$ on a rectangular domain

4.6.3 Comparison with the Finite Element Method

As the last example, we investigate the error in the time domain. For this purpose, we advance in applying the method to ultrasonic guided waves, but on a smaller domain. We do not present an analytical example, but a comparison with a high-order FEM.

For the time-domain, find the displacement $\boldsymbol{u}(t, \mathbf{x})$, such that

$$\rho \partial_{tt} \boldsymbol{u} = \boldsymbol{\nabla} \cdot \underline{\boldsymbol{\sigma}}(\boldsymbol{u}) \qquad (t, \mathbf{x}) \in [0, T] \times \Omega \tag{4.47}$$

$$\underline{\boldsymbol{\sigma}}(\boldsymbol{u})\mathbf{n} = \boldsymbol{\tau}_\mathbf{x} \cdot \tau_t \qquad (t, \mathbf{x}) \in [0, T] \times \Gamma \tag{4.48}$$

$$\boldsymbol{u} = \mathbf{0} \qquad (t, \mathbf{x}) \in \{0\} \times \Omega \tag{4.49}$$

$$\partial_t \boldsymbol{u} = \mathbf{0} \qquad (t, \mathbf{x}) \in \{0\} \times \Omega. \tag{4.50}$$

The traction varies in time as a Gaussian pulse with a center frequency f_0 of 1 MHz, i.e.,

$$\tau_t(t) = \sin(2\pi\, t f_0) \cdot \exp\big(-0.5(t - 0.25 f_0^{-1})^2 / (f_0^{-1})^2\big), \tag{4.51}$$

while it varies in space as a constant function of $x = 0$, and the rest of the boundary is traction-free, i.e.,

$$\tau_\mathbf{x}(\mathbf{x}) = \begin{cases} 100\mathbf{n} & x = 0 \\ \mathbf{0} & x > 0. \end{cases} \tag{4.52}$$

The material parameters are given in Table A.1d and plane strain is assumed. The time step is chosen as $(100 f_0)^{-1}$ in the Newmark's method. This is a comparatively small time step. Both methods are simulated with the same time scheme. Thus, the error due to the mesh dominates the difference between approximation and reference solution.

The approximation at different points is compared. To the best of the author's knowledge, there is no theoretical convergence rate for the point error in FEM, but point evaluations are critical in many applications. As the evaluation of ultrasonic waves is often based on single points, investigating the approximation at these points is crucial. The point error between the reference

solution and the current approximation is computed as follows

$$\text{point error} = \sqrt{\sum_i \sum_j \left(\boldsymbol{u}^h(\mathrm{P}_j, t_i) - \boldsymbol{u}^{\mathrm{ref}}(\mathrm{P}_j, t_i)\right)^2} \Big/ \sqrt{\sum_i \sum_j \left(\boldsymbol{u}^{\mathrm{ref}}(\mathrm{P}_j, t_i)\right)^2}, \tag{4.53}$$

where t_i are the time steps and P_j are the points of interest. In this case, P_j are the points marked with black crosses in Figure 4.10 at the right boundary. The reference solution is computed with the Finite Element Method on a highly refined mesh, with Figure 4.10b) showing a coarse version. Linear problems are scalable with the excitation. So, the time series in this thesis is normalized by dividing through the maximum value of both directions

$$A_i^{\max} = \max_t \max_{j \in \{x,y\}} |u_j(t, P_i)|. \tag{4.54}$$

Figure 4.11 shows an example normalized displacement for the top point $\mathrm{P}_1 = (8\,\mathrm{mm}, 1\,\mathrm{mm})^\mathsf{T}$ for u_x and u_y. Figure 4.12 shows the point error for h- and p-refinement. We can observe that the convergence behavior is the same as for the FEM. Again, the high polynomial degrees $\mathrm{p} = 7$ and $\mathrm{p} = 9$ lead to unstable approximations, while $\mathrm{p} = 8$ is stable.

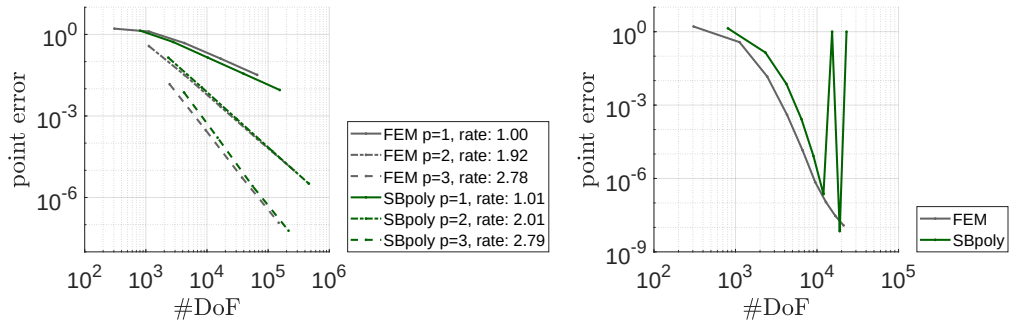

(a) Point error for h-refinement

(b) Point error for p-refinement with $\mathrm{p} = 1, \ldots, 9$

Figure 4.12: Point error for the rectangular domain

4.7 Theory for Dynamic Problems with Singularity

As mentioned in Section 3.1.5, dynamic problems in the low-frequency range should behave similarly to static problems. For a small area around a point and a sufficiently small time frame, a dynamic system can be approximated by a loaded static problem. Consequently, the static singular modes can be used as an approximation near a critical point also in dynamic problems.

Many methods that can handle singular behavior for static problems can be extended to dynamic problems in the time domain. If the approach can represent artificial body loads, an extension to dynamic problems should be promising, especially if the formulation allows the computation of a mass matrix. So, the methods mentioned in Section 3 are applicable if they fulfill these criteria. To name a few, this includes Singular Elements [12, 69, 71], XFEM [56, 74, 140], extended IGA [59], and meshless methods [95].

Alternatively, the meshing can be adapted to singular points. Graded meshes apply to a large majority of mesh-based methods. The effectiveness of graded meshes can be increased if a local p-decrease is utilized for small elements near the point of singularity. But even with this local p-decrease, a graded mesh needs more degrees of freedom, as presented below and in [22].

We follow the approach of many researchers,e.g., [42, 76, 127, 182], and utilize a static crack tip approximation in the dynamic analysis. The results of the following section indicate the validity of this approach.

4.8 Numerical Experiments for Dynamic Problems with Singularity

Two problems are presented for dynamic systems with singular stresses: On the one hand, the L-shaped domain, which is a typical benchmark problem [152], on the other hand, a linear crack. In this section, only linear effects are investigated, while in Section 5.3.2 a contact model extends the linear crack model.

4.8.1 L-shaped Domain under Dynamic Load

As a first example, we consider the classic re-entrant corner of an L-shaped domain. The re-entrant corner has a singular stress mode. The singular stress mode is the main reason why sharp re-entrant corners should be avoided in engineering structures. Nevertheless, it is a classic benchmark example for numerical analysis with a singular stress distribution [152]. We will analyse three models: 1) a normal p-refinement for FEM 2) a graded hp-refined mesh for FEM 3) the enrichment approach as presented in Section 3.8 with the improvements specified in Remark 3.8.2.

Figure 4.13a gives an overview of the problem. The L-shape is excited on the left side with a GAUSSIAN pulse with a center frequency f_0 (see Equation (4.51)). In this example, only the numerical influences are to be investigated, so artificial material properties are used that can be scaled to a physically feasible problem if needed. Two center frequencies, $f_0 = 1\,\mathrm{Hz}$ and $f_0 = 2\,\mathrm{Hz}$, are studied. The shear modulus $G = 1\,\mathrm{GPa}$, the POISSON's ratio $\nu = 0.3$ and the density $\rho = 1\,\mathrm{kg\,m^{-3}}$ are utilized, and plane strain is assumed. The time simulation advances with the NEWMARK's scheme for a duration of $25 f_0^{-1}$ with a small time step of $\Delta t = 7.81 \times 10^{-4}\,\mathrm{s}$. Note that all models and the reference solution are computed with the same time scheme, so the time-dependent part of the error is equal for all simulations.

Figure 4.13b illustrates the mesh of the first model, which is a uniform FEM mesh with p-refinement. The second model, shown in Figure 4.13c, has a strongly graded mesh toward the point singularity at the origin. The mesh is optimized so that the elements next to the origin are only h-refined if the refinement is more efficient with respect to the number of degrees of freedom. Thereby only the grading factor of 0.15 is investigated [120]. It is worth mentioning that such a strong grading factor requires knowledge about the position of the singularity. Typically, adaptive methods lead to grading with a factor of 0.5 because, in most implementations, elements can only be bisected in the adaptive procedure. For smaller elements, the degree is reduced to achieve the same error with fewer degrees of freedom [179]. The third model follows the enrichment approach (Section 3.8). The enriched area is marked in gray in Figure 4.13d. The point-error (Equation (4.53)) is evaluated with respect to a reference solution $\mathbf{u}^{\mathrm{ref}}$ at the point $\mathrm{P} = (0.5\,\mathrm{m}, -1\,\mathrm{m})$ (Figure 4.13a). The reference solution is based on an hp-refined mesh which is graded similarly to Figure 4.13c, but with a higher degree ($\mathrm{p} = 14$) and more layers of elements in the vicinity of the singularity. The reference is a so-called overkill approximation generated for precision only, without any efficiency in mind. The exponential convergence of hp-refined meshes makes it an appropriate reference solution [179]. Figure 4.14 shows the reference solution and displacement result obtained using the enrichment approach for $f_0 = 1\,\mathrm{Hz}$. Additionally, Figure 4.15 depicts the performance of all three approaches for the two frequencies $f_0 = 1\,\mathrm{Hz}$ and $f_0 = 2\,\mathrm{Hz}$. For uniform p-refinement, the singularity reduces the convergence significantly. The other two approaches reach quickly an error under 1%. The enrichment approach requires the fewest degrees of freedom of the tested methods.

4.8.2 Waveguide with a Crack

As a second example, we consider an application for NDT or SHM. The cross-section of a plate with a crack is analyzed regarding its numerical properties. The plate acts as a waveguide due to the small thickness compared with the wavelength. In this part, the model is entirely linear so that both crack faces can penetrate each other, and no contact model is applied. The material is construction steel (Table A.1d), and plane strain is assumed. For a waveguide, the ultrasonic pulses can only travel in specific modes. These modes have frequency-dependent propagation properties. For example, the wavelength and group velocity are dispersive. The group velocity is

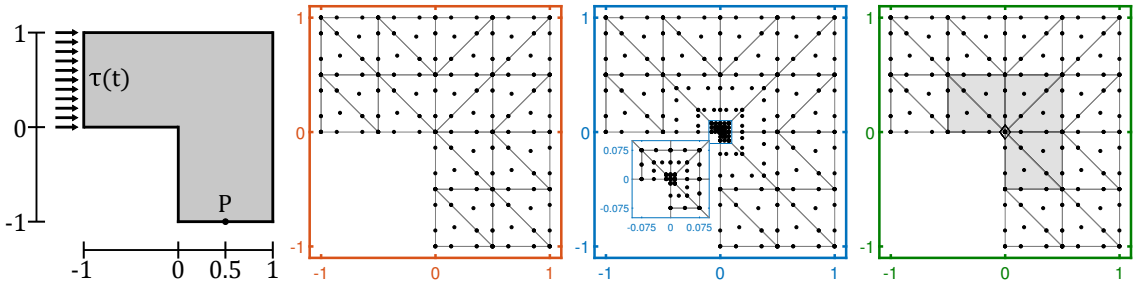

(a) Overview in m (b) FEM with p-ref. [22] (c) FEM with hp-ref. [22] (d) eFEM with p-ref. [22]

Figure 4.13: Example meshes for the three methods used to model an L-shaped domain

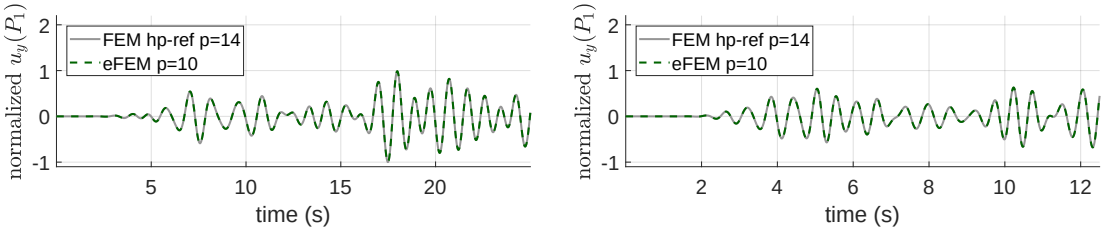

(a) Signal $\boldsymbol{u}_y$(P) for 1 Hz (b) Signal $\boldsymbol{u}_y$(P) for 2 Hz

Figure 4.14: Signal at point P on the L-shaped domain (Figure 4.13a)

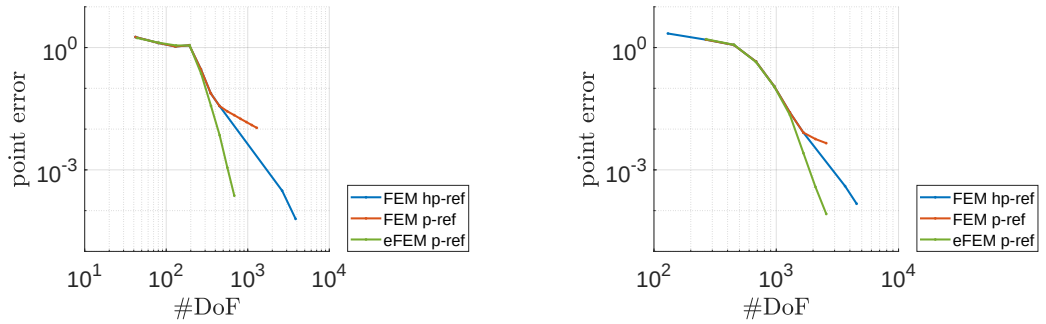

(a) Point error for $f_0 = 1\,\text{Hz}$ with $p = 2, \ldots, 10$ (b) Point error for $f_0 = 2\,\text{Hz}$ with $p = 2, \ldots, 11$

Figure 4.15: Point error for the L-shaped domain for two different center frequencies (Equation (4.51)) at point P

the propagation speed of the energy and wave packages. The number of modes that can propagate depends on the material, the thickness of the waveguide, and the frequency. Considering only the displacement in x- and y-direction, there are two modes, A0 and S0, which can propagate in the whole frequency range. This thesis focuses on these two modes. In a specific setup, the excitation of the ultrasonic wave will determine the amplitude of the different modes.

Figure 4.16 shows the relationship between the experimental and mathematical model of the excitation. The boundary condition models a double transducer setup [142]. This setup can excite symmetric and anti-symmetric guided-wave modes depending on the signs of the electric signal sent to the transmitter. Figure 4.17 gives an overview of the complete model. Here, the left-hand edge $\Gamma_{\boldsymbol{u}}$ of the model is the symmetry plane of the transducer and has the boundary condition $\mathbf{u} \cdot \mathbf{n} = 0$. The traction at both sides varies in time as a Gaussian pulse (Figure 4.18a) with a center frequency f_0 of 500 kHz. Figure 4.18b shows the spectrum of the excitation and the dispersion curves for the group velocity. The part with relevant amplitudes is in the range where only the two fundamental modes, S0 and A0, can propagate. The dispersion curves are computed using the

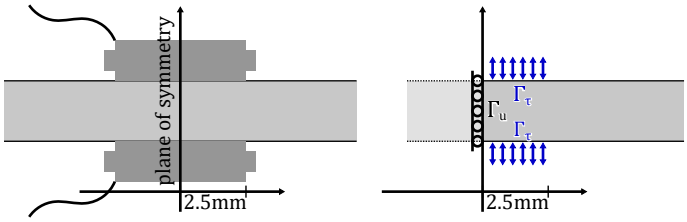

Figure 4.16: Relationship between the experimental and mathematical model for a double transducer

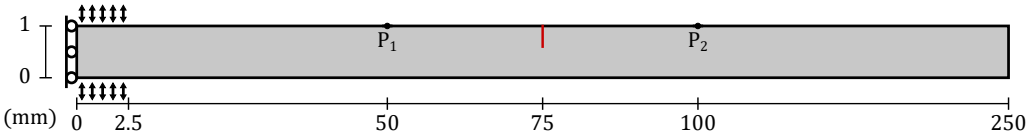

Figure 4.17: Waveguide with a linear crack

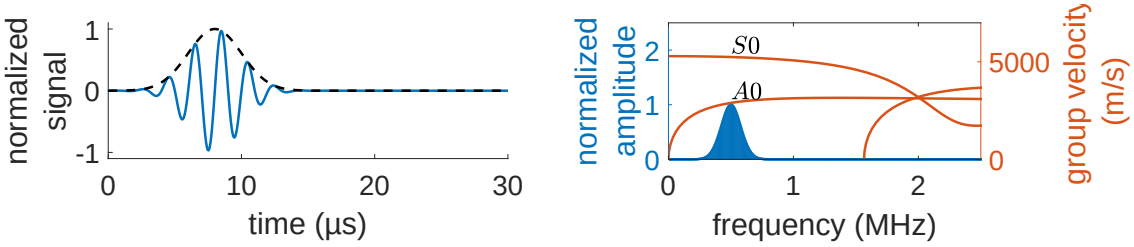

(a) Excitation signal

(b) Excitation spectrum

Figure 4.18: Time- and frequency-dependence of the excitation with $f_0 = 500\,\mathrm{kHz}$

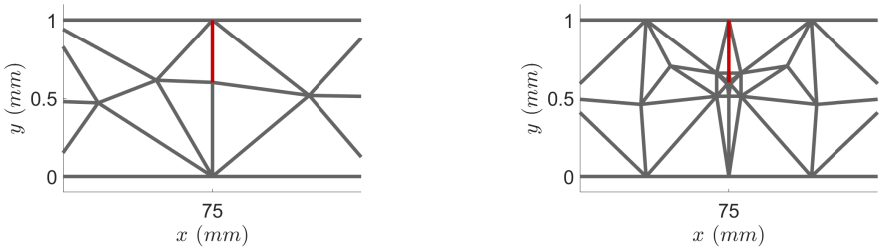

(a) Mesh for quasi-uniform FEM

(b) Mesh for graded FEM

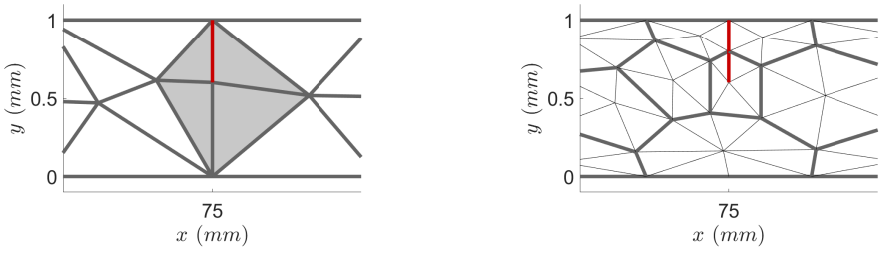

(c) Mesh for eFEM

(d) Mesh for SBpoly

Figure 4.19: Mesh details around the crack tip for the waveguide

SBFEM [21, 65]. The derivation of the approach can be found in [65], while the algorithm utilized here solves the dispersion curves for each wavenumber as in [21].

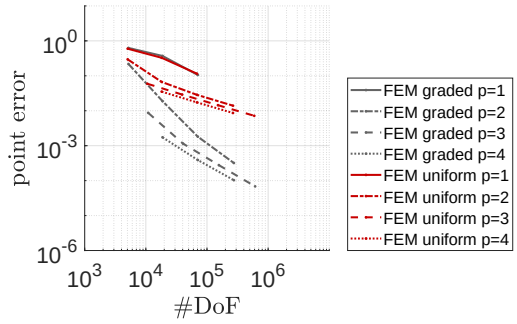

(a) Point error for quasi-uniform FEM vs. graded FEM with S0-excitation

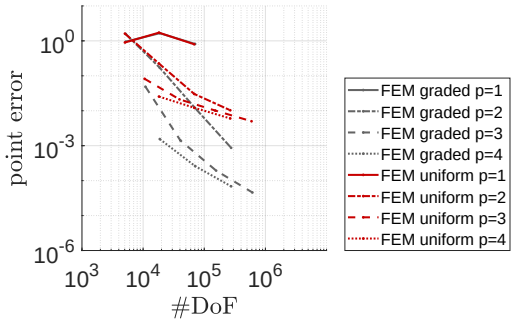

(b) Point error for quasi-uniform FEM vs. graded FEM with A0-excitation

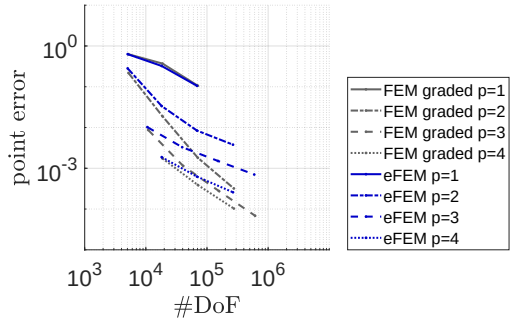

(c) Point error for eFEM vs. graded FEM with S0-excitation

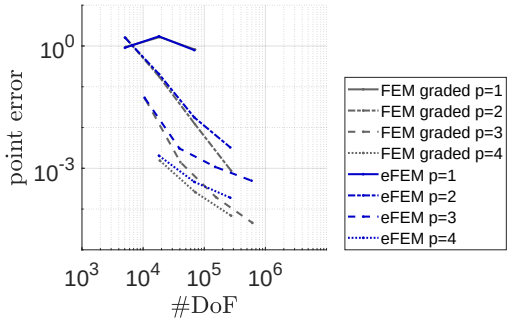

(d) Point error for eFEM vs. graded FEM with A0-excitation

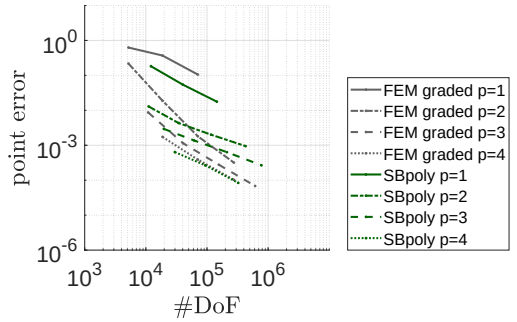

(e) Point error for SBpoly vs. graded FEM with S0-excitation

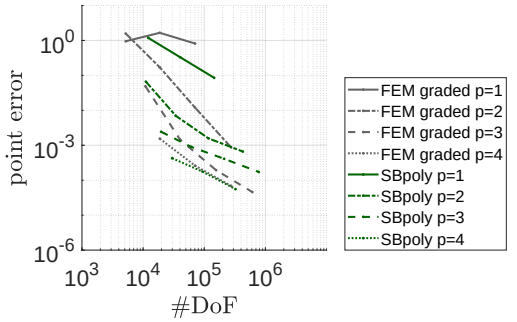

(f) Point error for SBpoly vs. graded FEM with A0-excitation

Figure 4.20: Point error for the linear waveguide

To excite the two different guided wave modes, two spatial tractions $\boldsymbol{\tau}_{\mathbf{x}}$ can be applied:

$$\text{for S0:} \quad \boldsymbol{\tau}_{\mathbf{x}}(\mathbf{x}) = \mathbf{n}\tau_0 \qquad \text{for A0:} \quad \boldsymbol{\tau}_{\mathbf{x}}(\mathbf{x}) = \mathbf{e}_2\tau_0 \qquad \mathbf{x} \in \Gamma_{\boldsymbol{\tau}}, \tag{4.55}$$

where $\mathbf{n}$ is the outer normal vector, $\mathbf{e}_2$ is the second unit vector, and $\Gamma_{\boldsymbol{\tau}}$ are the boundary parts between 0 mm and 2.5 mm as indicated in Figure 4.17. The pressure τ_0 is a positive constant depending on the transducer. In this thesis, we consider only problems, which are scalable by positive constants. Therefore, the value can be chosen arbitrarily to obtain numerical stability. Except for the boundaries $\Gamma_{\boldsymbol{u}}$ and $\Gamma_{\boldsymbol{\tau}}$, the model is traction-free.

We present four different approaches to simulate the problem:

1. FEM with a quasi-uniform,
2. FEM with a graded mesh,
3. the enrichment approach with a quasi-uniform mesh,
4. SB shape functions with a polygonal mesh.

The differences are illustrated in Figure 4.19, where a close-up of the crack is depicted. The construction of the graded mesh usually takes more time from the part of the researcher because it needs more requirements, and it is advisable to check the construction visually. The other meshes are created automatically, without much effort for the researcher.

The simulations are evaluated at the points P_1 and P_2 (Figure 4.17). The point error of both points with respect to a reference solution is shown in Figure 4.20. The reference solution is computed with the graded FEM mesh because it is a well-established method to solve problems with a singularity. Figure 4.21 shows the signals at point P_1 of the in-plane movement for both excitations. It can be observed that the S0-mode is faster than the A0-mode.

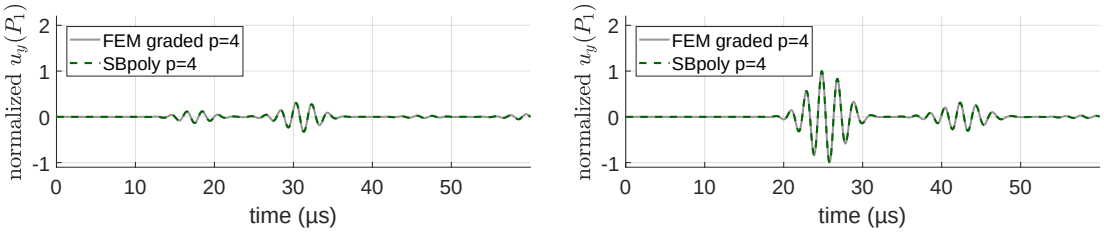

(a) Signal $\boldsymbol{u}_y(P_1)$ for S0-excitation

(b) Signal $\boldsymbol{u}_y(P_1)$ for A0-excitation

Figure 4.21: Signal at point P_1 for the linear waveguide (Figure 4.17)

It is worth mentioning that we only analyze the numerical performance. There are excellent works on the interaction of guided ultrasonic waves with linear cracks. Examples from the SBFEM community are: For instance, Gravenkamp *et al.* [63] present a linear crack model with the continued-fraction-based SBFEM. The same author proposed a highly efficient linear approach for the simulation of waveguides in the frequency domain [61]. Reflection-coefficients are evaluated in [26] and an inverse approach is presented in [25] and [19]. Except for the first one, these approaches consider the waveguide in the frequency domain.

4.9 Conclusion to Dynamic Problems with Singularities

For singularities in dynamics, we observe similar effects as for static problems. This is even more prevalent in the lower frequency range. In general, the influence of the singularity on the error is frequency-dependent, where the singularity dominates in the lower frequency range. This is, for example, visible in Figure 4.15. However, the inefficiency of the FEM on a quasi-uniform mesh (Figures 4.15 and 4.20) illustrates that the point singularity has to be handled in dynamic analysis.

The enrichment and the SB shape functions mainly influence the initial error. This makes p-refinement especially attractive. The error under h-refinement does not improve in the same way. The reason is likely similar to the static case: the area, enriched or approximated with the SB shape functions, is not constant under h-refinement but shrinks with the refinement. On the other hand, the enrichment seems sufficient to reach an error under 1%, an essential threshold for applications.

For applications, however, a graded FEM mesh is attractive due to its simplicity and good performance. It is not optimal, as clearly visible for the L-shaped domain. On the other hand, considering the number of degrees of freedom for the waveguide model, a small number of extra degrees will likely not be decisive whether the model is computable or requires too much memory. It is worth mentioning that a graded polygonal mesh in combination with the SB shape functions is an alternative. However, the grading process increases the meshing burden.

For the polygonal mesh, SIFs could be evaluated during the time analysis (see Section 3.9.2). A crack growth algorithm would lead to a combination of ultrasonic inspection and mechanical fracture analysis [31]. This could deliver more realistic crack models. The evaluation of SIFs is also possible for the enrichment approach without additional effort for the simulation.

4.10 Dynamic Problems with Continuity Conditions

The following section reviews the different approaches to incorporate continuity conditions with two boundaries. The different methods were initially researched to directly incorporate the formulation into the SBFEM, but only the direct elimination led to a solvable system. For simplicity, the notation is limited to two boundaries $\Gamma_{(a)}, \Gamma_{(b)}$, but all methods can be applied to problems with multiple boundaries. The focus is on methods that follow the mortar concept. The Mortar Method [85], also known as Master/Slave [163] concept, declares one of the boundaries as the main boundary and the other as a secondary boundary. The main boundary is called the non-mortar or master side, while the secondary boundary is called the mortar or slave side. We will continue with the word pair non-mortar/mortar. Without loss of generality, $\Gamma_{(a)}$ is the non-mortar boundary, and $\Gamma_{(b)}$ is the mortar boundary. In general, all quantities are evaluated on the non-mortar boundary. All non-mortar points are paired with a point on the mortar boundary via the closest point projection $\mathcal{P}(\mathbf{x})\colon \Gamma_{(a)} \to \Gamma_{(b)}$. Figure 4.22 shows the projection. Note that the line between a non-mortar point and its mortar projection point is orthogonal to the mortar boundary.

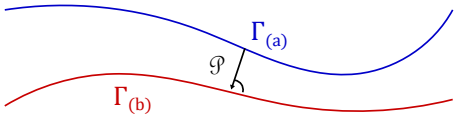

Figure 4.22: Mortar concept

With the definition of the closest point projection $\mathcal{P}$, the following two continuity conditions can be introduced:

the perfect bond

$$\boldsymbol{u}(\mathbf{x}) - \boldsymbol{u}\big(\mathcal{P}(\mathbf{x})\big) = \mathbf{0} \qquad \mathbf{x} \in \Gamma_{(a)}, \tag{4.56}$$

and the vanishing normal gap

$$\Big(\boldsymbol{u}(\mathbf{x}) - \boldsymbol{u}\big(\mathcal{P}(\mathbf{x})\big)\Big)\mathbf{n} = 0 \qquad \mathbf{x} \in \Gamma_{(a)}, \tag{4.57}$$

where $\mathbf{n}$ is the outer normal vector of the non-mortar boundary $\Gamma_{(a)}$.

Remark 4.10.1. *The Mortar Method is mainly criticised for its unsymmetrical formulation because one boundary is chosen as the main boundary. Other formulations consider both boundaries equal [118]. A simple symmetrical formulation would, for example, introduce a third boundary in the middle, and both outer boundaries have to project on the middle boundary [101].*
Another critical aspect is that the closest point projection is not always unique. There can be several points with the same distance for a concave mortar boundary.

In this thesis, however, we only consider boundaries that have no initial gap, i.e., $\|\mathbf{x} - \mathcal{P}(\mathbf{x})\| = 0$, so that the mentioned critical aspects are neglectable.

4.11 Methods for Continuity Conditions

Many methods enforce continuity conditions over two boundaries. This section focuses on methods that are general enough so that both boundaries can be discretized differently. Strictly speaking,

the standard assembly process can be seen as enforcement of continuity conditions over element boundaries, where the element boundaries have to coincide.

A complete list of available methods would go beyond the scope of this thesis, so only a few representatives of the largest classes are described. In the following section, the methods are designed to implement the constraints given in Equation (4.56) and Equation (4.57).

Other constraints, like DIRICHLET boundary conditions, are usually implemented by eliminating degrees of freedom. The methods presented in the following can also be used to implement DIRICHLET boundary conditions, but this is not the focus of the section.

4.11.1 LAGRANGE Multiplier Method (LMM)

The basic idea of the LAGRANGE Multiplier Method (LMM) is to enforce the constraints (Equation (4.56) and Equation (4.57)) weakly. Therefor, an auxiliary function, the LAGRANGE multiplier, is utilized. From a physical point of view, the LAGRANGE multipliers are new variables for the tractions of the system.

For simplicity, assuming $\mathcal{P}$ is bijective, the boundary conditions for the LMM are:

For perfect bonding (Equation (4.56))

$$\underline{\underline{\boldsymbol{\sigma}}}(\boldsymbol{u})\mathbf{n} = \underline{\underline{\boldsymbol{\sigma}}}\big(\boldsymbol{u}(\mathcal{P})\big)\mathbf{n} \qquad \underline{\underline{\boldsymbol{\sigma}}}(\boldsymbol{u})\mathbf{n} = \boldsymbol{\lambda} \qquad \big(\boldsymbol{u} - \boldsymbol{u}(\mathcal{P})\big) = \mathbf{0} \qquad \mathbf{x} \in \Gamma_{(a)}, \tag{4.58}$$

and for a vanishing normal gap (Equation (4.57))

$$\underline{\underline{\boldsymbol{\sigma}}}(\boldsymbol{u})\mathbf{n} = \underline{\underline{\boldsymbol{\sigma}}}\big(\boldsymbol{u}(\mathcal{P})\big)\mathbf{n} \qquad \underline{\underline{\boldsymbol{\sigma}}}(\boldsymbol{u})\mathbf{n} = \mathbf{n}\lambda \qquad \mathbf{n}\big(\boldsymbol{u} - \boldsymbol{u}(\mathcal{P})\big) = 0 \qquad \mathbf{x} \in \Gamma_{(a)}. \tag{4.59}$$

This leads to the integrals, which have to be added to the weak form, e.g., Equation (2.10),

$$\ldots + \int \big(\boldsymbol{\delta u} - \boldsymbol{\delta u}(\mathcal{P})\big) \cdot \boldsymbol{\lambda} \, \mathrm{d}\Gamma_{(a)} + \int \big(\boldsymbol{u} - \boldsymbol{u}(\mathcal{P})\big) \cdot \boldsymbol{\delta\lambda} \, \mathrm{d}\Gamma_{(a)}, \tag{4.60}$$

$$\ldots + \int \big(\boldsymbol{\delta u} - \boldsymbol{\delta u}(\mathcal{P})\big) \cdot \mathbf{n}\lambda \, \mathrm{d}\Gamma_{(a)} + \int \big(\boldsymbol{u} - \boldsymbol{u}(\mathcal{P})\big) \cdot \mathbf{n}\delta\lambda \, \mathrm{d}\Gamma_{(a)}, \tag{4.61}$$

for perfect bonding and vanishing normal gap, respectively. Again, $\boldsymbol{\delta u}$ is the virtual displacement.

We define a new matrix

$$\mathbf{L} = \int \big(\boldsymbol{N}^{\mathbf{u}} - \boldsymbol{N}^{\mathbf{u}}(\mathcal{P})\big) \cdot \boldsymbol{N}^{\lambda} \, \mathrm{d}\Gamma_{(a)}, \tag{4.62}$$

$$\mathbf{L} = \int \Big(\big(\boldsymbol{N}^{\mathbf{u}} - \boldsymbol{N}^{\mathbf{u}}(\mathcal{P})\big) \cdot \mathbf{n}\Big) \cdot \boldsymbol{N}^{\lambda} \, \mathrm{d}\Gamma_{(a)}, \tag{4.63}$$

where $\boldsymbol{N}^{\mathbf{u}}$ is the matrix of shape functions of the displacement and $\boldsymbol{N}^{\lambda}$ the matrix of shape functions of the LAGRANGE multiplier either vector-valued for perfect bonding or scalar for a vanishing normal gap. Note that the LAGRANGE multipliers 'live' on the non-mortar boundary and one-dimensional shape functions are utilized.

The final matrix system is: Find $\mathbf{u} \in \mathbb{R}^N, \boldsymbol{\lambda} \in \mathbb{R}^M$ such that

$$\begin{pmatrix} \mathbf{S} & \mathbf{L} \\ \mathbf{L}^{\mathsf{T}} & \mathbf{0} \end{pmatrix} \begin{pmatrix} \mathbf{u} \\ \boldsymbol{\lambda} \end{pmatrix} = \begin{pmatrix} \mathbf{f} \\ \mathbf{0} \end{pmatrix}, \tag{4.64}$$

where $\mathbf{S}$ is the static or dynamic stiffness matrix, depending on the problem.

Remark 4.11.1 (Saddle Point Problem)**.** *The structure of the final linear system of equations is known as a saddle point problem. As for all saddle point problems, the basis of two variables must satisfy the LBB-condition [122]*[⋆2]*. There are zero entries on the diagonal of the final linear system of equations. The matrix of the saddle point problem is not positive definite, which affects the choice of available solvers for the linear system of equations.*

[⋆2] The LADYZHENSKAYA–BABUŠKA–BREZZI condition is also known as inf-sup-condition.

Alternatively to solving the saddle point problem directly, a different approach can be taken as specified in the following remark.

Remark 4.11.2 (Parallelization)**.** *Start with Equation* (4.64)*, multiply the first line by* $\mathbf{L}^\mathsf{T}\mathbf{S}^{-1}$ *and subtract the second line to get*

$$\mathbf{C}\boldsymbol{\lambda} = \mathbf{L}^\mathsf{T}\mathbf{S}^{-1}\mathbf{f} \tag{4.65}$$

with the Schur *complement* $\mathbf{C} = \left(\mathbf{L}^\mathsf{T}\mathbf{S}^{-1}\mathbf{L}\right)$ *[185]. For a known nodal* Lagrange *multiplier* $\boldsymbol{\lambda}$*, the nodal displacement* $\mathbf{u}$ *is computed by*

$$\mathbf{S}\mathbf{u} = \mathbf{f} - \mathbf{L}\boldsymbol{\lambda}. \tag{4.66}$$

If the domain is split into two sub-domains $\Omega_{(a)}$ *and* $\Omega_{(b)}$ *by the boundary* $\Gamma_{(a)}$*, Equation* (4.64) *has the following form*

$$\begin{pmatrix} \mathbf{S}_{(a)(a)} & \mathbf{0} & \mathbf{L}_{(a)} \\ \mathbf{0} & \mathbf{S}_{(b)(b)} & \mathbf{L}_{(b)} \\ \mathbf{L}_{(a)}^\mathsf{T} & \mathbf{L}_{(b)}^\mathsf{T} & \mathbf{0} \end{pmatrix} \begin{pmatrix} \mathbf{u}_{(a)} \\ \mathbf{u}_{(b)} \\ \boldsymbol{\lambda} \end{pmatrix} = \begin{pmatrix} \mathbf{f}_{(a)} \\ \mathbf{f}_{(b)} \\ \mathbf{0} \end{pmatrix}, \tag{4.67}$$

where $\mathbf{S}_{(a)(a)}$ *and* $\mathbf{S}_{(b)(b)}$ *are either the static or dynamic stiffness matrix of the sub-domain* $\Omega_{(a)}$ *and* $\Omega_{(b)}$*, respectively. For a known nodal* Lagrange *multiplier* $\boldsymbol{\lambda}$*, Equation* (4.66) *can be solved separately and parallel, i.e.,*

$$\mathbf{S}_{(a)(a)}\mathbf{u}_{(a)} = \mathbf{f}_{(a)} - \mathbf{L}_{(a)}\boldsymbol{\lambda}, \tag{4.68}$$

$$\mathbf{S}_{(b)(b)}\mathbf{u}_{(b)} = \mathbf{f}_{(b)} - \mathbf{L}_{(b)}\boldsymbol{\lambda}. \tag{4.69}$$

Remark 4.11.3 (Uzawa Algorithm)**.** *The* Uzawa *iteration is an algorithm for solving saddle point problems that bypass the solver issues of Remark 4.11.1. The* Uzawa *algorithm alternatively solves the linear system of equations for both types of variables similar to the steps in Remark 4.11.2, but in an approximated and iterative manner [154, 185]. The main reason is that the matrix* $\mathbf{C}$ *is requires a high computational effort. The classic* Uzawa *algorithm replaces* $\mathbf{C}$ *with a diagonal matrix. [154, 185].*

Optimal convergence can be obtained as the following remark summarizes.

Remark 4.11.4 (Optimal Convergence)**.** *The LMM obtains the optimal convergence properties when choosing a suitable basis for the* Lagrange *multipliers [122, 158]. In particular, for continuous* Lagrange *multipliers, the shape functions must have the same degree as the shape functions of the displacements. Depending on the boundary conditions, the* Lagrange *multipliers may require local modifications [122].*

4.11.2 Direct Elimination Method (DEM)

As an alternative to the LMM, the constraints (Equation (4.56) and Equation (4.57)) can be included in the shape functions [44]. This process can be called Direct Constraint Elimination [163], Weak Substitution Method [44], or Mortar Tying [101].

The elimination process leads to a smaller linear system of equations for a modified displacement vector $\tilde{\mathbf{u}}$. The displacement vector $\tilde{\mathbf{u}}$ is a linear combination of the entries of the original displacement vector $\mathbf{u}$. We define a transformation matrix $\mathbf{H} \in \mathbb{R}^{\tilde{N}\times N}$ with $\tilde{N} \leq N$, where N and $\tilde{N}$ are the numbers of degrees of freedom of the original displacement $\mathbf{u}$ and the new displacement $\tilde{\mathbf{u}}$, respectively. The elimination process can formally be written as

$$\mathbf{H}\tilde{\mathbf{u}} = \mathbf{u} \qquad\qquad \mathbf{H}\boldsymbol{\delta}\tilde{\mathbf{u}} = \boldsymbol{\delta}\mathbf{u} \tag{4.70}$$

and leads to

$$\tilde{\mathbf{S}}\tilde{\mathbf{u}} = \tilde{\mathbf{f}} \tag{4.71}$$

with $\tilde{\mathbf{S}} = \mathbf{H}^\mathsf{T}\mathbf{S}\mathbf{H}$ and $\tilde{\mathbf{f}} = \mathbf{H}^\mathsf{T}\mathbf{f}$.

To calculate the transformation matrix, divide the new displacement vector $\tilde{\mathbf{u}}$ into two sets. The first vector $\tilde{\mathbf{u}}_\Omega$ contains the degrees of freedom that do not belong to the interface, and the second vector $\tilde{\mathbf{u}}_{\Gamma_c}$ contains the degrees of freedom belonging to the interface. On the other hand, divide the old displacement vector $\mathbf{u}$ into three sets. The first vector $\mathbf{u}_\Omega$ contains the degrees of freedom that do not belong to the interface, and the second vector $\mathbf{u}_{(a)}$ contains the degrees of freedom belonging to the non-mortar boundary, while the third vector $\mathbf{u}_{(b)}$ contains the degrees of freedom belonging to the mortar boundary. Equation (4.70) is structured as

$$\begin{pmatrix} \mathbf{I} & \mathbf{0} \\ \mathbf{0} & \mathbf{H}_{(a)} \\ \mathbf{0} & \mathbf{H}_{(b)} \end{pmatrix} \begin{pmatrix} \tilde{\mathbf{u}}_\Omega \\ \tilde{\mathbf{u}}_{\Gamma_c} \end{pmatrix} = \begin{pmatrix} \mathbf{u}_\Omega \\ \mathbf{u}_{(a)} \\ \mathbf{u}_{(b)} \end{pmatrix}. \tag{4.72}$$

For $\tilde{\mathbf{u}}_{\Gamma_c}$, the condition for weak continuity reads as

$$\mathbf{0} = \begin{pmatrix} \mathbf{L}_{(a)}^\mathsf{T} & \mathbf{L}_{(b)}^\mathsf{T} \end{pmatrix} \begin{pmatrix} \mathbf{H}_{(a)} \\ \mathbf{H}_{(b)} \end{pmatrix} \tilde{\mathbf{u}}_{\Gamma_c}. \tag{4.73}$$

There are several variants the choice of $\tilde{\mathbf{u}}_{\Gamma_c}$. We choose $\tilde{\mathbf{u}}_{\Gamma_c}$ of the same size as $\mathbf{u}_{(b)}$ and use the following definitions

$$\mathbf{H}_{(a)} = -\mathbf{L}_{(a)}^{-\mathsf{T}}\mathbf{L}_{(b)}^\mathsf{T}, \tag{4.74}$$

$$\mathbf{H}_{(b)} = \mathbf{I}. \tag{4.75}$$

The matrix $\mathbf{H}_{(a)}$ defines how the shape functions of the mortar boundary continue on the non-mortar boundary. Note that the matrix $\mathbf{L}_{(a)}$ by definition is a square matrix with full rank because the LAGRANGE multipliers are defined on the non-mortar side.

Remark 4.11.5 (Dense Matrix)**.** *In general, the matrix $\mathbf{H}_{(a)}$ is dense. There are alternative methods that lead to sparse matrices [43].*

Figure 4.23 shows an examples of the Direct Elimination Method. A single shape function is plotted in each figure, and the shape is colored depending on the non-mortar or mortar side. The shape is similar but not equal on both sides. It is worth mentioning that Direct Constraint Elimination can be equivalent to the standard assembly process for the total domain Ω if the discretizations on the interfaces match.

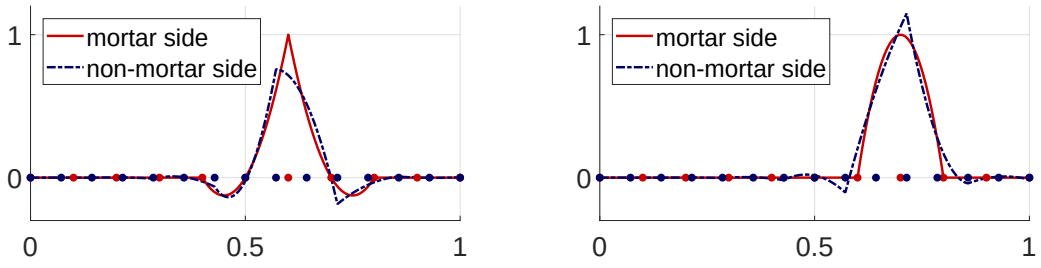

(a) Shape function for element transition

(b) Shape function for the middle node

Figure 4.23: Example of two continued shape functions of p = 2

4.11.3 Penalty Method (PM)

The Penalty Method simply adds a very stiff spring boundary condition to the interface.

Choose a penalty function ϵ, which acts as the spring function. Then, the following integrals can be added to the weak form, e.g., Equation (2.10),

$$\ldots + \int \epsilon\big(\boldsymbol{\delta u} - \boldsymbol{\delta u}(\mathcal{P})\big) \cdot \big(\boldsymbol{u} - \boldsymbol{u}(\mathcal{P})\big)\, \mathrm{d}\Gamma_{(a)}, \tag{4.76}$$

$$\ldots + \int \epsilon\Big(\big(\boldsymbol{\delta u} - \boldsymbol{\delta u}(\mathcal{P})\big) \cdot \mathbf{n}\Big)\Big(\mathbf{n} \cdot \big(\boldsymbol{u} - \boldsymbol{u}(\mathcal{P})\big)\Big)\, \mathrm{d}\Gamma_{(a)} \tag{4.77}$$

for perfect bonding and vanishing normal gap, respectively.

We obtain the penalty matrix

$$\mathbf{P} = \int \epsilon\big(\boldsymbol{N}^{\mathbf{u}} - \boldsymbol{N}^{\mathbf{u}}(\mathcal{P})\big) \cdot \big(\boldsymbol{N}^{\mathbf{u}} - \boldsymbol{N}^{\mathbf{u}}(\mathcal{P})\big)\, \mathrm{d}\Gamma_{(a)}, \tag{4.78}$$

$$\mathbf{P} = \int \epsilon\Big(\big(\boldsymbol{N}^{\mathbf{u}} - \boldsymbol{N}^{\mathbf{u}}(\mathcal{P})\big) \cdot \mathbf{n}\Big)\Big(\mathbf{n} \cdot \big(\boldsymbol{N}^{\mathbf{u}} - \boldsymbol{N}^{\mathbf{u}}(\mathcal{P})\big)\, \mathrm{d}\Gamma_{(a)} \tag{4.79}$$

$$= \int \epsilon\big(\boldsymbol{N}^{\mathbf{u}} - \boldsymbol{N}^{\mathbf{u}}(\mathcal{P})\big)(\mathbf{n} \otimes \mathbf{n})\big(\boldsymbol{N}^{\mathbf{u}} - \boldsymbol{N}^{\mathbf{u}}(\mathcal{P})\big)\, \mathrm{d}\Gamma_{(a)}, \tag{4.80}$$

where $\boldsymbol{N}^{\mathbf{u}}$ is the shape function matrix of the displacement. The final linear system of equations is

$$(\mathbf{S} + \mathbf{P})\, \mathbf{u} = \mathbf{f}. \tag{4.81}$$

The Penalty Method is not accurate but punishes violations of the constraint. Usually, the penalty function is chosen as a constant function , i.e., $\epsilon(\mathbf{x}) = \epsilon_0$. The value ϵ_0 is called penalty parameter. Two advantages of this method are the relative ease of implementation and no additional variables need to be introduced. One drawback is that the right choice of the penalty parameter requires some expertise.

Remark 4.11.6 (Balance of the Penalty Parameter)**.** *On the one hand, the higher the penalty parameter ϵ, the more accurate the results. On the other hand, a penalty parameter ϵ, which is too high, leads to numerical instability [172]. Additionally, the penalty parameter depends on the element size* h *and the polynomial degree* p*. At least for the* Poisson *equation, to obtain optimal convergence, the penalty parameter can be chosen as $\epsilon_0 = \mathcal{C} \cdot \mathrm{h}^{-(p+1)}$ with a sufficiently large constant $\mathcal{C} > 0$ that is independent of the element size* h *and the polynomial degree* p *[6]. Unlike the* Lagrange *Multiplier Method, the Penalty Method leads to more desirable matrix properties. The matrix is positive-definite. For dynamic problems, this allows the use of a* Cholesky *decomposition (Appendix A.2) to solve the final system.*

The Penalty Method can be formally derived from the Lagrange Multiplier Method 4.11.1 by selecting the Lagrange multiplier proportional to the jumps, i.e.,

$$\boldsymbol{\lambda} = \frac{\epsilon}{2}\big(\boldsymbol{u} - \boldsymbol{u}(\mathcal{P})\big) \qquad \boldsymbol{\delta\lambda} = \frac{\epsilon}{2}\big(\boldsymbol{\delta u} - \boldsymbol{\delta u}(\mathcal{P})\big) \tag{4.82}$$

$$\lambda = \frac{\epsilon}{2}\mathbf{n} \cdot \big(\boldsymbol{u} - \boldsymbol{u}(\mathcal{P})\big) \qquad \delta\lambda = \frac{\epsilon}{2}\mathbf{n} \cdot \big(\boldsymbol{\delta u} - \boldsymbol{\delta u}(\mathcal{P})\big), \tag{4.83}$$

for Equation (4.56) and Equation (4.57), respectively.

4.11.4 Nitsche Method

The Nitsche Method is closely linked to the Discontinuous Galerkin Method [5]. Historically, however, the Nitsche Method was created first. The method was introduced to treat Dirichlet boundary conditions without changing the ansatz space [96]. We limit the discussion to the case of perfect bonding. Here, the two domains are linked by the mean flux $\bar{\boldsymbol{\tau}}$. The mean flux and its variation are defined as

$$\bar{\boldsymbol{\tau}} = \frac{1}{2}(\underline{\underline{\boldsymbol{\sigma}}}^{(a)}\mathbf{n}_{(a)} + \underline{\underline{\boldsymbol{\sigma}}}^{(b)}\mathbf{n}_{(b)}) \qquad \boldsymbol{\delta\bar{\tau}} = \frac{1}{2}(\boldsymbol{\delta}\underline{\underline{\boldsymbol{\sigma}}}^{(a)}\mathbf{n}_{(a)} + \boldsymbol{\delta}\underline{\underline{\boldsymbol{\sigma}}}^{(b)}\mathbf{n}_{(b)}) \tag{4.84}$$

with the traction vector $\underline{\underline{\boldsymbol{\sigma}}}^{(\cdot)}\mathbf{n}_{(\cdot)}$, which is the traction of each boundary. The stress tensor $\underline{\underline{\boldsymbol{\sigma}}}^{(\cdot)}$ is taken from the domain next to the boundary. In addition, a penalty term is needed for stability [5, 96].

The integrals which can be added to the weak form, e.g., Equation (2.10), are

$$\ldots + \int \big(\boldsymbol{\delta u} - \boldsymbol{\delta u}(\mathcal{P})\big) \cdot \bar{\boldsymbol{\tau}}\, \mathrm{d}\Gamma_{(a)} + \int \big(\boldsymbol{\delta u} - \boldsymbol{\delta u}(\mathcal{P})\big) \cdot \boldsymbol{\delta\bar{\tau}}\, \mathrm{d}\Gamma_{(a)} \tag{4.85}$$

$$+ \int \epsilon\big(\boldsymbol{\delta u} - \boldsymbol{\delta u}(\mathcal{P})\big) \cdot \big(\boldsymbol{u} - \boldsymbol{u}(\mathcal{P})\big)\, \mathrm{d}\Gamma_{(a)}. \tag{4.86}$$

The final linear system of equations is

$$\left(\mathbf{S} + \mathbf{N} + \mathbf{N}^{\mathsf{T}} + \mathbf{P}\right) \mathbf{u} = \mathbf{f}, \tag{4.87}$$

where the matrix $\mathbf{N}$ is associated to Equation (4.86) and $\mathbf{P}$ is the penalty matrix (Equation (4.80)).

The NITSCHE Method is an attractive method as it considers essential boundary conditions in a weak way without using LAGRANGE multipliers. This method is not the only method that uses a numerical flux as a coupling condition. Nevertheless, we limit ourselves here only to the NITSCHE Method and refer to the literature for other methods [5]. In principle, any numerical flux used in the Discontinuous GALERKIN Methods can also be used as a coupling condition. The material parameters on both sides influence the right choice of the numerical flux. The final stiffness matrix is positive-definite [10]. The main difference is the number of off-diagonal terms. Note that the traction of all shape functions in the elements adjacent to the interface is non-zero. This leads to coupling terms for all shape functions in these elements - not only the boundary functions. The mean flux must be adjusted if both boundaries have different material parameters. In the original work [96] for DIRICHLET boundary conditions, NITSCHE showed that the method is stable for $\mathrm{p} = 1$ if one uses the stabilization $\epsilon = \mathcal{C}\mathrm{h}^{-1}$ with a sufficiently large constant $\mathcal{C}$ that is independent of the element size h. Similar to the Penalty Method, the NITSCHE Method can formally be derived from the LAGRANGE Multiplier Method 4.11.1 by choosing [10]

$$\boldsymbol{\lambda} = \bar{\boldsymbol{\tau}} + \frac{\epsilon}{2}\big(\boldsymbol{u} - \boldsymbol{u}(\mathcal{P})\big) \qquad\qquad \boldsymbol{\delta\lambda} = \boldsymbol{\delta\bar{\tau}} + \frac{\epsilon}{2}\big(\boldsymbol{\delta u} - \boldsymbol{\delta u}(\mathcal{P})\big). \tag{4.88}$$

4.11.5 Other Methods

In this part, some other methods are described. The focus is on the advantages and disadvantages, while the underlying mathematics recede into the background.

The Augmented LAGRANGE Method is a mixture of the LAGRANGE Multiplier Method 4.11.1 and the Penalty Method 4.11.3 [163]. The final linear system of equations is given by

$$\begin{pmatrix} \mathbf{S} + \mathbf{P} & \mathbf{L} \\ \mathbf{L}^{\mathsf{T}} & \mathbf{0} \end{pmatrix} \begin{pmatrix} \mathbf{u} \\ \boldsymbol{\lambda} \end{pmatrix} = \begin{pmatrix} \mathbf{f} \\ \mathbf{0} \end{pmatrix}. \tag{4.89}$$

For the Augmented LAGRANGE Method, Remark 4.11.1 has to be considered. The Augmented LAGRANGE Method is often combined with an algorithm which is similar to the UZAWA Algorithm (Remark 4.11.3) [154], which makes it possible to calculate the linear system of equations only for the displacements, while an update step calculates the LAGRANGE multipliers. This update step is based on Equation (4.82) or Equation (4.83).

At first, the SCHWARZ Method considered overlapping sub-domains. An iterative process is used, whereby the different sub-domains are solved individually [81]. Later, the method was applied to the case of non-overlapping subdomains [81].

The Perturbed LAGRANGE Multiplier Method is another mixture of the Penalty Method 4.11.3 and the LAGRANGE Multiplier Method 4.11.1 [163]. For this method, there is no block with diagonal entries that are zero. This avoids some of the negative features of the LAGRANGE Multiplier Method that are summarized in Remark 4.11.1. This method is - similar to the Penalty Method - only for the limit $\epsilon \to \infty$ exact.

4.12 Aspects of Discrete Boundaries

So far, the Mortar Method is presented for general boundaries. When dealing with a finite element approximation of the boundaries, some aspects have to be considered. Figure 4.24a shows that, in general, the quadrature points of one non-mortar element can project onto more than one mortar element. However, if a quadrature point is on a node, the closest point projection can miss its counterpart due to numerical errors. So it can be advantageous to extend the elements slightly. We will call elements with at least one common quadrature point a contact element pair.

If the elements are straight, the closest point projection is geometrically computable. An additional iterative NEWTON-RAPHSON-Method has to be used if the elements are curved. The

iterative process can leave an element and may have to be continued on another element. Some methods use an additional smooth curve related to the boundaries to deal with these issues [101].

Remark 4.12.1 (Normal Contact Pairs)**.** *The contact element pairs for FEM and the discretized boundary of the polygons are the same because the shape functions coincide on the boundary. Particular elements must be constructed for the crack tip if an enrichment occurs.*

It is worth mentioning that, if the elements are aligned and a GAUSS-LOBATTO-quadrature is chosen, the Mortar Method simplifies to a node-to-node contact element pair [163]. This is depicted in Figure 4.24b.

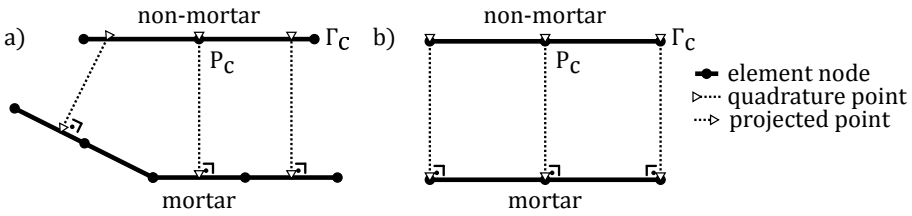

Figure 4.24: Discrete mortar elements

4.13 Numerical Experiments with Continuity Conditions

For continuity conditions, three examples are considered. The first demonstrates the necessary quadrature and the differences between the LAGRANGE Multiplier Method and the Penalty Method. The second example shows the combination of the LAGRANGE Multiplier Method and the SB shape functions on polygonal meshes. The third example presents a crack with a vanishing normal gap to clarify the implementation details at the crack tip.

4.13.1 Patch Test for LMM, DEM, and PM

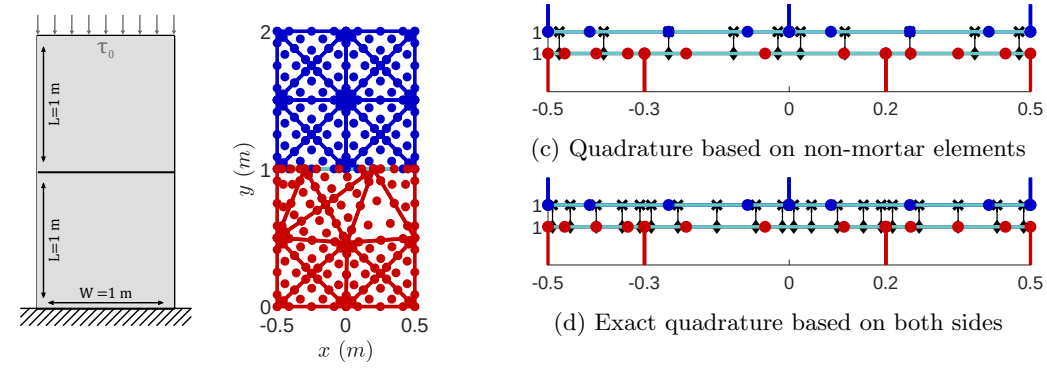

(a) Overview of the patch test

(b) Divided mesh

(c) Quadrature based on non-mortar elements

(d) Exact quadrature based on both sides

Figure 4.25: Static patch tests with FEM in combination with the Mortar Method

As a first example, we consider a static patch test (see Figure 4.25a) to clarify the required quadrature and compare the LAGRANGE Multiplier Method (LMM - Section 4.11.1), the Direct Elimination Method (DEM - Section 4.11.2) and the Penalty Method (PM - Section 4.11.3). This test is performed with finite elements as the standard contact element pairs are independent of the approximation inside a crackless domain (Remark 4.12.1). The first sub-domain's measurements are $(-0.5\,\mathrm{m}, 0.5\,\mathrm{m}) \times (0\,\mathrm{m}, 1\,\mathrm{m})$, while the second sub-domain's measurements are $(-0.5\,\mathrm{m}, 0.5\,\mathrm{m}) \times$

$(1\,\mathrm{m}, 2\,\mathrm{m})$. A constant pressure of $\tau_0 = -1\,\mathrm{GPa}$ is applied to the top edge in y-direction. The bottom edge is fixed in y-direction, and the origin is fixed in both directions. An artificial material, which is given in Table A.1a, is selected for an easy calculation of the analytical solution. The error is measured by the relative deviation of the internal energy, i.e.,

$$\text{energy error} = \frac{|\mathcal{E}^{\mathrm{h}} - \mathcal{E}^{\mathrm{ref}}|}{|\mathcal{E}^{\mathrm{ref}}|}. \tag{4.90}$$

The reference energy is $1/3\,\mathrm{GJ}$. The patch test is performed with the LMM, DEM and PM. For the LMM, the shape functions of the displacement and the LAGRANGE multiplier have the same degree p.

Consider the LAGRANGE Multiplier Method first. This method should pass the patch test if the quadrature is accurate enough. Two different types of quadrature are tested. In Figure 4.25c a quadrature based only on the non-mortar elements is depicted. Both subdomains are plotted with a small gap to illustrate the procedure. The shape functions of the non-mortar side are evaluated at the quadrature points (black crosses), while the shape functions of the mortar side are evaluated at the closest point projection of the quadrature points (black diamonds). The nodes of the LAGRANGE multipliers coincide with the blue nodes on the interface. Additionally, an exact quadrature has been implemented, based on both mortar and non-mortar elements (see Figure 4.25d). The exact quadrature takes the endpoints of both sides into account.

Figure 4.26a shows results for the uniform p-refinement. The LAGRANGE Multiplier Method passes the patch test for each polynomial degree p only if the exact quadrature is used. From now on, the exact quadrature will be used for all other results unless otherwise stated. With the exact quadrature, the correct results are achieved for LMM and DEM under h-refinement (Figure 4.26b). Instead of an exact quadrature at low polynomial degrees, a quadrature with more points may also be used for the non-mortar elements [54].

The performance of the Penalty Method (Figure 4.26c) depends on the constant $\mathcal{C}$ given in Remark 4.11.6. In particular, a constant whose value is too high leads to numerical instabilities. Those can be observed in the example for $\mathcal{C} = 1 \times 10^4$ (Remark 4.11.6). Figure 4.26d shows the PM for h-refinement with a fixed constant $\mathcal{C} = 1$.

4.13.2 Domains with Internal Interfaces

As a second example, we want to test the LMM in combination with SB shape functions. The test is mainly performed to evaluate experimentally if the LBB-condition (Remark 4.11.1) is satisfied for this choice of shape functions. A rectangular domain is sub-divided as indicated with the colors in Figure 4.27a and Figure 4.28a.

The problem is: Find the displacement and LAGRANGE multiplier $(\boldsymbol{u}(\mathbf{x}), \boldsymbol{\lambda}(\mathbf{x}))$, such that

$$(\mathrm{i}\,\omega)^2 \rho \boldsymbol{u} = \boldsymbol{\nabla} \cdot \underline{\underline{\boldsymbol{\sigma}}}(\boldsymbol{u}) + \boldsymbol{f} \qquad \mathbf{x} \in \Omega \tag{4.91}$$

$$\underline{\underline{\boldsymbol{\sigma}}}(\boldsymbol{u})\mathbf{n} = \boldsymbol{\tau} \qquad \mathbf{x} \in \Gamma_{\boldsymbol{\tau}} \tag{4.92}$$

$$\underline{\underline{\boldsymbol{\sigma}}}(\boldsymbol{u})\mathbf{n} = \underline{\underline{\boldsymbol{\sigma}}}\big(\boldsymbol{u}(\mathcal{P})\big)\mathbf{n} \qquad \mathbf{x} \in \Gamma_{(a)} \tag{4.93}$$

$$\underline{\underline{\boldsymbol{\sigma}}}(\boldsymbol{u})\mathbf{n} = \boldsymbol{\lambda} \qquad \mathbf{x} \in \Gamma_{(a)} \tag{4.94}$$

$$\big(\boldsymbol{u} - \boldsymbol{u}(\mathcal{P})\big) = \mathbf{0} \qquad \mathbf{x} \in \Gamma_{(a)} \tag{4.95}$$

with $\omega = 2\pi\,\mathrm{s}^{-1}$. Here, $\Gamma_{\boldsymbol{\tau}}$ is the outer boundary of the rectangle, and $\Gamma_{(a)}$ are the inner boundaries indicated with black lines in Figure 4.27a and Figure 4.28a. Consider a traction $\boldsymbol{\tau} = \underline{\underline{\boldsymbol{\sigma}}}(\boldsymbol{u}^{\mathrm{ref}})\mathbf{n}$ and a body force $\boldsymbol{f} = -\boldsymbol{\nabla}\cdot\underline{\underline{\boldsymbol{\sigma}}}(\boldsymbol{u}^{\mathrm{ref}}) + (\mathrm{i}\,\omega)^2\rho\boldsymbol{u}^{\mathrm{ref}}$ such that the analytical solution $\boldsymbol{u}^{\mathrm{ref}}$ in Equation (4.36) is taken.

The convergence rates in Figure 4.27b and Figure 4.28b are in agreement with the theoretical convergence rates (Remark 4.6.1 and 4.11.1), hence indicating that the LBB-condition is fulfilled.

The division into three sub-domains contains a so-called cross-point [17, 158], where the three sub-domains meet. At this point, the LAGRANGE multipliers are approximated discontinuously, so this node has six LAGRANGE multiplier degrees of freedom.

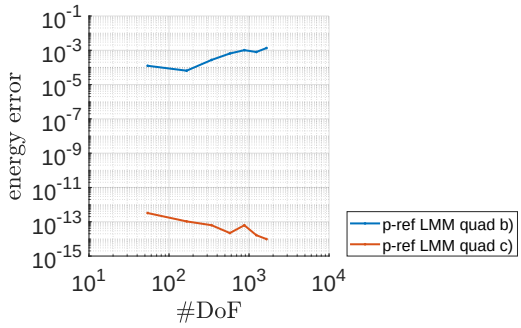

(a) Energy error for p-refinement

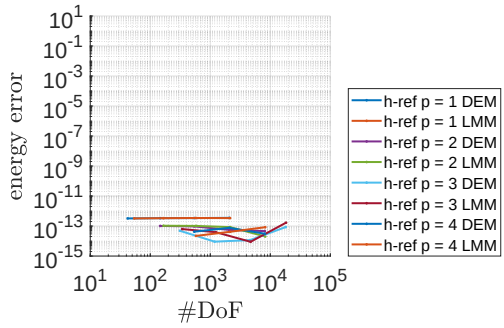

(b) Energy error for h-refinement with exact quadrature

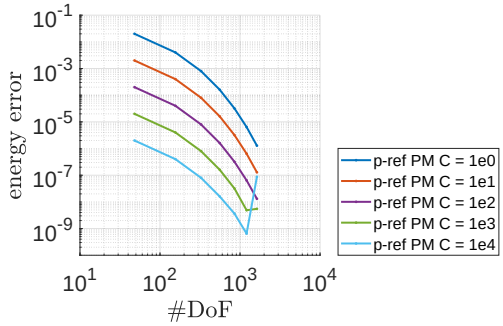

(c) Energy error for p-refinement

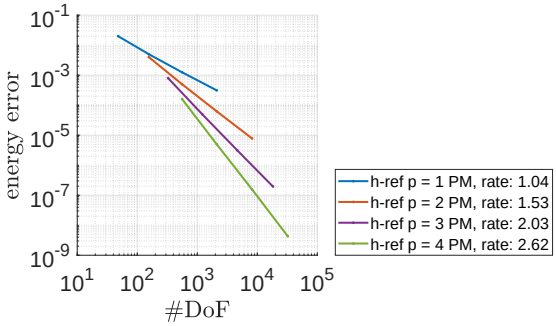

(d) Energy error for h-refinement with $\mathcal{C} = 1$

Figure 4.26: Energy errors for the patch test on a rectangular divided domain with LMM, DEM and PM

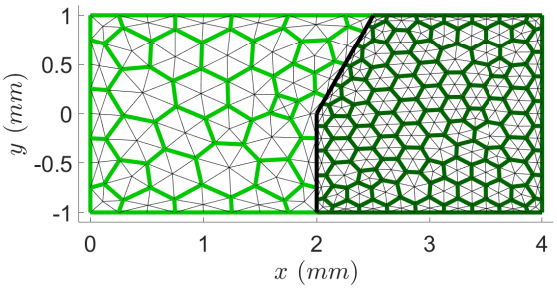

(a) SBFEM-mesh

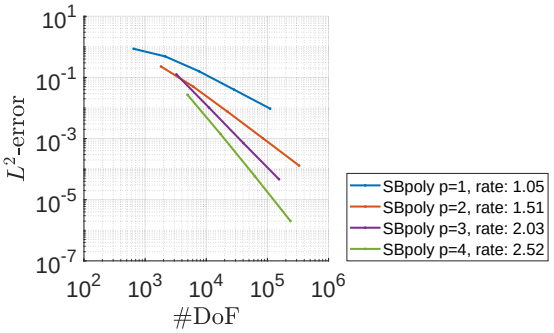

(b) L^2-error for h-refinement

Figure 4.27: Domain consisting of two sub-domains

4.13.3 Tests with Vanishing Normal Gap

The last example investigates all details around a crack tip with a vanishing normal gap. These details are rarely reported. The domain is a simple cracked square. Figures 4.29a, 4.29c and 4.29e show coarse versions of the meshes with the crack highlighted in red.

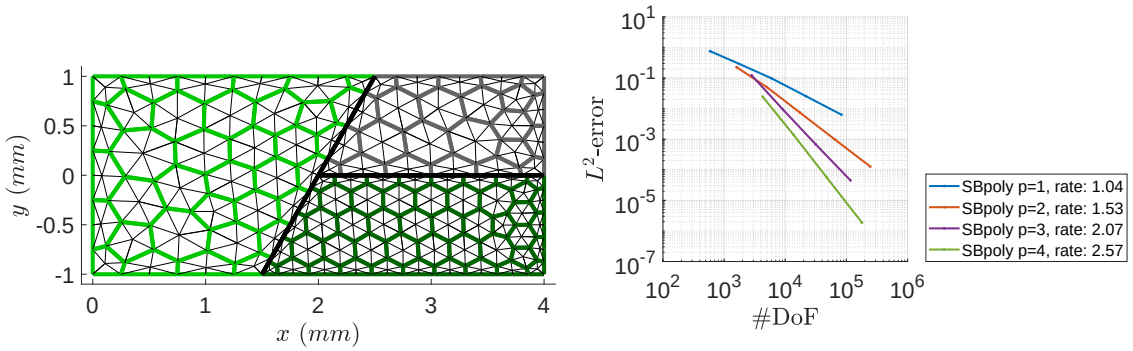

(a) SBFEM-mesh

(b) L^2-error for h-refinement

Figure 4.28: Domain consisting of three sub-domains

The problem is: Find the displacement and LAGRANGE multiplier $(\boldsymbol{u}(\mathbf{x}), \lambda(\mathbf{x}))$, such that

$$(\mathrm{i}\,\omega)^2 \rho \boldsymbol{u} = \boldsymbol{\nabla} \cdot \underline{\underline{\boldsymbol{\sigma}}}(\boldsymbol{u}) + \boldsymbol{f} \qquad \mathbf{x} \in \Omega \tag{4.96}$$

$$\underline{\underline{\boldsymbol{\sigma}}}(\boldsymbol{u})\mathbf{n} = \boldsymbol{\tau} \qquad \mathbf{x} \in \Gamma_{\boldsymbol{\tau}} \tag{4.97}$$

$$\underline{\underline{\boldsymbol{\sigma}}}(\boldsymbol{u})\mathbf{n} = \underline{\underline{\boldsymbol{\sigma}}}(\boldsymbol{u}(\mathcal{P}))\mathbf{n} \qquad \mathbf{x} \in \Gamma_{(a)} \tag{4.98}$$

$$\underline{\underline{\boldsymbol{\sigma}}}(\boldsymbol{u})\mathbf{n} = \mathbf{n}\lambda \qquad \mathbf{x} \in \Gamma_{(a)} \tag{4.99}$$

$$\big(\boldsymbol{u} - \boldsymbol{u}(\mathcal{P})\big) \cdot \mathbf{n} = 0 \qquad \mathbf{x} \in \Gamma_{(a)} \tag{4.100}$$

with $\omega = 2\pi\,\mathrm{s}^{-1}$. Here, $\Gamma_{\boldsymbol{\tau}}$ is the outer boundary of the square and $\Gamma_{(a)}$ is the inner boundary. The inner boundary models the above mentioned crack.

The body load and traction are once again chosen in such a way that a specific analytical solution $\boldsymbol{u}^{\mathrm{ref}}$ is taken

$$\boldsymbol{u}^{\mathrm{ref}}(x, y) = \begin{pmatrix} \cos(k_x^u x) \\ \cos(k_y^v y) \end{pmatrix} \mu\mathrm{m} \tag{4.101}$$

with $k_x^u = 2\pi\,\mathrm{mm}^{-1}$ and $k_y^v = 2\pi\,\mathrm{mm}^{-1}$. Figure 4.30 shows the approximation of the displacement with SB shape functions. The key feature of this analytical solution is that

$$\mathbf{t}\underline{\underline{\boldsymbol{\sigma}}}\mathbf{n} = 0 \qquad \mathbf{x} \in \Gamma_{(a)}, \tag{4.102}$$

where $\mathbf{t}$ and $\mathbf{n}$ are the tangential and normal vectors of the crack. So, there is no shear traction on the crack, and the traction can be represented with a scalar LAGRANGE multiplier (Equation (4.99)).

Figure 4.29f demonstrates that optimal convergence rates are reached for the SB shape functions with body load and traction terms if the displacement and the LAGRANGE multiplier have the same degree p except for the crack tip. A polynomial degree of $\mathrm{p} - 1$ is utilized as described in Section 3.5.3.

The test is also performed with the FEM to get information about the LAGRANGE multiplier at the crack tip. We observe optimal convergence (Figure 4.29b) if the LAGRANGE multiplier is fixed at the crack tip, i.e., $\lambda(\mathbf{x}^c) = 0$ with the crack tip $\mathbf{x}^c$.

The last case is the enrichment approach presented in Section 3.8. In Figure 4.29c the enrichment area is marked in gray. A local adjustment for the LAGRANGE multiplier is required. Figure 4.31 shows the quadrature for an enriched pair next to a standard contact element pair. The local adjustments are summarized in the remark:

Remark 4.13.1 (Local adjustments for the enriched contact pair)**.** *An hp-refined quadrature is used for the enriched contact element pair. This quadrature is the one-dimensional version of the two-dimensional quadrature used for the domain. As for FEM, the* LAGRANGE *multiplier at the crack tip is fixed, i.e.,* $\lambda(\mathbf{x}^c) = 0$ *with the crack tip* $\mathbf{x}^c$*. Furthermore, in the boundary element next to the crack tip, the polynomial degree of the* LAGRANGE *multiplier increases by one.*

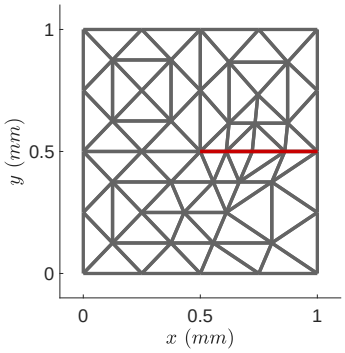

(a) FEM-mesh

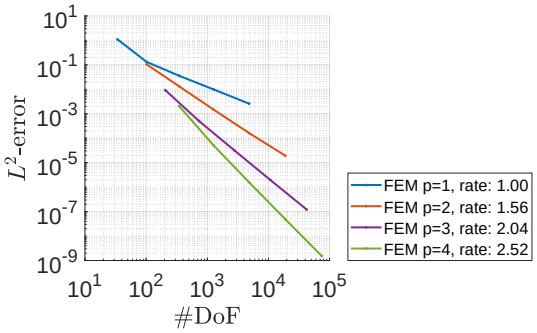

(b) L^2-error for h-refinement

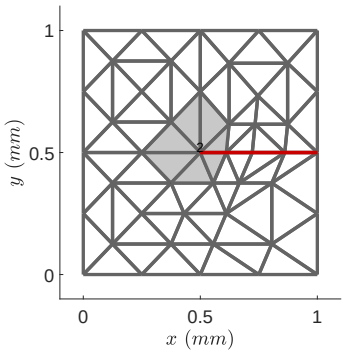

(c) eFEM-mesh

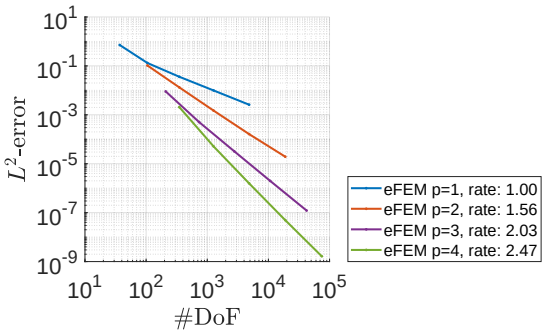

(d) L^2-error for h-refinement

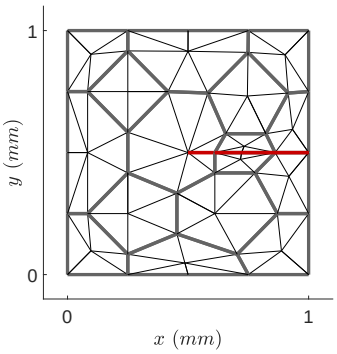

(e) SBFEM-mesh

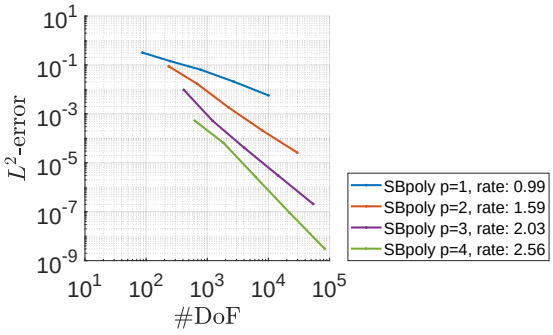

(f) L^2-error for h-refinement

Figure 4.29: Three crack models with vanishing normal gap

The extra degree of the LAGRANGE multiplier seems to be heuristically necessary because of the extra degrees in the elements due to enrichment. Figure 4.29d shows the convergence properties with the described adjustment. It is worth mentioning that local changes in the degree of the LAGRANGE multiplier are also known for other interactions between boundary conditions [122].

4.14 Conclusion for Continuity Conditions

We successfully extended all approaches from the static analysis to the dynamic case. The extension to dynamic cases yields additional shape functions corresponding to body load terms for the SB shape functions. Due to these additional terms, the theoretically optimal convergence rates are reached. A stable combination with the LAGRANGE multiplier is demonstrated for the SB polygonal

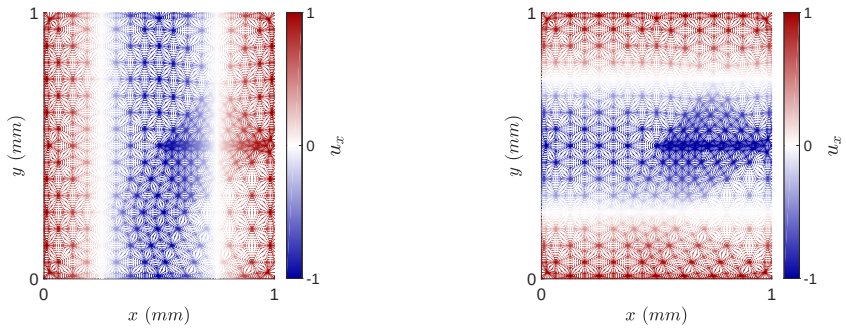

(a) u_x^{h} µm (b) u_y^{h} µm

Figure 4.30: Approximation of the displacement (Equation (4.101)) with SB shape functions

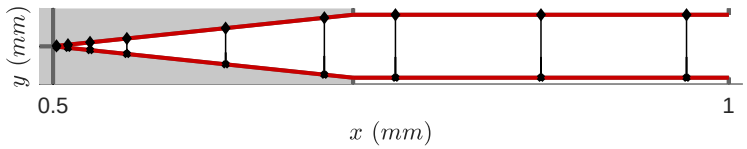

Figure 4.31: Quadrature detail for the enrichment

shape functions. All approaches are tested with continuity conditions. Optimal convergence rates are also obtained in tests with known non-singular analytical solutions for the FEM, the enrichment approach, and the SB shape functions. The crack tip requires local adjustments for the LAGRANGE multipliers.

Chapter 5

Dynamic Contact Problems

In this section, time-dependent contact conditions are introduced to model contact acoustic non-linearity in thin structures. The continuity conditions from Section 4.10 are modified such that they are limited to the current contact area of the considered structure. Breathing cracks and delaminations are analyzed with the defined contact model.

In general, the simulation of breathing cracks in waveguides is commonly investigated with the FEM. This includes studies with commercial tools [73, 110, 155], non-commercial codes [75, 76, 80, 97] as well as comparisons between both [123–125]. While for studies with commercial tools, the contact algorithm is often not specified, the in-house codes are frequently based on node-to-node contact elements with the Penalty Method [76, 80] or similarly to the latter an activation/deactivation approach for elements [123–125].

In [123–125] and [75], a single surface crack in a cross-sectional model is considered. Here, a non-linearity index is calculated depending on the crack depth. Both fundamental modes, the S0- and A0-mode, are evaluated. Cracks with no connection to the surface are analyzed in [155] and [80]. Again, the main evaluation method for the size of the crack is a non-linearity index. Additionally, the authors of [80] include a numerical study of their approach, which is based on a coupling between the high-order and low-order FEM. The high-order FEM is used for the undamaged part, while the low-order FEM approximates the area around the crack and includes the contact model. In [110], the commercial tool ANSYS is utilized to investigate a representative damage in a composite material with several delaminations. An approach with non-linear elements and multiple damaged areas is presented in [97]. Reference [76] shows an imaging method based on higher harmonics. The same study also includes singular elements around the crack tips. Shen *et al.* [123–125] present three-dimensional scattering of ultrasonic waves by a breathing crack simulated with finite differences.

Contact algorithms in the SBFEM are also mainly based on the node-to-node contact scheme. Xing *et al.* investigated two-dimensional problems with friction [166]. The work is extended to three-dimensional problems in [167]. An adaptive contact analysis is considered in [108] by utilizing the contact algorithm in Abaqus, a commercial program, with a self-defined scaled boundary element and error-estimator for the adaptivity. Crack propagation problems under contact conditions are studied in [181] and [182]. The latter considers a dynamic load but in the low-frequency range. In [181, 182], no body load terms are defined in the proposed SB shape functions. Breathing cracks are analyzed in [121] with the continued-fraction approach, which neglects contact forces near the crack tip.

Nowadays, the XFEM usually defines the crack independent of the mesh and a specific boundary. This is conflicting with the contact forces, which act on the boundary. There are approaches, e.g., [42, 91], but to the best of the author's knowledge, breathing cracks for ultrasonic waves are still an open issue.

As explained in Section 2.2.2, the contact algorithm in this thesis is based on 'small deformation theory'. Section 2.2.2 gives a brief overview of the different methods to detect contact. The section focuses on acoustic contact conditions and the specific contact detection implemented for this thesis. Depending on the approximation method for the domain, either the Penalty Method or the Lagrange Multiplier Method could be a better choice. Consequently, both methods are

presented for contact conditions.

5.1 Model problem for CAN

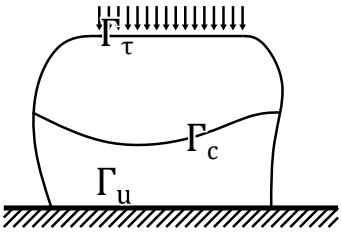

Figure 5.1: Model problem for CAN

For the simulation of CAN, we consider the following model problem:

$$\rho \partial_{tt} \boldsymbol{u} = \nabla \cdot \underline{\underline{\boldsymbol{\sigma}}} + \boldsymbol{f} \qquad \mathbf{x} \in \Omega \tag{5.1}$$

$$\underline{\underline{\boldsymbol{\sigma}}} \mathbf{n} = \boldsymbol{\tau} \qquad \mathbf{x} \in \Gamma_{\boldsymbol{\tau}} \tag{5.2}$$

$$\boldsymbol{u} = \mathbf{0} \qquad \mathbf{x} \in \Gamma_{\boldsymbol{u}}, \tag{5.3}$$

where $\underline{\underline{\boldsymbol{\sigma}}}$ is the linear stress tensor, $\boldsymbol{u}$ the displacement, $\boldsymbol{f}$ the body load and $\boldsymbol{\tau}$ a prescribed traction. Figure 5.1 illustrates the model problem.

Additionally, the KUHN-TUCKER conditions for frictionless contact are assumed

$$g \geq 0, \quad \tau_{\mathbf{n}} \leq 0, \quad g \cdot \tau_{\mathbf{n}} = 0, \quad \tau_{\mathbf{t}} = 0, \qquad \mathbf{x} \in \Gamma_c, \tag{5.4}$$

where g is the normal gap, $\tau_{\mathbf{n}}$ is the normal pressure and $\tau_{\mathbf{t}}$ is the tangential friction (compare Equation (3.20)). As mentioned in Section 3.1.1, the conditions can also be written in term of zones, i.e.,

1. a separation zone Γ_{sp}, where

$$g(x) > 0, \quad \tau_{\mathbf{n}}(x) = 0, \quad \tau_{\mathbf{t}}(x) = 0, \tag{5.5}$$

2. a slip zone Γ_{sl}, where

$$g(x) = 0, \quad \tau_{\mathbf{n}}(x) \leq 0, \quad \tau_{\mathbf{t}}(x) = 0. \tag{5.6}$$

The non-linear term $g \cdot \tau_{\mathbf{n}} = 0$ vanishes, but the zones must be determined based on an iterative procedure during the simulation.

The normal gap is given by

$$g = (\boldsymbol{u} - \boldsymbol{u}(\mathcal{P})) \cdot \mathbf{n}, \tag{5.7}$$

where a vanishing initial gap is assumed, i.e., $\|\mathbf{x} - \mathcal{P}(\mathbf{x})\| = 0$. This assumption can be made for crack applications where the contact area is inside a crack of zero thickness.

5.1.1 Time Stepping Scheme for Contact Problems

The choice of an appropriate time stepping scheme for dynamic contact analysis is not unambiguous. Many time integration schemes have their pros and cons. Particular attention should be paid to the high frequencies in ultrasonic applications. The author makes a practical choice here. The same time stepping method is implemented as in ANSYS to compare the results with this commercial simulation tool. The Generalized α-Method with the parameters from HILBER-HUGHES-TAYLOR [70] is an extension to the well-known NEWMARK method, which is one of the standard approaches for linear problems. Unfortunately, the NEWMARK method with its standard parameters itself shows instabilities in case of contact problems for small time steps [36, 45]. While

the Generalized α-Method prevents these spurious oscillations, it violates energy conservation in contact events. There are alternatives, e.g., [1, 8], but with another time scheme, a direct comparison with ANSYS would be impossible. In general, there are different ways to define a contact time scheme because the contact condition can be applied to the displacement, the velocity, or the acceleration [45].

5.2 Generalized α-Method

This section presents the time integration family Generalized α-Method. It is a time integration scheme with three parameters (α, β, γ), which can be adjusted to the problem. The choice of these three parameters includes some special cases. For these parameters, the method is implicit, unconditionally stable for non-contact problems, and second-order accurate.

1. The classic NEWMARK's parameters $(\alpha, \beta, \gamma) = (0, 0.25, 0.5)$: Unfortunately, contact events lead to spurious oscillations for contact problems [36, 45].

2. The HILBER-HUGHES-TAYLOR (HHT) parameters $(\alpha, \beta, \gamma) = (0.1, 0.3025, 0.6)$: Additionally, the time stepping is dissipative in the higher frequencies, which makes it applicable for contact problems. Indeed, the parameters are designed for contact problems [70].

3. The BATHE-CHAUDHARY parameters $(\alpha, \beta, \gamma) = (0, 0.5, 0.5)$: For contact events, the energy is conserved in a better way and hence the parameters are suited for contact problems [28].

In this thesis, the HHT parameters are utilized for contact problems. The BATHE-CHAUDHARY parameters could be used but showed a more significant error in linear convergence tests. The instability of NEWMARK's parameters for contact problems is observable for ultrasonic applications, so the author advises against their usage.

We use the common notation for time stepping algorithms

$$\mathbf{w}_n = \mathbf{w}(t_n) \text{ with } 0 < t_1 < \ldots < t_n < \ldots < t_N, \tag{5.8}$$

where $\mathbf{w}$ is either the nodal displacement $\mathbf{u}$, nodal velocity $\mathbf{v}$, nodal acceleration $\mathbf{a}$ or nodal force $\mathbf{f}$. The main idea of the Generalized α-Method is to define for some quantities a sub-step which is approximated by a convex combination of the current and the previous time step, i.e.,

$$\begin{aligned} \mathbf{w}_{n+1-\alpha} &= \mathbf{w}(t_{n+1-\alpha}) && (5.9)\\ &\approx (1-\alpha)\mathbf{w}_{n+1} + \alpha \mathbf{w}_n. && (5.10) \end{aligned}$$

These convex combinations are used to modify the equation of motion, i.e.,

$$\mathbf{M}\mathbf{a}_{n+1} = -\boldsymbol{\mathcal{K}}\big(\mathbf{u}_{n+1-\alpha}\big) + \mathbf{f}_{n+1-\alpha}, \tag{5.11}$$

where $\boldsymbol{\mathcal{K}}$ is a non-linear relationship in the displacement and $\mathbf{M}$ the linear mass matrix. In this case, the Generalized α-Method with $\mathbf{u}$ as primary variable can be defined by

$$\begin{aligned} \mathbf{u}_{n+1} &= \vartheta_1^u \mathbf{u}_{n+1-\alpha} - \vartheta_2^u \mathbf{u}_n, && (5.12)\\ \mathbf{v}_{n+1} &= \vartheta_1^v (\mathbf{u}_{n+1} - \mathbf{u}_n) + \vartheta_2^v \mathbf{v}_n + \vartheta_3^v \mathbf{a}_n, && (5.13)\\ \mathbf{a}_{n+1} &= \vartheta_1^a (\mathbf{u}_{n+1} - \mathbf{u}_n) - \vartheta_2^a \mathbf{v}_n - \vartheta_3^a \mathbf{a}_n && (5.14) \end{aligned}$$

with

$$\Delta t = t_{n+1} - t_n, \qquad \vartheta_1^u = \frac{1}{(1-\alpha)}, \qquad \vartheta_2^u = \frac{\alpha}{(1-\alpha)}, \tag{5.15}$$

$$\vartheta_1^v = \frac{\gamma}{\beta \Delta t}, \qquad \vartheta_2^v = \left(1 - \frac{\gamma}{\beta}\right), \qquad \vartheta_3^v = \left(1 - \frac{\gamma}{2\beta}\right) \Delta t, \tag{5.16}$$

$$\vartheta_1^a = \frac{1}{\beta \Delta t^2}, \qquad \vartheta_2^a = \frac{1}{\beta \Delta t}, \qquad \vartheta_3^a = \frac{0.5 - \beta}{\beta}. \tag{5.17}$$

Merging all terms depending on the previous time step to write predictor quantities $\mathbf{w}^p$ gives

$$\begin{aligned}
\mathbf{u}_{n+1} &= \vartheta_1^u \mathbf{u}_{n+1-\alpha} - \vartheta_2^u \mathbf{u}_n && && (5.18)\\
&= \vartheta_1^u \mathbf{u}_{n+1-\alpha} + \mathbf{u}^p && \text{with } \mathbf{u}^p = -\vartheta_2^u \mathbf{u}_n, && (5.19)\\
\mathbf{v}_{n+1} &= \vartheta_1^v (\mathbf{u}_{n+1} - \mathbf{u}_n) + \vartheta_2^v \mathbf{v}_n + \vartheta_3^v \mathbf{a}_n && && (5.20)\\
&= \vartheta_1^v \mathbf{u}_{n+1} + \mathbf{v}^p && \text{with } \mathbf{v}^p = -\vartheta_1^v \mathbf{u}_n + \vartheta_2^v \mathbf{v}_n + \vartheta_3^v \mathbf{a}_n, && (5.21)\\
\mathbf{a}_{n+1} &= \vartheta_1^a (\mathbf{u}_{n+1} - \mathbf{u}_n) - \vartheta_2^a \mathbf{v}_n - \vartheta_3^a \mathbf{a}_n && && (5.22)\\
&= \vartheta_1^a \mathbf{u}_{n+1} + \mathbf{a}^p && \text{with } \mathbf{a}^p = -\vartheta_1^a \mathbf{u}_n - \vartheta_2^a \mathbf{v}_n - \vartheta_3^a \mathbf{a}_n. && (5.23)
\end{aligned}$$

For most non-linear equations, it is advantageous to formulate them as a residual equation:

$$\begin{aligned}
\mathbf{0} &= \mathbf{M}\mathbf{a}_{n+1} + \boldsymbol{\mathcal{K}}\big(\mathbf{u}_{n+1-\alpha}\big) - \mathbf{f}_{n+1-\alpha} && (5.24)\\
&= \vartheta_1^a \mathbf{M}\mathbf{u}_{n+1} + \mathbf{M}\mathbf{a}^p + \boldsymbol{\mathcal{K}}\big(\mathbf{u}_{n+1-\alpha}\big) - \mathbf{f}_{n+1-\alpha} && (5.25)\\
&= \vartheta_1^a \vartheta_1^u \mathbf{M}\mathbf{u}_{n+1-\alpha} + \vartheta_1^a \mathbf{M}\mathbf{u}^p + \mathbf{M}\mathbf{a}^p + \boldsymbol{\mathcal{K}}\big(\mathbf{u}_{n+1-\alpha}\big) - \mathbf{f}_{n+1-\alpha} && (5.26)\\
&= \vartheta_1^a \vartheta_1^u \mathbf{M}\mathbf{u}_{n+1-\alpha} + \boldsymbol{\mathcal{K}}\big(\mathbf{u}_{n+1-\alpha}\big) + \mathbf{f}^p && (5.27)\\
&= \boldsymbol{\mathcal{R}}\big(\mathbf{u}_{n+1-\alpha}\big) && (5.28)
\end{aligned}$$

with

$$\mathbf{f}^p = \vartheta_1^a \mathbf{M}\mathbf{u}^p + \mathbf{M}\mathbf{a}^p - \mathbf{f}_{n+1-\alpha}. \tag{5.29}$$

The time stepping scheme is summarized in Algorithm 1.

Algorithm 1 The Generalized α-Method

Require: $\mathbf{u}_0, \mathbf{v}_0, \mathbf{a}_0$

for $n = 1, \dots, N$ **do**
  $\mathbf{u}^p \leftarrow -\vartheta_2^u \mathbf{u}_n$
  $\mathbf{v}^p \leftarrow -\vartheta_1^v \mathbf{u}_n + \vartheta_2^v \mathbf{v}_n + \vartheta_3^v \mathbf{a}_n$
  $\mathbf{a}^p \leftarrow -\vartheta_1^a \mathbf{u}_n - \vartheta_2^a \mathbf{v}_n - \vartheta_3^a \mathbf{a}_n$
  $\mathbf{u}_{n+1-\alpha}$ is solution of $\mathbf{0} = \boldsymbol{\mathcal{R}}\big(\mathbf{u}_{n+1-\alpha}\big)$ ▷ see Algorithm 2 for PM ▷ see Algorithm 3 for LMM
  $\mathbf{u}_{n+1} \leftarrow \vartheta_1^u \mathbf{u}_{n+1-\alpha} + \mathbf{u}^p$
  $\mathbf{v}_{n+1} \leftarrow \vartheta_1^v \mathbf{u}_{n+1} + \mathbf{v}^p$
  $\mathbf{a}_{n+1} \leftarrow \vartheta_1^a \mathbf{u}_{n+1} + \mathbf{a}^p$
end for

Penalty Method for contact problems There are several ways to explain the Penalty Method. On the one hand, it can be considered as an iterative process, where an initial displacement is computed. Afterward, the contact area is approximated based on the quadrature points, which have a negative normal gap $g < 0$. For these points, a penalty is added to force them towards the equality $g = 0$. On the other hand, this method can be considered as a non-linear spring boundary condition. The non-linear spring has zero stiffness if the gap is positive and a high stiffness if the gap is negative.

The aim is to solve the residual Equation (5.28)

$$\mathbf{0} = \boldsymbol{\mathcal{R}}\big(\mathbf{u}_{n+1-\alpha}\big). \tag{5.30}$$

The solution is computed iteratively with a pseudo [⋆1] Newton-Raphson-Method. Let $\mathbf{u}^i$ be the iterative displacements and g^i the associated normal gap. Then, we follow an active set strategy on the quadrature point $\mathbf{x}_q \in \mathbf{X}_q$ [54], where $\mathbf{X}_q$ is the set of all quadrature points of Γ_c. Update the

[⋆1] The word 'pseudo' is used because overall contact problems are non-differentiable.

current set every iteration by adding the new quadrature points where the normal gap is smaller than zero, i.e.,

$$\mathcal{A}^{i+1} = \mathcal{A}^i \cup \{\mathbf{x}_q \in \mathbf{X}_q : g^i(\mathbf{x}_q) < 0\}. \tag{5.31}$$

Note that the active set $\mathcal{A}^{i+1}$ is extended in each step, such that it contains all quadrature points from the previous step. This should prevent the solution from 'zigzagging' between two states.

For the contact, insert a penalty function into Equation (4.80) which is only active in the contact area. We introduce formally an interpolative function $\chi_{\mathcal{A}^i}$ to define the penalty function (Equation (4.80)) as

$$\epsilon = \epsilon_0 \chi_{\mathcal{A}^i}(\mathbf{x}) \tag{5.32}$$

with the following properties

$$\chi_{\mathcal{A}^i}(\mathbf{x}) = 1 \qquad \mathbf{x} \in \mathcal{A}^i \tag{5.33}$$

$$\chi_{\mathcal{A}^i}(\mathbf{x}) = 0 \qquad \mathbf{x} \in \mathbf{X}_q \setminus \mathcal{A}^i. \tag{5.34}$$

The residual equation is then solved with a pseudo Newton-Raphson-Method

$$\mathbf{S}^i \Delta\mathbf{u}^{i+1}_{n+1-\alpha} = -\boldsymbol{\mathcal{R}}\big(\mathbf{u}^i_{n+1-\alpha}\big) \tag{5.35}$$

$$\mathbf{u}^{i+1}_{n+1-\alpha} = \mathbf{u}^i_{n+1-\alpha} + \Delta\mathbf{u}^{i+1}_{n+1-\alpha}, \tag{5.36}$$

where $\mathbf{S}^i = \mathrm{D}_{\mathbf{u}}\,\boldsymbol{\mathcal{R}}|_{\mathbf{u}^i_{n+1-\alpha}}$ is the best linear approximation of $\boldsymbol{\mathcal{R}}$ at the point $\mathbf{u}^i_{n+1-\alpha}$. The best linear approximation is derived in the following. For the sake of a convenient notation, the indices i and $n+1-\alpha$ are dropped.

The non-linear operator $\boldsymbol{\mathcal{K}}(\boldsymbol{u})$ for the Penalty Method is

$$\boldsymbol{\mathcal{K}}(\boldsymbol{u}) = \int \boldsymbol{\varepsilon}(\boldsymbol{\delta u})\underline{\underline{\boldsymbol{\sigma}}}(\boldsymbol{u})\,\mathrm{d}\Omega + \int \epsilon_0 \chi_{\mathcal{A}} \Big(\big(\boldsymbol{\delta u} - \boldsymbol{\delta u}(\mathcal{P})\big) \cdot \mathbf{n} \Big) \Big(\big(\mathbf{n} \cdot (\boldsymbol{u} - \boldsymbol{u}(\mathcal{P}))\big) \Big)\,\mathrm{d}\Gamma_c, \tag{5.37}$$

where $\boldsymbol{u}$ is the displacement and $\boldsymbol{\delta u}$ the virtual displacement. For a given contact area/active set $\mathcal{A}$, the best linear approximation $\mathrm{D}_{\mathbf{u}}\,\boldsymbol{\mathcal{K}}\Delta\boldsymbol{u}$ of $\boldsymbol{\mathcal{K}}$ is

$$\mathrm{D}_{\mathbf{u}}\,\boldsymbol{\mathcal{K}}\Delta\boldsymbol{u} = \int \boldsymbol{\varepsilon}(\boldsymbol{\delta u})\underline{\underline{\boldsymbol{\sigma}}}(\Delta\boldsymbol{u})\,\mathrm{d}\Omega + \int \epsilon_0 \chi_{\mathcal{A}} \Big(\big(\boldsymbol{\delta u} - \boldsymbol{\delta u}(\mathcal{P})\big) \cdot \mathbf{n} \Big) \Big(\big(\mathbf{n} \cdot (\Delta\boldsymbol{u} - \Delta\boldsymbol{u}(\mathcal{P}))\big) \Big)\,\mathrm{d}\Gamma_c, \tag{5.38}$$

which leads to the matrix

$$\big(\mathbf{K} + \mathbf{P}_{\mathcal{A}}\big)\Delta\mathbf{u}, \tag{5.39}$$

where $\mathbf{P}_{\mathcal{A}}$ is computed as in Equation (4.80), but only over the active quadrature points [54]. Since the mass matrix is already a linear operator of $\mathbf{u}$, the best linear approximation is the matrix itself, i.e.,

$$\mathrm{D}_{\mathbf{u}}\left(\vartheta_1^a \vartheta_1^u \mathbf{M}\mathbf{u}\right)\Delta\mathbf{u} = \vartheta_1^a \vartheta_1^u \mathbf{M}\Delta\mathbf{u} \tag{5.40}$$

and the constant term is

$$\mathrm{D}_{\mathbf{u}}\left(\mathbf{f}^p\right)\Delta\mathbf{u} = \mathbf{0}. \tag{5.41}$$

We obtain the best linear approximation

$$\mathbf{S}^i = \vartheta_1^a \vartheta_1^u \mathbf{M} + \mathbf{K} + \mathbf{P}_{\mathcal{A}} \tag{5.42}$$

for the pseudo Newton-Raphson-Method.

Defining the current residual $\mathbf{r}$ by $\mathbf{r} = -\boldsymbol{\mathcal{R}}\big(\mathbf{u}^i_{n+1-\alpha}\big)$, this derivation leads to the following Algorithm 2.

This algorithm is categorized as a segment-to-segment approach for contact [54].

Remark 5.2.1. *For aligned elements with Gauss–Lobatto quadrature points (see Figure 4.24b), this approach simplifies to the classic point-to-point contact elements. Additionally, if the quadrature points and the nodes are aligned, $\mathbf{P}_{\mathcal{A}}$ is faster to compute.*

Algorithm 2 pseudo NEWTON-RAPHSON-Method for the Penalty Method

Require:
ϵ_0 ▷ the penalty parameter
tol ▷ the termination tolerance
Ensure: $\mathbf{0} = \boldsymbol{\mathcal{R}}(\mathbf{u})$

$\mathcal{A} \leftarrow \emptyset$
$\mathbf{S} \leftarrow \vartheta_1^a \vartheta_1^u \mathbf{M} + \mathbf{K}$
$\mathbf{r} \leftarrow -\mathbf{f}^p$
$\mathbf{u} \leftarrow \mathbf{0}$
for $i = 1, \dots$ **do**
  $\boldsymbol{\Delta}\mathbf{u} \leftarrow \mathbf{S} \backslash \mathbf{r}$
  $\mathbf{u} \leftarrow \mathbf{u} + \boldsymbol{\Delta}\mathbf{u}$
  $\mathcal{A} = \mathcal{A} \cup \{\mathbf{x}_q \in \mathbf{X}_q : g(\mathbf{x}_q) < 0\}$ ▷ evaluate $g(\mathbf{x}_q)$ with the new $\mathbf{u}$
  $\mathbf{S} \leftarrow \vartheta_1^a \vartheta_1^u \mathbf{M} + \mathbf{K} + \mathbf{P}_{\mathcal{A}}$
  $\mathbf{r} \leftarrow -\mathbf{f}^p - \mathbf{S}\mathbf{u}$
  if $\|\mathbf{r}\| <$ tol **then**
    return u
  end if
end for

LAGRANGE **Multiplier Method for contact problems** Similar to the Penalty Method, the contact area has to be detected. The contact area is linked to the quadrature points for the penalty parameter. However, since shape functions define the LAGRANGE multipliers, they have a support over several quadrature points. An active set over the quadrature points is therefore inadequate [54]. There are several ways to define the contact area for LAGRANGE multipliers. If only nodal shape functions are used, a node-based decision can be made [163]. Alternatively, a segment-to-segment algorithm can be applied [163]. For this, sub-segments of the elements are activated and deactivated depending on the contact state. In the case of SB shape functions, the crack tip does not allow further sub-segmentation, so another approach is investigated in this thesis. The shape functions themselves are activated or deactivated, and the contact detection is done weakly. This is inspired by [54, 159]. Let g^i be the current normal gap dependent on the nodal displacement $\mathbf{u}^i$ and N_j^λ be the j-th LAGRANGE multiplier shape function. Then, the shape becomes active if

$$0 > \int g^i N_j^\lambda \, \mathrm{d}\Gamma_{(a)} \tag{5.43}$$

$$= \int \Big(\big(\boldsymbol{N}^{\mathbf{u}} - \boldsymbol{N}^{\mathbf{u}}(\mathcal{P}) \big) \cdot \mathbf{n} \Big) N_j^\lambda \, \mathrm{d}\Gamma_{(a)} \mathbf{u}^i \tag{5.44}$$

$$= (\mathbf{L}^\mathsf{T} \mathbf{u}^i)_j, \tag{5.45}$$

where $\mathbf{L}$ is the matrix in Equation (4.63), and $(\cdot)_j$ is the j-th component of a vector. The active set becomes updated by

$$\mathcal{A}^{i+1} = \mathcal{A}^i \cup \{j : (\mathbf{L}^\mathsf{T} \mathbf{u}^i)_j < 0\}. \tag{5.46}$$

Note that the active set is again growing in each step containing the shape functions from the previous iteration. Let $\mathbf{L}_{\mathcal{A}^i}$ be a matrix that has the same column as $\mathbf{L}$ if the column's index is part of the active set, and a zero column otherwise. Denoting the global vector of unknowns by $\mathbf{w} = (\mathbf{u}^\mathsf{T}, \boldsymbol{\lambda}^\mathsf{T})^\mathsf{T}$, Algorithm 3 gives the pseudo NEWTON-RAPHSON-Method.

Moreover, for the examples in this thesis, the LAGRANGE multiplier matrix $\mathbf{L}_{\mathcal{A}}$ is small in comparison to the dynamic stiffness matrix $\vartheta_1^a \vartheta_1^u \mathbf{M} + \mathbf{K}$. Therefore, the linear system $\mathbf{S} \backslash \mathbf{r}$ is solved as in the first part of Remark 4.11.2 where Equation (4.66) is computed utilizing CHOLESKY decomposition (Appendix A.2).

Remark 5.2.2 (LMM faster in MATLAB than PM)**.** *The matrix $\mathbf{L}_{\mathcal{A}}$ is a sub-matrix of $\mathbf{L}$. Therefore, the matrix $\mathbf{L}$ can be stored once and $\mathbf{L}_{\mathcal{A}}$ is retrieved in each iteration from the stored values*

Algorithm 3 pseudo NEWTON-RAPHSON-Method for the LAGRANGE Multiplier Method

Require: tol
Ensure: $\mathbf{0} = \boldsymbol{\mathcal{R}}(\mathbf{u})$

$\mathcal{A} \leftarrow \emptyset$
$\mathbf{S} \leftarrow \begin{pmatrix} \vartheta_1^a \vartheta_1^u \mathbf{M} + \mathbf{K} & \mathbf{0} \\ \mathbf{0} & \mathbf{0} \end{pmatrix}$
$\mathbf{r} \leftarrow -\begin{pmatrix} \mathbf{f}^p \\ \mathbf{0} \end{pmatrix}$
$\mathbf{w} \leftarrow \begin{pmatrix} \mathbf{0} \\ \mathbf{0} \end{pmatrix}$
for $i = 1, \ldots$ **do**
  $\boldsymbol{\Delta}\mathbf{w} \leftarrow \mathbf{S} \backslash \mathbf{r}$ ▷ solve only over the non-zero rows and columns
  $\mathbf{w} \leftarrow \mathbf{w} + \boldsymbol{\Delta}\mathbf{w}$
  $\mathcal{A} = \mathcal{A} \cup \{j : (\mathbf{L}^\mathsf{T}\mathbf{u})_j < 0\}$
  $\mathbf{S} \leftarrow \begin{pmatrix} \vartheta_1^a \vartheta_1^u \mathbf{M} + \mathbf{K} & \mathbf{L}_\mathcal{A} \\ \mathbf{L}_\mathcal{A}^\mathsf{T} & \mathbf{0} \end{pmatrix}$
  $\mathbf{r} \leftarrow -\mathbf{S}\mathbf{w} - \begin{pmatrix} \mathbf{f}^p \\ \mathbf{0} \end{pmatrix}$
  if $\|\mathbf{r}\| <$ tol **then**
    return u
  end if
end for

of $\mathbf{L}$. *At least in* MATLAB, *this leads to a significant run-time advantage of the LMM compared to the Penalty Method, where the matrix* $\mathbf{P}_{\mathcal{A}^i}$ *has to be recalculated in each iteration.*

5.3 Numerical Experiments for CAN

For the non-linear simulations, four examples are presented. The first one shows the validity of the implementation. The second and third examples are parametric studies for an NDT or SHM application. The fourth one illustrates other capabilities of the presented approach.

5.3.1 Comparison with ANSYS

The implementation of the contact algorithm is first demonstrated by comparing it with a commercial reference program. A simple example of CAN is given by two plates that are in contact with each other. Figure 5.2 shows an overview of the arrangement. As illustrated in the figure, one of the plates is excited with an ultrasonic wave, while the other plate is clamped at the end. The material properties are those of construction steel (Table A.1d), and plane strain is assumed. The excitation varies in time as a GAUSSIAN pulse (Equation (4.51)) with a center frequency of 600 kHz. Figure 5.3 depicts the signal at point P_1 (see Figure 5.2). The x-displacement shows that the first plate is pushed back in the negative direction due to the ultrasonic wave. The Figure presents the normalized signal with a normalization using the coefficient presented in Equation (4.54). It is important to note that the problem remains scalable with a positive constant due to the assumption of a vanishing initial gap. To simplify, if the excitation is doubled, also the signal will double. Changing the sign of the excitation, however, will change the signal. A normalization by a positive value is still a valid representation. The two proposed contact methods are tested for the FEM implementation. Since the contact elements are independent of the considered elements for the domain, a test for the finite elements is sufficient. The penalty parameter is $\epsilon = 100E$, where E is YOUNG's modulus. Figure 5.4 shows the x-displacement of the midpoint P_c of the contact area Γ_c for both plates and both methods. It can be observed that there are multiple contact events.

The HHT scheme advances the simulation in time with a time step of $\Delta t = (100 f_0)^{-1}$, where f_0, again, is the center frequency. The small time step is necessary to capture also the super-harmonic

waves which originate from the contact faces. A rule of thumb considers $\Delta t = (20 f_{\max})^{-1}$ to be a sufficiently small time step for ultrasonic applications [155], where $f_{\max}$ is the maximal relevant frequency. Due to this choice, a high number of super-harmonics are resolved by the approximation. Figure 5.5 depicts the point error (Equation (4.53)) with respect to the reference solution computed with ANSYS. The ANSYS simulation uses quadratic elements, while the self-implemented FEM utilizes higher-order shape functions with p-refinement. The self-implemented FEM is in good agreement with the ANSYS solution. Both approximations are computed on different irregular meshes. A difference below 1% is only possible because both implementations use the same time scheme.

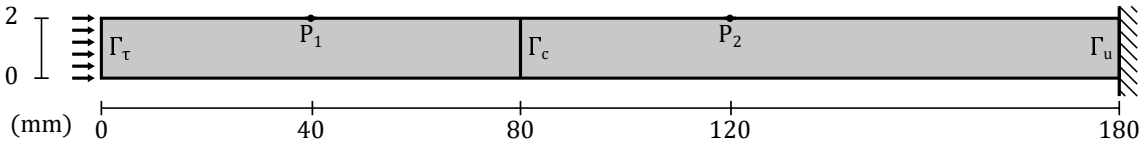

Figure 5.2: Two waveguides in contact

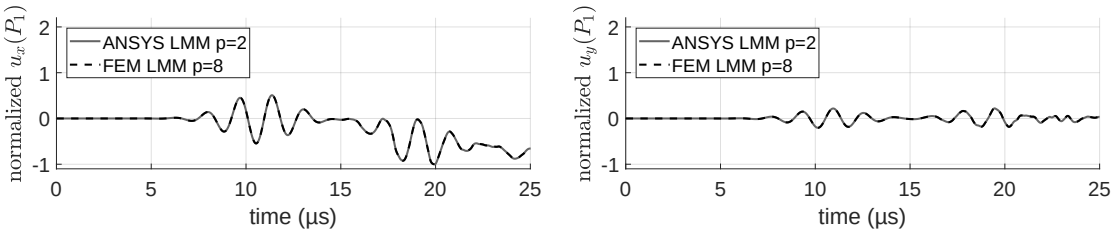

(a) $u_x(\mathrm{P}_1)$ (b) $u_y(\mathrm{P}_1)$

Figure 5.3: Signal at point P_1 for two waveguides in contact (Figure 5.2)

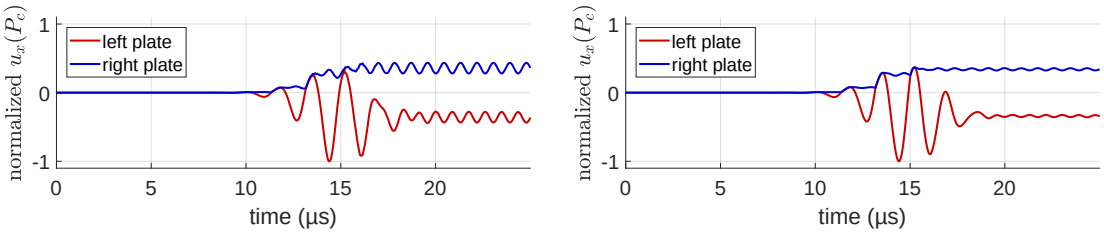

(a) LMM (b) PM

Figure 5.4: Signal at the midpoint of the contact area for two waveguides in contact (Figure 5.2)

5.3.2 Waveguide with a Breathing Crack

The next example studies a breathing crack. We revisit the waveguide from Section 4.8.2. Figure 5.6 shows the domain as an overview. As a reminder, the boundary conditions in Equation (4.55) can excite both fundamental modes. The Gaussian pulse, used as an excitation signal, has a center frequency of 500 kHz. Construction steel (Table A.1d) is simulated under plane strain conditions.

The time integration is performed with the HHT-parameters. The time step is chosen to be $\Delta t = (60 f_0)^{-1}$. The small time step is required to capture also the super-harmonic waves which originate from the breathing crack. To also resolve the super-harmonic waves, the highest relevant frequency $f_{\max}$ is assumed to be smaller than three times the center frequency of the excitation and the rule of thumb from above is utilized.

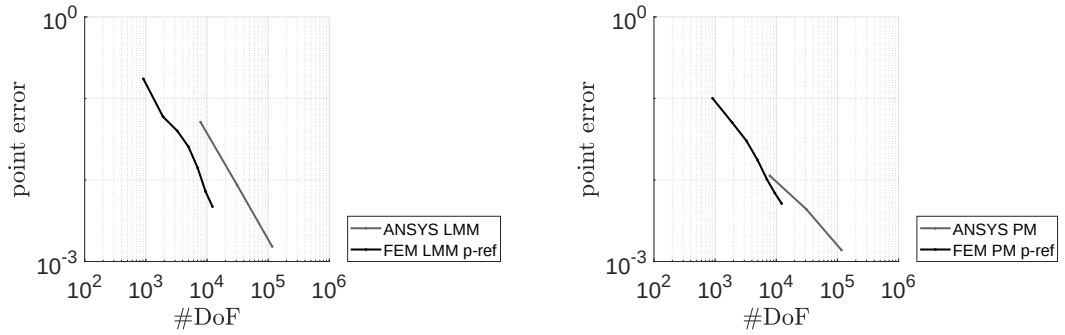

(a) LMM (b) PM

Figure 5.5: Point error for two waveguides in contact (Figure 5.2)

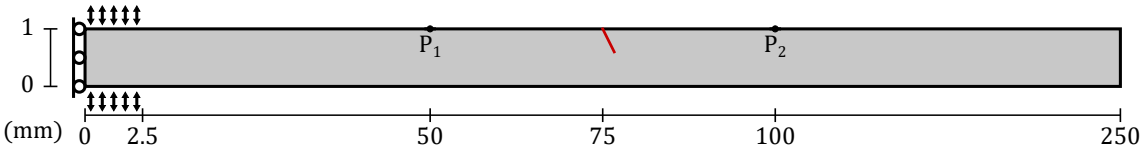

Figure 5.6: Waveguide with a breathing crack

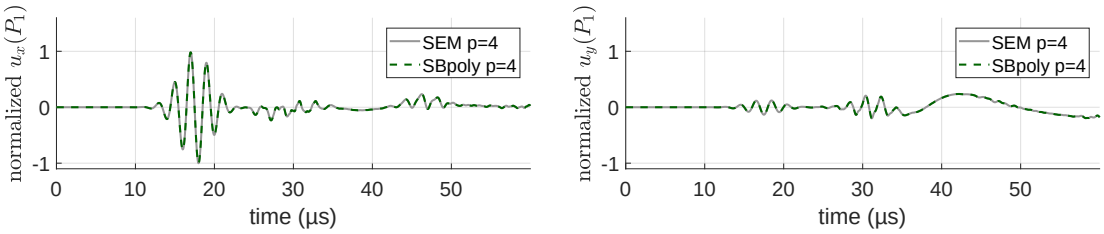

(a) $u_x(\mathrm{P}_1)$ (b) $u_y(\mathrm{P}_1)$

Figure 5.7: Signal at point P_1 for the breathing crack in the waveguide (Figure 5.6)

The results of the different methods are compared at point P_1. Figure 5.7 shows the signals at this point. In Figure 5.7b, a sub-harmonic wave with a lower frequency arrives between 38 µs and 50 µs. Five different approaches are studied:

1. FEM with a uniform mesh in conjunction with the Lagrange Multiplier Method,
2. FEM with a graded mesh in conjunction with the Lagrange Multiplier Method,
3. the enrichment approach (eFEM) with the Lagrange Multiplier Method,
4. the enrichment approach (eFEM) with the Penalty Method,
5. SB shape functions (SBpoly) with the the Lagrange Multiplier Method.

The penalty parameter is the same as in the previous example. The point errors (Equation (4.53)) with respect to the reference solution are shown in Figure 5.8. The reference solution is computed on the graded mesh (see Figure 4.19b) with LMM. As for the linear case, FEM on a uniform mesh suffers from the influence of the singularity. A graded mesh is a good alternative. The Lagrange Multiplier Method and Penalty Method yield different results for the enrichment approach. The Penalty Method shows a smaller error indicating that the Lagrange Multiplier shape functions (Remark 4.13.1) are suboptimal. In the current implementation, the penalty procedure is slower by a factor of between 10 and 100, depending on the mesh and the polynomial degree p. The main

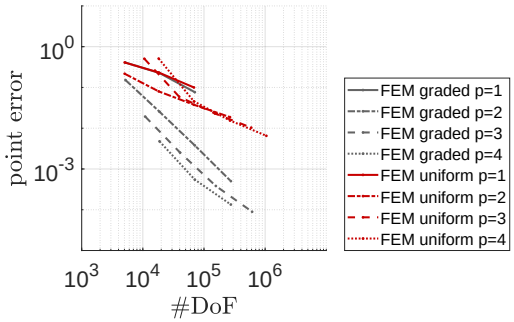

(a) Quasi-uniform FEM with LMM vs graded FEM with LMM

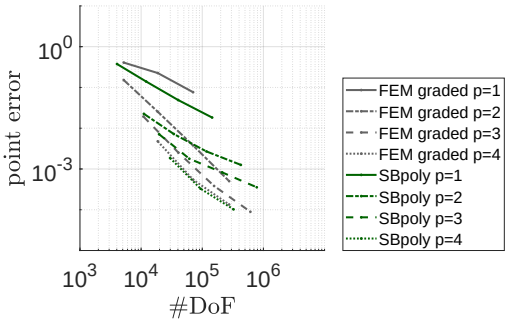

(b) SBpoly with LMM vs graded FEM with LMM

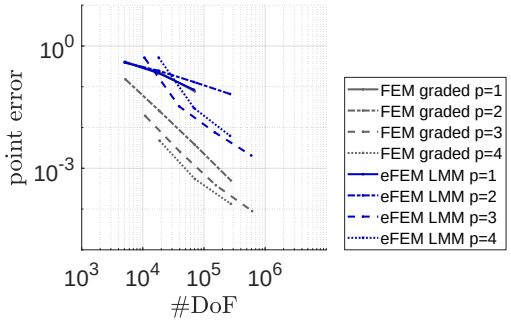

(c) eFEM with LMM vs graded FEM with LMM

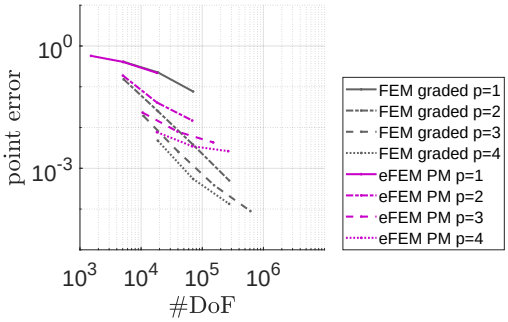

(d) eFEM with PM vs graded FEM with LMM

Figure 5.8: Point error for S0-excitation for the breathing crack in the waveguide

reason is the repeated computation of the penalty matrix, while the LAGRANGE multiplier matrix is only computed once (Remark 5.2.2).

The SB shape functions combined with the faster LAGRANGE Multiplier Method show a good performance. Moreover, the polygonal mesh is generated automatically and does not need many requirements around the crack tip. In contrast, the graded FEM mesh increases the effort to create an appropriate mesh.

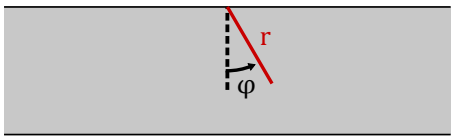

(a) Overview of the parameters

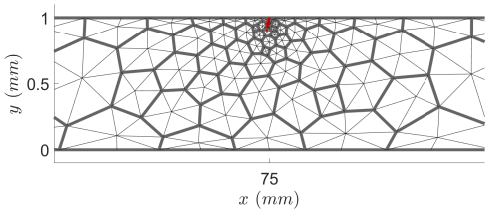

(b) Example of SBFEM-mesh for the smallest defects

Figure 5.9: Details on the breathing crack in the waveguide

The following parametric studies are only performed with the SB shape functions of degree p = 3 on comparatively coarse meshes. A refined zone is introduced in the vicinity of the crack such that the crack and the super-elements have a similar size. A parametric study is carried out for different crack lengths r and angles φ (see Figure 5.9a). The mesh with the smallest investigated crack is shown in Figure 5.9b. Similar to [97, 123–125], a non-linearity index is evaluated. The non-linearity index is based on the y-displacement, which is easier to measure experimentally.

In [97, 123–125], the non-linearity index is defined as the ratio $A(2f_0)/A(f_0)$ of the amplitudes between the center frequency (first harmonic) and its second harmonic $2f_0$, where $A(f)$ is the amplitude at a given frequency f, and f_0 is the center frequency of the excitation. A single amplitude, however, is prone to numerical errors. Alternatively to a single value, a weighted amplitude, which also includes the values in the vicinity of a specific amplitude, is proposed in the following.

Define the GAUSSIAN window as a weighting function

$$w(f, f^*, \varsigma) = \exp\left(-0.5\frac{(f - f^*)^2}{\varsigma^2}\right) \tag{5.47}$$

with an offset f^* and a width ς. The width of the excitation transformed into the frequency domain is $f_0(2\pi)^{-1}$. The width can be derived from Equation (4.51) via FOURIER transform, and it is a canonical choice for the weighting, i.e., $\varsigma = f_0(2\pi)^{-1}$. A weighted amplitude for a specific frequency f^* can be defined as

$$A_w(f^*) = \frac{\int_0^\infty A(f)w(f; f^*, \varsigma)\,\mathrm{d}f}{\int_0^\infty w(f; f^*, \varsigma)w(f; f^*, \varsigma)\,\mathrm{d}f}, \tag{5.48}$$

where $A(f)$ is the amplitude dependent on the frequency f.

The weighted amplitude is computed numerically for the center frequency and the second harmonic

$$A_w(f_0) \approx \frac{\mathbf{A}\cdot\mathbf{w}_1}{\mathbf{w}_1\cdot\mathbf{w}_1}, \qquad A_w(2f_0) \approx \frac{\mathbf{A}\cdot\mathbf{w}_2}{\mathbf{w}_2\cdot\mathbf{w}_2}, \tag{5.49}$$

where the amplitude vector $\mathbf{A}$ is computed by the fast FOURIER transform of the y-displacement at a point P_i. The weighting vectors $\mathbf{w}_1$ and $\mathbf{w}_2$ correspond to $w(f; f_0, \varsigma)$ and $w(f; 2f_0, \varsigma)$, respectively. Finally, a non-linearity index can be defined as

$$\mathrm{NI}(\mathrm{P}_i) = \frac{A_w(2f_0)}{A_w(f_0)}. \tag{5.50}$$

Figure 5.10a shows the spectrum of the y-displacement at point P_2. Additionally, the two products of the amplitude and weighting windows are plotted. The second harmonic is located at a frequency of around 1 MHz. As the second harmonic is only present due to the contact model, the index measures the non-linearity. This can be observed comparing the model's spectrum in Figure 5.10a with its linear counterpart from Section 4.8.2 in Figure 5.10b. Both models have the same settings except for the contact model. It is worth highlighting that NI is a ratio and independent of the signal's amplitude.

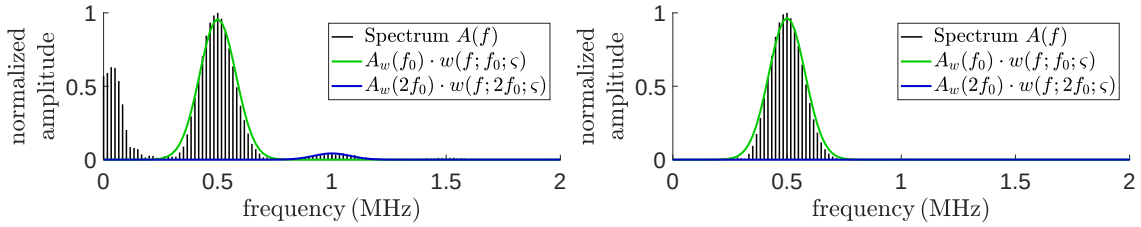

(a) $A(\mathrm{P}_2)$ for the non-linear model of Section 5.3.2 (b) $A(\mathrm{P}_2)$ for the linear model of Section 4.8.2

Figure 5.10: Spectrum at point P_2 for the y-displacement of the waveguide with the breathing crack

Figure 5.11 shows the non-linearity index measured for the reflected signal at P_1 and the transmitted signal at P_2 depending on the angle φ and the crack length r. The angle varies between $-10°$ and $10°$ with a step size of $2.5°$. The crack length changes between 0.1 mm and 0.5 mm with a step size of 0.05 mm. This parameter grid leads to 81 simulations with a computation time of

approx. 210 s per parameter pair. Additionally, the data is padded with zero values for $r = 0\,\text{mm}$. Each parameter pair is simulated with S0- and A0-excitation.

For each parameter point, the non-linearity index NI has a larger value for S0-excitation. For S0-excitation, it is monotonic until approx. $r = 0.35\,\text{mm}$. For this range, it is an appropriate damage index. For A0-excitation, the values are smaller, but the monotonic range increases. A monotonic behavior is important for a unique result and a simple connection between damage size and damage index. For both excitations and a short crack length r, the non-linearity index is insensitive to the angle. For a longer crack, the angle influences the non-linearity index NI. Qualitatively, the curves for an angle $\varphi = 0°$ for the non-linearity index are in agreement with [97, 123–125].

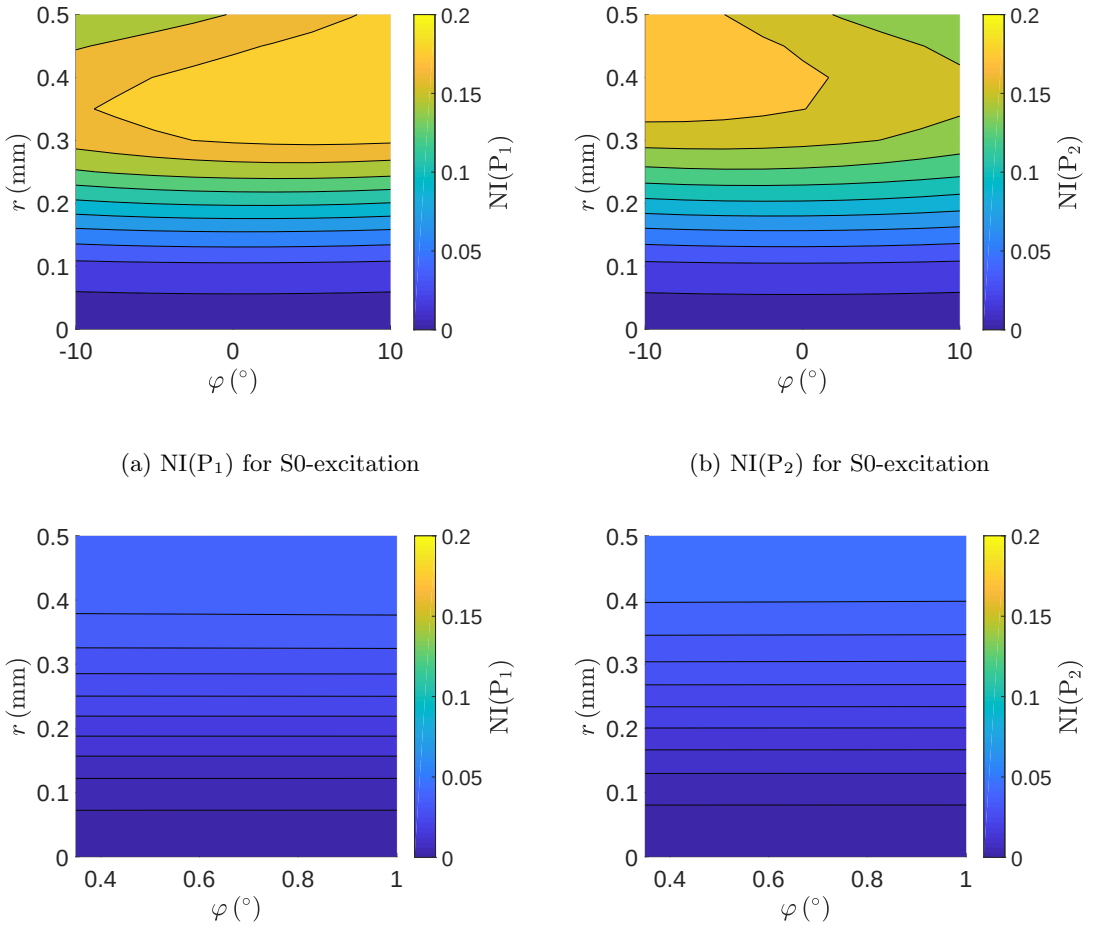

(a) NI(P_1) for S0-excitation

(b) NI(P_2) for S0-excitation

(c) NI(P_1) for A0-excitation

(d) NI(P_2) for A0-excitation

Figure 5.11: Non-linearity index for reflection and transmission depending on crack length r and angle φ for the center frequency $f_0 = 500\,\text{kHz}$

Figure 5.12 depicts the dependence of the non-linearity index on the center frequency f_0 and the crack length r. Here, only cracks parallel to the y-axis are considered. The crack length changes as above. The center frequency, on the other hand, varies between 350 kHz and 1 MHz with a step size of 50 kHz. This leads to 126 parameter points. The values for a vanishing crack length are padded with zeros for all frequencies. The non-linearity index is clearly frequency-dependent, but the value is monotonic up to approx. $r = 0.35\,\text{mm}$ for all frequencies. Again, S0-excitation leads to larger values for all investigated center frequencies if the same crack length is considered. The mesh is globally refined by one h-refinement step to take the higher frequencies into account. The computation time per parameter point is below five minutes, but due to the 126 parameter pairs,

an automation and fast calculation are required for such a contour plot.

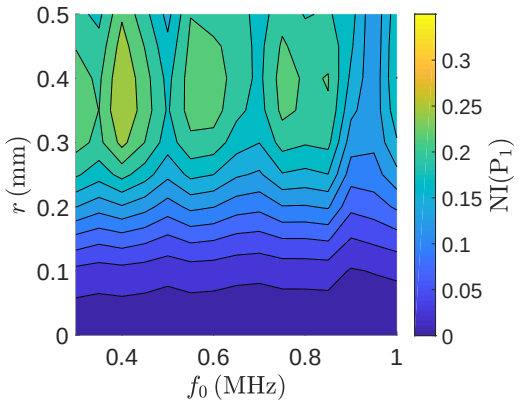

(a) NI(P$_1$) for S0-excitation

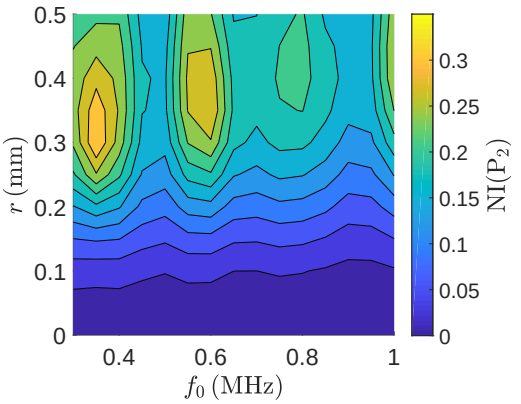

(b) NI(P$_2$) for S0-excitation

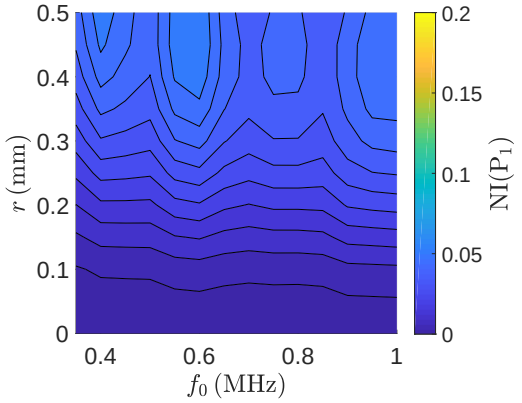

(c) NI(P$_1$) for A0-excitation

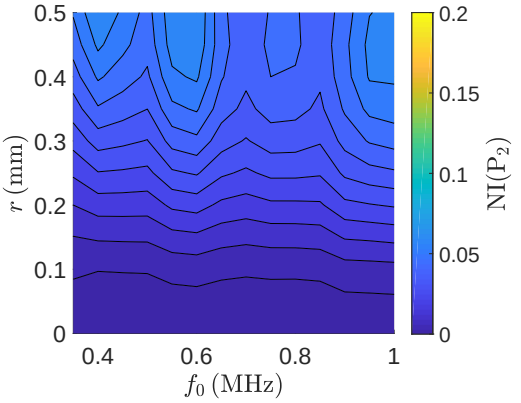

(d) NI(P$_2$) for A0-excitation

Figure 5.12: Non-linearity index for reflection and transmission depending on crack length r and center frequency f_0 for the angle $\varphi = 0°$

5.3.3 Waveguide with a Breathing Delamination

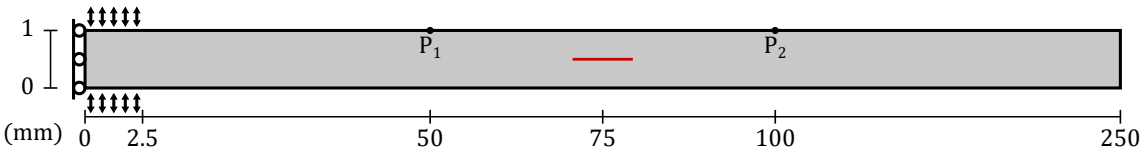

Figure 5.13: Waveguide with a breathing delamination

The next parametric study has nearly the same setup. The main difference is the type of damage which is a breathing delamination (see Figure 5.13). In this example, also the SB shape functions of degree $p = 3$ are utilized to study a delamination. Figure 5.14b shows an exemplary polygonal mesh with the defect. The parameters for the delamination are its length r and its y-position h_y in the cross-section (see Figure 5.14a). The delamination length r varies between 1 mm and 5 mm with a step size of 0.5 mm. The delamination height h_y varies between 0.3 mm and 0.7 mm with a step size of 0.05 mm. This leads to 81 parameter pairs.

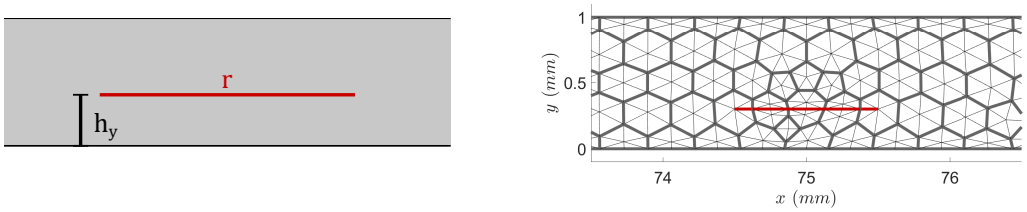

(a) Overview of the parameters

(b) Example of SBFEM-mesh for the smallest defects

Figure 5.14: Details on the breathing delamination in the waveguide

The non-linearity index NI for these parameters is shown in Figure 5.15. The relationship between the non-linearity index and the delamination length strongly depends on the y-position h_y in the cross-section. For the position $h_y = 0.5\,\text{mm}$ in the middle of the waveguide, the value of NI nearly vanishes. The mode shapes can explain the small value. For the S0-mode, the y-displacement is very small (see Figure 5.16a), and there is not much movement to close the contact. For the position in the middle, the delamination leads to no mode conversion for A0-excitation [19]. Thus, both sides can oscillate in phase. If both sides move equally, the contact is not closed. Additionally, the vanishing non-linearity index for a delamination in the middle of the waveguide is presumably increased due to the frictionless model. Therefore, the non-linearity index is not an easy-to-evaluate damage index for delaminations, which can occur at any y-position for isotropic media. For other materials, the y-position can often be narrowed down by prior knowledge of different layers [84].

5.3.4 Waveguide with Multiple Cracks

The last example presents other possibilities to investigate non-linear behavior with SB shape functions. Again, a waveguide as in Figure 5.13 is considered. The same setup is utilized, but the waveguide has multiple small cracks at $x = 75\,\text{mm}$. Figure 5.17 shows the polygonal mesh, where the defects are marked in red. S0-excitation is investigated with two different excitation signals in time. The first excitation τ_t is a narrow banded Gaussian pulse with a center frequency f_0 (Figure 5.18a):

$$\tau_t(t) = \sin(2\pi\, t f_0) \cdot \exp\big(-0.5(t - 0.25 f_0^{-1})^2/(0.5 f_0^{-1})^2\big), \tag{5.51}$$

where the center frequency f_0 is again 500 kHz. The second excitation should demonstrate frequency mixing, e.g., [80], and is a Gaussian pulse modulated with two frequencies (Figure 5.18b),i.e.,

$$\tau_t(t) = \big(\sin(2\pi\, t f_0) + \sin(2\pi\, t 2 f_0/3)\big) \cdot \exp\big(-0.5(t - 0.25 f_0^{-1})^2/(0.5 f_0^{-1})^2\big). \tag{5.52}$$

The approximation utilizes shape functions of a polynomial degree $p = 3$. A comparison with the next h-refinement step gives a point error below 0.2% for the signals at P_1 and P_2. The same time stepping as in the two previous examples are used.

Figure 5.18c and 5.18d show the spectrum of the y-displacement at point $P_2 = (100\,\text{mm}, 1\,\text{mm})$ for the S0-excitation with Equation (5.51) and Equation (5.52), respectively. Additionally, in Figure 5.18c the two weightings for the center frequency and the second harmonic are shown. Due to the narrow banded Gaussian window, the width ς in Equation (5.47) is $f_0(4\pi)^{-1}$. The non-linear index from the previous sections is

$$\frac{A_w(2f_0)}{A_w(f_0)} \approx 0.031. \tag{5.53}$$

Figure 5.18d depicts more peaks for the mixed excitation. The highest peaks correspond to the two frequencies $2f_0/3$ and f_0 and their higher harmonics, and there is also a peak at approx. 0.83 MHz which corresponds to the mixed frequency ($f_0 + 2f_0/3 \approx 0.83\,\text{MHz}$). A mixed non-linearity index

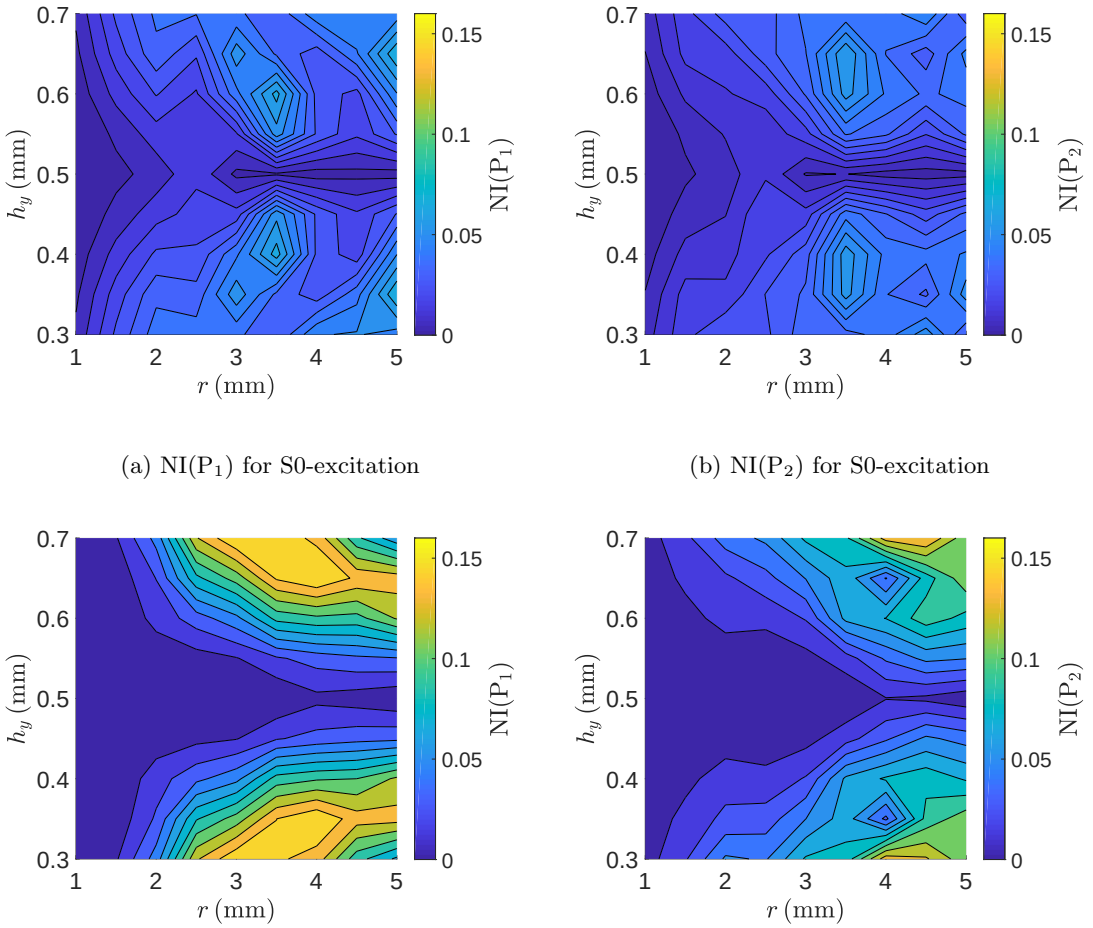

(a) NI(P$_1$) for S0-excitation

(b) NI(P$_2$) for S0-excitation

(c) NI(P$_1$) for A0-excitation

(d) NI(P$_2$) for A0-excitation

Figure 5.15: Non-linearity index for reflection and transmission depending on delamination length r and y-position h_y in the cross-section for the center frequency $f_0 = 500\,\mathrm{kHz}$

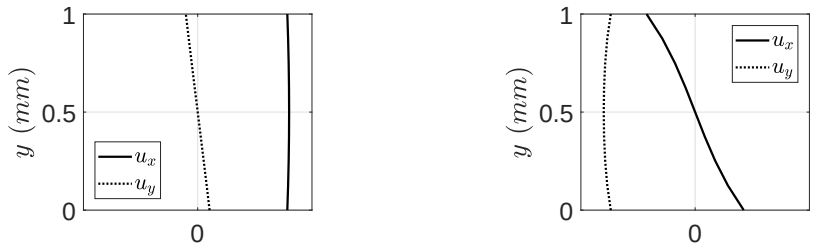

(a) S0 mode shape

(b) A0 mode shape

Figure 5.16: Mode shapes of the waveguide for the center frequency $f_0 = 500\,\mathrm{kHz}$

can be evaluated based on the mixed frequency

$$\frac{A_w(5f_0/3)}{A_w(f_0)} \approx 0.093. \tag{5.54}$$

In this case, frequency mixing leads to a higher non-linearity index. In general, higher values are preferable because they indicate a higher sensitivity of the method. But also the noise resistance is

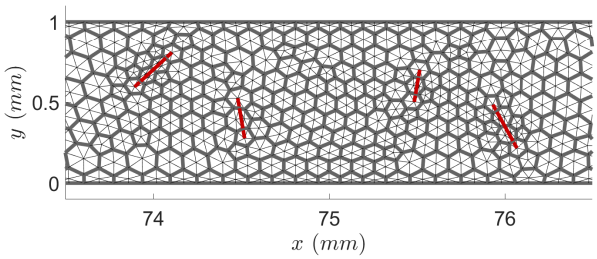

Figure 5.17: Details on the mesh with multiple cracks

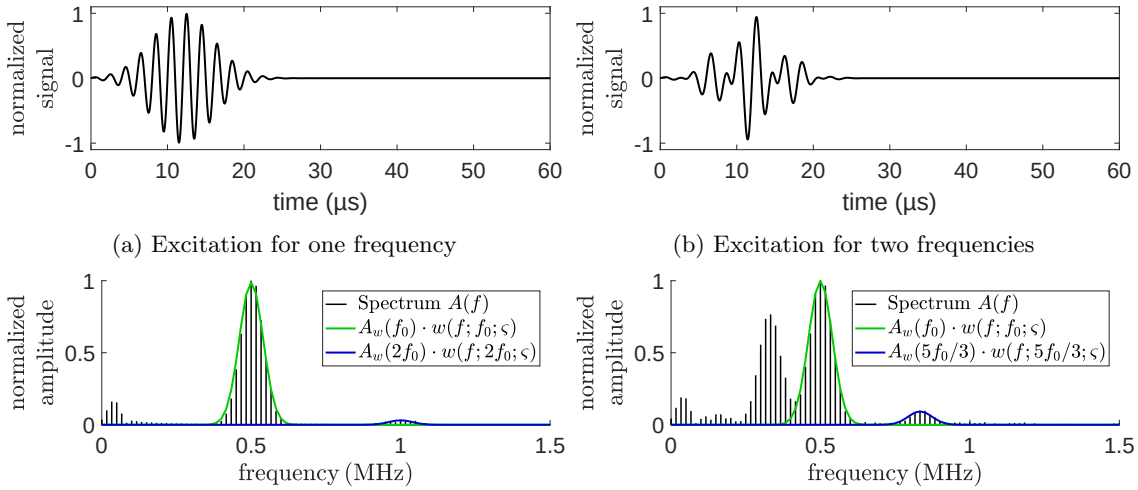

(a) Excitation for one frequency

(b) Excitation for two frequencies

(c) Spectrum at point P_2 for the y-displacement for excitation with one frequency

(d) Spectrum at point P_2 for the y-displacement for excitation with two frequencies

Figure 5.18: Example with mixed frequencies for a waveguide with multiple cracks

a deciding factor which excitation is better. Analysis of the noise resistance and mixed frequency excitation will be part of future work.

This example shows that also multiple defects can be analyzed. Due to the automated meshing, investigations are possible to gain statistical results as in [110, 153].

5.4 Conclusion for CAN

The two proposed methods, the enrichment approach and the SB shape functions on a polygonal mesh, are extended by a contact model to investigate breathing cracks and delaminations. Both methods show a good agreement with the reference approximation computed on a graded FEM mesh. The Penalty Method outperformed the Lagrange Multiplier Method for the enrichment approach. The better performance of the Penalty Method could hint at a suboptimal choice of the Lagrange multiplier shape functions near the crack tip. The Penalty Method is slower in the current implementation due to the recalculation of the penalty matrix.

On the other hand, the SB shape functions on a polygonal mesh show an overall good performance. Here, the Lagrange Multiplier Method leads to a fast algorithm. The combination with automatic mesh generation yields a tool to study breathing cracks and delaminations in more detail.

For the evaluation of breathing cracks and delaminations, a non-linearity index is proposed, including a window around the center frequency and the second harmonic. Contour plots illustrate the dependencies of the non-linearity on a single defect. The non-linearity index shows promising results for a simple damage index for surface cracks. For delaminations, the relationship between

damage size and non-linearity index is more complicated; thus, additional information must be considered, or a more complex inverse procedure must be implemented.

Chapter 6

Conclusion and Outlook

This section draws the conclusion of the thesis and gives an outlook on future research topics.

6.1 Conclusion

This thesis aimed at simulating breathing cracks for an application in Structural Health Monitoring (SHM) and Non-Destructive-Testing (NDT). Breathing cracks and delaminations are examples of contact acoustic non-linearity (CAN) with a crack-tip singularity. Therefore, the thesis focused on singularity and the simulation of contact acoustic non-linearity considering two-dimensional problems. In detail, the thesis presents shape functions, continuity, and contact conditions developed for the 2D simulation. Therefore, the research presented in this thesis is essential groundwork before an extension to three-dimensional problems can be done.

The approximation of structures with contact acoustic non-linearity is the starting point for discussing singular stresses and their relationship to continuity and contact conditions. A more profound knowledge of singular stresses, continuity, and contact conditions makes it possible to develop a more efficient algorithm to simulate breathing cracks. This knowledge of the singularity is gained by the Scaled Boundary Finite Element Method (SBFEM) that gives a semi-analytical solution of the singular point, which in turn facilitates the construction of shape functions leading to a more efficient simulation. The shape functions are required to simulate problems with singular stresses, continuity, and contact conditions which was done with mesh-based Galerkin methods in this work.

For defects such as breathing cracks and delaminations, a numerical simulation must consider two aspects. First, the edges of the defect, i.e., the endpoints in a two-dimensional simulation, have a singular stress field. Second, contact conditions must be incorporated. The semi-analytical SBFEM allows the investigation of those two effects. It confirms that the endpoints of a defect, e.g., the crack tips, are the only points with singular stress. Furthermore, the SBFEM can be used to analyze how contact pressure and singular modes influence each other. In general, the singular mode and the contact pressure depend on each other in a non-linear fashion. Therefore, singular modes and contact pressure are represented by power functions. Investigations presented in Section 3 indicate that for a crack tip in a single isotropic material the contact pressure can be approximated by polynomials.

The possibility to approximate the contact pressure with polynomials allows various shape functions in the Galerkin method. This thesis investigated two approaches:

1. An enrichment approach for higher-order finite elements based on the modes constructed with the SBFEM.

2. The construction of scaled boundary (SB) shape functions with bubble functions for the body load and the traction.

Additionally, graded meshes for the crack tip were studied as a reference method. The two main approaches are summarized in the following.

1. The enrichment approach is a general technique to treat singular stress points on triangular finite element meshes. The enrichment function is constructed with the SBFE-modes and allows a simple automation concerning different angles and material configurations. The support of the enrichment shape function includes only the elements adjacent to the critical point, which makes transitional elements unnecessary. A special quadrature is proposed for appropriate integration. It is demonstrated that enriched finite elements lead to the theoretical convergence rates for non-singular problems. For singular problems, the error decreases significantly for p-refinement. The convergence rates for h-refinement remained suboptimal. Nevertheless, the suboptimal convergence rates under h-refinement are usually reported for similar approaches, where the enriched area is not constant under h-refinement [3, 78, 116]. Additionally, stress intensity factors are evaluated with two different methods, namely the displacement-based method and the stress-based method. While the displacement-based technique leads to more precise results, the stress-based method requires no preliminary knowledge about the analytical solution. For dynamic problems with singularities but without contact, the approach still significantly improves with p-refinement. The improvement makes the enrichment approach attractive for linear SHM and NDT applications. For contact acoustic non-linearity, the enrichment approach is extended by two different methods, the Lagrange Multiplier Method and the Penalty Method. Those two methods integrate the contact pressure into the model and show better results than the Finite Element Method on a uniform mesh. Both methods showed different results when compared to the reference solution. While the Penalty Method has a good performance with respect to the number of degrees of freedom, the Lagrange Multiplier Method does not reach the same efficiency. The better performance of the Penalty Method indicates that the choice of Lagrange multiplier shape functions might be susceptible to improvement.

2. The construction of SB shape functions with bubble functions for the body load and the traction requires a more rigorous examination due to the novelty of the SB shape functions [72, 98, 181]. Modifying the computation of the SB shape functions, a stabilized algorithm is proposed in this thesis. The SB shape functions utilize a polygonal mesh. The presented numerical tests show that the shape functions lead to higher-order convergence in dynamic problems on a simply connected domain. This thesis constitutes the first convergence study of continuity conditions in conjunction with the SB shape functions. It demonstrates that the Lagrange Multiplier Method and SB shape functions lead to higher-order convergence on non-matching meshes. SB shape functions that include body loads and traction terms are presented for crack tips for the first time. These new shape functions show optimal convergence for an appropriate linear example. The performance in linear crack problems without contact forces is similar to the enrichment approach and makes the SB shape functions a good choice for linear SHM and NDT applications. The combination of the SB shape functions with the Lagrange Multiplier Method is demonstrated in the final approach for the computation of CAN on an example of breathing cracks and delaminations.

Two parametric studies showed the possibility to model CAN in an NDT or SHM application with ultrasonic waves. The SB shape functions were utilized to carry out these investigations. The investigated structures are plates with a thickness in the magnitude of the wavelength. The ultrasonic wave propagates as a Lamb wave with different modes in these plates. The non-linearity index is computed as a function of damage parameters. The two fundamental modes, S0 and A0, are investigated separately. For an angled crack, the dependency between the non-linearity index and the crack length is unique up to a particular length. The non-linearity index is shown to be insensitive to the angle. For the delamination, the relationship is more complicated. An inverse problem could be formulated to evaluate the non-linearity index for delaminations and more complex problems. An efficient forward model, which can automatically generate many defect configurations, is required for an inverse problem. The proposed model based on the SB shape functions is shown to be a promising candidate for a forward model.

6.2 Outlook

Further research on the topics of this thesis can be pursued which are presented in the following.

- The work can be extended to investigations in three dimensions. In the three-dimensional case, two different kinds of singularity can arise: 1) singularities that are associated with a point, and 2) singularities that are associated with an edge. An extension of the proposed method for both kinds may be possible. The extension to point singularities in three dimensions presents itself as a natural next step since scaled boundary two-dimensional and three-dimensional coordinate systems have very similar properties. For three dimensions, however, the boundary also contains singular terms, and the FEM mesh on the boundary needs to be adjusted [68]. In contrast, the edge singularity has to be considered in the scaling line coordinate system [13] which leads to a different ordinary differential equation.
- Regarding the scaled boundary shape functions for a breathing crack, a combination with a crack growth algorithm would enhance the analytical setup. The combination would lead to a realistic crack geometry under given loading conditions. Moreover, friction laws can be applied to the crack [181, 182]. Additional terms for the friction forces then have to be added to the shape functions because these forces are not represented in the current shape functions (see Section 3.5.3). Friction laws may lead to a better agreement between simulation and physical experiments.
- For the enrichment approach, a definition of a geometric method having a similar enrichment area under h-refinement would enhance the convergence. This geometric approach could also be further improved by a more mesh-independent formulation where the crack is not defined by a double node on the boundary but by means of a one-dimensional enrichment by a step function. These mesh-independent approaches are challenging to combine with contact forces [42, 91].
- To couple different meshes in order to reach better approximation results, the continuity conditions are beneficial as they can be combined with many approaches. For example, near-field and far-field approaches, e.g., [119] can have different optimal meshes which have to be coupled. The coupling of different methods is, in general, appealing in many applications. Section 4.13 tested the fundamentals and showed them to be stable for the Lagrange Multiplier Method. An investigation of the Nitsche Method could lead to an exact method that does not require extra degrees of freedom like the Lagrange Multiplier Method does since it does not utilize the inversion of a matrix like the Direct Elimination Method.
- For a breathing crack, a non-linearity parameter for predicting the damage size was calculated. As a next step, to evaluate the parameter's quality, an analysis of the sensitivity of the non-linearity parameter concerning noise is necessary. Additionally, the experimental validation remains an open task. If there is a mismatch between experimental and numerical results, the model can be extended with more assumptions to overcome the mismatch. The assumptions might be friction, residual stress, or plastic deformations around the crack-tip, just to name a few. These additional problem parameters can be studied purely numerically to estimate their influence. Unfortunately, a specimen where all parameters are known is an unrealistic case for NDT and SHM applications. As proposed in this thesis, a simple model considering physical properties might be preferable over a sophisticated model with unknown parameters.

Appendix A

Appendix

The Appendix contains additional information about the material models, matrix decompositions, and hp-quadrature.

A.1 Additional Information about Material Models

This appendix presents an overview of the elastic matrix in the VOIGT notation for different material laws. The overview includes the basic matrices, the two-dimensional simplifications, plane stress and plane strain, and rotation matrices. A list of tables with material parameters is incorporated at the end.

A.1.1 Isotropic Material

Isotropic materials show the simplest material behavior. A material is isotropic if the elastic properties are independent of the direction, and all material rotations lead to the same parameters. The elasticity matrix depends on two independent parameters. In this thesis, the material properties are given in most cases by YOUNG's modulus E and the POISSON's ratio ν.

HOOKE's law in VOIGT notation is

$$\boldsymbol{\sigma} = \mathbf{D}\boldsymbol{\varepsilon} \tag{A.1}$$

with

$$\boldsymbol{\sigma} = (\sigma_{xx}, \sigma_{yy}, \sigma_{zz}, \sigma_{yz}, \sigma_{yx}, \sigma_{xy})^{\mathsf{T}}, \tag{A.2}$$

$$\boldsymbol{\varepsilon} = (\varepsilon_{xx}, \varepsilon_{yy}, \varepsilon_{zz}, 2\varepsilon_{yz}, 2\varepsilon_{yx}, 2\varepsilon_{xy})^{\mathsf{T}} \tag{A.3}$$

Let G be the shear modulus, then it is related to the YOUNG's modulus E and the POISSON's ratio ν by

$$G = \frac{E}{2(1+\nu)}. \tag{A.4}$$

The elasticity matrix of an isotropic material is

$$\mathbf{D} = \begin{pmatrix} \frac{2(1-\nu)}{(1-2\nu)}G & \frac{2\nu}{(1-2\nu)}G & \frac{2\nu}{(1-2\nu)}G & 0 & 0 & 0 \\ * & \frac{2(1-\nu)}{(1-2\nu)}G & \frac{2\nu}{(1-2\nu)}G & 0 & 0 & 0 \\ * & * & \frac{2(1-\nu)}{(1-2\nu)}G & 0 & 0 & 0 \\ * & * & * & G & 0 & 0 \\ * & * & * & * & G & 0 \\ * & * & * & * & * & G \end{pmatrix}, \tag{A.5}$$

where $*$ is an entry, which leads to a symmetric matrix.

A.1.2 Transversely Isotropic Material

Transversely isotropic materials have one symmetry axis. The direction associated to the symmetry axis behaves differently than the other two directions which lie in the plane orthogonal to the symmetry axis. The elasticity matrix depends on five independent parameters. In this thesis, the following five parameters are utilized: YOUNG's modulus E_1 associated with the symmetry axis, YOUNG's modulus E_2 associated with the plane, shear modulus G_{12}, shear modulus G_{23}, and POISSON's ratio ν_{12}. The index 1 refers to the direction of the symmetry axis, while the indices 2 and 3 refer to the plane orthogonal to the symmetry axis. For a convenient definition, we use

$$\nu_{21} = \frac{E_2 \nu_{12}}{E_1}, \tag{A.6}$$

$$\nu_{23} = \frac{E_2}{2G_{23}} - 1, \tag{A.7}$$

$$\lambda = \frac{\nu_{12}\nu_{21} + \nu_{23}}{(1 - \nu_{23} - 2\nu_{12}\nu_{21})(1 + \nu_{23})} E_2. \tag{A.8}$$

The elasticity matrix of a transversely isotropic material is given by

$$\mathbf{D} = \begin{pmatrix} \frac{1-\nu_{23}}{1-\nu_{23}-2\nu_{12}\nu_{21}} E_1 & 2\nu_{12}(\lambda + G_{23}) & 2\nu_{12}(\lambda + G_{23}) & 0 & 0 & 0 \\ * & \lambda + 2G_{23} & \lambda & 0 & 0 & 0 \\ * & * & \lambda + 2G_{23} & 0 & 0 & 0 \\ * & * & * & G_{23} & 0 & 0 \\ * & * & * & * & G_{12} & 0 \\ * & * & * & * & * & G_{12} \end{pmatrix}, \tag{A.9}$$

where $*$ is an entry, which leads to a symmetric matrix.

A.1.3 Rotation Matrix

Sometimes the material directions are not aligned with the global coordinate system. For a given elasticity matrix $\mathbf{D}_\theta$ with a rotated material coordinate system, the elasticity matrix $\mathbf{D}$ in the global coordinate system can be calculated using a transformation matrix $\mathbf{R}$ and the following matrix product

$$\mathbf{D} = \mathbf{R}\mathbf{D}_\theta\mathbf{R}^\mathsf{T}. \tag{A.10}$$

The transformation matrix $\mathbf{R}_y^\theta$ for a rotation of θ around the y-axis is

$$\mathbf{R}_y^\theta = \begin{pmatrix} c^2 & 0 & s^2 & 0 & +2cs & 0 \\ 0 & 1 & 0 & 0 & 0 & 0 \\ s^2 & 0 & c^2 & 0 & -2cs & 0 \\ 0 & 0 & 0 & +c & 0 & -s \\ -cs & 0 & +cs & 0 & c^2 - s^2 & 0 \\ 0 & 0 & 0 & +s & 0 & +c \end{pmatrix} \tag{A.11}$$

with

$$c = \cos(\theta), \qquad s = \sin(\theta). \tag{A.12}$$

The transformation matrix $\mathbf{R}_z^\theta$ for a rotation of θ around the z-axis is [114]

$$\mathbf{R}_z^\theta = \begin{pmatrix} c^2 & s^2 & 0 & 0 & 0 & +2cs \\ s^2 & c^2 & 0 & 0 & 0 & -2cs \\ 0 & 0 & 1 & 0 & 0 & 0 \\ 0 & 0 & 0 & +c & -s & 0 \\ 0 & 0 & 0 & +s & +c & 0 \\ -cs & +cs & 0 & 0 & 0 & c^2 - s^2 \end{pmatrix}. \tag{A.13}$$

A.1.4 Plane Strain and Plane Stress

A common simplification of the physical problems can be utilized if particular fields in the domain only change inside a two-dimensional plane. In elastodynamics, there is no general two-dimensional case, but there are several assumptions which can be applicable. The two most common assumptions are plane strain and plane stress.

Plane strain Plane strain can be assumed if only the three strains $\varepsilon_{xx}, \varepsilon_{yy}, \varepsilon_{xy}$ in the xy-plane are changing and the values of $\varepsilon_{xz}, \varepsilon_{yz}, \varepsilon_{zz}$ are neglectable. This is mostly the case if the domain in the z-direction is very long and can be thought of as infinite. Then, the displacements in x- and y-direction are independent of the z-displacement. HOOKE's law in VOIGT-Notation can be reduced to

$$\begin{pmatrix} \sigma_{xx} \\ \sigma_{yy} \\ \sigma_{xy} \end{pmatrix} = \mathbf{D}_{\mathrm{2D}} \begin{pmatrix} \varepsilon_{xx} \\ \varepsilon_{yy} \\ \varepsilon_{xy} \end{pmatrix}. \tag{A.14}$$

The elasticity matrix $\mathbf{D}_{\mathrm{2D}} \in \mathbb{R}^{3\times 3}$ for plane strain can be computed with the elasticity matrix $\mathbf{D}_{\mathrm{3D}}$ for three dimensions as

$$\mathbf{D}_{\mathrm{2D}} = \mathbf{T}\mathbf{D}_{\mathrm{3D}}\mathbf{T}^{\mathsf{T}} \tag{A.15}$$

with

$$\mathbf{T} = \begin{pmatrix} 1 & 0 & 0 & 0 & 0 & 0 \\ 0 & 1 & 0 & 0 & 0 & 0 \\ 0 & 0 & 0 & 0 & 0 & 1 \end{pmatrix}. \tag{A.16}$$

Plane stress Plane stress can be assumed if only $\sigma_{xx}, \sigma_{yy}, \sigma_{xy}$ vary in the xy-plane. This is usually applied to very thin structures. Similarly to plane strain, the z-displacement is independent of the other two displacements. The elasticity matrix $\mathbf{D}_{\mathrm{2D}} \in \mathbb{R}^{3\times 3}$ for plane stress can be computed with the elasticity matrix $\mathbf{D}_{\mathrm{3D}}$ for three dimensions as

$$\mathbf{D}_{\mathrm{2D}} = \left(\mathbf{T}\mathbf{D}_{\mathrm{3D}}^{-1}\mathbf{T}^{\mathsf{T}}\right)^{-1} \tag{A.17}$$

with $\mathbf{T}$ from Equation (A.16), where $\mathbf{D}_{\mathrm{3D}}^{-1}$ is the compliance matrix, that gives the linear dependency of the strain on the stress, i.e.,

$$\boldsymbol{\varepsilon} = \mathbf{D}_{\mathrm{3D}}^{-1}\boldsymbol{\sigma}. \tag{A.18}$$

A.1.5 Tables

This part contains all parameters concerning the different materials.

Isotropic material								
E:	7/3	GPa	ν:	1/3	ρ:	1	$\mathrm{g\,cm^{-3}}$	

(a) Patch Test Material

Isotropic material $\Omega_{(a)}$								
E:	$2.6\left(\frac{1+\alpha}{1-\alpha}\right)$	GPa	ν:	0.3	ρ:	1	$\mathrm{g\,cm^{-3}}$	
Isotropic material $\Omega_{(b)}$								
E:	2.6	GPa	ν:	0.3	ρ:	1	$\mathrm{g\,cm^{-3}}$	

(b) α-Test Materials

Isotropic material								
E:	70	GPa	ν:	1/3	ρ:	2.70	$\mathrm{g\,cm^{-3}}$	

(c) Aluminum

Isotropic material								
E:	200	GPa	ν:	0.3	ρ:	7.85	$\mathrm{g\,cm^{-3}}$	

(d) Structural steel

Transversely isotropic material								
E_1:	171	GPa	G_{12}:	5.3	GPa	ν_{12}:	0.32	
E_2:	9	GPa	G_{23}:	2.8	GPa	ρ:	1.57	$\mathrm{g\,cm^{-3}}$

(e) Carbon fiber reinforced polymer [113]

Isotropic material								
E:	24	GPa	ν:	0.2	ρ:	$25\pi^2$	$\mathrm{g\,cm^{-3}}$	

(f) Artificial material

Table A.1: Material parameters of the investigated examples

A.2 Appendix Matrix Decompositions

Eigenvalue Decomposition Let $\mathbf{Z} \in \mathbb{C}^{n\times n}$ be a matrix with n linearly independent eigenvectors. Then, $\mathbf{Z}$ can be factorized as

$$\mathbf{Z} = \mathbf{V}\boldsymbol{\Lambda}\mathbf{V}^{-1}, \tag{A.19}$$

where $\boldsymbol{\Lambda}$ is a diagonal matrix of the eigenvalues.

A complex normal matrix $\mathbf{Z}$ (i.e., $\mathbf{Z}^*\mathbf{Z} = \mathbf{Z}\mathbf{Z}^*$) has an orthogonal eigenvector basis, so a normal matrix can be decomposed as

$$\mathbf{Z} = \mathbf{Q}\boldsymbol{\Lambda}\mathbf{Q}^*, \tag{A.20}$$

where $\mathbf{Q}$ is a unitary matrix (i.e., $\mathbf{Q}\mathbf{Q}^* = \mathbf{I}$) and $\boldsymbol{\Lambda}$ is a diagonal matrix of the eigenvalues.

If the matrix $\mathbf{Z}$ is a real symmetric matrix, the eigenvalues are real and the eigenvectors can be chosen such that they are orthogonal.

CHOLESKY **decomposition** The CHOLESKY decomposition of a HERMITIAN (i.e., $\mathbf{Z}^* = \mathbf{Z}$) positive-definite matrix $\mathbf{Z} \in \mathbb{C}^{n\times n}$ is a decomposition of the form

$$\mathbf{Z} = \mathbf{L}\boldsymbol{\Lambda}\mathbf{L}^*, \tag{A.21}$$

where $\mathbf{L}$ is a lower unit triangular matrix, and $\boldsymbol{\Lambda}$ is a diagonal matrix.

SCHUR **decomposition** The SCHUR decomposition of $\mathbf{Z} \in \mathbb{C}^{n\times n}$ reads as

$$\mathbf{Z} = \mathbf{Q}\mathbf{U}\mathbf{Q}^*, \tag{A.22}$$

where $\mathbf{Q}$ is a unitary matrix, and $\mathbf{U}$ is a quasi-upper triangular matrix, which is called a SCHUR form of $\mathbf{Z}$. The matrix $\mathbf{U}$ has 2-by-2 blocks on the diagonal. Since $\mathbf{U}$ is similar to $\mathbf{Z}$, it has the same spectrum, and since it is triangular, its eigenvalues are the diagonal entries of $\mathbf{U}$.

A.3 hp-refined Quadrature

The presented hp-refined quadrature is utilized in this thesis to integrate singular functions as well as polynomial functions on a reference triangle T. For a singular function, the singular point is assumed to be the origin of the triangle.

Let ζ_i^n be a GAUSS point of the n-point GAUSS quadrature rule, ω_i^n its corresponding weight on $[-1,+1]$, and g the function to integrate. The inverse of DUFFY's transformation (Equation (3.140)) is defined by

$$\mathfrak{d}^{-1}\colon (\hat{\xi},\hat{\eta}) \mapsto (\hat{\alpha},\hat{\beta}) = \left(\hat{\xi}\frac{1}{2}(\hat{\eta}-1), \hat{\xi}\frac{1}{2}(\hat{\eta}+1)\right), \tag{A.23}$$

where $\hat{\alpha},\hat{\beta} \in [0,1]$ are the local triangle coordinates with $\hat{\alpha}+\hat{\beta} \leq 1$, $\hat{\xi} \in [0,1]$ and $\hat{\eta} \in [-1,+1]$. For K cells, the hp-refined GAUSSquadrature [120] the reference triangle T is given by

$$\iint_T g(\hat{\alpha},\hat{\beta})\,\mathrm{d}\hat{\alpha}\,\mathrm{d}\hat{\beta} \approx \sum_{n=1}^{K}\sum_{i=1}^{n}\sum_{j=1}^{n} g\big(\mathfrak{d}^{-1}(\hat{\xi}_i^n,\hat{\eta}_j^n)\big)\omega_i^n\omega_j^n\frac{\hat{\xi}_i^n}{4}(a_{n+1}-a_n) \tag{A.24}$$

with

$$\hat{\xi}_i^n = \zeta_i^n\frac{1}{2}(a_{n+1}-a_n) + \frac{1}{2}(a_{n+1}+a_n), \tag{A.25}$$

$$\hat{\eta}_i^n = \zeta_i^n, \tag{A.26}$$

$$a_n = \begin{cases} 0 & \text{for } n=1 \\ (0.15)^{(K+1-n)} & \text{for } n=2,\ldots,K+1 \end{cases}. \tag{A.27}$$

Bibliography

[1] V. Acary. "Energy conservation and dissipation properties of time-integration methods for nonsmooth elastodynamics with contact". In: *ZAMM-Journal of Applied Mathematics and Mechanics/Zeitschrift für Angewandte Mathematik und Mechanik* 96.5 (2016), pp. 585–603.

[2] J. Achenbach and A. Norris. "Loss of specular reflection due to nonlinear crack-face interaction". In: *Journal of Nondestructive Evaluation* 3.4 (1982), pp. 229–239.

[3] K. Agathos, E. Chatzi, and S. P. Bordas. "A unified enrichment approach addressing blending and conditioning issues in enriched finite elements". In: *Computer Methods in Applied Mechanics and Engineering* 349 (2019), pp. 673–700.

[4] T. L. Anderson. *Fracture mechanics: fundamentals and applications*. CRC press, 2017.

[5] D. N. Arnold, F. Brezzi, B. Cockburn, and L. D. Marini. "Unified analysis of discontinuous Galerkin methods for elliptic problems". In: *SIAM Journal on Numerical Analysis* 39.5 (2002), pp. 1749–1779.

[6] I. Babuška. "The finite element method with penalty". In: *Mathematics of Computation* 27.122 (1973), pp. 221–228.

[7] M. Bach, A. M. Khludnev, and V. A. Kovtunenko. "Derivatives of the energy functional for 2D-problems with a crack under Signorini and friction conditions". In: *Mathematical Methods in the Applied Sciences* 23.6 (2000), pp. 515–534.

[8] K.-J. Bathe. "Conserving energy and momentum in nonlinear dynamics: a simple implicit time integration scheme". In: *Computers & structures* 85.7-8 (2007), pp. 437–445.

[9] M. H. Bazyar and C. Song. "A continued-fraction-based high-order transmitting boundary for wave propagation in unbounded domains of arbitrary geometry". In: *International Journal for Numerical Methods in Engineering* 74.2 (2008), pp. 209–237.

[10] R. Becker, P. Hansbo, and R. Stenberg. "A finite element method for domain decomposition with non-matching grids". In: *ESAIM: Mathematical Modelling and Numerical Analysis* 37.2 (2003), pp. 209–225.

[11] L. Beirão da Veiga, F. Brezzi, L. D. Marini, and A. Russo. "The hitchhiker's guide to the virtual element method". In: *Mathematical Models and Methods in Applied Sciences* 24.08 (2014), pp. 1541–1573.

[12] S. E. Benzley. "Representation of singularities with isoparametric finite elements". In: *International Journal for Numerical Methods in Engineering* 8.3 (1974), pp. 537–545. ISSN: 1097-0207. DOI: 10.1002/nme.1620080310. URL: http://onlinelibrary.wiley.com/doi/10.1002/nme.1620080310/abstract.

[13] C. Birk and R. Behnke. "A modified scaled boundary finite element method for three-dimensional dynamic soil-structure interaction in layered soil". In: *International Journal for Numerical Methods in Engineering* 89.3 (2012), pp. 371–402.

[14] M. G. Blyth and C. Pozrikidis. "A Lobatto interpolation grid over the triangle". In: *IMA Journal of Applied Mathematics* 71.1 (2006), pp. 298–313. ISSN: 02724960. DOI: 10.1093/imamat/hxh111. URL: http://dx.doi.org/10.1093/imamat/hxh111.

[15] L. Bos, M. Taylor, and B. Wingate. "Tensor product Gauss-Lobatto points are Fekete points for the cube". In: *Mathematics of Computation* 70.236 (2001), pp. 1543–1547.

[16] M. Briani, A. Sommariva, and M. Vianello. “Computing Fekete and Lebesgue points: simplex, square, disk”. In: *Journal of Computational and Applied Mathematics* 236.9 (2012), pp. 2477–2486.

[17] E. Brivadis, A. Buffa, B. Wohlmuth, and L. Wunderlich. “Isogeometric mortar methods”. In: *Computer Methods in Applied Mechanics and Engineering* 284 (2015), pp. 292–319.

[18] D. Broda, W. Staszewski, A. Martowicz, T. Uhl, and V. Silberschmidt. “Modelling of nonlinear crack–wave interactions for damage detection based on ultrasound—A review”. In: *Journal of Sound and Vibration* 333.4 (2014), pp. 1097–1118.

[19] J. Bulling, B. Jurgelucks, J. Prager, and A. Walther. “Defect reconstruction in a two-dimensional semi-analytical waveguide model via derivative-based optimization”. In: *The Journal of the Acoustical Society of America* 152.2 (2022), pp. 1217–1229.

[20] J. Bulling and H. Gravenkamp. “A Combination of the Scaled Boundary Finite Element Method with the Mortar Method”. In: *14th WCCM-ECCOMAS Congress* (2021). DOI: 10.23967/wccm-eccomas.2020.004. URL: https://doi.org/10.23967%5C%2Fwccm-eccomas.2020.004.

[21] J. Bulling, G. Franosch, Y. Lugovtsova, and J. Prager. “Sensitivity of Ultrasonic Guided Waves to Elastic Constants: A Numerical Study”. In: *European Workshop on Structural Health Monitoring* (2020), pp. 759–768.

[22] J. Bulling and H. Gravenkamp. “Comparison of different models for stress singularities in higher order finite element methods for elastic waves”. In: *PAMM* 19.1 (2019), e201900095.

[23] J. Bulling, H. Gravenkamp, and C. Birk. “A high-order finite element technique with automatic treatment of stress singularities by semi-analytical enrichment”. In: *Computer Methods in Applied Mechanics and Engineering* 355 (2019), pp. 135–156.

[24] J. Bulling, V. John, and P. Knobloch. “Isogeometric analysis for flows around a cylinder”. In: *Applied Mathematics Letters* 63 (2017), pp. 65–70.

[25] J. Bulling, B. Jurgelucks, J. Prager, and A. Walther. “Ein inverses Verfahren zur Schadensrekonstruktion mittels geführter Wellen”. In: *Tagungsband DAGA 2021*. Deutsche Gesellschaft für Akustik (DEGA). 2021, pp. 1–4.

[26] J. Bulling and J. Prager. “Bestimmung der Rissgeometrie bei der zerstörungsfreien Ultraschallprüfung mit geführten Wellen”. In: *DAGA 2019*. Vol. 45. Deutsche Gesellschaft für Akustik eV. 2019, p. 1063.

[27] A. Byfut and A. Schröder. “hp-adaptive extended finite element method”. In: *International Journal for Numerical Methods in Engineering* 89.11 (2012), pp. 1392–1418.

[28] A. B. Chaudhary and K.-J. Bathe. “A solution method for static and dynamic analysis of three-dimensional contact problems with friction”. In: *Computers & Structures* 24.6 (1986), pp. 855–873.

[29] D. Chen, C. Birk, C. Song, and C. Du. “A high-order approach for modelling transient wave propagation problems using the scaled boundary finite element method”. In: *International Journal for Numerical Methods in Engineering* 97.13 (2014), pp. 937–959.

[30] M. C. Chen, K. Y. Sze, and H. T. Wang. “Analysis of singular stresses in bonded bimaterial wedges by computed eigen solutions and hybrid element method”. In: *Communications in Numerical Methods in Engineering* 17.7 (2001), pp. 495–507. ISSN: 10698299. DOI: 10.1002/cnm.425. URL: http://dx.doi.org/10.1002/cnm.425.

[31] I. Chiong, E. T. Ooi, C. Song, and F. Tin-Loi. “Scaled boundary polygons with application to fracture analysis of functionally graded materials”. In: *International Journal for Numerical Methods in Engineering* 98.8 (2014), pp. 562–589.

[32] K. O. Coelho, P. R. Devloo, and S. M. Gomes. “Error estimates for the scaled boundary finite element method”. In: *Computer Methods in Applied Mechanics and Engineering* 379 (2021), p. 113765.

[33] M. Comninou. "Interface crack with friction in the contact zone". In: *Journal of Applied Mechanics* 44.4 (1977), pp. 780–781. ISSN: 00218936. DOI: 10.1115/1.3424179. URL: http://appliedmechanics.asmedigitalcollection.asme.org/article.aspx?articleid=1403617.

[34] J. A. Cottrell, T. J. R. Hughes, and Y. Bazilevs. *Isogeometric analysis: toward integration of CAD and FEA*. John Wiley & Sons, 2009.

[35] J. A. Cottrell, T. J. R. Hughes, and A. Reali. "Studies of refinement and continuity in isogeometric structural analysis". In: *Computer Methods in Applied Mechanics and Engineering* 196.41-44 (2007), pp. 4160–4183. DOI: 10.1016/j.cma.2007.04.007. URL: http://dx.doi.org/10.1016/j.cma.2007.04.007.

[36] A. Czekanski, N. El-Abbasi, and S. Meguid. "Optimal time integration parameters for elastodynamic contact problems". In: *Communications in Numerical Methods in Engineering* 17.6 (2001), pp. 379–384.

[37] L. B. Da Veiga, F. Brezzi, and L. D. Marini. "Virtual elements for linear elasticity problems". In: *SIAM Journal on Numerical Analysis* 51.2 (2013), pp. 794–812.

[38] L. Demkowicz, W. Rachowicz, and P. Devloo. "A fully automatic hp-adaptivity". In: *Journal of Scientific Computing* 17.1-4 (2002), pp. 117–142.

[39] L. Demkowicz, J. T. Oden, W. Rachowicz, and O. Hardy. "Toward a universal hp adaptive finite element strategy, Part 1. Constrained approximation and data structure". In: *Computer Methods in Applied Mechanics and Engineering* 77.1-2 (1989), pp. 79–112.

[40] J. P. Dempsey and G. B. Sinclair. "On the stress singularities in the plane elasticity of the composite wedge". In: *Journal of Elasticity* 9.4 (1979), pp. 373–391.

[41] X. Deng. "On stationary and moving interface cracks with frictionless contact in anisotropic bimaterials". In: *Proceedings of the Royal Society of London. Series A: Mathematical and Physical Sciences* 443.1919 (1993), pp. 563–572.

[42] J. Dolbow, N. Moës, and T. Belytschko. "An extended finite element method for modeling crack growth with frictional contact". In: *Computer Methods in Applied Mechanics and Engineering* 190.51-52 (2001), pp. 6825–6846.

[43] W. Dornisch, J. Stoeckler, and R. Müller. "Dual and approximate dual basis functions for B-splines and NURBS–Comparison and application for an efficient coupling of patches with the isogeometric mortar method". In: *Computer Methods in Applied Mechanics and Engineering* 316 (2017), pp. 449–496.

[44] W. Dornisch, G. Vitucci, and S. Klinkel. "The weak substitution method–an application of the mortar method for patch coupling in NURBS-based isogeometric analysis". In: *International Journal for Numerical Methods in Engineering* 103.3 (2015), pp. 205–234.

[45] D. Doyen, A. Ern, and S. Piperno. "Time-integration schemes for the finite element dynamic Signorini problem". In: *SIAM Journal on Scientific Computing* 33.1 (2011), pp. 223–249.

[46] C. A. Duarte, I. Babuška, and J. T. Oden. "Generalized finite element methods for three-dimensional structural mechanics problems". In: *Computers & Structures* 77.2 (2000), 215–232.

[47] S. Duczek, A. A. Saputra, and H. Gravenkamp. "High order transition elements: The xNy-element concept—Part I: Statics". In: *Computer Methods in Applied Mechanics and Engineering* 362 (2020), p. 112833.

[48] J. Dundurs and M. Lee. "Stress concentration at a sharp edge in contact problems". In: *Journal of Elasticity* 2.2 (1972), pp. 109–112. ISSN: 03743535. DOI: 10.1007/BF00046059.

[49] J. Dundurs and M. Comninou. "Some consequences of the inequality conditions in contact and crack problems". In: *Journal of Elasticity* 9.1 (1979), pp. 71–82.

[50] A. W. Egger, E. N. Chatzi, and S. P. Triantafyllou. "An enhanced scaled boundary finite element method for linear elastic fracture". In: *Archive of Applied Mechanics* 87.10 (2017), pp. 1667–1706. ISSN: 14320681. DOI: 10.1007/s00419-017-1280-7. URL: http://dx.doi.org/10.1007/s00419-017-1280-7.

[51] S. Eisenträger, J. Eisenträger, H. Gravenkamp, and C. Provatidis. "High order transition elements: The xNy-element concept, Part II: Dynamics". In: *Computer Methods in Applied Mechanics and Engineering* 387 (2021), p. 114145.

[52] A. England. "A crack between dissimilar media". In: *Journal of Applied Mechanics* 32.2 (1965), pp. 400–402.

[53] C. R. Farrar and K. Worden. "An introduction to structural health monitoring". In: *Philosophical Transactions of the Royal Society A: Mathematical, Physical and Engineering Sciences* 365.1851 (2007), pp. 303–315.

[54] K. Fischer and P. Wriggers. "Frictionless 2D contact formulations for finite deformations based on the mortar method". In: *Computational Mechanics* 36.3 (2005), pp. 226–244.

[55] M. S. Floater and M.-J. Lai. "Polygonal spline spaces and the numerical solution of the Poisson equation". In: *SIAM Journal on Numerical Analysis* 54.2 (2016), pp. 797–824.

[56] T. Fries and T. Belytschko. "The extended/generalized finite element method: an overview of the method and its applications". In: *International Journal for Numerical Methods in Engineering* 84.3 (2010), pp. 253–304. ISSN: 17359260.

[57] E. Gdoutos and P. Theocaris. "Stress concentrations at the apex of a plane indenter acting on an elastic half plane". In: *Journal of Applied Mechanics* 42.September 1975 (1975), pp. 688–692.

[58] J. Geuzaine C. Remacle. "Gmsh: A 3-D finite element mesh generator with built-in pre- and post-processing facilities". In: *International Journal for Numerical Methods in Engineering* 79.11 (2009), pp. 1309–1331. ISSN: 0743-1619. arXiv: 1201.4903. URL: http://arxiv.org/abs/1201.4903.

[59] S. S. Ghorashi, N. Valizadeh, S. Mohammadi, and T. Rabczuk. "T-spline based XIGA for fracture analysis of orthotropic media". In: *Computers & Structures* 147 (2015), pp. 138–146. ISSN: 0045-7949. DOI: 10.1016/j.compstruc.2014.09.017. URL: http://dx.doi.org/10.1016/j.compstruc.2014.09.017.

[60] S. Ghosh and R. Mallett. "Voronoi cell finite elements". In: *Computers & Structures* 50.1 (1994), pp. 33–46.

[61] H. Gravenkamp. "Efficient simulation of elastic guided waves interacting with notches, adhesive joints, delaminations and inclined edges in plate structures". In: *Ultrasonics* 82 (2018), pp. 101–113.

[62] H. Gravenkamp and S. Natarajan. "Scaled boundary polygons for linear elastodynamics". In: *Computer Methods in Applied Mechanics and Engineering* 333 (2018), pp. 238–256.

[63] H. Gravenkamp, J. Prager, A. A. Saputra, and C. Song. "The simulation of Lamb waves in a cracked plate using the scaled boundary finite element method". In: *The Journal of the Acoustical Society of America* 132.3 (2012), pp. 1358–1367.

[64] H. Gravenkamp, A. A. Saputra, and S. Duczek. "High-order shape functions in the scaled boundary finite element method revisited". In: *Archives of Computational Methods in Engineering* (2019), pp. 1–22.

[65] H. Gravenkamp, C. Song, and J. Prager. "A numerical approach for the computation of dispersion relations for plate structures using the scaled boundary finite element method". In: *Journal of Sound and Vibration* 331.11 (2012), pp. 2543–2557.

[66] H. Gravenkamp, C. Song, and J. Zhang. "On mass lumping and explicit dynamics in the scaled boundary finite element method". In: *Computer Methods in Applied Mechanics and Engineering* 370 (2020), p. 113274.

[67] C. Grossmann, H.-G. Roos, and M. Stynes. *Numerical treatment of partial differential equations*. Vol. 154. Springer, 2007.

[68] S. Hell and W. Becker. "The scaled boundary finite element method for the analysis of 3D crack interaction". In: *Journal of computational science* 9 (2015), pp. 76–81.

[69] R. D. Henshell and K. G. Shaw. "Crack tip finite elements are unnecessary". In: *International Journal for Numerical Methods in Engineering* 9.3 (1975), pp. 495–507. ISSN: 0029-5981. DOI: 10.1002/nme.1620090302. URL: http://dx.doi.org/10.1002/nme.1620090302.

[70] H. M. Hilber, T. J. Hughes, and R. L. Taylor. "Improved numerical dissipation for time integration algorithms in structural dynamics". In: *Earthquake Engineering & Structural Dynamics* 5.3 (1977), pp. 283–292.

[71] T. J. R. Hughes and J. E. Akin. "Techniques for developing 'special' finite element shape functions with particular reference to singularities". In: *International Journal for Numerical Methods in Engineering* 15.5 (1980), pp. 733–751.

[72] Y.-M. Jia, C.-J. Li, Y. Zhang, and J. Chen. "The high-order completeness analysis of the scaled boundary finite element method". In: *Computer Methods in Applied Mechanics and Engineering* 362 (2020), p. 112867.

[73] J. Jingpin, M. Xiangji, H. Cunfu, and W. Bin. "Nonlinear Lamb wave-mixing technique for micro-crack detection in plates". In: *Ndt & E International* 85 (2017), pp. 63–71.

[74] B. L. Karihaloo and Q. Z. Xiao. "Modelling of stationary and growing cracks in FE framework without remeshing: A state-of-the-art review". In: *Computers & Structures* 81.3 (2003), pp. 119–129. ISSN: 00457949. DOI: 10.1016/S0045-7949(02)00431-5. URL: http://dx.doi.org/10.1016/S0045-7949(02)00431-5.

[75] K. Kawashima, R. Omote, T. Ito, H. Fujita, and T. Shima. "Nonlinear acoustic response through minute surface cracks: FEM simulation and experimentation". In: *Ultrasonics* 40.1-8 (2002), pp. 611–615.

[76] M. Kögl, S. Hurlebaus, and L. Gaul. "Finite element simulation of non-destructive damage detection with higher harmonics". In: *NDT & E International* 37.3 (2004), pp. 195–205.

[77] F. Krome and H. Gravenkamp. "A semi-analytical curved element for linear elasticity based on the scaled boundary finite element method". In: *International Journal for Numerical Methods in Engineering* 109 (2017), pp. 790–808. ISSN: 10970207. DOI: 10.1002/nme.5306. URL: http://dx.doi.org/10.1002/nme.5306.

[78] P. Laborde, J. Pommier, Y. Renard, and M. Salaün. "High-order extended finite element method for cracked domains". In: *International Journal for Numerical Methods in Engineering* 64.3 (2005), pp. 354–381.

[79] J. Lee and H. Gao. "A generalized Comninou contact model for interface cracks in anisotropic elastic solids". In: *International Journal of Fracture* 67.1 (1994), pp. 53–68.

[80] F. Li and F. Zou. "A hybrid spectral/finite element method for accurate and efficient modelling of crack-induced contact acoustic nonlinearity". In: *Journal of Sound and Vibration* 508 (2021), p. 116198.

[81] P.-L. Lions. "On the Schwarz alternating method. III: a variant for nonoverlapping subdomains". In: *Third international symposium on domain decomposition methods for partial differential equations*. Vol. 6. SIAM Philadelphia, PA. 1990, pp. 202–223.

[82] X. Y. Liu, Q. Z. Xiao, and B. L. Karihaloo. "XFEM for direct evaluation of mixed mode SIFs in homogeneous and bi-materials". In: *International Journal for Numerical Methods in Engineering* 59.8 (2004), pp. 1103–1118. ISSN: 00295981. DOI: 10.1002/nme.906. URL: https://doi.org/10.1002/nme.906.

[83] Y. Lugovtsova, J. Bulling, C. Boller, and J. Prager. "Analysis of guided wave propagation in a multi-layered structure in view of structural health monitoring". In: *Applied Sciences* 9.21 (2019), p. 4600.

[84] Y. Lugovtsova et al. "Damage quantification in an aluminium-CFRP composite structure using guided wave wavenumber mapping: Comparison of instantaneous and local wavenumber analyses". In: *NDT & E International* (2021), p. 102472.

[85] Y. Maday, C. Mavriplis, and A. T. Patera. *Nonconforming mortar element methods: Application to spectral discretizations*. 1988.

[86] M. Mengolini, M. F. Benedetto, and A. M. Aragón. "An engineering perspective to the virtual element method and its interplay with the standard finite element method". In: *Computer Methods in Applied Mechanics and Engineering* 350 (2019), pp. 995–1023.

[87] N. Miyazaki, T. Ikeda, T. Soda, and T. Munakata. "Stress intensity factor analysis of interface crack using boundary element method - application of contour-integral method". In: *Engineering Fracture Mechanics* 45.5 (1993), pp. 599–610. ISSN: 00137944. DOI: 10.1016/0013-7944(93)90266-U. URL: https://doi.org/10.1016/0013-7944(93)90266-U.

[88] N. Moës, J. Dolbow, and T. Belytschko. "A finite element method for crack growth without remeshing". In: *International Journal for Numerical Methods in Engineering* 46.1 (1999), pp. 131–150. ISSN: 00295981.

[89] S. E. Mousavi and N. Sukumar. "Generalized Duffy transformation for integrating vertex singularities". In: *Computational Mechanics* 45.2-3 (2010), pp. 127–140. ISSN: 01787675.

[90] S. E. Mousavi and N. Sukumar. "Numerical integration of polynomials and discontinuous functions on irregular convex polygons and polyhedrons". In: *Computational Mechanics* 47.5 (2011), pp. 535–554. ISSN: 01787675. DOI: 10.1007/s00466-010-0562-5. URL: https://doi.org/10.1007/s00466-010-0562-5.

[91] D. Mueller-Hoeppe, P. Wriggers, and S. Loehnert. "Crack face contact for a hexahedral-based XFEM formulation". In: *Computational Mechanics* 49.6 (2012), pp. 725–734.

[92] I. Müller, A. Konyukhov, P. Vielsack, and K. Schweizerhof. "Parameter estimation for finite element analyses of stationary oscillations of a vibro-impacting system". In: *Engineering Structures* 27.2 (2005), pp. 191–201.

[93] S. Natarajan and C. Song. "Representation of singular fields without asymptotic enrichment in the extended finite element method". In: *International Journal for Numerical Methods in Engineering* 96.13 (2013), pp. 813–841.

[94] S. Nazarov. "A crack at the interface of anisotropic bodies. Singularities of the elastic fields and a criterion for fracture when the crack surfaces are in contact". In: *Journal of Applied Mathematics and Mechanics* 69.3 (2005), pp. 473–483.

[95] V. P. Nguyen, T. Rabczuk, S. Bordas, and M. Duflot. "Meshless methods: A review and computer implementation aspects". In: *Mathematics and Computers in Simulation* 79.3 (2008), pp. 763–813. ISSN: 03784754. DOI: 10.1016/j.matcom.2008.01.003. arXiv: 10.1.1.160.1721. URL: https://doi.org/10.1016/j.matcom.2008.01.003.

[96] J. Nitsche. "Über ein Variationsprinzip zur Lösung von Dirichlet-Problemen bei Verwendung von Teilräumen, die keinen Randbedingungen unterworfen sind". In: *Abhandlungen aus dem mathematischen Seminar der Universität Hamburg*. Vol. 36. Springer. 1971, pp. 9–15.

[97] J.-i. Okada, T. Ito, K. Kawashima, and N. Nishimura. "Finite element simulation of nonlinear acoustic behavior at minute cracks using singular element". In: *Japanese Journal of Applied Physics* 40.5S (2001), p. 3579.

[98] E. T. Ooi, C. Song, and S. Natarajan. "Construction of high-order complete scaled boundary shape functions over arbitrary polygons with bubble functions". In: *International Journal for Numerical Methods in Engineering* 108.9 (2016), pp. 1086–1120.

[99] E. T. Ooi, C. Song, F. Tin-Loi, and Z. Yang. "Polygon scaled boundary finite elements for crack propagation modelling". In: *International Journal for Numerical Methods in Engineering* 91.3 (2012), pp. 319–342.

[100] E. Ooi, H. Man, S. Natarajan, and C. Song. "Adaptation of quadtree meshes in the scaled boundary finite element method for crack propagation modelling". In: *Engineering Fracture Mechanics* 144 (2015), pp. 101–117.

[101] P. Otto, L. De Lorenzis, and J. F. Unger. "Explicit dynamics in impact simulation using a NURBS contact interface". In: *International Journal for Numerical Methods in Engineering* 121.6 (2020), pp. 1248–1267.

[102] S. S. Pageau and S. B. Biggers Jr. "Enrichment of finite elements with numerical solutions for singular stress fields". In: *International Journal for Numerical Methods in Engineering* 40.14 (1997), pp. 2693–2713.

[103] S. S. Pageau and S. B. Iggers. "Enriched finite elements for regions with multiple, interacting singular fields". In: *AIAA Journal* 34.9 (1996), pp. 1927–1933. ISSN: 0001-1452. DOI: 10.2514/3.13327. URL: http://arc.aiaa.org/doi/10.2514/3.13327.

[104] S. S. Pageau and S. B. Biggers Jr. "Enrichment of finite elements with numerical solutions for singular stress fields". In: *International Journal for Numerical Methods in Engineering* 40.14 (1997), pp. 2693–2713.

[105] S. S. Pageau and S. B. Biggers Jr. "A finite element approach to three-dimensional singular stress states in anisotropic multi-material wedges and junctions". In: *International Journal of Solids and Structures* 33.1 (1996), pp. 33–47.

[106] S. S. Pageau and S. B. iggers. "Enriched finite elements for regions with multiple, interacting singular fields". In: *AIAA Journal* 34.9 (1996), pp. 1927–1933.

[107] T. Pin and T. H. H. Pian. "On the convergence of the finite element method for problems with singularity". In: *International Journal of Solids and Structures* 9.3 (1973), pp. 313–321.

[108] A. Pramod, E. T. Ooi, C. Song, S. Natarajan, et al. "An adaptive scaled boundary finite element method for contact analysis". In: *European Journal of Mechanics-A/Solids* 86 (2021), p. 104180.

[109] J. R. M. Radok. "On the solution of problems of dynamic plane elasticity". In: *Quarterly of Applied Mathematics* 14.3 (1956), pp. 289–298.

[110] N. Rauter, R. Lammering, and T. Kühnrich. "On the detection of fatigue damage in composites by use of second harmonic guided waves". In: *Composite Structures* 152 (2016), pp. 247–258.

[111] J. Rice. "Elastic fracture mechanics concepts for interfacial cracks". In: *Journal of Applied Mechanics* 55.1 (1988), pp. 98–103.

[112] R. Rodriguez and J. Solomin. "The order of convergence of eigenfrequencies in finite element approximations of fluid-structure interaction problems". In: *Mathematics of Computation* 65.216 (1996), pp. 1463–1475.

[113] M. Rogge and C. Leckey. "Characterization of impact damage in composite laminates using guided wavefield imaging and local wavenumber domain analysis". In: *Ultrasonics* 53.7 (2013), pp. 1217–1226.

[114] S. Rokhlin, D. Chimenti, and P. Nagy. *Physical ultrasonics of composites*. Oxford University Press, 2011.

[115] Y. Ryoji and C. Sang-Bong. "Efficient boundary element analysis of stress intensity factors for interface cracks in dissimilar materials". In: *Engineering Fracture Mechanics* 34.1 (1989), pp. 179–188. ISSN: 00137944. DOI: 10.1016/0013-7944(89)90251-8. URL: https://doi.org/10.1016/0013-7944(89)90251-8.

[116] A. G. Sanchez-Rivadeneira and C. A. Duarte. "A stable generalized/eXtended FEM with discontinuous interpolants for fracture mechanics". In: *Computer Methods in Applied Mechanics and Engineering* 345 (2019), pp. 876–918.

[117] A. Saputra, C. Birk, and S. C. "Computation of three-dimensional fracture parameters at interface cracks and notches by the scaled boundary finite element method". In: *Engineering Fracture Mechanics* 148 (2015), pp. 213–242. ISSN: 0013-7944. DOI: 10.1016/j.engfracmech.2015.09.006. URL: http://dx.doi.org/10.1016/j.engfracmech.2015.09.006.

[118] R. A. Sauer and L. De Lorenzis. "A computational contact formulation based on surface potentials". In: *Computer Methods in Applied Mechanics and Engineering* 253 (2013), pp. 369–395.

[119] M. Schauer and G. R. Rodriguez. "A coupled FEM-SBFEM approach for soil-structure-interaction analysis using non-matching meshes at the near-field far-field interface". In: *Soil Dynamics and Earthquake Engineering* 121 (2019), pp. 466–479.

[120] C. Schwab. "Variable order composite quadrature of singular and nearly singular integrals". In: *Computing* 53.2 (1994), pp. 173–194.

[121] N. Sepehry, M. Ehsani, W. Zhu, and F. Bakhtiari-Nejad. "Application of scaled boundary finite element method for vibration-based structural health monitoring of breathing cracks". In: *Journal of Vibration and Control* (2020), p. 1077546320968646.

[122] P. Seshaiyer and M. Suri. "Convergence results for non-conforming hp methods: The mortar finite element method". In: *Contemporary Mathematics* 218 (1998), pp. 453–459.

[123] Y. Shen and V. Giurgiutiu. "Predictive modeling of nonlinear wave propagation for structural health monitoring with piezoelectric wafer active sensors". In: *Journal of Intelligent Material Systems and Structures* 25.4 (2014), pp. 506–520.

[124] Y. Shen and V. Giurgiutiu. "Predictive simulation of nonlinear ultrasonics". In: *Health Monitoring of Structural and Biological Systems 2012*. Vol. 8348. International Society for Optics and Photonics. 2012, 83482E.

[125] Y. Shen and V. Giurgiutiu. "Simulation of interaction between Lamb waves and cracks for structural health monitoring with piezoelectric wafer active sensors". In: *Smart Materials, Adaptive Structures and Intelligent Systems*. Vol. 45097. American Society of Mechanical Engineers. 2012, pp. 615–623.

[126] G. Sih. "Some elastodynamic problems of cracks". In: *International Journal of Fracture Mechanics* 4.1 (1968), pp. 51–68.

[127] G. Sih, G. Embley, and R. Ravera. "Impact response of a finite crack in plane extension". In: *International Journal of Solids and Structures* 8.7 (1972), pp. 977–993.

[128] I. Y. Solodov. "Ultrasonics of non-linear contacts: propagation, reflection and NDE- applications". In: *Ultrasonics* 36.1-5 (1998), pp. 383–390.

[129] C. Song. "Analysis of singular stress fields at multi-material corners under thermal loading". In: *International Journal for Numerical Methods in Engineering* 65.5 (2006), pp. 620–652. ISSN: 00295981. DOI: 10.1002/nme.1456. URL: http://dx.doi.org/10.1002/nme.1456.

[130] C. Song, F. Tin-Loi, and W. Gao. "A definition and evaluation procedure of generalized stress intensity factors at cracks and multi-material wedges". In: *Engineering Fracture Mechanics* 77 (2010), pp. 2316–2336. DOI: 10.1088/1757-899X/10/1/012042. URL: http://dx.doi.org/10.1088/1757-899X/10/1/012042.

[131] C. Song and J. P. Wolf. "Body loads in scaled boundary finite-element method". In: *Computer Methods in Applied Mechanics and Engineering* 180.1-2 (1999), pp. 117–135. ISSN: 00457825. DOI: 10.1016/S0045-7825(99)00052-3. URL: http://dx.doi.org/10.1016/S0045-7825(99)00052-3.

[132] C. Song and J. P. Wolf. "The scaled boundary finite-element method - alias consistent infinitesimal finite-element cell method - for elastodynamics". In: *Computer Methods in Applied Mechanics and Engineering* 147.3-4 (1997), pp. 329–355. ISSN: 00457825. DOI: 10.1016/S0045-7825(97)00021-2. URL: http://dx.doi.org/10.1016/S0045-7825(97)00021-2.

[133] C. Song. "The scaled boundary finite element method in structural dynamics". In: *International Journal for Numerical Methods in Engineering* 77.8 (2009), pp. 1139–1171.

[134] C. Song. *The Scaled Boundary Finite Element Method: Introduction to Theory and Implementation*. Wiley, 2018.

[135] C. Song, E. T. Ooi, and S. Natarajan. "A review of the scaled boundary finite element method for two-dimensional linear elastic fracture mechanics". In: *Engineering Fracture Mechanics* 187 (2018), pp. 45–73.

[136] C. Song and J. P. Wolf. "Body loads in scaled boundary finite-element method". In: *Computer Methods in Applied Mechanics and Engineering* 180.1-2 (1999), pp. 117–135.

[137] C. Song and J. P. Wolf. "Consistent infinitesimal finite-element cell method: three- dimensional vector wave equation". In: *International Journal for Numerical Methods in Engineering* 39.13 (1996), pp. 2189–2208.

[138] A. Stroh. "Dislocations and cracks in anisotropic elasticity". In: *Philosophical Magazine* 3.30 (1958), pp. 625–646.

[139] A. Stroh. "Steady state problems in anisotropic elasticity". In: *Journal of Mathematics and Physics* 41.1-4 (1962), pp. 77–103.

[140] T. Strouboulis, K. Copps, and I. Babuška. "The generalized finite element method". In: *Computer Methods in Applied Mechanics and Engineering* 190.32-33 (2001), pp. 4081–4193. DOI: 10.1016/S0045-7825(01)00188-8. URL: http://dx.doi.org/10.1016/S0045-7825(01)00188-8.

[141] G. R. Stultz, R. W. Bono, and M. I. Schiefer. "Fundamentals of resonant acoustic method NDT". In: *Advances in Powder Metallurgy and Particulate Materials* 3 (2005), p. 11.

[142] Z. Su and L. Ye. "Selective generation of Lamb wave modes and their propagation characteristics in defective composite laminates". In: *Proceedings of the Institution of Mechanical Engineers, Part L: Journal of Materials: Design and Applications* 218.2 (2004), pp. 95–110.

[143] N. Sukumar. "Quadratic maximum-entropy serendipity shape functions for arbitrary planar polygons". In: *Computer Methods in Applied Mechanics and Engineering* 263 (2013), pp. 27–41.

[144] N. Sukumar and A. Tabarraei. "Conforming polygonal finite elements". In: *International Journal for Numerical Methods in Engineering* 61.12 (2004), pp. 2045–2066.

[145] Z. Suo. "Singularities, interfaces and cracks in dissimilar anisotropic media". In: *Proceedings of the Royal Society of London. A. Mathematical and Physical Sciences* 427.1873 (1990), pp. 331–358.

[146] A. Sutin and V. Nazarov. "Nonlinear acoustic methods of crack diagnostics". In: *Radiophysics and Quantum Electronics* 38.3-4 (1995), pp. 109–120.

[147] B. A. Szabo and A. K. Mehta. "p-convergent finite element approximations in fracture mechanics". In: *International Journal for Numerical Methods in Engineering* 12.3 (1978), pp. 551–560.

[148] B. Szabó and I. Babuska. *Finite Element Analysis*. John Wiley & Sons, 1991, p. 387.

[149] K. Y. Sze and H. t. Wang. "Simple finite element formulation for computing stress singularities at bimaterial interfaces". In: *Finite Elements in Analysis and Design* 35.2 (1999), pp. 97–118. ISSN: 0168874X. DOI: 10.1016/S0168-874X(99)00057-8.

[150] M. A. Taylor, B. A. Wingate, and R. E. Vincent. "An algorithm for computing Fekete points in the triangle". In: *SIAM Journal on Numerical Analysis* 38.5 (2000), pp. 1707–1720.

[151] D. K. L. Tsang and S. O. Oyadiji. "Super singular element method for two-dimensional crack analysis". In: *Proceedings of the Royal Society of London A: Mathematical, Physical and Engineering Sciences* 464.2098 (2008), pp. 2629–2648. ISSN: 1364-5021. DOI: 10.1098/rspa.2007.0265. URL: http://dx.doi.org/10.1098/rspa.2007.0265.

[152] K. Tschöke and H. Gravenkamp. "On the numerical convergence and performance of different spatial discretization techniques for transient elastodynamic wave propagation problems". In: *Wave Motion* 82 (2018), pp. 62–85.

[153] K. Tschöke et al. "Feasibility of Model-Assisted Probability of Detection Principles for Structural Health Monitoring Systems based on Guided Waves for Fibre-Reinforced Composites". In: *IEEE Transactions on Ultrasonics, Ferroelectrics, and Frequency Control* (2021).

[154] H. Uzawa. "Iterative methods for concave programming". In: *Studies in Linear and Nonlinear Programming* 6 (1958), pp. 154–165.

[155] X. Wan, Q. Zhang, G. Xu, and P. W. Tse. "Numerical simulation of nonlinear Lamb waves used in a thin plate for detecting buried micro-cracks". In: *Sensors* 14.5 (2014), pp. 8528–8546.

[156] M. Williams. "Stress singularities resulting from various boundary conditions in angular corners of plates in extension". In: *Journal of Applied Mechanics* 19.4 (1952), pp. 526–528. ISSN: 00218936. DOI: 10.1115/1.321174.

[157] M. Williams. "The stresses around a fault or crack in dissimilar media". In: *Bulletin of the Seismological Society of America* 49.2 (1959), pp. 199–204.

[158] B. I. Wohlmuth. "A mortar finite element method using dual spaces for the Lagrange multiplier". In: *SIAM Journal on Numerical Analysis* 38.3 (2000), pp. 989–1012.

[159] B. I. Wohlmuth and R. H. Krause. "Monotone multigrid methods on nonmatching grids for nonlinear multibody contact problems". In: *SIAM Journal on Scientific Computing* 25.1 (2003), pp. 324–347.

[160] J. P. Wolf and C. Song. "Dynamic-stiffness matrix in time domain of unbounded medium by infinitesimal finite element cell method". In: *Earthquake Engineering & Structural Dynamics* 23 (1994), pp. 1181–1198. ISSN: 10969845. DOI: 10.1002/eqe.4290231103. URL: http://dx.doi.org/10.1002/eqe.4290231103.

[161] J. P. Wolf and C. Song. "The scaled boundary finite-element method - a primer: derivations". In: *Computers & Structures* 78 (2000), pp. 191–210.

[162] J. P. Wolf. *The Scaled Boundary Finite Element Method*. Wiley, 2003.

[163] P. Wriggers and G. Zavarise. *Computational contact mechanics*. Springer, 2004.

[164] Q. Z. Xiao and B. L. Karihaloo. "An overview of a hybrid crack element and determination of its complete displacement field". In: *Engineering Fracture Mechanics* 74.7 (2007), pp. 1107–1117. ISSN: 00137944. DOI: 10.1016/j.engfracmech.2006.12.022. URL: http://dx.doi.org/10.1016/j.engfracmech.2006.12.022.

[165] Q. Z. Xiao and B. L. Karihaloo. "Implementation of hybrid crack element on a general finite element mesh and in combination with XFEM". In: *Computer Methods in Applied Mechanics and Engineering* 196.13-16 (2007), pp. 1864–1873. ISSN: 00457825.

[166] W. Xing, C. Song, and F. Tin-Loi. "A scaled boundary finite element based node-to-node scheme for 2D frictional contact problems". In: *Computer Methods in Applied Mechanics and Engineering* 333 (2018), pp. 114–146.

[167] W. Xing, J. Zhang, C. Song, and F. Tin-Loi. "A node-to-node scheme for three-dimensional contact problems using the scaled boundary finite element method". In: *Computer Methods in Applied Mechanics and Engineering* 347 (2019), pp. 928–956.

[168] Y. Yamada and H. Okumura. "Finite element analysis of stress and strain singularity eigenstate in inhomogeneous media or composite materials". In: *International Symposium on Hybrid and Mixed Finite Element Methods, Atlanta, GA*. 1981, p. 1981.

[169] K. Yamanaka, T. Mihara, and T. Tsuji. "Evaluation of closed cracks by model analysis of subharmonic ultrasound". In: *Japanese Journal of Applied Physics* 43.5S (2004), p. 3082.

[170] W. Yang, Z. Suo, and C. Shih. "Mechanics of dynamic debonding". In: *Proceedings of the Royal Society of London. Series A: Mathematical and Physical Sciences* 433.1889 (1991), pp. 679–697.

[171] Z. J. Yang, A. J. Deeks, and H. Hao. "A Frobenius solution to the scaled boundary finite element equations in frequency domain for bounded media". In: *International Journal for Numerical Methods in Engineering* 70.12 (2007), pp. 1387–1408.

[172] Z. Yang, X. Wang, D. Yin, and C. Zhang. "A non-matching finite element-scaled boundary finite element coupled method for linear elastic crack propagation modelling". In: *Computers & Structures* 153 (2015), pp. 126–136.

[173] Z. Yang, Z. Zhang, G. Liu, and E. Ooi. "An h-hierarchical adaptive scaled boundary finite element method for elastodynamics". In: *Computers & Structures* 89.13-14 (2011), pp. 1417–1429.

[174] W. Yao, Z. Cai, and X. Hu. "A new symplectic analytical singular element for crack problems under dynamic loading condition". In: *Engineering Fracture Mechanics* 188 (2018), pp. 431–447. ISSN: 00137944. DOI: 10.1016/j.engfracmech.2017.09.016. URL: https://doi.org/10.1016/j.engfracmech.2017.09.016.

[175] W. A. Yao and X. F. Hu. "A novel singular finite element of mixed-mode crack problems with arbitrary crack tractions". In: *Mechanics Research Communications* 38.3 (2011), pp. 170–175. ISSN: 00936413. DOI: 10.1016/j.mechrescom.2011.03.009. URL: https://doi.org/10.1016/j.mechrescom.2011.03.009.

[176] J. R. Yeh and I. G. Tadjbakhsh. "Stress singularity in composite laminates by finite element method". In: *Journal of composite materials* 20.July (1986), pp. 347–364.

[177] J. Yeh and I. Tadjbakhsh. "Stress singularity in composite laminates by finite element method". In: *Journal of Composite Materials* 20.4 (1986), pp. 347–364.

[178] Z. Yosibash and B. Szabó. "Numerical analysis of singularities in two-dimensions part 1: Computation of eigenpairs". In: *International Journal for Numerical Methods in Engineering* 38.12 (1995), pp. 2055–2082.

[179] N. D. Zander. "Multi-level hp-FEM: dynamically changing high-order mesh refinement with arbitrary hanging nodes". PhD thesis. Technische Universität München, 2017.

[180] J. Zhang, A. Ankit, H. Gravenkamp, S. Eisenträger, and C. Song. "A massively parallel explicit solver for elasto-dynamic problems exploiting octree meshes". In: *Computer Methods in Applied Mechanics and Engineering* 380 (2021), p. 113811.

[181] P. Zhang, C. Du, X. Tian, and S. Jiang. "A scaled boundary finite element method for modelling crack face contact problems". In: *Computer Methods in Applied Mechanics and Engineering* 328 (2018), pp. 431–451.

[182] P. Zhang, C. Du, W. Zhao, and L. Sun. "Dynamic crack face contact and propagation simulation based on the scaled boundary finite element method". In: *Computer Methods in Applied Mechanics and Engineering* 385 (2021), p. 114044.

[183] Z. Zhang, Z. Yang, and J. Li. "An adaptive polygonal scaled boundary finite element method for elastodynamics". In: *International Journal of Computational Methods* 13.02 (2016), p. 1640015.

[184] Z. Zhang, Z. Yang, G. Liu, and Y. Hu. "An adaptive scaled boundary finite element method by subdividing subdomains for elastodynamic problems". In: *Science China Technological Sciences* 54.1 (2011), pp. 101–110.

[185] W. Zulehner. "Analysis of iterative methods for saddle point problems: a unified approach". In: *Mathematics of Computation* 71.238 (2002), pp. 479–505.

List of Figures

1.1 Schematic diagram of a breathing crack 1

2.1 Different types of meshes for a trapezoidal domain 7
2.2 Element mappings 8
2.3 Example of shape functions in 2D 8
2.4 Example of shape functions with a local degree; polynomial degree changes over an edge 11
2.5 Finite deformation vs. small deformation 13
2.6 Schematic diagram of a discretized contact area 14

3.1 Crack coordinate system 17
3.2 Sketch of a rectangular body sliding over a larger body 18
3.3 Crack with the different contact transitions 20
3.4 Singular modes of a crack 22
3.5 The scaled boundary coordinate system 24
3.6 Example of SB shape functions with vanishing traction 27
3.7 Example for the three modified SB shape functions gained by direct elimination . . 29
3.8 Domain and SBFEM-mesh for the transition problem between a frictionless contact zone and a separation zone 30
3.9 $\lambda_{\min}$ in the transition problem for isotropic materials 31
3.10 Normal stress at point P_c for the singular mode with $\gamma = \pi$ for the model in Figure 3.8 32
3.11 $\lambda_{\min}$ in the transition problem for transversally isotropic materials 33
3.12 Example of the SB shape function associated with a constant traction 37
3.13 Test for a single super-element with a crack; constant traction and one material . . 40
3.14 Eigenvalues of a single super-element with a crack; one material 40
3.15 Test for a single super-element with a crack; non-polynomial traction and one material 41
3.16 Nodal comparison between Direct Elimination Method and LAGRANGE Multiplier Method 41
3.17 Test for a single super-element with a crack; constant traction and two materials . 42
3.18 Eigenvalues of a single super-element with a crack; two materials 42
3.19 Nodal comparison between Direct Elimination Method and LAGRANGE Multiplier Method for the tests of a crack between two materials 42
3.20 Definition of an SBFE-polygon within a triangular finite element mesh [23] 43
3.21 Eigenvalues of the SBFE-polygon given in Figure 3.20b for an isotropic material (plane strain, $\nu = 1/3$) [23] 45
3.22 Transformation maps between different coordinate systems [23] 46
3.23 Example of an enrichment function according to Equation (3.141) for the grid in Figure 3.20b with $\lambda_i = -0.62$ [23] 46
3.24 Grading for singular points 47
3.25 Domain with DIRICHLET boundary conditions [23] 49
3.26 Comparison of energy-errors between the standard FEM and the current approach for the problem defined by Equations (3.152) [23] 50

3.27 Relative error in K_c obtained using method 3.9.2.1, method 3.9.2.2, and replacing the polygon around the crack tip with an SBFEM-polygonal element for p = 1, . . . , 8 [23] . . . 51
3.28 Comparison of energy-errors between the standard FEM and the current work for the problem defined by Equations (3.155) – the lines coincide [23] . . . 52
3.29 Crack under shear load (dimensions in mm) [23] . . . 53
3.30 Relative deviation from the reference $\|\mathbf{u}^{\text{ref}}\|_{\mathcal{E}} = 4.967356034022807$ for the crack under shear [23] . . . 53
3.31 Bi-material crack under tension (dimensions in mm) [23] . . . 54
3.32 Isotropic-anisotropic crack under tension (dimensions in mm) . . . 54
3.33 SIFs computed with the stress-based method 3.9.2.1 for the anisotropic-isotropic crack under tension for p-refinement with p = 2, . . . , 10. The dashed lines correspond to reference values from [130] . . . 56
3.34 Example involving multiple stress concentrations (dimensions in mm) [23] . . . 56
3.35 Relative deviation from the reference $\|\mathbf{u}^{\text{ref}}\|_{\mathcal{E}} = 89.264095354384537$ for the example with multiple singularities [23] . . . 56

4.1 Example of SB shape functions associated with a constant body load . . . 62
4.2 Example polygon and matrix plots . . . 64
4.3 Dual meshes and h-refinement for polygonal meshes . . . 65
4.4 Domain and approximation of Equation (4.36) for a trapezoidal domain . . . 66
4.5 L^2-error with respect to Equation (4.36) for the trapezoidal domain (Figure 4.4a) 67
4.6 Condition number for the trapezoidal domain (Figure 4.4a) . . . 67
4.7 Meshes with sb-refinement of a trapezoidal domain . . . 68
4.8 Analysis with sb-refinement for a trapezoidal domain . . . 68
4.9 Analysis of the eigenfrequencies of a unit square . . . 69
4.10 Comparison of rectangular domains . . . 70
4.11 Signal for the point $P_1 = (8\,\text{mm}, 1\,\text{mm})^\mathsf{T}$ on a rectangular domain . . . 70
4.12 Point error for the rectangular domain . . . 71
4.13 Example meshes for the three methods used to model an L-shaped domain . . . 73
4.14 Signal at point P on the L-shaped domain (Figure 4.13a) . . . 73
4.15 Point error for the L-shaped domain for two different center frequencies (Equation (4.51)) at point P . . . 73
4.16 Relationship between the experimental and mathematical model for a double transducer . . . 74
4.17 Waveguide with a linear crack . . . 74
4.18 Time- and frequency-dependence of the excitation with $f_0 = 500\,\text{kHz}$ . . . 74
4.19 Mesh details around the crack tip for the waveguide . . . 74
4.20 Point error for the linear waveguide . . . 75
4.21 Signal at point P_1 for the linear waveguide (Figure 4.17) . . . 76
4.22 Mortar concept . . . 77
4.23 Example of two continued shape functions of p = 2 . . . 80
4.24 Discrete mortar elements . . . 83
4.25 Static patch tests with FEM in combination with the Mortar Method . . . 83
4.26 Energy errors for the patch test on a rectangular divided domain with LMM, DEM and PM . . . 85
4.27 Domain consisting of two sub-domains . . . 85
4.28 Domain consisting of three sub-domains . . . 86
4.29 Three crack models with vanishing normal gap . . . 87
4.30 Approximation of the displacement (Equation (4.101)) with SB shape functions . . 88
4.31 Quadrature detail for the enrichment . . . 88

5.1 Model problem for CAN . . . 90
5.2 Two waveguides in contact . . . 96
5.3 Signal at point P_1 for two waveguides in contact (Figure 5.2) . . . 96
5.4 Signal at the midpoint of the contact area for two waveguides in contact (Figure 5.2) 96

5.5 Point error for two waveguides in contact (Figure 5.2) 97
5.6 Waveguide with a breathing crack 97
5.7 Signal at point P_1 for the breathing crack in the waveguide (Figure 5.6) 97
5.8 Point error for S0-excitation for the breathing crack in the waveguide 98
5.9 Details on the breathing crack in the waveguide 98
5.10 Spectrum at point P_2 for the y-displacement of the waveguide with the breathing crack 99
5.11 Non-linearity index for reflection and transmission depending on crack length r and angle φ for the center frequency $f_0 = 500\,\mathrm{kHz}$ 100
5.12 Non-linearity index for reflection and transmission depending on crack length r and center frequency f_0 for the angle $\varphi = 0^\circ$ 101
5.13 Waveguide with a breathing delamination 101
5.14 Details on the breathing delamination in the waveguide 102
5.15 Non-linearity index for reflection and transmission depending on delamination length r and y-position h_y in the cross-section for the center frequency $f_0 = 500\,\mathrm{kHz}$ . . . 103
5.16 Mode shapes of the waveguide for the center frequency $f_0 = 500\,\mathrm{kHz}$ 103
5.17 Details on the mesh with multiple cracks 104
5.18 Example with mixed frequencies for a waveguide with multiple cracks 104

List of Tables

3.1 Results of the complex stress intensity factor K_c for the cracked domain under shear load [23] 52
3.2 K_c results for the bi-material crack under tension with the displacement-based method 3.9.2.2 55
3.3 Eigenvalues for the singular points (cf. Figure 3.34b) 55

A.1 Material parameters of the investigated examples 114

Acknowledgements

I would like to express my gratitude to Professor Carolin Birk for her supervision of this dissertation. Her professional competence and patient manner have greatly contributed to this work. I am particularly grateful for her commitment during the final stage of the project. In the same breath, I must also thank Dr. Hauke Gravenkamp, who not only gave the original research idea, but also supervised the work along the way. Through his initiative, the cooperation between the University of Duisburg-Essen and the Bundesanstalt für Materialforschung und -prüfung (BAM) was continued. I would like to extend my appreciation to Professor Andrea Walther for agreeing to be the second reviewer. Moreover, I am grateful to the examination committee, namely Professor Renatus Widmann, Professor Bettina Detmann, and Professor Doru C. Lupascu.

My expressions of gratitude go to the institution and the employees of BAM. I would like to thank: Thomas Heckel for his trust and far-reaching support, Jens Prager for his expertise in guided ultrasound waves, his support for presentations and the introduction to scientific community, and Friedrich Bake for the decisive push to the finish line. I would not like to miss Yevgeniya Lugovtsova's enthusiasm for guided ultrasound and the countless interesting discussions. To get an insight into our collaboration on data analysis of experiments, I refer to her dissertation. Thanks to Fabian Krome and Paul Wasmar for the discussions on numerical methods in general and SBFEM in particular. I am very grateful to my colleagues Reinhard Böhm, Blaž Brence, Gerald Hönig, and Tobias Homann for our discussions. Finally, I thank Daniel Lozano Duarte for our collaboration and his continued research on SBFEM.

I would like to thank friends and family members for their support, especially those who proofread this thesis. Special thanks go to my wife for her constant support.